



UNIVERSITAT DE  
BARCELONA

## Metal Oxides for Optoelectronic and Resistive Switching Applications

Josep Oriol Blázquez Gómez

**ADVERTIMENT.** La consulta d'aquesta tesi queda condicionada a l'acceptació de les següents condicions d'ús: La difusió d'aquesta tesi per mitjà del servei TDX ([www.tdx.cat](http://www.tdx.cat)) i a través del Dipòsit Digital de la UB ([diposit.ub.edu](http://diposit.ub.edu)) ha estat autoritzada pels titulars dels drets de propietat intel·lectual únicament per a usos privats emmarcats en activitats d'investigació i docència. No s'autoritza la seva reproducció amb finalitats de lucre ni la seva difusió i posada a disposició des d'un lloc aliè al servei TDX ni al Dipòsit Digital de la UB. No s'autoritza la presentació del seu contingut en una finestra o marc aliè a TDX o al Dipòsit Digital de la UB (framing). Aquesta reserva de drets afecta tant al resum de presentació de la tesi com als seus continguts. En la utilització o cita de parts de la tesi és obligat indicar el nom de la persona autora.

**ADVERTENCIA.** La consulta de esta tesis queda condicionada a la aceptación de las siguientes condiciones de uso: La difusión de esta tesis por medio del servicio TDR ([www.tdx.cat](http://www.tdx.cat)) y a través del Repositorio Digital de la UB ([diposit.ub.edu](http://diposit.ub.edu)) ha sido autorizada por los titulares de los derechos de propiedad intelectual únicamente para usos privados enmarcados en actividades de investigación y docencia. No se autoriza su reproducción con finalidades de lucro ni su difusión y puesta a disposición desde un sitio ajeno al servicio TDR o al Repositorio Digital de la UB. No se autoriza la presentación de su contenido en una ventana o marco ajeno a TDR o al Repositorio Digital de la UB (framing). Esta reserva de derechos afecta tanto al resumen de presentación de la tesis como a sus contenidos. En la utilización o cita de partes de la tesis es obligado indicar el nombre de la persona autora.

**WARNING.** On having consulted this thesis you're accepting the following use conditions: Spreading this thesis by the TDX ([www.tdx.cat](http://www.tdx.cat)) service and by the UB Digital Repository ([diposit.ub.edu](http://diposit.ub.edu)) has been authorized by the titular of the intellectual property rights only for private uses placed in investigation and teaching activities. Reproduction with lucrative aims is not authorized nor its spreading and availability from a site foreign to the TDX service or to the UB Digital Repository. Introducing its content in a window or frame foreign to the TDX service or to the UB Digital Repository is not authorized (framing). Those rights affect to the presentation summary of the thesis as well as to its contents. In the using or citation of parts of the thesis it's obliged to indicate the name of the author.

Tesi doctoral

# Metal Oxides for Optoelectronic and Resistive Switching Applications

Josep Oriol Blázquez Gómez



UNIVERSITAT<sub>DE</sub>  
BARCELONA



# Metal Oxides for Optoelectronic and Resistive Switching Applications

Programa de doctorat en Física

Autor/a: Josep Oriol Blázquez Gómez

Director/a: Dr. Sergi Hernández Márquez  
Dr. Blas Garrido Fernández

Tutor/a: Dr. Blas Garrido Fernández

Departament d'Enginyeria Electrònica i Biomèdica



UNIVERSITAT DE  
BARCELONA



*Dedicat al la meva família,  
especialment a la Marta, la meva parella,  
i al Roc, acabat de néixer;  
als meus amics i als companys de feina,  
per recolzar-me en cada moment,  
per ajudar-me cadascú a la seva manera,  
per fer realitat aquesta etapa de la meva vida.*



## Abstract

Transparent Conductive Oxides (TCOs) are inorganic materials that simultaneously exhibit both optical transparency and electrical conductivity. TCOs are currently being employed as top electrode in a large number of optoelectronic devices. Recent developments in TCOs have shown their feasibility as active layers for solar cells, light emitting diodes, thin film transistors, optical and electrical sensors and plasmonic devices. However, these developments are based on individual devices fabricated from different materials and technologies. The possibility to use these materials in integrated optoelectronics is a high-tech solution to perform advanced functionalities together with efficient energy consumption for the microelectronics industry. One interesting possibility is using TCOs as host matrix for rare earth (RE) atoms, whose intra-atomic transitions benefit from a narrow and well-defined emission spectrum. Their emission can be modulated by selecting the adequate RE species, being Er typically used for telecommunication wavelengths or Ce, Tb and Eu for visible range applications.

Nowadays, resistive switching materials are providing a solution to the fast scaling in micro- and nano-electronic devices as resistive random access memory (ReRAM) thanks to the possibility to switch between two different resistive states, high resistance state (HRS) and low resistance state (LRS), when a voltage is applied. This resistive switching has its origin in the creation and destruction of conductive paths, mainly promoted by either metal diffusion from electrodes or valence change mechanism. Among the different materials that exhibit this resistive switching properties, metal oxides take advantage of the diffusion of oxygen ions for promoting the generation of oxygen vacancies, consequently inducing the formation of the conductive paths. The excellent electrical conductivity of TCOs in pristine state seems the main drawback for resistive switching applications; however, these compounds can become insulators using the appropriate fabrication process. Thus, the control of the conductivity of these metal oxides (i.e., the control of their stoichiometry) could be employed for using them as active layers for resistive switching applications, or as transparent electrodes in optoelectronics applications.



In this Thesis, both electro-optical and resistive switching properties of different materials have been explored. The first material studied in this Thesis consists of silicon-aluminum oxynitride (SiAlON), whose controlled stoichiometry modification and the incorporation of RE ions as luminescent centers were carried out. In this case, the material exhibits excellent optical properties, showing emission from the RE species. Moreover, SiAlON presents also good resistive switching properties, in which the formation mechanism of conductive paths has been studied at the nanoscale by transmission electron microscopy. This material was also explored by stacking Al-Tb/SiO<sub>2</sub> nanomultilayers via electron beam evaporation. This deposition methodology demonstrated the incorporation of RE ions into the SiO<sub>2</sub> layers, exhibiting both photoluminescence (PL) and electroluminescence (EL) from the Tb<sup>3+</sup> ions. In addition, this material is also showing resistive switching properties under specific voltage excitation.

The other material studied in this Thesis is ZnO. In this case, this material was employed both for hosting RE ions and as a transparent electrical contact. Ions like Tb and Eu were used to determine their compatibility with the ZnO active layer, obtaining excellent results in terms of emission. In addition, this metal oxide presents also good resistive switching properties with and without the inclusion of the RE species. In fact, the incorporation of Tb ions was found to modify the resistive switching properties, which permitted studying their influence over the oxygen diffusion during the creation of the conductive paths. Furthermore, ZnO has been combined with an active layer of silicon nanocrystals, in order to analyze the ZnO properties as a top transparent contact. The EL emission obtained from ZnO/Si NCs/*p*-type Si devices confirms the viability of employing ZnO as *n*-type transparent electrode. Moreover and thanks to the resistive switching properties of Si NCs inside SiO<sub>2</sub>, these devices also permitted analyzing the light emission in different resistive switching states, opening the possibility to fabricate resistive switching devices, whose resistive state can be read both electrically and optically.

## Acknowledgements

Després de més de quatre anys fent el Doctorat en Física, un servidor ha tingut la oportunitat de conèixer molta gent. Tot i que hi ha hagut companys de departament amb els quals hi ha hagut només una simple relació cordial de passadís, una bona part d'ells han estat clau pel bon desenvolupament d'aquest treball tant a nivell professional com personal.

S'ha de dir que el finançament rebut al llarg del doctorat com a becari predoctoral en formació de personal investigador (FPI) dins el projecte nacional *LEOMIS* dirigida pel catedràtic Dr. Blas Garrido, m'ha permès gaudir de la tranquil·litat econòmica requerida en una inversió de futur com aquesta. També he de mencionar el nou projecte nacional *METALONIC* en que, actualment, estem involucrats en el grup de recerca, i del qual està sortint el finançament dels últims estudis realitzats, així com de nou equipament pels laboratoris. També m'agradaria fer un petit recordatori al projecte europeu *NASCEnT*, el qual em va permetre gaudir d'una petita beca de col·laboració dins el grup durant el període d'investigació en el Màster en Nanociència i Nanotecnologia que em va permetre posteriorment fer el salt al doctorat.

És evident que sense els meus directors de tesi res de tot això no hauria estat possible. Primer de tot, voldria agrair al catedràtic Dr. Blas Garrido, qui a través dels seus projectes he pogut introduir-me al món de la recerca, obtenir grans coneixements en el camp científic i gaudir d'una beca predoctoral al llarg de la tesi. Els seus consells, juntament amb el fet que comparteixi experiències en el món de la gestió de projectes amb la resta de grup, m'ha donat una visió científica més enllà d'una simple labor de laboratori. També agrair al Dr. Sergi Hernández, per la seva proximitat en la direcció de la tesis. El seu constant interès per tot el desenvolupament del meu treball m'ha permès obtenir el suport necessari en tot moment i els seus experimentats consells han servit perquè molts cops pogués veure llum on semblava que no n'hi havia.

Cal agrair infinitament els meus companys de grup i de *Despatx Patera*. Amb ells he passat la millor època de la meua vida, vivint

grans moments i sobretot passant-ho molt bé. Primer de tot vull agrair el Dr. Julià López, amb el qual he treballat colza a colza durant tot el doctorat, i amb el que les hores de laboratori mai han sigut avorrides i qui considero el meu tercer director de tesi. També voldria recordar el Dr. Joan Manel Ramírez i en Dr. Yonder Berencén per l'ajuda que hem van donar en els meus inicis en el grup de recerca. Com no agrair el nostre nou estudiant de doctorat Juan Luís Frieiro, que des del primer moment ha estat totalment implicat a tots els nivells i ha mostrat unes capacitats més enllà del que es requereix en un nou estudiant de doctorat. També agrair a l'Adrià Huguet, l'únic de tots nosaltres que ha sabut utilitzar d'una forma intel·ligent els LEDs. Una especial dedicació a la gent del *LENS*, la majoria companys de despatx com en Dr. Lluís López, que ha gaudit d'una FPI que no constava; la Dra. Gemma Martín, qui sempre manté el somriure fins i tot quan està enfadada; en Josep Rebled, inventor de les samarretes 3D; la Catalina Coll, la persona que més beques ha obtingut i ha hagut de renunciar a totes; en Pau Torruella, capaç de llençar una patata a més 200 m amb un desodorant; al Javier Blanco, que encara no ha descobert que les samarretes poden tenir mànigues i al Daniel del Pozo Bueno, llurs maduixes sempre estan disponibles per tothom. No voldria deixar-me les directores del *LENS*, la catedràtica Dra. Francesca Peiró i la Dra. Sonia Estradé, per l'aportació científica en microscòpia electrònica que han aportat en aquesta tesi i la companyia indiscutible a l'hora de dinar. Voldria recordar també el Dr. Giovanni Vescio, company de despatx "post-doc" amb qui he passat bones estones. També aprofitar per desitjar molta sort als futurs estudiants de doctorat del nostre grup Ferrant Bonet i Sergio González, que els sigui tant de profit com ha sigut per mi.

Part d'aquest treball ha sigut gràcies a col·laboracions externes. Voldria agrair al Dr. Pablo Sanchis de la Universitat Politècnica de Valencia, estret col·laborador dels projectes nacionals del nostre grup. També a la Dra. Rosalia Serna i al Dr. Ivan Camps del Institut de Òptica de Madrid (CSIC). Agrair també la col·laboració amb la catedràtica Dra. Margit Zacharias de la Universitat Albert-Ludwigs de Fraiburg, i al Dr. Christophe Labbé i al Dr. Xavier Portier, juntament amb els seus estudiants Dr. Florian Ehré i Clément Guillaume de la Universitat de Caen; a tots ells per la fabricació de fines capes i pel seu interès en els nostres sistemes de mesura electròptica. Finalment, voldria fer una menció especial al Dr. Jordi Ibáñez del

Institut de Ciències de la Terra Jaume Almera (CSIC), el qual m'ha aportat bons consells tant científics com personals i amb el qual he tingut la oportunitat de fer alguna petita col·laboració.

No em vull deixar altra gent del departament, alguns d'ells col·laboradors d'estudis de recerca i d'altres simplement de menjador, tals com la Raquel Pruna, el Dr. Manel López, el Dr. Albet Cirera, el Dr. Albert Romano, el Dr. Paolo Pelegrino, el Dr. Mauricio Moreno i el director del departament el catedràtic Dr. Albert Cornet. També a companys de docència com la Dra. Aïda Varea i el Dr. Oscar Castaño entre altres, i als companys de secretaria especialment la Roser Marzo, Montserrat Farré, per l'ajuda rebuda en molts tràmits.

Finalment, voldria agrair també a la meva família. Especialment a la Marta amb qui ja fa més de tretze anys que vam començar una aventura junts i que aquest juliol ha donat com a fruit en Roc. Sense el seu suport no hagués mai arribat fins aquí. Agrair també als meus pares i les meves germanes els quals sempre han confiat en mi.



# Contents

<b>ABSTRACT .....</b>	<b>V</b>
<b>ACKNOWLEDGEMENTS .....</b>	<b>VII</b>
<b>CONTENTS.....</b>	<b>XI</b>
<b>1. INTRODUCTION.....</b>	<b>13</b>
<b>1.1. METAL OXIDES .....</b>	<b>15</b>
<b>1.2. RARE EARTHS .....</b>	<b>17</b>
<b>1.3. SILICON NANOCRYSTALS.....</b>	<b>21</b>
<b>1.4. RESISTIVE SWITCHING .....</b>	<b>25</b>
<b>1.5. OBJECTIVE OF THE DOCTORAL THESIS.....</b>	<b>28</b>
<b>1.6. OUTLINE OF THE THESIS.....</b>	<b>30</b>
<b>2. DEPOSITION METHODS AND SAMPLE CHARACTERIZATION .....</b>	<b>33</b>
<b>2.1. SAMPLE FABRICATION METHODS.....</b>	<b>33</b>
2.1.1. Chemical Deposition Techniques .....	34
2.1.1.1. Plasma-Enhanced Chemical-Vapor Deposition.....	35
2.1.1.2. Atomic Layer Deposition .....	37
2.1.2. Physical Deposition Techniques .....	38
2.1.2.1. Sputtering .....	39
2.1.2.2. Pulsed-Laser Deposition.....	40
2.1.2.3. Electron-Beam Evaporation .....	42
2.1.3. Photolithography process .....	44
<b>2.2. STRUCTURAL AND CHEMICAL CHARACTERIZATION .....</b>	<b>46</b>
2.2.1. Electron Microscopy Techniques .....	46
2.2.2. X-Ray Photoelectron Spectroscopy .....	48
<b>2.3. OPTICAL CHARACTERIZATION .....</b>	<b>49</b>
2.3.1. Photoluminescence Spectroscopy .....	50
2.3.2. Time-Resolved Photoluminescence .....	53
<b>2.4. ELECTRICAL CHARACTERIZATION .....</b>	<b>54</b>
2.4.1. Charge Transport Mechanisms .....	55
2.4.1.1. Bulk-Limited Mechanisms .....	56
2.4.1.2. Electrode-Limited Mechanisms.....	58
2.4.2. Resistive Switching Characterization.....	61
<b>2.5. ELECTRO-OPTICAL CHARACTERIZATION.....</b>	<b>62</b>
2.5.1. Electroluminescence Spectroscopy.....	62
2.5.2. Time-Resolved Electroluminescence.....	62
<b>3. SI-BASED MATERIALS FOR OPTOELECTRONICS AND RESISTIVE SWITCHING</b>	<b>65</b>
<b>3.1. SILICON-ALUMINUM OXYNITRIDE (SiAlON) .....</b>	<b>65</b>
3.1.1. Optical and Electro-Optical Properties.....	67
3.1.1.1. Ce-doped SiAlON by RF sputtering.....	67
3.1.1.2. Eu-doped SiAlON by PLD .....	68
3.1.2. Resistive Switching Properties .....	70
3.1.2.1. SiAlON as resistive switching device.....	70

## Contents

<b>3.2. MULTILAYERED AL-Tb/SiO<sub>2</sub></b> .....	<b>72</b>
3.2.1. Optical and Electro-Optical Properties .....	73
3.2.1.1. Al and Tb delta-doped SiO <sub>2</sub> by e-beam evaporation .....	73
3.2.1.2. Structural and optical properties of Al-Tb/SiO <sub>2</sub> .....	75
3.2.1.3. Electroluminescence of Al-Tb/SiO <sub>2</sub> devices .....	77
3.2.2. Resistive Switching Properties .....	79
3.2.2.1. Tb-Al/SiO <sub>2</sub> as resistive switching device.....	79
<b>3.3. PAPER I</b> .....	<b>84</b>
<b>3.4. PAPER II</b> .....	<b>99</b>
<b>3.5. PAPER III</b> .....	<b>107</b>
<b>3.6. PAPER IV</b> .....	<b>115</b>
<b>3.7. PAPER V</b> .....	<b>123</b>
<b>4. MATERIALS FOR OPTOELECTRONICS AND RESISTIVE SWITCHING</b> .....	<b>131</b>
<b>4.1. Tb- AND Eu-DOPED ZnO</b> .....	<b>131</b>
4.1.1. Optical and Electro-Optical Properties .....	132
4.1.2. Resistive Switching Properties .....	138
4.1.2.1. ITO/ZnO/ <i>p</i> -Si structure as resistive switching device .....	138
4.1.2.2. Effect of RE ions on the resistive switching properties .....	140
<b>4.2. ZnO/Si-NCs/<i>p</i>-Si LIGHT EMITTER</b> .....	<b>143</b>
4.2.1. Optical and Electro-Optical Properties .....	144
4.2.1.1. Modulation of ZnO emission via pulsed excitation .....	144
4.2.1.2. Effect of Si <sub>3</sub> N <sub>4</sub> inversion layer on Si-NCs emission .....	146
4.2.2. Resistive Switching Properties .....	149
4.2.2.1. ZnO/Si-NCs/ <i>p</i> -Si as resistive switching device .....	149
<b>4.3. PAPER VI</b> .....	<b>155</b>
<b>4.3. PAPER VII</b> .....	<b>167</b>
<b>4.4. PAPER VIII</b> .....	<b>173</b>
<b>5. SUMMARY AND CONCLUSIONS</b> .....	<b>183</b>
<b>6. RESUM EN CATALÀ</b> .....	<b>187</b>
<b>A. LIST OF PUBLICATIONS PRESENTED IN THIS THESIS</b> .....	<b>189</b>
<b>A.1. LIST OF ARTICLES</b> .....	<b>189</b>
<b>A.2. PAPER CONTRIBUTION STATEMENT</b> .....	<b>190</b>
<b>B. CURRICULUM VITAE</b> .....	<b>193</b>
<b>B.1. JOURNAL PUBLICATIONS</b> .....	<b>193</b>
<b>B.2. BOOK CHAPTERS</b> .....	<b>195</b>
<b>B.3. CONFERENCE CONTRIBUTIONS</b> .....	<b>195</b>
<b>B.4. SEMINARS, WORKSHOPS AND/OR COURSES</b> .....	<b>200</b>
<b>B.5. PARTICIPATION IN RESEARCH PROJECTS</b> .....	<b>200</b>
<b>B.6. EXPERIENCE SUPERVISING THESIS AND/OR DEGREE PROJECTS</b> .....	<b>201</b>
<b>B.7. TEACHING EXPERIENCE</b> .....	<b>202</b>
<b>BIBLIOGRAPHY</b> .....	<b>205</b>

# 1. Introduction

---

*“Because it is so clear, it takes a long time to realize it. If you immediately know the candlelight is fire, the meal was cooked a long time ago”*

*Oma Desala*

---

Since the development of electronics during the second half of the past century, silicon (Si) became the most employed semiconducting material due to its excellent physical properties [1, 2]. With its rather low-energy band gap (1.12 eV, near infra-red) Si exhibits a high conductivity. Its mechanical and thermal stability, in part attributed to a high crystalline quality of its zinc-blende structure, added to its non-toxicity, Earth-abundance (Si is the second chemical element in the Earth’s crust after oxygen) and mining easiness, makes Si an optimum material for manipulation and mass-scale production. Indeed, the present microelectronics industry is based on Si, and industrial fabrication processes are well developed on very large scale.

Recently, the demand for faster interconnections and lower transmittance medium dependence has led to a dramatic change and development of the field of photonics, in which the main data transport takes place via photons instead of electrons. The need for non-material based (i.e., less susceptible to heat losses) connections has made way to the use of light through the so-called photonic integrated circuits (PICs), where the basic device components must transmit, emit and/or sense photons in a controlled way. This accomplishment would be a revolution in data computing and communications, providing to the industry a most promising low-cost technology for telecommunications, optical sensors and even biosensing applications [3–6].

The compatibility with the complementary metal-oxide-semiconductor (CMOS) technology is required to take advantage of its excellent fabrication reliability, together with the direct integration



## 1. Introduction

with other components. Therefore, the role of optoelectronics, i.e., the development of devices able to efficiently convert photons to electrons or vice versa, has acquired a great relevance for semiconductors industry, and the search for novel materials able to provide such efficient electron-to-photon conversion has been boosted. In this way, photonic devices have been developed like optical modulators [7], photodetectors [8] or light emitters [9] in the long-distance data transmission windows, which ranges between 1300 nm and 1550 nm of wavelength. In the visible range, light emitting devices have undergone an important evolution along decades with the light emitting diodes (LEDs), recently completing all the visible spectrum with the fabrication of the blue LED [10]. Unfortunately, the indirect nature of the bulk Si band gap states a bottleneck for an all-Si based photonics and optoelectronics, because the fundamental valence band (VB)-to-conduction band (CB) transition is strongly quenched due to the mismatching in wavevector in the reciprocal space. Different solutions for silicon-compatible light emitters have been proposed using metal oxides [11, 12], combining the properties of SiO<sub>2</sub> and Si<sub>3</sub>N<sub>4</sub> within silicon oxynitrides [13], doping the materials with rare earths (REs) [14, 15] or nanostructuring Si to improve its optical properties [16, 17].

Nowadays, the poor energy efficiency of CMOS transistors and the fast scaling in memories are considered a serious drawback within the new era of big data and Internet of Things. This fact leads to the search of a new generation of ultra-low-power nanodevices to overcome this important challenge that the electronics industry faces. Resistive switching (RS) memories or resistance random access memories have become a solution for the next generation of nonvolatile memories thanks to their low-power operation, high switching speed and compatibility with the CMOS technology. There are many different binary compounds that are currently under study for being used as resistive switches, such as metal oxides and refractory materials like TiO<sub>2</sub>, SnO<sub>2</sub>, HfO<sub>2</sub>, Ta<sub>2</sub>O<sub>5</sub>, and ZnO, among others. They have shown resistive switching response by forming Metal-Insulator-Metal (MIM) structures, where the metals are typically Ni, Al, Cu, Ag or Ti [18–26].

Thus, earth abundant metal oxides and/or refractory materials, which are compatible with the CMOS technology, would allow developing

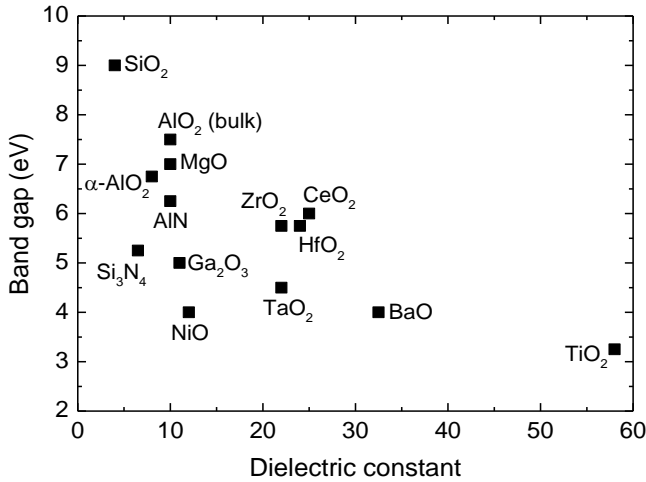
new devices and functionalities by the integration of electronic and photonic devices within the same chip. With the aim of developing the bases of a new technological platform that combines both ReRAM and electroluminescent devices, concepts and materials (on which this Thesis is focused) are introduced in the following subsections, in order to understand the fundamentals that govern them. In addition, the objectives pursued in this Thesis are enumerated at the end of this chapter. Finally, the contents of the different chapters of this Thesis are briefly summarized.

## 1.1. Metal Oxides

Beyond the hydrogenated amorphous silicon, which has been the most employed semiconductor in microelectronics, metal oxides (MOs) have been widely studied in order to overcome drawbacks like the optical opacity, mechanical flexibility or the low carrier mobility (around  $1 \text{ cm}^2 \text{ V}^{-1} \text{ s}^{-1}$ ) that it exhibits. The first thin-film transistor (TFT) based on MO was reported in 1964 using  $\text{SnO}_2$  [27], whose performances were enhanced in following studies [28]. Other TFTs were also reported based on polycrystalline MO materials like  $\text{In}_2\text{O}_3$  [29] or  $\text{ZnO}$  [30]. Amorphous MO semiconductors were also implemented, being one of the most interesting application the utilization of In-Ga-Zn oxide as active-matrix in displays [31]. The fact that many MOs present energy gaps larger than 3 eV is suitable for optical application due to the transparency in the visible range that these materials present. As well, electron mobility ( $\mu_e$ ) in MOs shows a power law dependence on the dielectric constant of the applied insulator gate [32]. This fact has been employed in the case of  $\text{ZnO}$  grown by radiofrequency magnetron sputtering, increasing the  $\mu_e$  from  $1.2 \text{ cm}^2 \text{ V}^{-1} \text{ s}^{-1}$  to  $50 \text{ cm}^2 \text{ V}^{-1} \text{ s}^{-1}$  using  $\text{Ta}_2\text{O}_5$  as gate insulator [33]. However, the carrier density can be difficult to control because of the large number of oxygen vacancies typically observed in MOs.

Other MOs, also of great interest, are the so-called transparent conductive oxides (TCOs). These materials are MOs that exhibit wide-range optical transparency due to its high energy band gap, while simultaneously presenting electrical conductivity. Oxides like  $\text{In}_2\text{O}_3$ ,  $\text{SnO}_2$  or  $\text{ZnO}$  have shown to be suitable as TCO, being implemented in a lot of transparent devices. The introduction of dopant ions can increase the optical band gap due to the Burstein-

## 1. Introduction



**Figure 1.1.** Energy band gap versus dielectric constant of different oxides and nitrides.

Moss effect, in which the states close to the conduction band are populated, thus obtaining a degenerated semiconductor and, consequently, increasing the energy band gap. The electrical and optical properties of TCOs depend on the electron concentration ( $N$ ) and  $\mu_e$ , shifting to shorter wavelength when  $N$  increases. However, in solar cell application, in which TCOs are employed as transparent electrode, a high carrier mobility with low  $N$  is preferable. Typically, doping has been the employed technique to increase  $N$ , but recently, epitaxy-grown SrVO<sub>3</sub> and CaVO<sub>3</sub> films have presented high conductivity and transparency, even at high values of  $N > 2.2 \times 10^{22} \text{ cm}^{-3}$  [34]. One of the most employed TCO is indium tin oxide (ITO), which exhibit very low resistivity (about  $10 \text{ } \Omega \text{ sq.}^{-1}$ ) and an excellent optical transparency due to its  $\sim 4.0 \text{ eV}$  of energy band gap.

Metal oxides have also demonstrated to be excellent host matrices for rare earth ions. Different studies have reported light emission from the rare earth in metal oxide matrices like Al<sub>2</sub>O<sub>3</sub> [35, 36] or ZnO [37–39], presenting excellent optical properties compared to SiO<sub>2</sub> one [40–42]. The differences in the band gap and their electrical properties have made these MOs of great interest to optimize the efficiency of these rare earths as luminescent centers. Moreover, some MOs are suitable for random access memories, in which different resistive states of the material can be selected. Both rare earth atoms and the resistive

switching properties will be introduced in the following subsections of this chapter.

Great efforts have been made to implement and understand MOs within the optoelectronics industry, demonstrating good advances in the past years. The integration of TCOs as transparent electrode in photovoltaics and light emitters and the possibility to be employed as host matrix for rare earth atoms has opened the possibility to develop transparent devices for several applications. In addition, the fact that the electrical and the optical properties of MOs can be tuned via the incorporation of some dopants or using their resistive switching properties, confirms the potential of these materials as the new generation of devices.

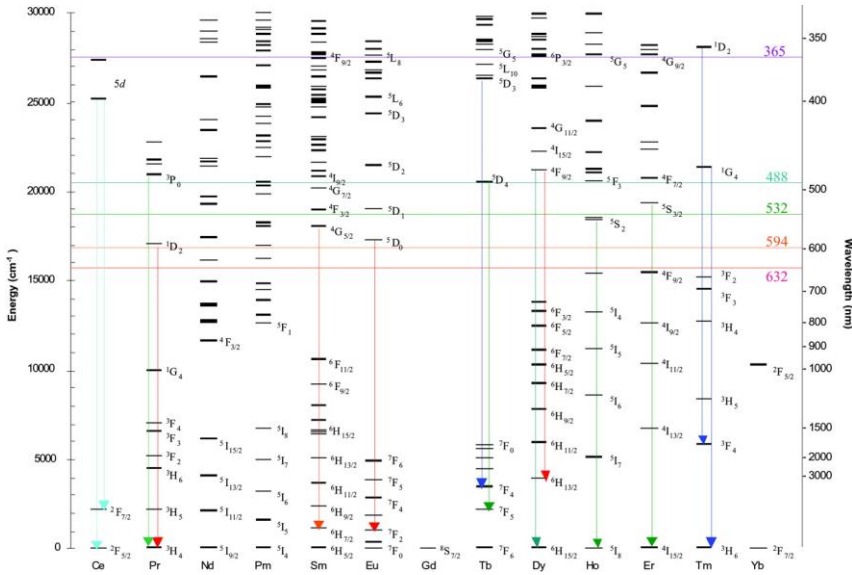
## 1.2. Rare Earths

Rare earths (REs) atoms, which belong to the lanthanide and actinide families, exhibit particular optical properties due to their intra  $f$ -shell transitions [43]. The 4- or  $5f^N$  energy levels arise from different atomic interactions as a result of solving the Schrödinger equation. In the case of an individual RE atom, its Hamiltonian can be written as an isolate ion with some perturbations expressed by

$$H(t) = H_0 + V_{RE-matter} + V_{EM}(t) + V_{RE-RE}(t), \quad (1.1)$$

where  $H_0$  is the Hamiltonian of an isolated ion,  $V_{RE-matter}$  the Hamiltonian attributed to the effect of the local environment on the RE,  $V_{EM}$  is the electromagnetic field influence and  $V_{RE-RE}$  the interaction between neighboring RE ions. The two first terms are time independent and result in the observed electronic structure of the RE atom. The other terms are time dependent and give rise to transitions between the states established by the static interactions. When these atoms are in the trivalent state, well-resolved and efficient electronic transitions can take place, presenting very low electron-phonon coupling. This optical activation is suitable to absorb and emit photons when ions are conformed in a pseudo-octahedral structure with  $C_{4v}$  symmetry into the host matrix [44]. Once electrons are promoted to other energetic levels, the de-excitation occurs emitting photons, whose energies are well defined and depend on the specimen. The dynamics of this process is typically around some milliseconds, being

1. Introduction



**Figure 1.2.** Energy level diagram of trivalent RE ions with dominant visible emission transitions observed in silicate glasses designated by arrows representing the approximate color of the luminescence. Horizontal lines extending across the diagram designate the location of common organic label excitation sources labeled by the wavelength in nm. The 365-nm line was used to excite the RE ions [122].

strongly dependent on the non-radiative processes induced by a local environment [45].

The narrow and intense emission of these transitions has attracted the attention of researchers to be employed as luminescent centers. Depending on the selected RE, a wide range of wavelengths can be obtained, being the 1.54- $\mu\text{m}$  line of  $\text{Er}^{3+}$  ions one of the most interesting ones for the possibility to work in the integrated telecommunication windows [46]. Visible range has also been benefited due to the possibility to cover all spectrum with different colors; blue ( $\text{Ce}^{3+}$  and  $\text{Tm}^{3+}$ ) [47–49], green ( $\text{Tb}^{3+}$  and  $\text{Er}^{3+}$ ) [48–52], yellow ( $\text{Dy}^{3+}$ ) [49, 53], orange ( $\text{Sm}^{+3}$ ) [54] and red ( $\text{Eu}^{3+}$ ) [52, 54], being their implementation in displays the most promising application [55]. In the Figure 1.2, a representation of the energetic levels of different REs is shown.

Several fabrication processes, compatible with the CMOS technology, have been used to develop RE-doped luminescent materials. In order to obtain a homogeneous distribution of REs into the host matrix, techniques like co-sputtering and co-evaporation have been commonly employed, in which the host matrix and the RE are simultaneously deposited from different targets at different deposition rates [56]. Other solution consists in using a single target that has been previously synthesized as a mixture of both RE and host matrix material in the adequate relative composition [54, 57]. A similar strategy uses the pulsed-laser deposition (PLD) technique, in which targets are ablated by the energetic pulse of a laser. Chemical deposition methods have also demonstrated to be an efficient, cheap and low-temperature doping technique, in which this doping takes place as a result of chemical reaction; sol-gel is the most common one, where the RE atoms are typically introduced via dissolution of corresponding inorganic salts [58, 59].

Sometimes, an annealing process is required for the optical activation of the REs, achieving the correct conformation in the local environment. In addition, the large size of this kind of atoms induces some local defects, which influence directly on the conformation of the RE ions. These defects can be also generated during the doping process, especially if the introduction of the REs is aggressive, such as in ion-implantation doping method [60]. In these cases, the thermal treatment can reduce these defects by structural reordering.

One of the key points for obtaining optical emission from the REs is to avoid non-radiative processes. This effect occurs when an energy transfer assisted by a phonon takes place between the RE atom and either the host matrix or another RE atom. The dynamics of these processes can be rapid and efficient if the electronic energy separation is close enough. In the case of high concentration of REs, the  $V_{RE-RE}$  interaction of the equation (1.1) plays an important role. This interaction can occur in different forms. The first one is related to the cross-relaxation process. When the energy transfer occurs from an ion at an excited state (donor) to another ion at a lower energy state (acceptor), a phonon can be involved if there is an energy mismatch between the energy gaps of both ions. Another possibility is the energy transfer up-conversion, in which both ions are initially excited and an energy transfer is carried out from the donor to the acceptor,

## 1. Introduction

thus promoting the acceptor ion to a higher energy state. The energy transfer of this ion, when relaxed to the ground state, can be higher than the obtained one from the donor ion. If the RE concentration is high enough, clustering can occur [61, 62]. This effect is attributed to the fact that RE ions need a coordination with non-bridging oxygens, but the host matrix is not able to supply all of that, increasing the enthalpy of the system. Consequently, RE ions tend to share these non-bridging oxygens, reducing this enthalpy. Different strategies have been explored to increase the solubility of REs ions into the host matrix [63, 64]. The most interesting consists in the introduction of metallic atoms inside the host matrix, such as Al [65, 66]. The formation of RE-Al complexes provide valence compensation of the RE ions for three substitutional Al ions. This effect can increase the number of optically-active RE ions, enhancing the efficiency of the luminescence.

In order to increase the excitation efficiency of REs, different strategies have also been explored. Typically, RE excitation can be obtained either via direct excitation using the same energy than the intra  $f$ -shell transition in the RE (resonant condition) or via energy transfer from excitons towards the material (non-resonant condition). In this second case, different kind of donor centers can be employed, being normally the own host matrix the main responsible of this energy transfer [47, 67]. However, the introduction of other elements such as other RE species has been used to induce alternative energy transfer processes. In the case of Tb and Eu co-doped ZnO thin films, an energy transfer from Tb<sup>3+</sup> ions to Eu<sup>3+</sup> ion has been observed [37], in which the energy emitted by the  $^5D_4 \rightarrow ^7F_6$  radiative transition of Tb<sup>3+</sup> is absorbed by Eu<sup>3+</sup> ions, thus inducing the  $^7F_6 \rightarrow ^5D_1$  transition of the latter.

Different Si-based matrices have been employed like SiO<sub>2</sub> or Si<sub>3</sub>N<sub>4</sub>, being the former the most employed one due to the low fabrication cost and the large band gap energy (9 eV) that it exhibits [68]. However, Si<sub>3</sub>N<sub>4</sub> has become a promising candidate as RE host matrix in optoelectronic devices for its excellent electrical properties. In spite of presenting lower band gap energy (5 eV), charge injection is easier than in SiO<sub>2</sub>, being more suitable to obtain electroluminescence from REs with low energetic photons emission, like Er<sup>3+</sup> ions, which emits in the near infrared (NIR) [42, 69]. In this way, other metal oxides

have also been explored as RE host matrices like  $\text{Al}_2\text{O}_3$  [70, 71],  $\text{TiO}_2$  [72, 73], even polymeric matrices, offering a low-cost alternative inorganic waveguide amplifiers [74, 75]. In addition, this matrix has also been used to host  $\text{Ce}^{3+}$  and  $\text{Tb}^{3+}$  ions, whose emission lies within the visible range [76]. Strong emission from  $\text{Tb}^{3+}$  ions was also observed in Tb-doped Si-rich oxide under the presence of Si-NCs. In samples annealed at low temperature, in which Si nanostructures have not yet been formed, no emission from intra  $f$ -shell transitions of the RE was observed. However,  $\text{Tb}^{3+}$  emission suddenly increases after the Si-NCs formation, once the samples were annealed at high temperature. Similar situation was observed in the case of Ce-doped Si-rich oxide, observing an enhancement of the RE emission at high temperature.

### 1.3. Silicon Nanocrystals

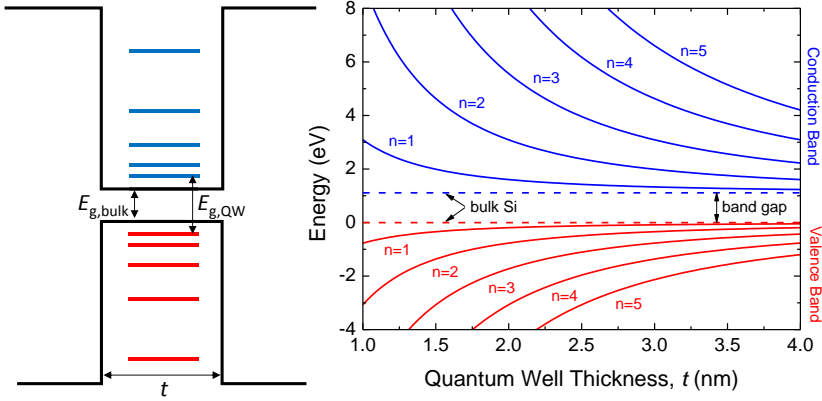
As it has been mentioned, silicon presents poor light emission properties due to the indirect band gap that it presents. This fact decreases substantially the band-to-band transition probability because of the change in the wavevector because of lattice phonon generation. The energy band gap of this transition corresponds to 1.12 eV, which is located in the NIR, avoiding the visible range (1.77 – 3.1 eV) and the third window of telecommunication (0.8 eV). These optical properties have become the main drawback to use Si for optical applications. However, when Si is nanostructured quantum confinement takes place. Consequently, carrier confinement is maximized in a small spatial region, which strongly reduces the probability of non-radiative recombination and, therefore, it increases the radiative recombination probability by delocalization of the wavefunction in the momentum space, which in turn induces electron-hole wavefunction overlap. In addition, a blue-shift emission towards the visible range is achieved, which depends on the Si-NC size.

In a perfect crystal, the potential associated to a particle into this structure can be described as a periodic function due to its translational symmetry. Hence, the wavefunction represented in the reciprocal space is called *Bloch function* and corresponds to:

$$\Psi(\vec{s}) = e^{i\vec{k}\cdot\vec{r}} u(\vec{s}), \quad (1.2)$$



## 1. Introduction



**Figure 1.3.** (left) Scheme of the band diagram showing the discrete and higher energy levels within the quantum well with thickness  $t$ . (right) Representation of the energy bands at different states  $n$  as a function of the quantum well thickness.

being  $u(\vec{s})$  a function with the period of the lattice structure and  $\vec{k}$  the wavevector. In the case of an infinite lattice, the allowed energy states  $E_n$  of these particles can be obtained through the Schrödinger equation:

$$H(\vec{s})\Psi_n(\vec{s}) = \left[ \frac{|\vec{p}|^2}{2m} + W(\vec{s}) \right] \Psi_n(\vec{s}) = E_n \Psi_n(\vec{s}), \quad (1.3)$$

where  $H(\vec{s})$  operates as Hamiltonian, which describes the kinetic and potential energies of the particle, with momentum  $p$  and mass  $m$ . Solving the Eq. (1.3), the obtained energy can be expressed as:

$$E_n(\vec{k}) = \frac{\hbar^2}{2m^*} (k_x^2 + k_y^2 + k_z^2), \quad (1.4)$$

being  $\hbar$  the reduced Plank's constant and  $m^*$  the effective mass of the carriers. However, when the crystal is nanostructured, and then it is no more considered infinite, this translational symmetry is lost and the boundary conditions must be taken into account. In the case that one lateral dimension of the crystal is reduced to some tenths of the lattice parameter (what is called a quantum well), the need to keep continuous both the carrier wavefunction and its derivative at the boundaries implies a discretization in the energetic states in the confinement direction in the form of

$$E_n(\vec{k}) = \frac{\hbar^2}{2m^*} \left( \frac{n^2 \pi^2}{t^2} + k_y^2 + k_z^2 \right), \quad (1.5)$$

where  $n$  is the energetic level and  $t$  the size of the crystal in the corresponding direction ( $x$  in this case). As a consequence, the energy band of electrons and holes are shifted with respect to the minimum of the CB and the maximum of the VB, respectively. This shift increases the band gap energy and it depends on the thickness of the quantum well (see Figure 1.3). This effect can be extended to the other directions, having 1-dimensional quantum wires ( $x,y$ -confinement) or 0-dimensional quantum dots ( $x,y,z$ -confinement). Hence, the band gap energy of a nanostructured crystal can be expressed as the band gap energy of the bulk material with energy perturbations related to the quantum confinement of the electron and hole energy bands, such as it is expressed in:

$$E_{g,conf} = E_{g,bulk} + \Delta E_{e,conf} + \Delta E_{h,conf}. \quad (1.6)$$

In the case of Si-NCs, which are quantum dots (QDs), many researchers have experimentally determined that this band gap energy can be expressed as:

$$E_{g,QD} = E_{g,bulk} + \frac{A}{d^N}, \quad (1.7)$$

in which the variation of the band gap is governed by a power law of the nanocrystals diameter [77–79]. Such as it is expressed in the Eq. (1.5), the theoretical value of  $n$  should be 2; however, lower values have been reported [80]. These discrepancies can be related with the presence of stress induced by the host matrix in which the nanocrystals are embedded, modulating the band gap energy. *Ab-initio* calculations have corroborated this hypothesis, obtaining good agreement with experimental results [81–83].

Light emission in the visible range from Si-NCs was observed and reported in 1988 by Furukwa and Miyasato [84], who also determined the optical band gap energy modulation as a function of the Si-NC size. Similar optical properties were observed by Canham in 1990, who published photoluminescence in the visible range from mesoporous Si [85]. In this case, the pore width played the role of Si

## 1. Introduction

quantum wire diameter, whose modification induced the shift of the peak emission. These optical properties have opened the possibility to introduce Si in optoelectronic applications, which have been since long governed by III-V semiconductor materials due to their better optical properties.

These Si-NCs properties have also been employed in light emitting devices using metal-insulator-semiconductor (MIS) structures, being the Si-NCs embedded in the insulator layer. Dielectric materials like  $\text{SiO}_2$  or  $\text{Si}_3\text{N}_4$  have demonstrated to be good host matrices for these nanostructures; however, the high current requirement for the luminescent centers excitation is a drawback for carrier injection, consequently achieving power efficiencies lower than 1 % [86]. In this case, the charge transport mechanism that governs the device can be crucial in the excitation of Si-NCs. For example, defective matrices like  $\text{Si}_3\text{N}_4$  present a charge transport via defects [87], while tunnel injection transport is typically reported on  $\text{SiO}_2$  [88]. These transport mechanisms and the subsequent electroluminescence of the Si-NCs have been largely investigated during the last years, being nowadays still under discussion.

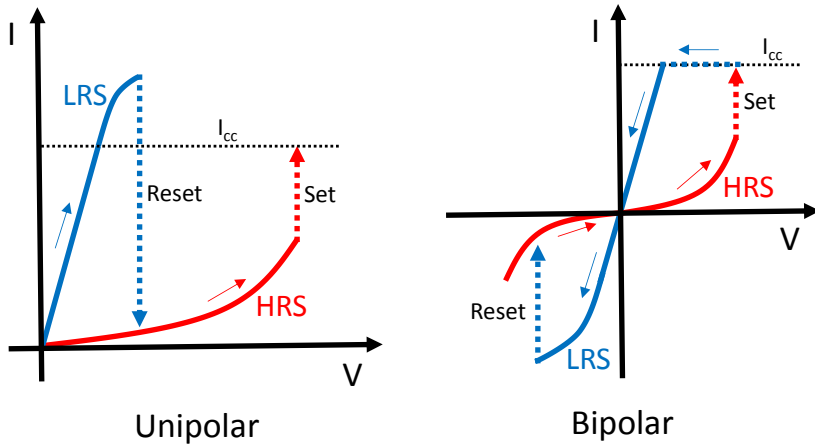
Different fabrication techniques have been employed for the Si-NC synthesis, in which an extra Si content in an oxide is the key for its formation. This non-stoichiometry is typically achieved either via Si ion implantation on stoichiometric  $\text{SiO}_2$  film or growing directly Si-rich  $\text{SiO}_x$ . The control of the Si-NC size and its crystalline degree lies in this non-stoichiometry and the post annealing treatment [89, 90]. It is in this post thermal process when the formation of these nanostructures takes place, via Si precipitation in the form of nanoaggregates. Annealing temperatures around 900 °C can promote the formation of these nanostructures in amorphous state; however, higher temperatures induce their crystallization. In the case of the multilayered structure, in which  $\text{SiO}_x/\text{SiO}_2$  stacks are sequentially deposited onto the substrate,  $\text{SiO}_2$  layers act as Si diffusion barrier, limiting the growth of the Si-NCs. Other materials were also employed as diffusion barriers using this approach, such as  $\text{Si}_3\text{N}_4$  [91, 92] and SiC [78, 93].

## 1.4. Resistive Switching

The increasing necessity to store more information in integrated circuits is being an important drawback in the microelectronics industry. Different random access memories (RAMs) have been developed using physical properties like magnetic tunnel junctions in magnetoresistive RAM (MRAM) or phase-change RAM (PRAM), in which the resistance changes due to the switching between amorphous and crystalline states. However, a new candidate called resistance RAM (ReRAM) has emerged and is being largely studied for its interesting electrical properties. In this kind of devices, the resistance can be modified thanks to the formation of conductive paths in the form of conductive nanofilaments (CNFs) across an insulating layer, thus connecting the two sandwiching electrodes. The formation of these CNFs takes place due to the electrical stress of the layer, which induces a partial breakdown of the insulator. This first formation (Electroforming) has to be accurate for an adequate operation of the device. Sometimes, this process occurs abruptly and an external current limitation is required to avoid permanent damage by setting a current compliance (CC). The possibility to dissolve or interrupt these CNFs allows these devices to switch between two resistance states, high resistance state (HRS) and low resistance state (LRS), depending on whether the CNFs are interrupted (Reset) or reconnected (Set), respectively.

In 1962, Hickmott observed hysteretic  $I(V)$  curves in metal-insulator-metal (MIM) made of Al/Al<sub>2</sub>O<sub>3</sub>/Al, suggesting this kind of behavior [94]. During the next years, other similar studies were also reported in other metal oxides like SiO and NiO [95, 96]. In 1971, Chua published an article theorizing this behavior [97], but it was in 2002 when the Sharp Corporation and the University of Houston demonstrated a thin film ReRAM based on CMOS technology using Pr<sub>0.7</sub>Ca<sub>0.3</sub>MnO<sub>3</sub> [98], and two years later, Samsung did it using transition metal oxides [99]. Since then, a lot studies using different materials have been presented and the mechanism of resistive switching has been investigated both experimentally [100, 101] and theoretically [102, 103].

## 1. Introduction



**Figure 1.4.** The two resistive switching modes. In Unipolar switching, Set and Reset occur at the same electrical polarity. However, in Bipolar, an opposite electrical polarity between the Set and the Reset is required for the resistive switching effect to take place. The ICC denotes the compliance current needed to avoid permanent damage.

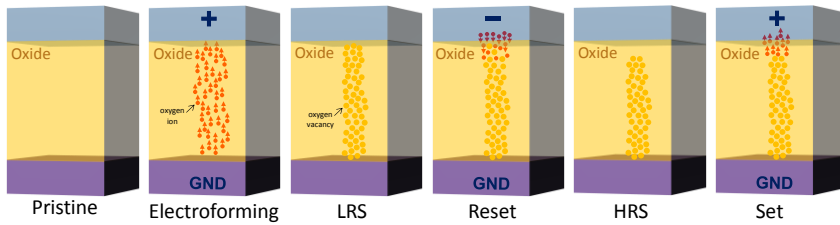
In terms of the  $I(V)$  characteristics, two kind of behaviors have been observed, unipolar and bipolar. In the first one, the resistive switching does not depend on the polarity of the applied voltage, being only the amplitude the critical parameter. In contrast, in bipolar resistive switching, a specific voltage polarization is required to change between resistance states. In the Figure 1.4, both modes are schemed, in which the arrows represent the evolution of the voltage ramps along the whole resistive switching cycle. Regarding the mechanism that governs the resistive switching process, this phenomenon can be classified depending on the mechanism of the conductive path formation. One possibility is metal diffusion, in the form of filament, from the electrode into the insulator, called electro-chemical metallization (ECM). In this case, a metallic electrode is required and it is typically observed in MIM devices. Hirose, in 1976, reported for the first time this effect using Ag-photodoped amorphous  $As_2S_3$  as insulator [104]. In this case, the Reset was achieved by the dissolution of this metal filament at the edge. This switching effect is observed in materials that are cation conductors such as Ag in  $Ag_2S$  or in  $GeSe_x$  [104], Cu in  $Ta_2O_5$  [105], or Zn and Cd in  $WO_3$  and  $SiO_2$  [106, 107]. Another possibility consists in the valence change mechanism (VCM), in which the conductive filament is formed due to the

formation of defective paths into the material. This kind of behavior is particularly observed in transition metal oxides, being oxygen vacancies the responsible of these conductive paths for the migration of the oxygen ions. When an opposite voltage is applied, oxygen ions can be recovered by the vacancies, inducing the reoxidation of the metal and, consequently, achieving the HRS. Resistive switching of metal oxides like  $Ta_2O_5$ ,  $Nb_2O_3$  or  $TiO_2$  have been reported, demonstrating this same behavior [108–110].

The most common employed materials in resistive switching applications are metal oxides. Despite some of them are governed by the ECM mechanism when metallic electrodes are used, the VCM is typically the main mechanism in this kind of materials. The Figure 1.5 describes, step by step, a complete resistive switching cycle, where both LRS and HRS states and the different processes of Electroforming, Set and Reset are represented. In this case, when a positive voltage is applied on the electrode of a pristine device, oxygen ions drift towards this electrode, leaving behind oxygen vacancies. These defects form the CNFs, connecting both electrodes and thus inducing the LRS. When a negative voltage is applied, oxygen ions drift to the oxide layer, oxidizing part of the CNFs near the electrode. Therefore, the CNFs are interrupted and the device recovers its HRS because of the metal oxide gap between the electrode and the rest of the CNFs. At this point, the LRS can be again achieved applying a positive voltage that induces the reconnection of electrodes via the generation of oxygen vacancies in the mentioned gap. Sometimes, these oxygen ions can be accumulated at the interface between the electrode and the metal oxide in the form of  $O_2$  gas due to the oxygen ion neutralization when contacted with a metallic electrode. If this gas eruption is strong enough, the electrode can suffer some mechanical deformations, typically resulting in a bubble-like shape.

Since the realization of the first memristor, the resistive switching effect has been extensively studied in the case of oxides, due to the structural nature of such materials. In particular, several works have been recently reported on different metal oxides, such as transition metal oxides and refractory materials like  $TiO_2$ ,  $SnO_2$ ,  $HfO_2$ ,  $Ta_2O_5$ , and  $ZnO$ , some of them in combination with suitable metallic electrodes, typically based on either Ni, Al, Cu, Ag or Ti [18, 21, 23].

## 1. Introduction



**Figure 1.5.** Sketch Sketch of a resistive switching device structure, showing the different steps and states along a cycle. In Pristine state, the material does not undergo any structural modification. In the Electroforming process, negative oxygen ions drift towards the top electrode while generating oxygen vacancies. The LRS is attained once the CNF is formed by the previously generated oxygen vacancies. In the Reset process, negative voltage is applied on the top electrode, inducing the diffusion of oxygen ions back to the insulator, which occupy the oxygen vacancies. The HRS is achieved when the CNF is interrupted close to the electrode. Finally, the Set process takes place after applying a positive voltage on the electrode, promoting again the oxygen ion diffusion and reconnecting again the CNF to the electrode.

Within the oxide materials group, ZnO,  $\text{Sn}_x\text{O}_2$  and ITO (In-doped  $\text{Sn}_x\text{O}_2$ ) require a particular mention, since they have proved to exhibit both optical transparency and high conductance, being thus candidates as TCOs. Another interesting system, compatible with the CMOS technology, is Si-NCs/ $\text{SiO}_2$  or, more in general, Si-rich oxide [111]. The ability to tune the Si excess in a controlled way during the material processing offers the possibility of attaining different configurations for CNF formation, whose effect on the electrical properties of the system can thus be analysed.

## 1.5. Objective of the Doctoral Thesis

As it has been already mentioned in this chapter, electronics industry has been focusing its attention on the integration, within the same chip, of electronic and photonic functionalities. Materials like TCOs have demonstrated to have excellent properties when working as transparent contacts. The implementation of this kind of electrodes has been largely employed in light emitting and photovoltaics, being their function optically passive. However, these materials can be optically active under specific fabrication and working conditions, presenting either band-to-band or defective emission. These properties can be combined with other materials that present resistive switching properties, which could modulate the current injection. In

addition, they can also be doped with REs or including Si-NCs for exhibiting luminescent properties. These impurities or luminescent centers could play an important role in the electrical properties, event influencing on the resistive switching mechanism. Hence, the objective of this Doctoral Thesis is to study optoelectronic materials to be employed in both light-emitting and resistive switching applications, and to explore the possibility of combining both functionalities. The possibility to achieve a ReRAM, compatible with the CMOS technology, that can be read both electrically and optically, could open a new generation of optoelectronic devices.

In order to achieve this goal, different objectives must be taking into account. The first one is to obtain light emitting and resistive switching layers, separately. Different materials will be explored and characterized, paying special attention in their electro-optical and resistive switching properties. Once both layers are obtained, their combination will be explored and their mutual influence will be studied in depth. In the case that the same layer could act as luminescent and resistive switching layer, the modification of the electro-optical properties induced by the formation of the conductive paths will be analyzed, which can give valuable information about the mechanism that governs this phenomenon. Therefore, the objective of this thesis can be listed as follows:

- To find light emitting materials with different kind of luminescent centers, compatible with the CMOS technology.
- To find resistive switching materials based on both metal and/or dielectric oxides.
- To find suitable TCOs as transparent electrode, compatible with the resistive switching mechanism.
- To combine all these elements in order to obtain a resistive switching device that can be read electrically and optically.

Part of this work has been developed in different projects. As result of the European Project *NASCEnT*, size controlled Si-NCs have been achieved, being their implementation in optoelectronics part of the aim of this Thesis. The electro-optical properties of different metal oxides, via rare earth doping, was studied in the national project *LEOMIS*. This last project had associated a PhD scholarship, *Formación de Personal Investigador* (FPI), being it the main



retribution of the author during this Thesis. Currently, the fabrication and characterization of transparent conductive oxides is being carried out in a new national project called *METALONIC*, in which resistive switching materials are being studied as well.

### 1.6. Outline of the Thesis

This Doctoral Thesis is the result of different studies related to the fabrication and the structural, optical, electrical and electro-optical characterization of different materials compatible with the CMOS technology. In order to achieve a good understanding of the work, the Thesis consists of five chapters following the standard organization in scientific reports. First of all, an introduction with the state-of-the-art is given, where the different concepts and materials, in which this Thesis is focused, are introduced. The next chapter consists in the experimental details, being all the employed instrumentation for the fabrication and characterization of materials and devices described in detail. In that chapter, some physical and chemical principles, required for a better understanding of the experiments, will be presented as well. The chapters three and four present all the results, being some of them published in international journals and presented in some national and international conferences. These two chapters are divided into Si- and ZnO-based materials, being each one subdivided into Optical and Electro-Optical and Resistive Switching properties. Finally, the summary and conclusions are written in the fifth chapter. Therefore, the outline of the Thesis is described by:

- Chapter 1: *Introduction*. An overview of the optoelectronic materials is given to understand the challenges that the current semiconductor technology is facing. Brief reviews of the different materials, in which this Thesis is focused, are presented, such as metal oxides, rare earth ions and silicon nanocrystals. Finally, the resistive switching phenomenon, which has developed a revolution in the random access memories, is also presented, being an important point in this Thesis.
- Chapter 2: *Deposition Methods and Sample Characterization*. This chapter is related to the experimental details. Sample fabrication is described, exposing the different deposition

techniques used in this Thesis. The techniques employed for the sample characterization are also described, being divided into structural and chemical, optical, and electrical and electro-optical characterization techniques. In addition, some physical and chemical fundamentals are discussed in order to better understand the experiments and the interpretation of the results, which are presented in the two following chapters.

- Chapter 3: *Si-based materials for optoelectronics and resistive switching*. This chapter is devoted to the study of Si-based materials for their use as active layer in either optoelectronics and/or resistive switching applications. Thus, the results of each material are divided into two subsections: Optical and Electro-Optical Properties, and Resistive Switching Properties. In this case, two materials are studied, silicon-aluminum oxynitride and multi-layered Al-Tb/SiO<sub>2</sub>. Some of these results have been published in international journals, and in this case, a brief summary is written, followed by the article.
- Chapter 4: *ZnO-based materials for optoelectronics and resistive switching*. Similar to the previous chapter, this chapter is focused on the results obtained in ZnO-based materials for being used in either optoelectronics and/or resistive switching applications. The chapter is divided depending on the role of the ZnO, either as active layer or as TCO. Some of the results have been published in international journals, and a brief summary is written, followed again by the corresponding article.
- Chapter 5: *Summary and Conclusions*. Finally, the most relevant results are summarized and the achievements obtained in this Thesis are presented. Considering the obtained results, future works are also proposed, which can contribute to an optimization of the devices, and even to explore new materials.



## 2. Deposition Methods and Sample Characterization

---

*“We can easily forgive a child who is afraid of the dark; the real tragedy of life is when men are afraid of the light”*

*Plato*

---

In this Thesis, different sample fabrication and characterization techniques have been employed depending on the study. This section is focused on the experimental details used along the work, and it is divided into four main subsections. In the first one, sample fabrication methods employed to manufacture the samples are described in detail, being catalogued in physical and chemical deposition techniques. The fabrication of the device structures are also explained, where photolithography and shadow mask are the employed methods to achieve the isolated top electrodes. The second subsection is related to the structural and chemical characterization, which describes different techniques to determine the structure and the chemical composition of the samples. In the third subsection, the optical characterization is presented, showing the main techniques employed for the sample analysis. Finally, the last subsection is devoted to the electrical and electro-optical characterization of devices, where electrical characteristics and the spectrum analysis of the light-emitting devices are presented.

### 2.1. Sample Fabrication Methods

Nowadays, several fabrication techniques are employed in the microelectronic industry in order to satisfy the continuous scaling of devices beyond the nanoscale. At this point, new fabrication techniques must overcome drawbacks attributed to operation at this level. In addition, they need to satisfy the strong demand from society and the high accuracy required in these kind of devices. Despite bottom-up strategies, in which nanostructures are synthesized by

atomic or molecular assembly, have become an excellent solution for the fabrication of structures smaller than few tens of nanometers, the lack of growth control and its random distribution are serious disadvantages for some applications. In contrast, top-down methods, being photolithography the most implemented technology, provide better control, and they are achieving the same resolutions compared to bottom-up techniques. However, their high economic cost is today one of the main problems, which only mass fabrication can compensate. In the next subsections, the specific fabrication techniques employed in this Thesis are described, and they have been separated into two categories, namely chemical and physical deposition techniques.

### **2.1.1. Chemical Deposition Techniques**

In chemical deposition techniques, a reaction between two or more compounds is required, obtaining as a product the desired material. Normally, gas reactions and solutions are the most common processes. These techniques have been largely employed in the design and manufacturing of advanced devices, being nowadays one of the most suitable techniques in a wealth of applications. Chemical deposition method can be separated into two groups, either via solution or in a vacuum. In the first one, liquid phase as mass transfer is used for the precipitation of the material, being sol-gel technique the most known. In the second one, the deposition takes place under vacuum conditions, typically using reactant gases as precursors. Techniques like molecular-beam epitaxy (MBE) or liquid-phase epitaxy (LPE) are used to deposit semiconductors, acting the crystalline substrate as a seed. Other vapor-phase techniques are also employed in the semiconductor industry, in which chemical reactions take place like metal-organic chemical-vapor deposition (MOCVD), low-pressure chemical-vapor deposition (LPCVD), or plasma-enhanced chemical-vapor deposition (PECVD). The last one has been used for the fabrication of the Si-NCs studied in this Thesis and will be described in detail in the next subsection, together with atomic layer deposition (ALD), employed to grow ZnO as top electrode.

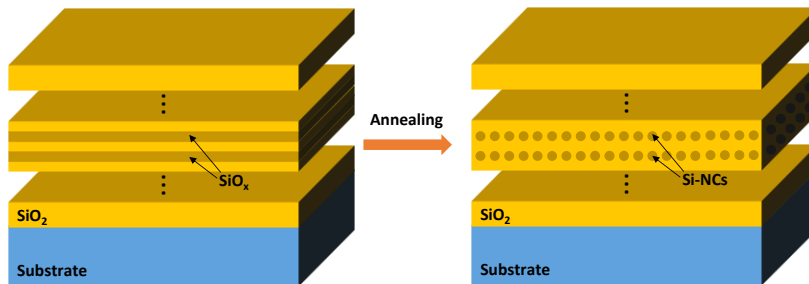
### 2.1.1.1. Plasma-Enhanced Chemical-Vapor Deposition

PECVD is a chemical technique largely employed for thin film deposition. The chemical reaction involved in the process is attained by the formation of a plasma between two electrodes, which induces the reaction of the precursor gases. This plasma can be created by either direct current (DC) or alternated current (AC). The first one is suitable to deposit conductive materials due to their capacity to be discharged. However, insulating materials cannot produce this discharge, being preferable the application of an AC or radio-frequency (RF) signal between the electrodes. Two different configurations of these electrodes are used. One possibility is using a single electrode, thus applying the voltage between it and the conductive walls of the reactor chamber. The second one, is the so-called parallel plate reactor, in which two cylindrical conductive electrodes are employed to apply the voltage signal. In the case of using AC signal, low- or high-frequency plasma can be excited. Using low frequencies, around 100 kHz, several hundreds of voltage is required to achieve a great discharge. However, working at high frequencies, being 13.56 MHz the standard one, lower voltages are enough to induce high plasma densities.

This technique permits relative fast deposition rates while keeping good film quality (defects and roughness), in comparison to with other fast deposition techniques. For example, the optics industry uses this system to create different layers like optical filters, anti-reflective films or materials with specific refractive index. Films of  $\text{Cr}_2\text{O}_3$  or  $\text{MgO}$  are also used to prevent corrosion in mechanical industry. In electronics and microelectronics, insulator layers of  $\text{SiO}_2$ , amorphous or polycrystalline semiconductors like Si and GaAs, or conductive materials such as Al, Au or Cr, are typically deposited as well, being part of some electronic devices like solar cells.

This deposition technique was used for the fabrication of Si-NCs. In this case, samples were deposited at the *Institut für Mikrosystemtechnik* (IMTEK, Albert-Ludwigs Universität Freiburg, Germany), as part of the collaboration with Prof. Margit Zacharias in the NASCEnT EU project. The employed system was an *Oxford Instruments Plasmalab 100* with a 13.56 MHz driven parallel plate reactor. Multilayered structures, alternating Si-rich oxides ( $\text{SiO}_x$ ) and

## 2. Deposition Methods and Sample Characterization



**Figure 2.1.** (left) Scheme of the multilayered structure of  $\text{SiO}_x/\text{SiO}_2$ , before the annealing process. (right) After the annealing process, the precipitation of the extra Si takes place in the form of Si-NCs.

$\text{SiO}_2$  sublayers, were deposited onto *p*-type Si and fused silica substrates. The deposition was made under ultra-high vacuum condition and keeping the substrate temperature at 375 °C. A mixture of silane ( $\text{SiH}_4$ ) and nitrous oxide ( $\text{N}_2\text{O}$ ) gases were used as precursors, together with Ar as carrier gas. By controlling the ratio between the precursor gases, both layers  $\text{SiO}_x$  and  $\text{SiO}_2$  can be obtained. Indeed, the presence of nitrogen in the deposition induced a silicon oxynitride ( $\text{SiO}_x\text{N}_y$ ), being  $y = 0.23$ , almost constant in all depositions. Once the multilayers (MLs) were deposited, a thermal annealing process is required to induce the precipitation of the extra Si, which can be expressed as:

$$\text{SiO}_x = \left(1 - \frac{x}{2}\right)\text{Si} + \frac{x}{2}\text{SiO}_2, \quad (2.1)$$

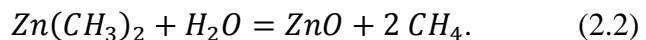
taking  $x$  values between 0.64 and 1.1. The annealing temperature ( $T_a$ ) and its duration are critical parameters to achieve a good crystallization of the Si nanoparticles. A conventional quartz tube furnace was employed to submit the samples at temperatures ranged between 900 °C and 1250 °C for 1 h in presence of inert  $\text{N}_2$  ambient. This thermal study demonstrated that 1150 °C is the optimum  $T_a$  for the correct precipitation of Si excess in form of Si-NCs. Figure 2.1 represents the formation of the Si-NCs under the annealing process. As mentioned in the Introduction *1.3 Silicon Nanocrystals*, the growth of these nanostructures are limited by the  $\text{SiO}_2$  barriers. Keeping constant  $x$ , larger Si-NCs are formed increasing the thickness of the SRO layers. This way, the quantum confinement of Si-NCs was

analyzed varying this parameter. Detailed fabrication process was reported in ref. [112].

### 2.1.1.2. Atomic Layer Deposition

Atomic layer deposition (ALD) is a thin film deposition technique in which, similar to other chemical deposition methods, a chemical reaction takes place by means of gas precursors. In contrast to PECVD, in which the precursors were mixed in the chamber, in ALD the precursors are sequentially introduced. Therefore, the reaction is directly between the precursor and the surface of the sample, finalizing the reaction when all the surface is reacted (ALD cycle). The nature of the precursor-surface interaction governs the possibility to grow thicker layers, varying the number of ALD cycles. Each layer deposition can be divided into four steps. The first one is introducing the reactant A, which interacts with the substrate depositing part of the reactant on the whole area. The second step consists of purging the chamber, removing reactant A. At this point, reactant B can be introduced as third step, in which this precursor reacts with the deposited layer, thus obtaining the desired compound in the form of monolayer. Finally, in the fourth step, a new purge is applied to prepare the chamber for the next cycle.

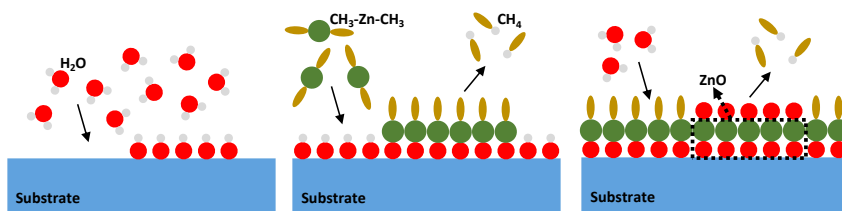
In this Thesis, ALD technique has been used to deposit ZnO layers using a commercial *OpAL Oxford Instruments* system, located in the *Institut für Mikrosystemtechnik* (IMTEK, Albert-Ludwigs Universität Freiburg, Germany). These ZnO layers were employed as TCO for the electro-optical characterization of the samples containing PECVD-deposited Si-NCs, as mentioned before. In this case, the ZnO layer was achieved by means of dimethylzinc [ $\text{Zn}(\text{CH}_3)_2$ ] and  $\text{H}_2\text{O}$  precursors. The sequential introduction of both gases induces the growth of controlled ZnO monolayers. The schematics corresponding to one ALD cycle of this reaction is represented in the Figure 2.2, being the involved chemical reaction defined by:



Different substrate temperatures, ranging between 100 °C and 200 °C, were analyzed, being the highest temperature the optimum one due to the lower resistivity that the resulting sample presents. This is an



## 2. Deposition Methods and Sample Characterization



**Figure 2.2.** Scheme of the different reactions involved in the ZnO deposition by ALD. (left) Molecules of  $\text{H}_2\text{O}$  are added on the surface by leaving an  $\text{OH}^-$  layer. (middle) The  $\text{Zn}(\text{CH}_3)_2$  molecules react with these  $\text{OH}^-$  molecules obtaining a monolayer of ZnO and producing volatile  $\text{CH}_4$ . (right) The first process is repeated again in a new ALD cycle to deposit a new ZnO monolayer.

important parameter to employ these layers as TCO, exhibiting enough conductivity to inject carriers to the active layers. In this case, a further annealing process was not required, because the crystallization of the layer is achieved during the growth, and it already presents high quality and homogeneity.

### 2.1.2. Physical Deposition Techniques

In contrast to the chemical techniques, physical techniques are employed using directly the desired material, which is submitted to physical processes such as cutting, molding, melting or evaporation, in order to obtain the final result. In the case of deposited layers, the film is obtained by means of the condensation of the vapor phase of the material, which has been previously evaporated via solid-liquid-vapor process or directly sublimated. Physical vapor deposition (PVD) techniques have been used in the chemical, electrical and optical industry, being the thin film solar panels one of the most employed applications [113]. Evaporation and sputtering techniques are common PVD process, being the first one divided into different methods depending on how the heating is carried out. Some samples presented in this Thesis have been fabricated by PVD techniques like sputtering, pulsed laser deposition or electrical beam evaporation. These techniques are presented in the following subsections, where the description of the fabricated samples will be given.

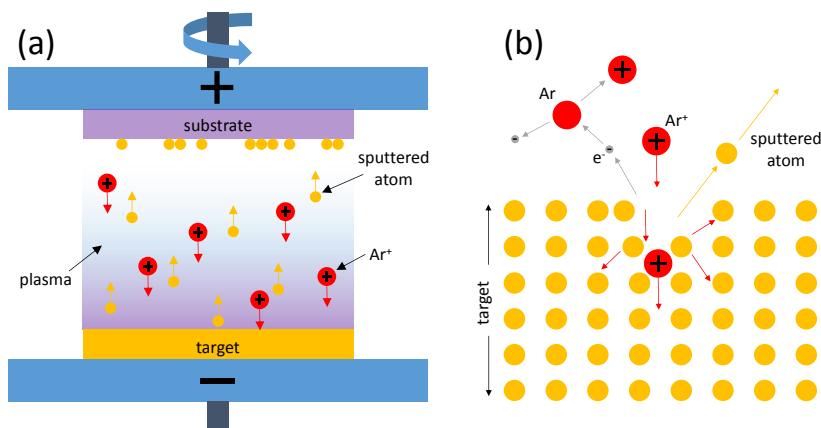
### 2.1.2.1. Sputtering

In the sputtering technique, the material is deposited onto a substrate by means of the ejection from a target, which is bombarded by energetic particles, normally gas ions. This process takes place when the energy of these particles is larger than the binding energy of the surface of the material. Similar to other deposition techniques, sputtering can work either using DC or AC voltage, being RF the most commonly used mode in the latter case. The energy field between the cathode (target) and the anode (substrate) induces to the creation of a plasma. When the gas atoms of the plasma have lost electrons, these ions accelerate towards the target, striking with enough energy to eject atoms or molecules from the target to the substrate. In order to avoid any undesired reaction induced by the plasma, Ar is typically employed, as noble gas with inert properties, thus not interacting with the target. The Figure 2.3 shows a scheme of the typical sputtering system with a detailed sketch of the involved process.

In this case, two different materials were deposited using sputtering systems, SiAlON doped with Ce, and ZnO doped with Tb and/or Eu, both depositions carried out at the *Center of Research on Ion Materials and Photonics (CIMAP)* at the *University of Caen Normandy (UNICAEN)*, as a collaboration with Dr. Xavier Portier and Dr. Christophe Labbé. Depending on the material, two different sputtering systems were employed, an *AJA International* for SiAlON samples and a *MECA 2000* for the ZnO ones.

On one hand, the Ce-doped SiAlON samples were grown onto *p*-type Si substrates at room temperature. A variable N<sub>2</sub> flux, together with the sputtering of CeO<sub>2</sub>, Al and Si targets, were used under an Ar flow set at 8 sccm. Fixed power density of 4.5 W cm<sup>-2</sup> was employed for the Si target, whereas CeO<sub>2</sub> and Al targets were sputtered varying the power density from 0 to 2.1 W cm<sup>-2</sup> and from 0 to 0.75 W cm<sup>-2</sup>, respectively. Finally, all samples were annealed at 900 °C using a classic thermal annealing furnace for 1 h under N<sub>2</sub> atmosphere. For the electro-optical characterization, device structure was fabricated in Barcelona, depositing ITO on top of the sample as TCO by means of EBE, using a shadow mask and Al in the rear side of the substrate (see 2.1.2.3. *Electron Beam Evaporation*).

## 2. Deposition Methods and Sample Characterization

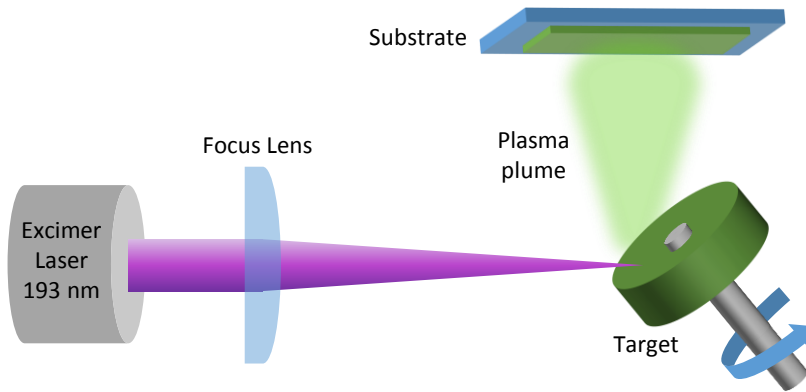


**Figure 2.3.** (a) Scheme of the sputtering system, where a plasma of  $\text{Ar}^+$  is induced by RF voltage, sputtering the materials from the target to the substrate. (b) Sketch of the sputtering process, where the interaction of the  $\text{Ar}^+$  ions with the target is shown.

On the other hand, Tb- and Eu-doped ZnO samples were obtained using  $\text{Tb}_4\text{O}_7$  and  $\text{Eu}_2\text{O}_3$  targets as dopants, and a ZnO target for the host matrix. Different samples were grown, undoped ZnO, Tb-doped ZnO, Eu-doped ZnO and Tb:Eu-codoped ZnO, all of them deposited onto *p*-type Si substrates as well. The growth of the ZnO layers required higher substrate temperatures than SiAlON, setting at 400 °C for a correct deposition. After the deposition, samples were annealed at 450 °C for 1 h, following the same process than the one mentioned before. In this case, device structure was obtained depositing ITO as top transparent electrode by means of photolithography (see subsection 2.1.2.4 *Photolithography Process*). This process was carried out at *Centre Nacional de Microelectrònica (CNM)*, which is a research institution of the *Consejo Superior de Investigaciones Científicas (CSIC)*. Finally, the back contact consisted in a full-area Al film.

### 2.1.2.2. Pulsed-Laser Deposition

In pulsed-laser deposition (PLD), a specific target is ablated by means of a high-power pulsed laser beam in a vacuum chamber, which can contain a low pressure of reactive gas like oxygen in order to induce partial or full oxidation of the deposited material. When the target absorbs the laser pulse, complex physical processes occur. Depending



**Figure 2.4.** Scheme of the PLD system, where a plasma plume is generated from the target to the substrate, exciting the target with a 193-nm line of an excimer laser.  $\text{Ar}^+$  ions are induced by RF voltage, sputtering the materials from the target to the substrate.

on the wavelength of the laser, and the refractive index and absorption coefficient of the target, the penetration of the laser can be different, being typically around 10 nm. Initially, when the laser pulse reaches the surface of the target, electron excitation of the material takes place and the corresponding free electrons interact with the material, heating it up until evaporation. Consequently, the target forms a plasma plume due to the Coulomb repulsion. The shape and distribution of this plasma plume depends on the target material and the chamber pressure. The ablated material is deposited onto the substrate, being parameters like the energy density of the laser pulse, the substrate temperature and the base pressure of the chamber critical for the correct growth of the film. In the Figure 2.4, a scheme of the PLD system is shown, in which the ablation of the target is represented.

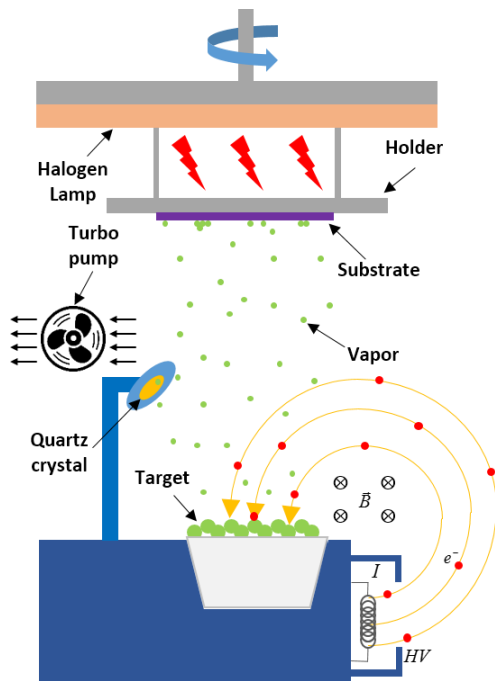
PLD was employed to grow thin films of SiAlON onto *p*-type Si substrate as well. The samples were grown by the *Laser Processing Group* at the *Instituto de Óptica* (CSIC) in Madrid under the supervision of the Dr. Rosalía Serna. The target ablation was achieved using the 193-nm line of an ArF excimer UV laser with a pulse duration of 20 ns. The energy density of each pulse was set at  $4.10 \text{ J cm}^{-2}$ , kept constant during all deposition process. In contrast to the deposition using sputtering, the employed targets consisted of SiAlON and Eu. The deposition process was achieved by means of 360 pulses on the SiAlON target, corresponding to a thickness of 2.5

## 2. Deposition Methods and Sample Characterization

nm, followed by 10 pulses on the Eu target. This sequence was repeated 60 times, depositing an extra SiAlON layer to protect the Eu from the last step. After deposition, an annealing process was carried out at temperatures between 300 and 800 °C for 1 h in air. Finally, the device structure was completed by depositing either Al or ITO circular dots as top contacts using a shadow mask by means of EBE, and full-area Al layer in the rear side of the Si wafer.

### 2.1.2.3. Electron-Beam Evaporation

Electron beam evaporation (EBE) technique is a physical deposition method that consists in evaporating a target by heating it via a high energetic electron beam. Typically, the electron source is a tungsten filament, which emits electrons when an electrical current is injected through it. These electrons are accelerated by a high voltage source and the electron beam is focused on the target using electro-magnets. As a consequence, the target increases its temperature until achieving the vapor phase, via solid-liquid-gas or sublimation processes, depending on the material. The whole process takes place in a vacuum chamber, with pressures between  $10^{-4}$  mbar and  $10^{-7}$  mbar. The evaporated material is deposited onto a substrate, which is located upside down at the top of the chamber. In order to have the control of the deposited layer thickness, a quartz crystal is typically employed, indicating the deposition rate and the total thickness of the material being simultaneously deposited onto the crystal at real time. To obtain better homogeneity of the deposited layers, the holder of the substrate can rotate during the deposition, avoiding differences as a function of the rotation angle. However, a decrease of thickness in the edges of the substrate with respect to the center can be observed due to the difference of the target-substrate distance and the angle. This effect also depends on the evaporated material, presenting different homogeneity levels. Sometimes, the substrate can be heated to increase the mobility of atoms or molecules when deposited onto the substrate, which avoids clustering and increases homogeneity. As well, the temperature of the substrate can play an important role on the deposition if the chamber is filled with a low pressure of reactive gas, such as oxygen, inducing an oxidation of the layer. In these conditions, the real thickness deposited onto the substrate can differ to the quartz crystal one because of the different material deposited on both surfaces. Whereas the quartz crystal is cooled down with a water



**Figure 2.5.** Sketch of the EBE system employed in some deposition processes within this Thesis. The target is heated up by energetic electrons, inducing an evaporation of the material, which is deposited onto the substrate.

circuit, the substrate temperature together with the reactive gas on the chamber can induce a chemical reaction, depositing a different material than the one the sensor detects.

The materials deposited by EBE presented in this Thesis have been obtained using a PFEIFFER VACUUM Classic 500 instrument with a Ferrotec GENIUS e-beam controller and a Ferrotec CaARRERA high-voltage (up to 10 kV) power supply. This system is located in the clean room of the Faculty of Physics at the University of Barcelona. The system was upgraded with a low pressure gas ( $O_2$ ,  $N_2$  or Ag) line, which permits different chemical reactions when the evaporated material is deposited on the substrate. Figure 2.5 shows a sketch of this system and the process of the evaporation.

This system was used to grow different materials presented in this Thesis. On one hand, the delta-doping approach was employed to introduce Tb atoms in a  $SiO_2$  matrix. Delta-doping approach consists in depositing very thin films (around 1 nm or less) of the dopant material between two layers of the material that acts as host matrix. By repeating this stack many times a multilayered structure can be

## 2. Deposition Methods and Sample Characterization

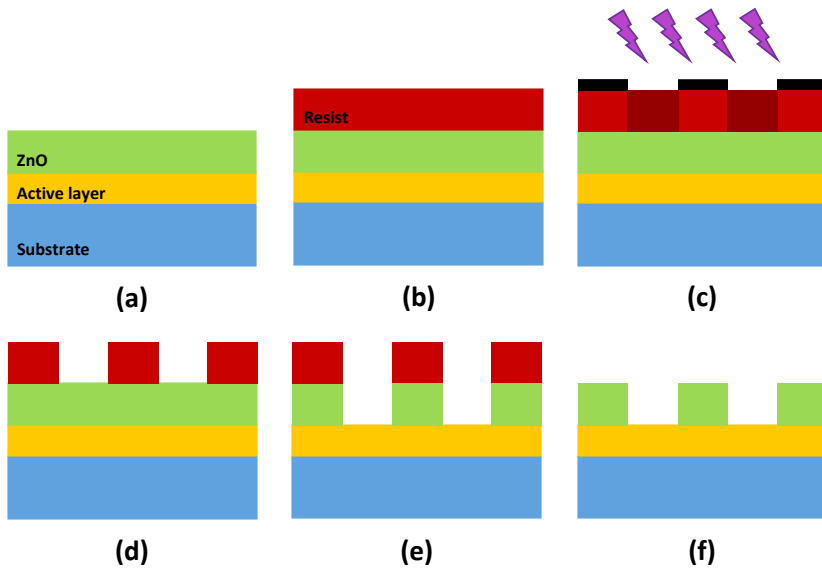
achieved, being the result similar to a doped bulk. In this way, multilayered structure of Tb/SiO<sub>2</sub>, was fabricated onto *p*-type Si substrate using metallic target of Tb for the delta-doping layers and SiO<sub>2</sub> target for the host matrix. Aluminum was introduced growing different combinations of the layers by the delta-doping approach as well. The deposition rate of both Al and Tb dopants corresponded to 0.2 Å s<sup>-1</sup>, while for SiO<sub>2</sub> it was 1.0 Å s<sup>-1</sup>. The whole deposition process was carried out keeping the substrate temperature constant at 100 °C. After deposition, samples were annealed at temperatures ranging from 700 to 1100 °C for 1 h in N<sub>2</sub> atmosphere.

On the other hand, the EBE system was used to deposit electrodes for the device structures. Two kinds of electrodes were deposited; Al as metallic electrodes, and ITO as TCO. The first one was employed in the rear side of the devices and as top electrode of some of them. In contrast, ITO layers were deposited on top of devices in which the electro-optical properties had to be explored. The deposition of Al was carried out at room temperature in order to avoid the oxidation of the layer, being the deposition rate around 3 Å s<sup>-1</sup>. However, ITO layers were grown at 1.0 Å s<sup>-1</sup>, heating the substrate at 100 °C and under a 2 sccm line of O<sub>2</sub>. In this case, ITO required an annealing process to induce the crystallization of the layer and to consequently become optically transparent. In order to separate different devices, the top contacts were deposited using a chromium shadow mask with circular dots.

### 2.1.3. Photolithography process

In order to carry out both electrical and electro-optical characterization of some materials, device structure was required, which was achieved by depositing electrodes. As mentioned in some deposition techniques just before, top electrodes have been obtained either using a shadow mask or by photolithography. In the case of using photolithography, two kinds of processes were employed, depending on the deposited material, either ITO or ZnO.

In the case of the ZnO top electrode as TCO, the photolithography was processed in the *Institut für Mikrosystemtechnik* (IMTEK, Albert-Ludwigs Universität Freiburg, Germany). Once the active layer was deposited and annealed, if required, 100-nm thick full-area layer of



**Figure 2.6.** (a) Sequence of the photolithography process carried out for the ZnO top electrode as TCO. (a) Deposition of the ZnO onto the active layer. (b) Resist application using spin coating and soft baking. (c) UV exposure using a mask, followed by a hard baking. (d) Development of the exposed resist with AZ 726 MIF. (e) Rinsing of the non-protected ZnO using HCl (5%) dissolution. (f) Rinsing of the rest of the resist using acetone.

ZnO via ALD at 100 °C was deposited. The lithography process of this TCO begins by depositing the resist (AZ 1518, positive resist) and homogeneously spreading it by spin-coating, thus obtaining a thickness around 2  $\mu\text{m}$ . A soft baking during 50 s at 100 °C and an UV exposure for 3 s with the mask were applied. After that, a hard baking at 115 °C for 50 s was carried out. To develop the resist from non-contact areas, AZ 726 MIF developer was applied during 2 min, followed by water rinsing. Using an HCl (5 %) dissolution for 5-7 s, ZnO on the previously developed samples was eliminated, only remaining the non-developed contacts. A new water rinsing was applied again. To get rid of remaining resist on the contact areas, acetone was applied for 1-2 s, followed by a new water rinsing. Isopropanol and water was employed to remove the remaining acetone on the sample surface. After this process, ZnO top electrode was achieved, with circular dots correctly isolated between them. In the Fig. 2.6 there is a sketch of the different steps of the whole



photolithography, from the full area ZnO layer to the definition device structure.

The other lithography process corresponds to the ITO top electrodes, which were deposited at the *Institute of Microelectronics of Barcelona* (IMB) of the *Centre Nacional de Microelectrònica (CNM), CSIC*. In this case, SiO<sub>2</sub> windows were opened before the deposition of the active layer, depositing 400 nm of SiO<sub>2</sub> at 1100 °C (wet oxidation). Using standard photolithography the windows of the field oxide were defined employing the CNM004 mask. The field oxide etching was obtained with a resist mask and the resist stripping was carried out via O<sub>2</sub> plasma. After general cleaning, the wafers were ready for the corresponding active layer deposition. Once the active layer was deposited, ITO was grown at 300 °C with a subsequent annealing at 200 °C in air. Standard photolithography was carried out using a similar mask than employed before, defining the region where the electrodes will be placed. By means of reactive-ion etching (RIE) the electrodes were well defined, followed by the stripping of the resist.

## **2.2. Structural and Chemical Characterization**

In order to determine the morphology of the deposited layers and their composition, structural and chemical characterization of the samples are required. These processes permit to obtain real thicknesses, roughness, homogeneity, porosity, crystalline quality or stoichiometry of the layers. In this Thesis, two techniques have been employed for the structural and chemical characterization. The first one consists of using different electron microscopy techniques, which allow for both structural and chemical characterization. The second one is the X-ray photoelectron spectroscopy, complementing the chemical composition information of the layers. These techniques are briefly described in the following subsections.

### **2.2.1. Electron Microscopy Techniques**

The strong limitation of spatial resolution that optical microscopy presents is an important drawback to observe structures at the

nanoscale range. This limitation is directly related to the wavelength of the employed light and it is expressed by:

$$d = \frac{\lambda}{2n \sin \theta} \approx \frac{\lambda}{2 \cdot NA}, \quad (2.3)$$

where  $d$  is the spatial resolution,  $\lambda$  is the wavelength of the employed light,  $n$  the diffraction index of the material,  $\theta$  is the collection angle and  $NA$  the numerical aperture of the system. As it is well known, electrons have associated a wavelength that depends on their energy following the expression:

$$\lambda_e = \frac{h}{2m_0 E_e \left(1 + \frac{E_e}{2m_0 c^2}\right)}, \quad (2.4)$$

being  $h$  the Planck's constant,  $m_0$  the electron mass in rest,  $E_e$  the energy of the electron and  $c$  the speed of light in vacuum. Using highly energetic electrons instead of light opens the possibility to reduce the associated incident wavelength, increasing substantially the resolution of the microscope. Working with electron energies between 80 and 300 keV, wavelengths of some pm can be obtained; however, this resolution normally is not achieved due to technical limitations like chromatic or spherical aberrations, being the latter the most critical drawback.

Two different electron microscopy techniques have been employed in this Thesis, scanning electron microscopy (SEM) and transmission electron microscopy (TEM). The first one was used to determine the surface morphology of some samples and the chemical composition as well, via energy dispersive spectroscopy (EDS). In this case, the X-ray emission from the sample, induced by the electron-matter interaction, gives rise to a specific spectrum ascribed to a unique atomic species of each sample. On the other hand, TEM measurements permitted high-resolution TEM (HRTEM) images, being visible nanometric structures like quantum dots or superlattices. The possibility to work in diffraction mode was useful to determine crystalline structures from the diffraction patterns. In addition, the system permits to obtain high angular annular dark field (HAADF) images in scanning mode (STEM), showing bright contrast that depends directly on the atomic number of the atomic specimen. Chemical characterization was also carried out using TEM techniques

## 2. Deposition Methods and Sample Characterization

like electron-energy loss spectroscopy (EELS) or energy-filtered TEM (EFTEM). When the incident electrons interact with the sample, some transmitted electrons have lost kinetic energy, which depends on the atomic species of the sample. Therefore, complete core-loss EELS spectrum image can be determined, bearing compositional information of each pixel of the TEM image. Filtering the electrons with particular kinetic energies allows determining the location of specific atomic specimens, being able to obtain composition maps.

In order to achieve electron transparency on the samples, an accurate sample preparation must be carried out. In homogeneous samples, conventional mechanical polishing method is enough because the cross-section is the same along the whole sample. However, focus-ion beam (FIB) coupled to a SEM is required to obtain the cross-section of a specific location. In this case, the sample can be cut focusing a highly energetic  $\text{Ar}^+$  beam, selecting the corresponding region of interest.

Different systems related to electron microscopy techniques have been employed in this Thesis. On one hand, the SEM employed for the structural and chemical characterization of samples was a Jeol JSM-7100F, operating at 20 kV, with a high-resolution spectrometer Gatan-MonoCL4. This system permits EDS measurements, detecting the X-ray emission from the samples. On the other hand, a Jeol 2010F TEM, operating at 200 kV and coupled to a GIF Gatan filter with 0.8 eV energy resolution was employed to obtain HRTEM and HAADF images, and EELS spectrum images. Finally, in some case, sample preparation using a Zeiss 1560XB Cross Beam FIB was carried out, reducing the thickness of a specific region down to about 50 nm for the electron transparency.

### **2.2.2. X-Ray Photoelectron Spectroscopy**

Chemical characterization can be also carried out using X-ray photoelectron spectroscopy (XPS). This technique permits to determine the quantitative atomic composition and the chemical state of the material. Irradiating monochromatic X-rays onto the sample, depth levels of the atomic structure are excited, inducing the emission of photoelectrons. The number and the kinetic energy of these emitted electrons can be analyzed, providing information about the chemical

composition of the samples. The kinetic energy ( $KE$ ) of the emitted electrons can be given by:

$$KE = h\nu - BE - \Phi_{sp}, \quad (2.5)$$

being  $h\nu$  the energy of the incident photon,  $BE$  the binding energy of the atomic orbital and  $\Phi_{sp}$  the spectrometer work function. Although it is a surface technique, the possibility to dig the sample using an ion beam, typically using  $Ar^+$  ions, allows the determination of the chemical composition along the whole sample cross-section. Depending on the material, the rate of the depth profile can be different, being also dependent on other factors like the ion energy, the incident angle and the nature of the employed ions. Regarding the spatial resolution, while lateral resolution is about some  $\mu m$ , average signal of some nm can be detected in depth direction. Once the signal data is corrected by a known reference, different oxidation states of the materials can be determined by the corresponding peak position shifts. Small variations on the binding energy between atoms can be observed in different oxidation states. The quantitative analysis can be determined from the peaks area of each atom, obtaining the stoichiometry of the samples.

The XPS analysis of some samples presented in this Thesis was performed by means of a PHI 5500 Multitechnique System, provided with a monochromatic X-ray source that uses the Al  $K\alpha$  line of 1486.6 eV with a power of 350 W. This system is located in the *Serveis Científic-Tècnics* (CCiT) of the *Universitat de Barcelona*.

## 2.3. Optical Characterization

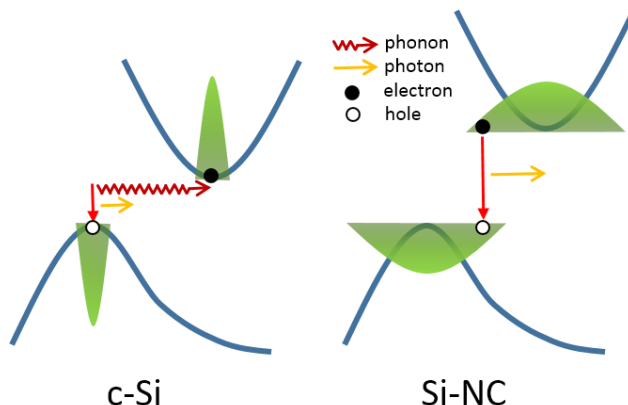
The fact that electromagnetic radiation interacts with matter has permitted to determine some properties directly related to material structures like atomic energy levels or energy bands. This light-matter interaction is strongly dependent on the wavelength of the incident light, which can be reflected, transmitted or absorbed. Analyzing the reflectance and transmittance spectra, the absorption one can be determined, which is the responsible for the matter excitation. In this section, the main optical characterization techniques employed in this Thesis are presented, being the photoluminescence the most explored one.

### 2.3.1. Photoluminescence Spectroscopy

As it is well known, some materials present luminescence resulting from other sources rather than heat. This effect can be induced by chemical or physical processes, exciting the material. The relaxation of the excited centers produce emission of photons, whose energies are characteristic of the specific luminescent centers. In the case that this excitation is via photon irradiation, the consequent luminescence is called photoluminescence (PL).

Depending on the luminescent center, different processes can take place. One of them is the called band-to-band transition, observed in semiconductors. In this case, the excitation can promote an electron to the conduction band (CB), leaving a hole in the valence band (VB). Typically, the electron relaxes toward the minimum of the CB and the hole to the maximum of the VB, via non-radiative processes. At this point, the radiative recombination of the electron-hole can take place, emitting a photon with the energy of the band gap. In the case of indirect band gap materials, the additional generation of a lattice phonon is required, being its momentum equal to the difference between electron and hole ones. As mentioned in the section *1.3 Silicon Nanocrystals*, the nanostructuring of Si, which presents an indirect band gap around 1.12 eV, displays a blue-shift emission due to the delocalization of the wavefunctions in the momentum space via quantum confinement.

In the case of ZnO, in which this Thesis is also focused, it exhibits a band gap energy around 3.3 eV, which is located in the near UV range. In contrast to Si, ZnO shows a direct band gap, being the radiative recombination more efficient. Some materials present defect-related emission attributed to the recombination of electron-holes between intra-band energy levels formed by the presence of impurities or defects. Typically, ZnO is one of these materials, obtaining PL spectrum with a broad band in the visible range. In the Figure 2.8, the calculated energy levels of some of these defects are presented as well. Oxygen vacancies are one of the most common defects in metal oxides. This lack of oxygen makes the oxygen vacancies to easily bind electrons, thus forming excitons with energies close to the minimum of the conduction band and thus promoting the PL intra-band



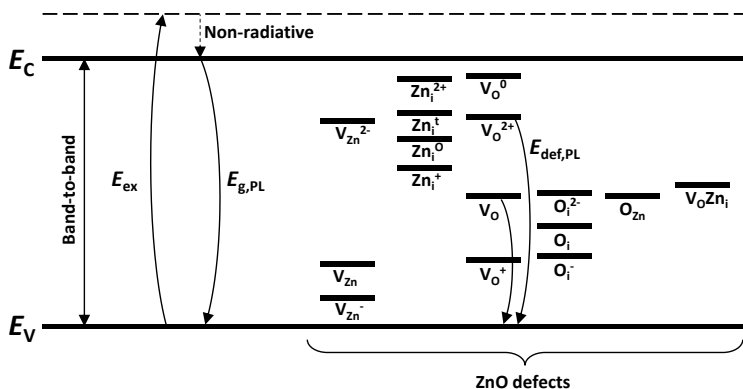
**Figure 2.7.** Comparison between radiative recombination taking place in in c-Si and Si-NC. The delocalization of the wavefunction in Si-NCs permits an almost-direct band gap photon emission.

excitation. This kind of defect-emission can be also visible in defective  $\text{SiO}_2$ , presenting similar broad emission than ZnO.

Other kind of luminescent centers are rare earth ions in the trivalent state. In this case, the incident photons promote electrons of the atoms to higher electronic levels, typically the  $^5\text{D}$  ones. The relaxation of these electrons to lower energy levels like  $^3\text{H}$ ,  $^6\text{H}$ ,  $^7\text{F}$  or  $^3\text{F}$  emits photons with specific energies, consequently obtaining a characteristic PL spectrum with narrow peaks that depends on the RE ion.

Two different excitation mechanisms can be carried out, via either non-resonant or resonant absorption. In the first case, the sample is excited using an energy higher than the band gap, being necessary a thermalization via non-radiative processes (see Figure 2.7). In the case that luminescent centers are embedded within a host matrix like Si-NCs or REs, their excitation can be carried out via energy transfer from the host matrix, which previously has absorbed the incident photons. In contrast, resonant excitation mechanism takes place when the energy of incident photons is very close to the band gap, contributing to a spontaneous emission by coherent processes. This mechanism can be interesting in the case of RE emission because the resonant excitation of a high-energy transition can induce more

## 2. Deposition Methods and Sample Characterization



**Figure 2.8.** Energy band diagram that represents the excitation ( $E_{ex}$ ) and the PL emission of band-to-band ( $E_{g,PL}$ ) and defects ( $E_{def,PL}$ ) of the ZnO. Calculated energy levels of different defects from literature are also represented, where  $V_{Zn}$ ,  $V_{Zn}^-$  and  $V_{Zn}^{2-}$  correspond to the neutral, single- and doubly-charged zinc vacancies.  $Zn_i^0$  and  $Zn_i^t$  are the neutral octahedral and tetrahedral zinc interstitials, while  $Zn_i^+$  and  $Zn_i^{2+}$  indicate singly- and doubly-charged zinc interstitials, respectively.  $V_O^0$  and  $V_O$  correspond to oxygen vacancies, while  $V_O^+$  and  $V_O^{2+}$  are single- and double-charged oxygen vacancies.  $O_i$  represents oxygen interstitials and  $V_OZn_i$  corresponds to a complex of oxygen vacancy and zinc interstitial. Image adapted from ref. [123].

efficiently the relaxation to lower-energy levels of the RE, obtaining the emission of their relaxation.

The photoluminescence experiments were carried out at the *Photoluminescence Laboratory* of the *Department of Electronics and Biomedical Engineering* of the *Universitat de Barcelona*. The samples were excited using either the 325-nm line of a He-Cd laser or the 488-nm line of an Ar<sup>+</sup> laser. The laser beam was filtered with a high-pass filter, to eliminate harmonic modes or parasite photons, and focused onto the sample through an optical path in backscattering configuration. The PL emission was filtered using a low-pass filter in order to avoid the laser signal detection. The signal was collected by a monochromator to be finally detected by a Hamamatsu R928 GaAs photomultiplier tube (PMT) connected to a standard lock-in amplifier.

### 2.3.2. Time-Resolved Photoluminescence

The dynamics of the luminescent centers can be studied analyzing the decay time ( $\tau$ ) of specific wavelength by means of pulsed incident light, using either pulsed laser or chopping a continuous-wave one. This study can contribute to obtain information about the origin of the luminescent centers, having a wide range of decay times depending on the nature of the samples. When the sample excitation is interrupted, PL intensity decreases following an exponential decay function. The general expression of the evolution of this emission can be given by:

$$I_{PL}(t) = I_{PL,0} + \exp\left[-\left(\frac{t}{\tau}\right)^\beta\right], \quad (2.6)$$

being  $I_{PL,0}$  the pre-exponential factor corresponding to the PL emission at the initial decay process,  $\tau$  the decay time and  $\beta$  is the stretched factor. In the case of  $\beta = 1$ , the expression corresponds to a single-exponential decay, having all the luminescent centers the same  $\tau$ . However,  $\beta < 1$  is obtained when a distribution of decay times is present in the emission. This effect could indicate either the contribution of different luminescent centers or the fact that these luminescent centers are under different conditions. This case is easily observed in Si-NCs, which usually exhibit different decay times depending on their size. The presence of size distribution contributes to a reduction of the  $\beta$  parameter, typically between 0.5 and 0.9.

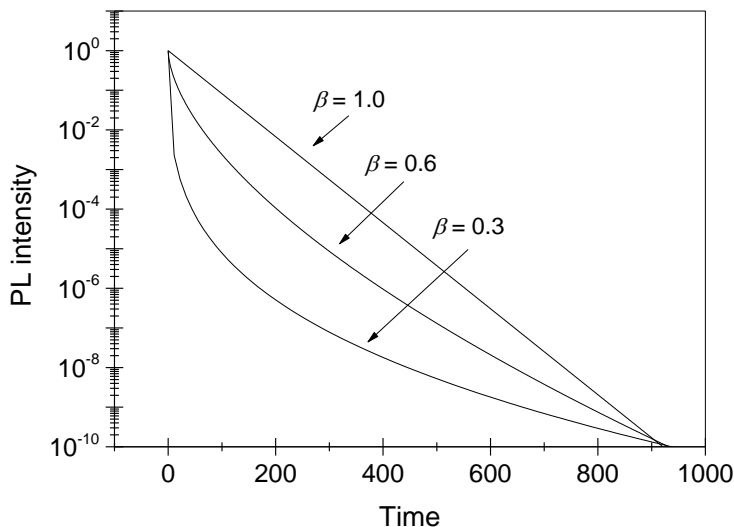
The lifetime of the PL emission is also strongly sensitive to non-radiative processes, which typically present very fast recombination. The measured decay time can be expressed as combination of the decay times of radiative and non-radiative processes by:

$$\frac{1}{\tau_{meas}} = \frac{1}{\tau_{rad}} + \sum \frac{1}{\tau_{non-rad}}, \quad (2.7)$$

where  $\tau_{meas}$  is the resulting measured decay time, while  $\tau_{rad}$  and  $\tau_{non-rad}$  are the decay times corresponding to the radiative and non-radiative processes, respectively. Hence, the presence of fast non-radiative processes decreases the lifetime of the measured PL emission.



## 2. Deposition Methods and Sample Characterization



**Figure 2.9.** Examples of stretched exponentials with different stretched factor  $\beta$ . In the case of  $\beta = 1$ , the function becomes a single exponential.

Two different employed systems were used to study the dynamics of the PL emission. The first one corresponds to using the continuous 325-nm line of a He-Cd laser, being mechanically square-chopped. The second one corresponds to using the third harmonic frequency of a Brilliant Nd<sup>3+</sup>:YAG 5-nm-pulsed laser (355 nm). In both cases, the signal was acquired using a PMT coupled to a monochromator, being the PL decay monitored with an *Agilent Infiniium DSO 8064A* oscilloscope.

## 2.4. Electrical Characterization

The electrical properties of some materials are of great interest and largely employed in the electronic industry. In order to achieve the corresponding charge injection, device structure is required by means of electrodes, being structures like metal-insulator-metal (MIM) or metal-insulator-semiconductor (MIS) the most employed. From the  $I(V)$  characteristics, electrical transport mechanisms, that govern the electrical conduction, can be determined. In addition, the resistive switching behavior, that some devices present, is obtained in this electrical characterization, stressing the active layer using a voltage supply. All of these analyses contribute to a better understanding of

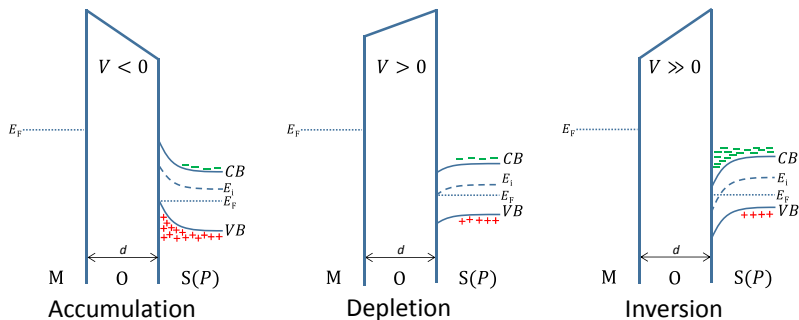
the electrical properties. The experimental details for the electrical characterization are presented, followed by some theoretical models.

### 2.4.1. Charge Transport Mechanisms

The charge transport through dielectrics has been largely studied in order to understand how do issues like charge trapping or leakage currents affect at different regimes of the applied electric field. Thanks to this study, novel materials have been proposed to have more control on the electrical properties, which depends on the nature of the material. Whereas some charge transport mechanisms depend on the temperature, others are governed by quantum effects like tunneling through the potential barriers. The conductivity of the material depends on several parameters like the layer thickness, the carrier density, their mobility or their effective mass into the material. In the case of semiconductors, like metal oxides, two opposite situations of interest can occur, which are dependent on their doping level: an intrinsic material with an electrical behavior typical from a dielectric, or a degenerate material with an electrical behavior close to metals.

Device structure and voltage polarization can also influence on the conduction. If devices present flat-band voltage due to a heterojunction, the charge transport depends on the regime in which it works. The Figure 2.10 represents the three working regimes of a MOS-structured device with *p*-type semiconductor. When negative voltage is applied on the top electrode (M), accumulation regime takes place, being the majority carriers of the substrate (holes) attracted towards the top electrode at the same time that the electrons are injected from the top electrode into the substrate. Applying positive voltage larger than the flat-band voltage, a depletion of the semiconductor band starts, presenting an accumulation of negative charge in the oxide-semiconductor interface. Finally, further increasing this voltage, minority carriers of the substrate (electrons) can flow through the oxide, which is known as inversion regime.

## 2. Deposition Methods and Sample Characterization



**Figure 2.10.** Energy band diagram corresponding to accumulation, depletion and inversion regimes band diagram corresponding to accumulation, depletion and inversion regimes.

The employed system for the electrical characterization consisted of a Cascade Microtech Summit 11000 probe station equipped with Faraday cage and a vacuum chuck with a thermal controller up to 300 °C. This system was connected to an Agilent B1500 semiconductor device analyzer, having a current resolution of some tens of fA.

### 2.4.1.1. Bulk-Limited Mechanisms

When the dielectric cannot evacuate all the injected charge from the electrode, the charge transport mechanism is considered bulk-limited. In this case, the intrinsic characteristics of the material like electron mobility, trap defect density or the dielectric constant are parameters that strongly affect the charge transport. Normally, at low voltages, the device presents ohmic behavior, having a linear dependence of the  $I(V)$  characteristics. However, non-linear dependence is observed for higher voltages, being the corresponding charge transport mechanism dominant in the conduction. Here, three different bulk-limited mechanisms are presented, being some of them the main mechanism observed in the devices studied in this Thesis.

- **Poole-Frankel mechanism (PF)**

Some defective materials present intra-band levels between the conduction and valence bands. These levels act as charge traps, in which electrons can move through them by means of trapping and detrapping processes. In order to jump from a trap to another, the electron needs to overcome the corresponding energy of the trap,

reaching the CB until being trapped again. Detrapping is modulated by the supplied voltage, reducing the trap ionization energy to overcome the Coulomb potential energy. Hence, the current density in this kind of materials can be expressed by the Pool-Frenkel (PF) model as:

$$J_{PF}(E, T) = q\mu_e N_t E \exp \left[ -\frac{q\phi_t - \sqrt{q^3 E / (\pi \epsilon_0 \epsilon_r)}}{k_B T} \right], \quad (2.8)$$

where  $q$  is the elemental charge,  $\mu_e$  the electron mobility,  $N_t$  the density of trapping centers,  $\phi_t$  the potential of the trap with respect to the conduction band,  $\epsilon_0$  and  $\epsilon_r$  the absolute and relative dielectric constants, respectively, and  $k_B$  the Boltzmann constant.

- **Space-charge limited current (SCLC)**

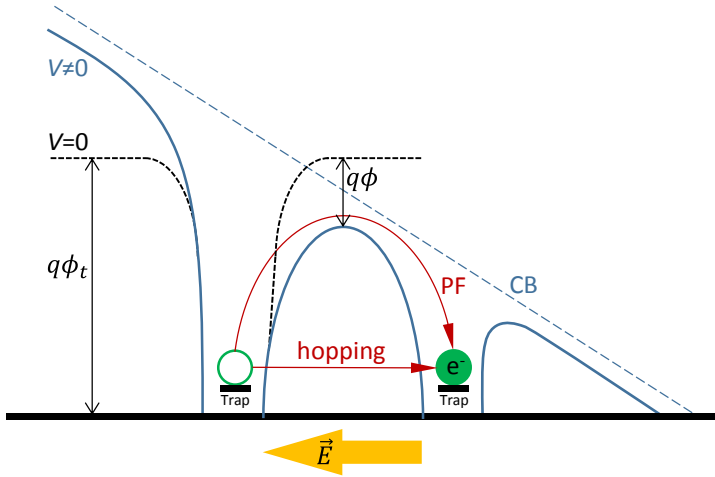
In the case that the dielectric cannot compensate the injected charge from the electrodes, the detrapping rate is lower than the carrier injection one. This effect induces charge accumulation at the electrode-dielectric interface due to the filling of some traps with carriers. Consequently, spatial deformation of the potential barrier takes place by the generation of an electric field, which compensates the carrier injection. When this occurs, transport lies within the space-charge limited current (SCLC) regime, and the current density can be expressed by:

$$J_{SCLC}(E) = \frac{9}{8} \mu_e \epsilon_0 \epsilon_r \frac{N_{inj} E^2}{N_t d} \exp \left[ -\frac{q\phi_t}{k_B T} \right], \quad (2.9)$$

being  $N_{inj}$  the concentration of injected carriers and  $d$  the thickness of the semiconductor layer. When all traps are filled, thus achieving the so-called trap-filled limit (TFL), injected carriers can move freely into the dielectric. In this case, the expression becomes

$$J_{SCLC}(E) = \frac{9}{8} \mu_e \epsilon_0 \epsilon_r \frac{E^2}{d}. \quad (2.10)$$

This kind of mechanism is observed in some defective materials like nitrides or oxynitrides when there are in the high injection regime.



**Figure 2.11.** Energy band diagram corresponding to PF and hopping transport mechanisms. The application of an external electric field ( $\vec{E}$ ) induces the bending of the band, reducing in  $q\phi$  the trap barrier energy  $q\phi_t$ .

- **Hopping mechanism**

When electrons hop from one trap to another one via tunneling through the potential barrier, hopping mechanism is considered. This tunneling takes place when electrons do not have enough energy to overcome the potential barrier, being the probability of the event dependent on the distance between traps. If this distance is short enough, the hopping mechanism can be written as:

$$J_{hopping}(E, T) = qan \exp \left[ \frac{qavE - E_a}{k_B T} \right], \quad (2.11)$$

where  $a$  is the mean hopping distance,  $n$  is the electron concentration at the CB of the dielectric,  $\nu$  the frequency of the thermal vibration of electrons at the traps and  $E_a$  is the activation energy corresponding to the energy of the trap with respect to the CB.

### 2.4.1.2. Electrode-Limited Mechanisms

In the case that the potential barrier height of the electrode-dielectric interface is high enough, electrode-limited transport mechanism takes

place. This transport mechanism is typically observed in low-defective materials with a large band offset. At high electric fields, a strong band bending occurs, thus accelerating the injected carriers with high kinetic energy (*hot carriers*). Depending on the potential barrier height and the temperature of the dielectric, different transport mechanisms can be considered.

- **Schottky emission**

If the potential barrier height is low and/or the dielectric temperature is high enough, Schottky emission mechanism takes place. This transport mechanism is strongly dependent on the temperature and it can be observed in thick insulators with low density of defects and low tunnel transparency. In this case, the current density can be written as:

$$J_{Schottky}(E, T) = \frac{4\pi q m^*}{h^3} (k_B T)^2 \exp \left[ -\frac{q\phi_b - \sqrt{q^3 E / (4\pi \epsilon_0 \epsilon_r)}}{k_B T} \right], \quad (2.12)$$

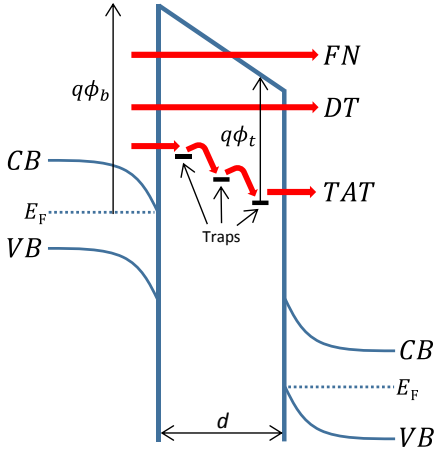
where  $m^*$  is the effective mass of electrons,  $h$  the Planck's constant and  $\phi_b$  the potential barrier height.

- **Direct tunneling (DT)**

Another possibility is that carriers overcome the potential barrier via tunneling mechanism, directly achieving the CB level without the necessity of intermediate-defective states (like hopping). Depending on the shape of the potential barrier, different tunneling mechanisms are considered. The first one is the called *direct tunneling* and it takes place when the carriers overcome a trapezoidal barrier, being the tunneling distance the thickness of the dielectric. Therefore, this transport mechanism is normally observed in thin layers with low dielectric constant. The current density, which does not depend on the temperature, can be expressed by:

$$J_{DT}(E) = \frac{q^2}{8\pi h (\phi_b^{3/2} - (\phi_b - Ed)^{3/2})^2} E^2 \exp \left[ -\frac{8\pi\sqrt{2qm^*}}{3hE} (\phi_b^{3/2} - (\phi_b - Ed)^{3/2}) \right]. \quad (2.13)$$

As it can be seen, the current density is independent on the temperature, being only the potential barrier height,  $\phi_b$ , the effective



**Figure 2.12.** Scheme of the energy band diagram corresponding to the electrode-limited mechanisms. The Fowler-Nordheim tunneling (FN) takes place through the triangular barrier, whereas direct tunneling (DT) occurs in the trapezoidal part of the barrier. In trap-assisted tunneling (TAT), the conduction is assisted by traps. The Fermi level ( $E_F$ ), conduction band (CB) and valence band (VB) are also indicated.  $q\phi_b$  and  $q\phi_t$  represent the energy barriers of electrode-dielectric interface and traps, respectively.

mass of electrons,  $m^*$ , and the thickness of the dielectric,  $d$ , the critical parameters in this kind of mechanism.

- **Fowler-Nordheim tunneling (FN)**

Under high electric field, larger than the electrode-dielectric barrier height, the bending of the band is enough to achieve a triangular-shaped barrier. Consequently, the effective thickness of the dielectric is reduced, increasing the tunneling probability of the carrier to the CB. In this case the current density is expressed by:

$$J_{FN}(E) = \frac{q^2}{8\pi h \phi_b} E^2 \exp \left[ -\frac{8\pi\sqrt{2qm^*}}{3hE} \phi_b^{3/2} \right]. \quad (2.14)$$

- **Trap-assisted tunneling (TAT)**

In both DT and FN mechanisms, described before, carriers arrive directly to the CB via tunneling of the electrode-dielectric barrier. However, in defective materials governed by electrode-limited mechanism, the electrical transport can become tunneling injection mediated by the intra-band defect states. In this case, the transport mechanism is called trap-assisted tunneling and the current density is expressed by:

$$J_{TAT}(E) = \frac{qN_t}{2\tau} \exp\left[-\frac{8\pi\sqrt{2qm^*}}{3hE} \phi_t^{3/2}\right]. \quad (2.15)$$

In this case, the conduction depends on the potential barrier of the traps  $\phi_t$ , which are lower than  $\phi_b$ . Therefore, this transport mechanism is normally obtained at low-medium electric fields.

### 2.4.2. Resistive Switching Characterization

The analysis of the resistive switching properties of some devices was carried out by means of the same experimental system employed for the electrical characterization described above. In order to achieve the different resistive states, a voltage stress protocol is required, supplying the voltage on the top electrode and keeping grounded the bottom one. Under enough voltage, typically positive, a sudden increase of the current (Set) is obtained by the formation of conductive filaments (CFs) in the dielectric layer. Sometimes, this process requires setting a current compliance (CC) in order to avoid a permanent damage in the devices. The properties of the CNFs are strongly dependent on the value of this CC, being its study of great interest. At this point, the device is in the low resistance state (LRS) and the  $I(V)$  characteristics keeps limited by the CC until the voltage is low enough to recover current below the CC. The high resistance state (HRS) is obtained applying opposite (bipolar) or the same (unipolar) voltage. In this case, no CC has to be set because sometimes the device needs high current through the CFs to partially dissolve them. When this occurs, the current suddenly decreases (Reset), recovering the HRS. However, this state is normally more conductive than the pristine state (before any structural or chemical modifications) because part of the CFs are not totally dissolved.

Once  $V_{Set}$  and  $V_{Reset}$  are determined by the  $I(V)$  characteristics, pulsed voltages can be applied to write the LRS and HRS and to do the read of the states. One resistive switching cycle consists of four consecutive pulses:  $V_{Set}$ ,  $V_{Read}$ ,  $V_{Reset}$  and  $V_{Read}$ . With this train of pulses, the LRS and HRS can be determined after changing the state, depending on the value of the current at  $V_{Read}$ . In order to carry out these pulses, an *Agilent B1500* semiconductor device analyzer was programed using *MatLab* software, resulting in total remote control of the voltages and applied times.



## 2.5. Electro-Optical Characterization

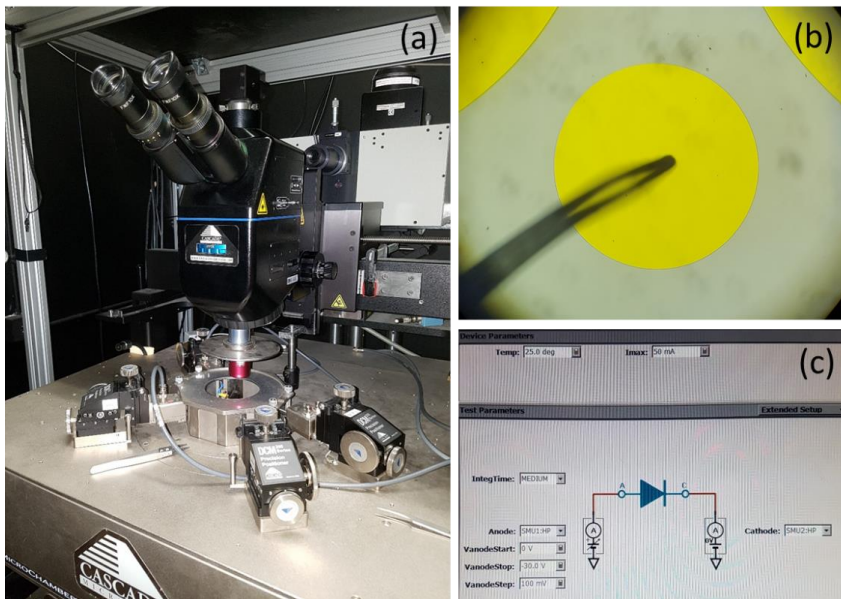
### 2.5.1. Electroluminescence Spectroscopy

When luminescent centers are excited as a result of the current injection, the emission is called electroluminescence (EL) and the spectra and their dynamics have great interest for the optoelectronics industry. In this case, device structure is required, having transparent electrode like TCOs to collect the emitted light. The excitation of the luminescent centers is more complex than in PL because it depends on the device design and on the electrical properties of the materials involved. This luminescence can take place through two different mechanisms, either via electron-hole recombination or via energy transfer of the carriers. The first one requires the simultaneous injection of electrons and holes from the anode and cathode, respectively, while in the second one the conduction electron impact on the luminescent center is the origin of the excitation

The experimental system employed to analyze the EL emission of some devices consisted of an *Agilent B1500* semiconductor device analyzer, used for the electrical excitation of the devices, with *Cascade Microtech Summit 11000* probe station, such as described before. The light emission was collected by a *Seiwa 888 L* microscope, working with a NIR 20× objective with NA = 0.4. Integrated emission was collected by means of a *Hamamatsu R928* GaAs PMT, collecting directly the light from the microscope and connected to a *HP* multimeter. EL spectra were acquired with a *Princeton Instruments* LN-cooled charge-coupled device (CCD), coupled to an *Oriel* monochromator.

### 2.5.2. Time-Resolved Electroluminescence

Analogously to PL measurements, the dynamics of the EL can be analyzed by means of pulsed excitation, obtaining information about the nature of the luminescent centers. In this case, the excitation is carried out by electrical pulses with enough voltage intensity to induce the excitation of the luminescent centers. In contrast to PL, both positive and negative polarizations can be explored, which is of great interest in devices that present rectification behavior. In this case, the



**Figure 2.13.** (a) Photograph of the system employed for the electrical and electro-optical characterization, which contains a probe station and a microscope to collect the EL emission from the devices, which can be detected either using a PMT or a CCD. (b) Photograph of a device contacted with a tip through the ocular of the microscope. (c) Screen of the software used for the analysis of the  $I(V)$  curves implemented into the Agilent B1500 semiconductor device analyzer.

dynamics of both accumulation and inversion regimes can be analyzed and information about the mechanisms that govern the process can be obtained. In addition, the possibility to alternate positive and negative voltages can avoid the charge accumulation that some devices present, typically at the interface between different materials. Sometimes, when the polarization of the voltage changes, this accumulated charge is discharged, inducing an overshoot in the current intensity in the device and consequently in the intensity of the emitted EL. This effect is observed in the case of the Si-NCs due to the accumulation of positive charge when the device works in accumulation regime, being neutralized by the electrons of the substrate when the inversion regime is induced.

This characterization was achieved using a pulse generator module implemented in the Agilent B1500 with a minimum pulse width of 10

## 2. Deposition Methods and Sample Characterization

ns. The corresponding EL emission was detected by the PMT and monitored by an *Agilent Infiniium DSO 8064A* oscilloscope.

# 3. Si-Based Materials for Optoelectronics and Resistive Switching

---

*“Change is never painful, only the resistance to change is painful”*

*Gautama Buddha*

---

An important part of this Thesis is focused on Si-based materials for optoelectronics and resistive switching applications. In this chapter, the results obtained from these materials are presented, including published papers with their corresponding summaries. These results are divided according to the two different materials under study. The first one consists of silicon-aluminum oxynitride (SiAlON), which has been used as RE host matrix, in particular doping it with cerium and europium ions by sputtering and PLD techniques. The resistive switching properties of undoped SiAlON thin films are presented, observing modification in their structural and chemical composition. The second Si-based explored material consists of multilayered Al-Tb/SiO<sub>2</sub>, fabricated via EBE using the delta-doping approach. The optimal layer configuration to enhance the Tb<sup>3+</sup> emission, together with the other fabrication parameters, was determined. Finally, the effect of this multilayered structure and the influence of the RE on the resistive switching properties were analyzed as well.

## 3.1. Silicon-Aluminum Oxynitride (SiAlON)

Despite the excellent optical properties that the SiO<sub>2</sub> host matrix has demonstrated when doped with REs, the low RE solubility in SiO<sub>2</sub> causes RE clustering [114]. In order to solve this problem, other Si-based materials have been explored as alternative host matrices, being Si<sub>3</sub>N<sub>4</sub> one of the most interesting ones for its larger RE ion solubility compared to the SiO<sub>2</sub> one. In addition, the lower band-gap (4–5 eV) of Si<sub>3</sub>N<sub>4</sub> can enhance the electroluminescence properties, thus

### 3. Si-Based Materials for Optoelectronics and Resistive Switching

becoming a good candidate for electro-optical applications [115]. Therefore, the possibility of combining both  $\text{SiO}_2$  and  $\text{Si}_3\text{N}_4$  host matrices ( $\text{SiO}_x\text{N}_y$ ) becomes an interesting idea, taking advantage of the electrical properties and good solubility of  $\text{Si}_3\text{N}_4$ , together with the presence of oxygen in  $\text{SiO}_2$  for the correct  $\text{C}_{4v}$  conformation that the REs require for optical activation. On the other hand, the introduction of other elements like Al ( $\text{SiAl}_x\text{O}_y\text{N}_z$ ) has provided the possibility of tuning the electrical properties, being this quaternary host matrix more adequate for electro-optical properties.

Beyond the excellent electro-optical properties of SiAlON as RE host matrix, its electrical properties, which can be modulated depending on the stoichiometry, can attract great interest as Si-based material compatible with CMOS technology. In addition, the fact that other related compounds like  $\text{SiO}_x$  [116],  $\text{AlO}_x$  [117] or  $\text{AlN}_x$  [118] present resistive switching properties, suggests that SiAlON could have a similar behavior, consequently becoming a good candidate for RRAM applications. In this respect, the resistive switching properties of SiAlON onto *p*-type Si substrate was explored, depositing Al electrodes in MIS structure.

In this way, two different collaborations have been carried out in order to study the electro-optical properties of RE-doped  $\text{SiAl}_x\text{O}_y\text{N}_z$ . The first collaboration consisted of Ce-doped  $\text{SiAl}_x\text{O}_y\text{N}_z$  samples fabricated in the *Center of Research on Ions, Materials and Photonics* (CIMAP) at the *University of Caen Normandy (UNICAEN)* led by Dr. Christophe Labbé. The materials were deposited onto *p*-type Si substrate by means of the RF sputtering technique using a combination of  $\text{CeO}_2$ , Si and Al targets under a  $\text{N}_2$  gas flow. Different stoichiometries were explored and the electro-optical properties of each compound were determined. The second collaboration consisted of Eu-doped SiAlON samples deposited by PLD onto *p*-type Si substrate. Samples were fabricated by the *Laser Processing Group* of the *Instituto de Óptica* (CSIC) in Madrid, led by Dr. Rosalía Serna. To explore the electroluminescence of the samples, the device structure was completed in the clean room facilities of the Faculty of Physics at the University of Barcelona, depositing ITO as top electrode and aluminum in the rear side of the Si substrate by EBE. The electrical and electro-optical characterization of all devices was carried out in the EL lab of the research group.

### 3.1.1. Optical and Electro-Optical Properties

The optical and electro-optical characterization of the RE-doped SiAlON is divided into two subsections, one for each collaboration. In the first one, the results obtained from Ce-doped SiAlON fabricated by sputtering in Caen are presented in detail, whereas the second one refers to the Eu-doped SiAlON PLD-fabricated in Madrid.

#### 3.1.1.1. Ce-doped SiAlON by RF sputtering

Samples were fabricated in Caen by means of RF sputtering technique. The layers were grown in a N<sub>2</sub> gas flow using a combination of CeO<sub>2</sub>, Si, Al, and SiO<sub>2</sub> targets. In a previous study of the group of C. Labbé [47], SiO<sub>x</sub>N<sub>y</sub> samples were explored, observing a dependence of the RE emission on the N concentration and suggesting different luminescent centers due to the different Ce atomic environment. The blue emission observed in PL measurements is related to the Ce<sup>3+</sup> ions, being more intense at higher N concentration. In our study, a red-shift of the Ce<sup>3+</sup> emission is observed with respect to the Ce-doped SiO<sub>x</sub> due to the introduction of nitrogen.

Both the electrical characterization and the EL acquisition were analyzed in the EL lab at UB. Different samples were studied, containing different concentrations of each species (Ce, Al, N). The *I(V)* characteristics suggest an electron transport mechanism governed by Poole-Frenkel model, especially at high N concentration, which increases the dielectric constant. The presence of RE ions seems to contribute to the dielectric constant modification, being slightly larger in doped samples. Regarding EL emission, the sample with 4at.% of Ce presents a clear blue emission related to the Ce<sup>3+</sup> ions, together with a broad emission around 900 nm attributed to defects. However, sample with 6at.% of Ce, does not exhibit any emission. This effect is in agreement with the emission quenching that samples with high RE concentration undergo, induced by the non-radiative interaction between RE.

The introduction of Al was found to enhance the electrical endurance by increasing the breakdown threshold voltage, consequently achieving larger electric fields and currents, which in turn increases

### 3. Si-Based Materials for Optoelectronics and Resistive Switching

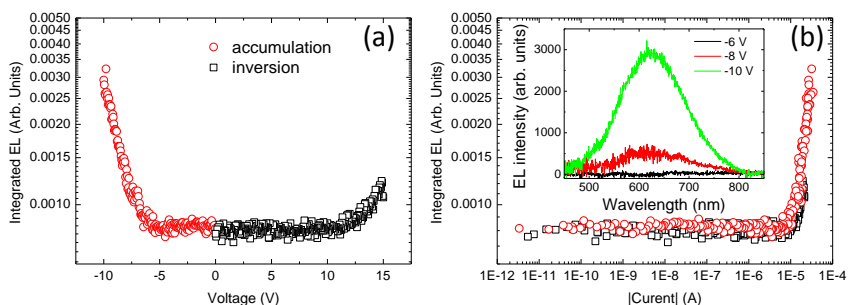
EL. Poole-Frenkel was also determined as the main electrical transport mechanism, being the dielectric constant very sensitive to the Al concentration. In contrast to the low EL emission from the sample without Al, co-doped sample with 3at.% Al induces  $\text{Ce}^{3+}$  emission increase by a factor 3, whereas larger Al concentrations decrease EL.

This study was presented as invited oral communication in the international conference of the 233<sup>rd</sup> *Electrochemical Society (ECS) Meeting* celebrated in Seattle (USA), in 2018 [see Section B.3. Conference Contributions (28)]. From this conference, a proceedings paper was published in *ECS Trans. Vol. 85(3) 9-21* [see Section A.I. *List of Articles (I)*].

#### 3.1.1.2. Eu-doped SiAlON by PLD

Following the study of SiAlON as optoelectronic material candidate, other samples were fabricated in Madrid. In this case, SiAlON layers were doped with Eu by means of PLD onto *p*-type Si at room temperature, using SiAlON and Eu targets. The doping process consisted of the ablation of targets, alternating 360 pulses of SiAlON and 10 pulses of Eu, being this process repeated 60 times and achieving a total thickness of 150 nm. Afterwards, a thermal annealing process was carried out at temperatures ranging between 300 °C and 800 °C for 1 h in air. By XPS analysis, a composition of Si (45at.%), O (12at.%), N (40at.%) and Al (3at.%) was determined in undoped SiAlON, while an Eu concentration of 1.4at.% was observed in doped samples, thus increasing the O/Si ratio. The easy oxidation of the RE benefits the incorporation of extra oxygen, resulting in the formation of europium oxide compounds. Broad spectra centered around 525 nm were observed in all Eu-doped samples annealed at different temperatures, which is attributed to the transition from the degenerated  $4f^65d^1$  level to the ground state  $^8S_{7/2}$  of  $\text{Eu}^{2+}$  ions. The intensity of the integrated emission increases with the annealing temperature, achieving the maximum signal at 600 °C and decreasing for higher annealing temperatures. This effect is ascribed to the reduction of the host matrix defects, which can contribute to a quenching of the emission. More information about this structural and optical characterization can be found in Ref. [52, 119].

### 3.1. Silicon-Aluminum Oxynitride (SiAlON)



**Figure 3.1.** Integrated EL emission as a function of (a) supplied voltage and (b) injected current. The inset in (b) represents the EL spectra at different supplied voltages.

Similar to the Ce-doped samples presented above, the electrical and electro-optical properties of the Eu-doped SiAlON were analyzed in Barcelona. Samples were completed as MIS structure, depositing ITO dots using a chromium shadow mask as top electrode and aluminum in the rear side of the Si substrate as bottom electrode, both by means of EBE.

In the Figure 3.1(a), the integrated EL emission of these devices are presented as a function of the supplied voltage. In accumulation regime ( $V < 0$ ), the sample presents a threshold voltage EL emission around  $-6$  V, whereas  $11$  V are required in inversion regime ( $V > 0$ ). The representation of this EL emission as a function of the injected current in log-log representation can be observed in the Figure 3.1(b), where the curves of both regimes have the same characteristics. In this case, the curves present the same threshold current around  $1 \times 10^{-5}$  A and follow a potential dependence between the integrated EL and the injected current. In order to determine the origin of this EL emission, the spectra were collected via a monochromator coupled to a CCD. The inset of the Figure 1(b) represents the EL spectra of a device supplied at different voltages. A clear emission is observed when voltages higher than  $-6$  V are supplied, in agreement with the observed integrated EL emission. In addition, the fact that these spectra present a broad emission confirms the  $\text{Eu}^{2+}$  state of the RE ions, as observed in PL emission.



### 3.1.2. Resistive Switching Properties

After the good results that SiAlON presented as RE host matrix, the resistive switching properties of this material were studied in order to explore its viability in RRAM applications. For this, devices were adequately electrically stimulated to achieve the Set and Reset processes between two resistive states, and the dominant electrical transport mechanism was determined in both cases. In addition, a detailed comparison between pristine and electroformed devices was carried out, analyzing both structural and chemical composition modifications between them.

#### 3.1.2.1. SiAlON as resistive switching device

An in-depth study of the resistive switching properties of Al/SiAlON/*p*-type Si devices was performed. The devices were fabricated using the analogous process employed for Eu-doped samples for the electro-optical characterization (see section 2.1.2.2. *Pulsed-Laser Deposition*), but in this case without the RE and replacing ITO for Al as top electrode. Before the electrode deposition, the samples were submitted to an annealing treatment at 700 °C for 1 h in air. For the resistive switching characterization, devices underwent a specific protocol applying on the top electrode a positive voltage ramp. A sudden increase of the current was observed around 20 V, inducing the switch to the LRS and requiring a compliance current of 0.5 mA to avoid permanent damage. This first step is known as electroforming process, in which the conductive paths are created for the first time. During this step, small features appeared in the top electrode, being visible *in situ* with the optical microscope of the system. The Reset process from LRS to HRS was achieved after applying a negative voltage ramp without compliance current, taking place around -4 V. At this point, the protocol was repeated, showing more conductivity in HRS than in pristine state and presenting  $V_{\text{SET}} \sim 15$  V, lower than during electroforming. Reading the resistive state at -0.5 V, a difference of 5 orders of magnitude in current between both resistive states was observed, being 6.6 k $\Omega$  cm and 2.5 G $\Omega$  cm the resistivities at LRS and HRS, respectively. Moreover, the electrical transport mechanisms corresponding to both states were analyzed, showing ohmic behavior in LRS and Poole-Frenkel as dominant mechanism in HRS.

In order to explore the small features appeared during the electroforming process, SEM images were acquired, showing bubble-like features in the Al top electrode. The cross-section of these features could be also observed by FIB, thus corroborating the bubble-like structure. Other smaller and irregular features were also observed, in this case attributed to a precipitation of SiAlON. To study better these features, HRTEM images were carried out on both structures. As observed by SEM, bubble-like features are formed as a consequence of the bending of the Al electrode. The fact that the Al electrode is detached from SiAlON layer suggests a gas eruption from SiAlON, similar to other observations on different metal oxides in which oxygen diffusion is the main process of conductive path formation via oxygen vacancies [120]. Regarding the SiAlON precipitate, irregular contrast was observed, indicating different local compositions within. In addition, and directly under the precipitate, the SiAlON layer presents a dark region in the bright-field TEM image, which suggests a different composition of the film. The chemical composition analysis of these regions was carried out using EELS. Color-coded plasmon energy maps showed a clear modification of the SiAlON composition in the precipitate, presenting higher-energy plasmons that were ascribed to a higher presence of either oxygen or nitrogen ( $\text{SiO}_2$  and  $\text{Si}_3\text{N}_4$  plasmon peaks). In contrast, the region under the precipitate exhibited a higher silicon concentration than unaltered SiAlON. These observations are in agreement with the out-diffusion of oxygen and/or nitrogen and they could be directly related to the conductive path formation. In order to determine which species (either oxygen or nitrogen) is responsible for the gas diffusion, composition density maps of the precipitate were carried out from core-loss EELS images, integrating the area under the K edges of N and O at 401 eV and 532 eV, respectively. This analysis concluded that the out-diffusion is attributed to both oxygen and nitrogen, being the precipitate rich in both elements and the region just above presenting a lack of nitrogen and oxygen.

This study was presented in the international conference of the *European Materials Research Society (EMRS) Spring Meeting* celebrated in Strasbourg (France) and in the national *Conference on Electron Devices (CDE)* celebrated in Barcelona (Spain), both in 2017, respectively as oral communication and poster presentation [see

Section B.3. Conference Contributions (26 and 19)]. This study was also published in *Nanotechnology Vol.29 235702* [see Section A.I. *List of Articles (II)*].

## 3.2. Multilayered Al-Tb/SiO<sub>2</sub>

As mentioned in the introduction of this thesis, [see Chapter 1.3. (*Rare Earth*)], the trivalent state of RE ions into a host matrix presents optical emission with narrowed spectra because of their  $4f$ -electronic levels in an open shell. In these conditions, terbium ions exhibit intense emission in the visible range due to their  $^5D_4 \rightarrow ^7F_i$  transitions ( $i = 6, 5, 4$  and  $3$ ), taking place around 488 nm, 542 nm, 586 nm and 622 nm, respectively. In this case, the 542-nm transition is the most intense one, giving the sample a green-colored emission. In order to obtain this RE emission and avoid the clustering, very low atomic percentage of the ions must be introduced into the host matrix (1%–3%) and distributed as homogeneously as possible. Another possibility makes use of the so-called *delta-doping* approach, in which the RE is introduced into the host matrix by depositing very thin layers of RE separated by layers of the matrix material. These RE layers should be as thin as possible, being thicknesses below the atomic radius the optimum ones to attain isolated RE atoms while preventing lateral clustering. The inter-RE distance in the growth direction can be controlled by the thickness of the host matrix, which separates the RE layers. On the other hand, it is well known that the introduction of metal atoms in the sample as co-doping element enhances the optical emission of the RE by modifying its local environment.

In this study, Tb-doped SiO<sub>2</sub> samples were fabricated by electron beam evaporation via the delta-doping approach, in which pure Tb and SiO<sub>2</sub> targets were alternatively evaporated to obtain a nanomultilayer (NML) structure. The nominal thickness of the Tb layer was 0.4 nm, which is the thinnest layer that the fabrication system permits. Other samples were also fabricated that were co-doped with Al in different layer configurations in order to obtain the best structure for the optical activation of the RE. Optical characterization of the samples was carried out via photoluminescence in the visible range, analyzing the spectra emission under the 325-nm line of a He-Cd laser. The effect of the thickness of the SiO<sub>2</sub> layer and the annealing temperature was also studied. The next step of this study

consisted of the structural and chemical characterization of samples, obtaining HRTEM images of the NMLs and their composition by means of EELS and XPS. The effect of Al on the photoluminescence was analyzed and discussed in depth and related to the emission dynamics of the RE. In order to complete the electro-optical characterization of the material, device structure was achieved after depositing ITO as top transparent electrode and Al in the rear side of the substrate. Electrical characterization allowed comparing the conductivity of the devices with and without Al, suggesting different charge transport mechanisms. Electroluminescence emission was also obtained, being the spectra in agreement with the PL measurements. A quenching of EL was observed in successively acquired spectra at constant injected current, which was directly correlated to a reduction in the resulting voltage. This fact was attributed to a conductive path formation via oxygen vacancies, which is one of the mechanisms for conductive filaments formation in resistive switching devices. These results induced us to explore both the resistive switching properties of these devices and the role of the RE in these electrical properties. Hence, the last part of this study was the resistive switching characterization of Al-doped and Al- and Tb-codoped SiO<sub>2</sub> devices, both presenting memristive behavior. The introduction of the RE presents clear differences in the Set and Reset voltages, even achieving self-compliance behavior in some cycles. In the next subsection, these studies are described more in detail and the corresponding paper publications are as well presented.

### 3.2.1. Optical and Electro-Optical Properties

#### 3.2.1.1. Al and Tb delta-doped SiO<sub>2</sub> by e-beam evaporation

This first part of the study is focused on fabrication parameters like the thickness of the SiO<sub>2</sub> layers ( $d$ ) and the annealing temperature ( $T_a$ ), aiming at determining the optimum process for the optical activation of the Tb<sup>3+</sup> ions. The NMLs were deposited onto crystalline  $p$ -type (100)-Si substrate by EBE. The employed system was a PFEIFFER VACUUM Classic 500 with a Ferrotec GENIUS electron beam controller and a Ferrotec CARRERA high-voltage power supply. In order to achieve delta-doping, the nominal thickness of the Tb<sup>3+</sup> layer was fixed at 0.4 nm, being the lowest thickness allowed by the system, and the substrate temperature was kept constant at 100 °C. The

structure of the samples consisted of  $15 \times (\text{Tb}/\text{SiO}_2)$  bilayers, with  $\text{SiO}_2$  sublayer thicknesses ranging from 1.0 nm to 3.0 nm (inter-RE ion distance in the growth direction). This structure was protected by two 10-nm-thick buffer and capping  $\text{SiO}_2$  layers, respectively at the bottom and on top of the NMLs. Finally, samples were submitted to an annealing process at 700 °C, 900 °C and 1100 °C for 1 h in  $\text{N}_2$  for the optical activation of the RE. The PL of the samples was analyzed in the visible range (400–700 nm), exciting the samples with the 325-nm line of a He-Cd laser and obtaining a  $\text{Tb}^{3+}$ -related emission in all the samples. Annealed samples exhibit the most intense luminescence due to a broad emission related to defects of  $\text{SiO}_2$  (oxygen vacancies). However, the intensity of  $\text{Tb}^{3+}$ , subtracting the defect-related emission, presents the most intense emission in the as-deposited sample. The fact that the annealing treatment does not improve the activation of more  $\text{Tb}^{3+}$  ions as luminescent centers, being these already optically activated during the deposition process, confirms their poor diffusion within the oxide and the role of matrix defects avoiding their optical activation. Regarding the intra-RE distance in the growth direction ( $d$ ), it was observed that the PL emission of the  $\text{Tb}^{3+}$  is very low for  $d \leq 1.4$  nm, whereas it clearly increases for thicker layers until values around  $d \sim 2.2$  nm, beyond which the emission keeps constant or slightly decreases. This fact confirms that thin  $\text{SiO}_2$  layers allow for the interaction between REs, which in turn increases the occurrence of non-radiative processes. Using thicker layers, however, the inter-RE distance in the growth direction prevents this effect, consequently obtaining a larger number of optically-activated  $\text{Tb}^{3+}$  ions.

The influence of Al on the optical properties of  $\text{Tb}^{3+}$  ions was investigated through the fabrication of new samples with different configurations of Al, Tb and  $\text{SiO}_2$  layers, presenting in all cases the same concentration of Tb. Al layers were deposited either separated by  $\text{SiO}_2$  layers or close to Tb layers in different structures. In contrast to the samples without Al, all co-doped samples exhibit clear enhancement of the PL emission of the  $\text{Tb}^{3+}$  ions when annealed, as high as one order of magnitude in the case of the structure in which the Tb is sandwiched by two Al layers. PL dynamics was analyzed via time-resolved measurements at the Tb-related emission wavelength of 542 nm, the samples without and with aluminum, under the best configuration in terms of optimum emission, being compared. Two

single exponential decay times were observed in both cases, suggesting more than one luminescent center. The fast decay time is different for both samples, being faster in the sample without Al with 0.6 ms, while the sample with Al presents a decay time of 1.2 ms. These fast decay times are ascribed to cross-relaxation processes due to the RE-RE interaction, which quenches the Tb<sup>3+</sup>-related emission. This effect is more evident in the sample without Al, where the interaction with the RE neighbors becomes more probable. However, the slow decay time is the same for both samples, with a value of 1.6 ms, which is attributed to the decay time of the Tb<sup>3+</sup> ions in a proper C<sub>4v</sub> configuration.

This study was presented in the international conference of the *European Materials Research Society (EMRS) Spring Meeting* celebrated in Lille (France) and in the *Society of Photographic Instrumentation Engineers (SPIE) Microtechnologies* celebrated in Barcelona, both in 2015, as oral communications [see Section B.3. Conference Contributions (9 and 12)]. From the second conference, a proceedings paper was published in *Proc. of SPIE Vol. 9520 95200K-1* [see Section A.1. *List of Articles (III)*].

### 3.2.1.2. Structural and optical properties of Al-Tb/SiO<sub>2</sub>

The next step consisted of analyzing how Tb and Al layers are distributed within the NML structure. In the case of the co-doped sample, the structure in which Tb layers are sandwiched by two Al layers was selected due to its better optical emission, as determined in the previous work [see Chapter 3.2.1.1. (*Al and Tb delta-doped SiO<sub>2</sub> by e-beam evaporation*)]. This structural characterization was carried out by means of HRTEM and HAADF images, and complemented with EELS, thus permitting the chemical composition analysis of the NMLs at nanoscopic level. Average composition was also measured by XPS, which allowed determining the oxidation state of aluminum. PL emission was again investigated, by comparing both doped and co-doped samples, whose dependence on the Tb<sup>3+</sup> ions and SiO<sub>2</sub> defects was explored in both as-deposited and annealed samples at 700 °C, 900 °C and 1100 °C. Finally, the emission dynamics of the samples was also investigated at 542 nm, showing a clear influence of the decay time on the annealing temperature.

### 3. Si-Based Materials for Optoelectronics and Resistive Switching

HRTEM images confirmed the NML structure with a small degree of waviness. No crystalline domains were observed in any regions, which implies that all layers are in amorphous phase. In order to better determine the distribution of the Al/Tb/Al stack, element distribution maps were acquired, filtering the signal at the energies of the core-loss edges corresponding to each element. No evidence of the sandwiched structure was observed in the Al/Tb/Al stack, being the present species totally intermixed and homogeneously distributed. However, these mixed layers are spatially isolated from the Si signal coming from the region where the SiO<sub>2</sub> layer is located. To study the Al dependence on the bonds surrounding Tb ions, XPS measurements were carried out at different depths. Spectra around the bond energies corresponding to Al 2p, Tb 4d, Si 2s and O 1s were acquired for both doped and co-doped samples, showing clear differences. In the case of O 1s, a narrow spectrum was observed at the surface, where only SiO<sub>2</sub> is present. Nevertheless, a red-shifted and broader spectrum was obtained at the middle of the NML, where Tb is present, which is attributed to the influence of the Tb ions on the oxygen binding energy. The co-doped sample shows more red-shifted and broader spectra than the doped one, thus adding another contribution ascribed to Al-O bonds. Taking into account the cross-section ratio of each element, atomic concentrations were estimated from relative areas of the spectra. From the top protective layer, good stoichiometry of the SiO<sub>2</sub> was obtained. At the middle of the NML an average atomic content of 2at.% of Tb was determined for the Tb-doped sample. In the Tb and Al co-doped sample, values of 1at.% and 10at.% were obtained for Tb and Al, respectively. In this case, an oxygen excess of 23at.% was detected and ascribed to the oxidation of the Al-Tb stack. Considering that all Al atoms are oxidized in Al<sub>2</sub>O<sub>3</sub> form (due to its easy oxidation), 45% of Tb atoms should be also oxidized in the form of Tb<sub>2</sub>O<sub>3</sub>, even forming an Al-Tb-O ternary compound. The fact that no extra oxygen was observed in the Tb-doped sample supports this assumption, the oxidation taking place only at the interfaces with the SiO<sub>2</sub> layers. Hence, the introduction of Al close to Tb ions strongly affects the local environment of the RE, favoring its oxidation and, consequently, having an impact on its emission properties.

The optical characterization was carried out in a similar way than in the previous study. In contrast to what was observed in the Tb-doped samples, in which the Tb<sup>3+</sup>-related PL emission did not depend on  $T_a$ ,

Al and Tb co-doped samples present a clear enhancement of the RE emission when annealed. The thermal treatment induces the optical activation of the RE due to a rearrangement of the local environment of the Tb<sup>3+</sup> ions by the Al presence. This annealing process also activates the defects of the SiO<sub>2</sub> host matrix, although this emission can be quenched when annealed at very high temperature (1100 °C), due to an improvement of the structural arrangement of the SiO<sub>2</sub>. Comparing the RE emission of Tb-doped and Al and Tb co-doped samples, annealed both at 1100 °C, an enhancement of one order of magnitude was observed in the latter. This fact evidences that the presence of Al contributes to improve the optical activation of the RE. Similar to the previous study, the emission dynamics of the co-doped samples annealed at different temperatures was analyzed at 542 nm. The as-deposited sample presents a single exponential decay with a decay time of 0.5 ms (similar to the as-deposited sample without Al). However, after annealing at intermediate temperatures (700 °C and 900 °C), two single exponentials were observed, one fast and another one slow with decay time of 1.2 ms and 1.7 ms, respectively. The dynamics corresponding to the sample annealed at 1100 °C shows only one single exponential with a decay time of 1.7 ms, which is the same slow decay time that samples annealed at intermediate temperatures exhibit. The two different decay times suggest that Tb<sup>3+</sup> ions are in two different optically-active spatial configurations. In fact, different recombination times are ascribed to different ratios of radiative and non-radiative processes within the material. A thermal treatment at high temperature reduces these non-radiative processes by decreasing the defects concentration, and consequently all optically-active Tb<sup>3+</sup> ions become in the optimum C<sub>4v</sub> configuration, thus showing only one decay time.

This study was published in *Journal of Applied Physics Vol. 120, 135302 (2016)* [see Section **A.1. List of Articles (IV)**], as a final result of the structural and optical characterization of the Al-Tb/SiO<sub>2</sub> samples.

### **3.2.1.3. Electroluminescence of Al-Tb/SiO<sub>2</sub> devices**

The electrical and EL properties of devices containing Al-Tb/SiO<sub>2</sub> on a *p*-type Si substrate were as well inspected. Indium tin oxide (ITO) was employed as transparent conductive oxide (TCO) to collect the



### 3. Si-Based Materials for Optoelectronics and Resistive Switching

light emission from the NMLs when an electric field is supplied. The measurement setup consisted of an Agilent B1500 semiconductor device analyzer and a Cascade Microtech Summit 11000 probe station, biasing the voltage on the top contact and grounding the bottom one. Electrical transport mechanisms were studied in accumulation regime ( $V < 0$ ), where the light emission from the  $Tb^{3+}$  ions was detected, matching the spectrum with the obtained from PL and cathodoluminescence (CL). Finally, the quenching of the EL emission from the RE, obtained along successive measurements, was correlated with a voltage reduction due to an increase of the conductivity of the layer via the formation of conductive paths.

In contrast to the samples fabricated for structural and optical characterization, in which  $15 \times (Al/Tb/Al/SiO_2)$  NML stacks were deposited between two 10-nm-thick  $SiO_2$  protective layers, thinner samples were employed for the device structure, containing only  $5 \times (Al/Tb/Al/SiO_2)$  NML stacks without the  $SiO_2$  protective layers. This thinner structure was selected in order to achieve enough current density at low voltages that enables EL emission. The top electrode was circle-patterned with ITO by EBE using a chromium shadow mask with 200  $\mu m$  of radius. An annealing treatment of ITO at 600  $^{\circ}C$  for 1h in  $N_2$  was required to increase its optical transparency. Finally, the bottom contact was achieved by depositing full area aluminum electrode by EBE as well. Prior to the electrical and electro-optical characterization, the samples were excited under resonant and non-resonant conditions using the 488-nm and the 325-nm lines of  $Ar^+$  ion and He-Cd lasers, respectively. Similar spectra were obtained in both cases, which match with the CL after exciting the samples with electrons at 2 keV. Via  $I(V)$  characteristics, electrode-limited conduction mechanism based on the Schottky emission model was found as the main electrical transport mechanism.

Integrated EL was obtained using a PMT, which exhibited an emission threshold voltage of 8.5 V. Linear dependence of the EL on the injected current was observed with a threshold current of 2  $\mu A$ . The spectrum of this emission was acquired using a  $LN_2$ -cooled CCD camera during 30 s, when the device was excited by injecting -100  $\mu A$  at -18 V. Successive measurements were carried out under the same electrical conditions, obtaining a clear quenching of the RE emission. Analyzing the evolution of the voltage in these measurements via  $V(t)$

characteristics, a direct correlation between EL intensity and voltage was obtained, showing a sudden decrease of the voltage after some seconds. This effect could be attributed to the conductive paths generation during the measurement, which increases current through them.

This study was presented in the international conference of the *European Materials Research Society (EMRS) Spring Meeting* celebrated in Strasbourg (France) in 2017, as poster presentation [see Section B.3. Conference Contributions (23)]. From the conference, a proceedings paper was published in *Physica Status Solidi A 1700451* [see Section A.1. *List of Articles (V)*], being selected as cover picture in the Vol. 215, Issue 3, published on February 7<sup>th</sup>, 2018.

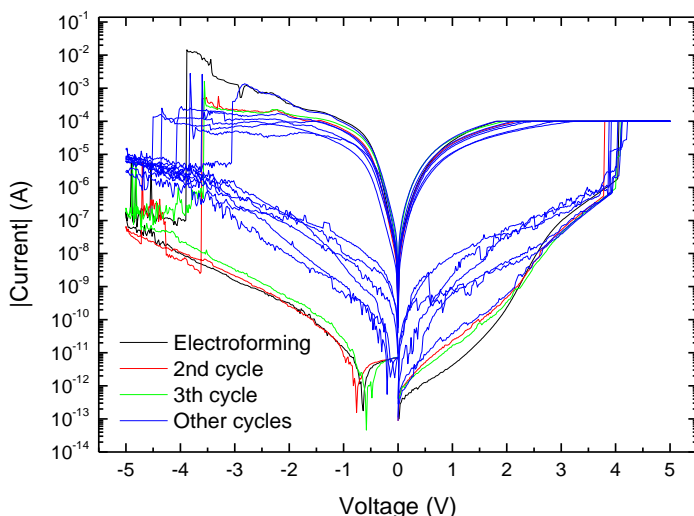
### 3.2.2. Resistive Switching Properties

In order to better analyze the formation of the conductive paths that the electro-optical characterization expects, the resistive switching properties of the Al-Tb/SiO<sub>2</sub> multilayers onto *p*-type Si, using either Al or ITO as top electrode, were explored to determine whether this structural modification can be reversible or not.

#### 3.2.2.1. Tb-Al/SiO<sub>2</sub> as resistive switching device

First of all, a device containing Al as top electrode was submitted to a positive voltage ramp to induce the electroforming process and, therefore, to achieve the LRS. In order to avoid permanent damage to the device, a compliance current of 100  $\mu$ A was set. As can be seen in the Figure 3.2, this electroforming takes place around 4 V. The Reset process was carried out after supplying a negative voltage ramp without current compliance, being around  $-4$  V the voltage at which this process occurs. This fact confirms that existence of conductive path formation and thus the possibility to modify the material to achieve the HRS again. After these interesting results, the device was submitted to a larger number of cycles, obtaining similar results. The second cycle (showed in red) presents a Set voltage threshold around 4 V, which is similar to the one observed in the electroforming process and having a similar curve in the LRS. The third cycle shows the same behavior as the second one. However, the following cycles (in blue) present more conductive properties in both resistive states. In this

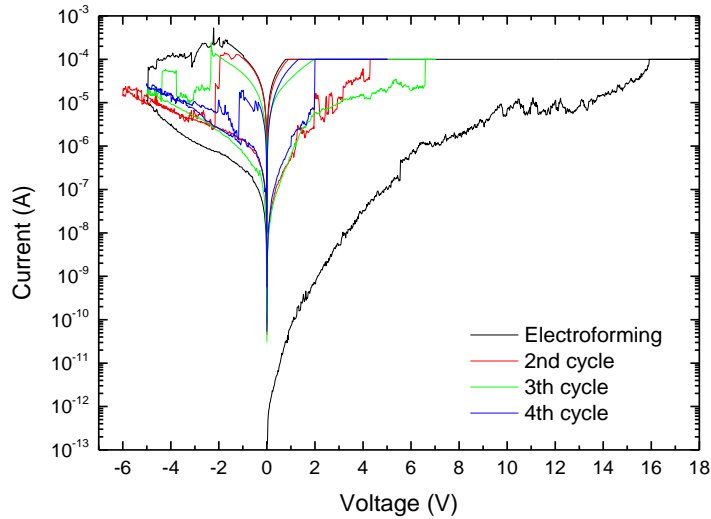
### 3. Si-Based Materials for Optoelectronics and Resistive Switching



**Figure 3.2.** Full  $I(V)$  cycles corresponding to a device containing multilayered Al-Tb/SiO<sub>2</sub> structure onto  $p$ -type Si and using Al as top electrode. The black, red and green curves correspond to the electroforming process, the second and the third cycles, respectively. Blue curves correspond to the following cycles.

case, the Set process occurs at the same voltage, but a clear voltage dispersion is observed. In addition, the shape of the curves indicates a decrease of the accumulated charge from  $-0.75$  V to  $-0.2$  V, even disappearing in some cases. This behavior change could be interpreted as the formation of more conductive paths along the cycle. In fact, all curves show a clear instability in the Reset, indicating the complexity of this process and how the HRS is strongly dependent on the conduction of the material after the Reset.

Once the resistive switching properties of this multilayered structure were confirmed, the same process was carried out in devices employed in the electro-optical characterization (see subsection 3.2.1.3. *Electroluminescence of Al-Tb/SiO<sub>2</sub> devices*), being the substitution of the Al by ITO as top electrode the only difference with respect to the device presented above. These devices were of great interest in order to correlate the EL emission previously observed with their resistive switching properties. The Figure 3.3 shows the  $I(V)$  characteristics of a device containing the ITO as top electrode contact. In this case, the device requires more voltage to induce the electroforming process. This fact could be attributed to the low

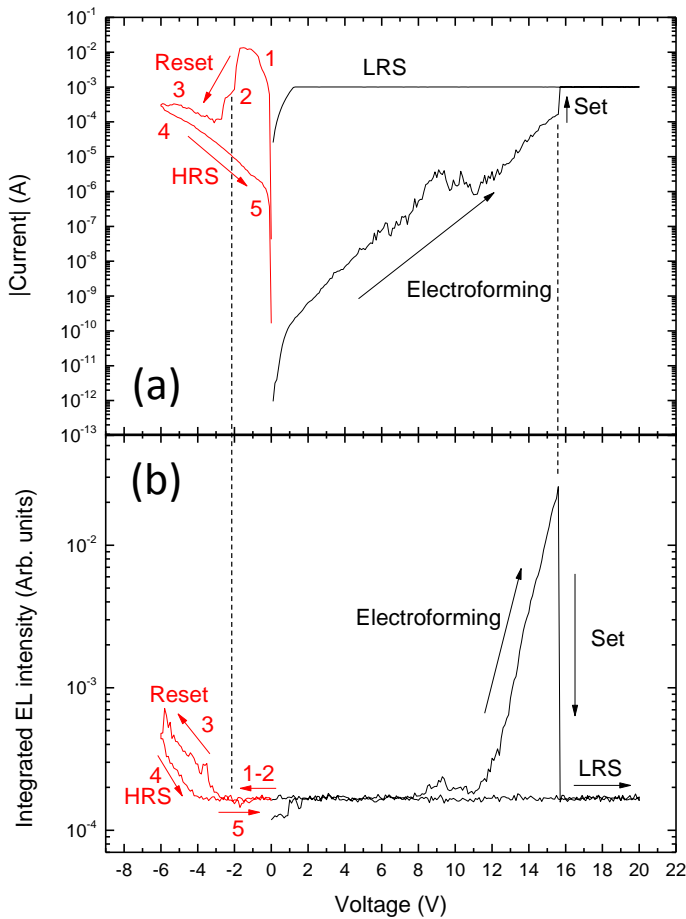


**Figure 3.3.**  $I(V)$  curves of different resistive switching curves of a device containing multilayered Al-Tb/SiO<sub>2</sub> structure onto p-type Si and using ITO as top electrode. The black, red, green and blue curves correspond to the electroforming process, the second, the third and the fourth cycles, respectively.

conductivity of the top electrode, being higher the supplied voltage in order to induce the first resistive switching. Regarding the Reset process, similar behavior can be observed, requiring a higher voltage with respect to the following cycles. In addition, the HRS obtained after the first Reset process achieves a resistive state less conductive than the other ones. The following cycles presented Set voltage thresholds lower than the electroforming one, showing more dispersive values around 4 V in comparison to devices containing Al as top electrode; therefore, it is clear that the incorporation of ITO as top electrode strongly influences on the resistive switching properties of the device. However, the necessity to have a TCO as top electrode is a requirement to use these kind of devices for electro-optical application, yielding light from them in specific conditions.

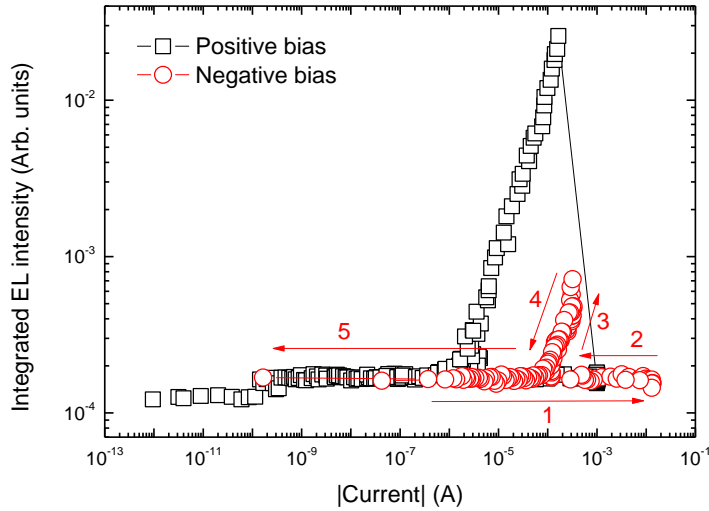
In order to determine whether the devices emit light via EL under these specific resistive conditions,  $I(V)$  characteristics was measured while simultaneously collecting the integrated EL emission. The Figure 3.4(a) shows a complete cycle with the electroforming and Reset processes and Figure 3.4(b) presents the corresponding

### 3. Si-Based Materials for Optoelectronics and Resistive Switching



**Figure 3.4.** (a) Complete  $I(V)$  resistive switching cycle corresponding to the device containing multilayered Al-Tb/SiO<sub>2</sub> structure onto *p*-type Si and using ITO as top electrode. (b) Integrated EL emission simultaneously collected with the  $I(V)$  characteristics of the resistive switching cycle presented in (a).

integrated EL emission. First of all, no emission is observed at low voltages due to the low current that the pristine device presents. Around 8 V, a current instability can be seen together with a slight EL emission. For supplied voltages higher than 12 V, the device recovers a current stability progressively increasing its current and showing an integrated EL emission with incremental value. About 16 V, the Set process takes place, being the current of the LRS limited by the current compliance. At this moment, the integrated EL emission is totally quenched, not exhibiting any EL emission along the rest of the



**Figure 3.5.** Integrated EL emission as a function of the injected current, in log-log representation, corresponding to the EL emission presented in the Figure 3.3 (b), which was simultaneously collected during the resistive switching cycles shown in the Figure 3.3 (a).

curve in the LRS. Analyzing the Reset process, a more complex behavior is observed. Supplying negative voltage, the device does not show EL emission while the LRS is present (see point 1). The Reset occurs in two processes. The first one is around  $-2$  V, decreasing the current through the device. However, the supplied voltage is enough for the correct excitation of the luminescent centers (see point 2). The second Reset process takes place around  $-3$  V, obtaining a more resistive state than the previous one. In this case, the device shows a slight EL emission, which progressively increases after higher negative voltage is applied (see point 3). Once the cycle reaches the maximum negative voltage and the voltage ramp goes back, this EL emission starts decreasing as well (see point 4) until  $-4$  V, where the EL emission is totally quenched (see point 5).

As it can be observed, there is a current difference between the points 3 and 4. This fact can be attributed to the instability of this resistive state, presenting continuous structural and chemical modifications of the material. In addition, the corresponding integrated EL in this region of the  $I(V)$  characteristics presents a lower-intensity light emission. The Figure 3.5 plots the integrated EL emission as a

### 3. Si-Based Materials for Optoelectronics and Resistive Switching

function of the injected current in log-log representation, which shows two clear emissions that correspond to the two voltage polarization states of the device. At positive voltages, corresponding to the electroforming process, a linear dependence of the integrated EL on the injected current is observed with a threshold current around  $2 \times 10^{-6}$  A. In contrast, the integrated EL emission after the Reset process, corresponding to negative voltages, shows higher threshold current around  $1 \times 10^{-4}$  A. In this latter case, the dependence is linear as well, thus indicating that the intensity of the EL directly depends on the injected current as long as the luminescent centers have enough energy excitation.

### Enhancing the Blue Emission in Ce doped Silicon Oxynitrides Thin Films for Electroluminescence Device Applications

F. Ehré<sup>a</sup>, C. Dufour<sup>a</sup>, O. Blázquez<sup>b</sup>, B. Garrido<sup>b</sup>, W. M. Jadwisieniczak<sup>c</sup>, D. C. Ingram<sup>d</sup>, F. Gourbilleau<sup>a</sup>, and C. Labbé<sup>a</sup>

<sup>a</sup> CIMAP Normandie Univ, ENSICAEN, UNICAEN, CEA, CNRS, 14050 Caen, France

<sup>b</sup> MIND-IN2UB, Departament d'Enginyeria Electrònica i Biomèdica, Universitat de Barcelona, Martí i Franquès 1, E 08028, Barcelona, Spain

<sup>c</sup> School of Electrical Engineering and Computer Science, Ohio University, Athens, OH 45701, USA

<sup>d</sup> Department of Physics and Astronomy, Ohio University, Athens, OH 45701, USA

Ce-doped  $\text{SiO}_x\text{N}_y$  and  $\text{SiAlON}$  matrices are promising materials for blue LED applications. The uniqueness of this approach stems from the fact that  $\text{SiO}_x\text{N}_y$ , as a host, combines specific properties of individual  $\text{SiO}_x$  and  $\text{SiN}_y$  matrices like solubility, efficient emission, 5 eV gap *etc.* with a broad excitation range (400 to 500 nm) of  $\text{Ce}^{3+}$  due to the  $4f-5d$  transitions. Furthermore, the co-doping with aluminum enhances the  $\text{Ce}^{3+}$  emission. In this work, we fabricated electroluminescent devices using  $\text{SiO}_x\text{N}_y$ :  $\text{Ce}^{3+}$  and  $\text{SiAlON}$ :  $\text{Ce}^{3+}$  as an active layers and studied the resulting emission under optical and electrical excitation as a function of nitrogen, cerium and aluminum concentrations.  $I-V$  measurements were conducted to determine the  $\text{SiO}_x\text{N}_y$ :  $\text{Ce}^{3+}$  layer electrical parameters. The transport through the devices obeys a Poole-Frenkel conduction mechanism. It was demonstrated that by optimizing the  $\text{SiO}_x\text{N}_y$ : $\text{Ce}^{3+}$  material growth parameters an improvement of electroluminescence yield can be achieved with maximum intensity achieved for devices with Ce content of 4 at.%.

#### Introduction

Rare earth (RE) doped silicon based materials have been extensively investigated in the past years. Various hosts were doped with  $\text{Er}^{3+}$  ions that emitted at 1.5  $\mu\text{m}$  corresponding to the maximum transparency of silica used in telecommunication. (1). For the  $\text{Ce}^{3+}$  ion, only a few studies have been reported on its electroluminescence (2). Among the silicon-based matrices, silica ( $\text{SiO}_2$ ) and silicon nitride ( $\text{Si}_3\text{N}_4$ ) have been extensively explored; however each of them present certain advantages and drawbacks. In the case of silica matrices, achievement of strong  $\text{RE}^{3+}$  ions emission is limited by a low excitation cross section (3), the highly insulating nature of the  $\text{SiO}_2$  matrix, a low RE solubility as well as RE cluster formation (4). However, the main drawback limiting the  $\text{SiO}_2$ :  $\text{RE}^{3+}$  light emitting applications comes from the large band gap of the matrix ( $\sim 9$  eV) resulting in low electrical conductivity. On the other hand,  $\text{Si}_3\text{N}_4$  with a smaller energy band gap (4 eV) and reduced tendency of the RE to form clusters seems to be more suitable for RE doping (5,6). However despite these advantages the emission efficiency from  $\text{RE}^{3+}$  ion in a nitride matrix is much lower than in silica matrix (7). To capitalize on the advantages offered to the RE doping by both oxide and nitride silicon matrices, a Ce-doped  $\text{SiO}_x\text{N}_y$  matrix has been explored by Ramirez *et al.* (8). It was reported that the maximum



### 3. Si-Based Materials for Optoelectronics and Resistive Switching

ECS Transactions, 85 (3) 9-21 (2018)

electroluminescence (EL) peak from  $\text{Ce}^{3+}$  ion shifted from 400 nm to 476 nm as function of the nitrogen concentration (*i.e.* the nephelauxetic effect) (8). Koao *et al.* showed that aluminum co-doping  $\text{Ce}^{3+}$  doped  $\text{SiO}_2$  glasses leads to an enhancement of photoluminescence emission (9). In this work, Ce-doped  $\text{SiO}_x\text{N}_y$  layers with a typical thickness of 50 nm were grown by sputter deposition. Photoluminescence (PL) from the  $\text{SiO}_x\text{N}_y$ : Ce layers and EL from capacitive devices having a  $\text{SiO}_x\text{N}_y$ : Ce active layer were examined for device performance as function of growth parameters and material composition.

#### Experimental Techniques

##### Active Layer Preparation

The devices were fabricated in a few step process. First, the Ce-doped  $\text{SiO}_x\text{N}_y$  active layer was grown by magnetron reactive sputtering on 2-inch diameter (001) p-type silicon wafers under an argon plasma at the CIMAP laboratory. During the growth, the chamber base pressure was fixed at 3 mTorr, the argon flow was 8 sccm and the substrate temperature was kept at 300 K. Samples were deposited from  $\text{CeO}_2$ , aluminum and silicon targets under a fixed nitrogen flux with the density of power on the  $\text{CeO}_2$  and Al targets varied from 0 to  $2.1 \text{ W}\cdot\text{cm}^{-2}$ , 0.3 to  $0.75 \text{ W}\cdot\text{cm}^{-2}$ , respectively and fixed at  $4.5 \text{ W}/\text{cm}^2$  for the Si target. As-deposited films were thermally annealed in the  $600^\circ\text{C}$  to  $1200^\circ\text{C}$  temperature range for 1 hr. in nitrogen ambient at atmosphere pressure.

##### Device Fabrication

Figure 1 summarizes the device obtained and shows the thicknesses of the layers. The individual indium tin oxide (ITO) top electrical contacts were deposited on the  $\text{SiO}_x\text{N}_y$ : Ce layer by electron beam evaporation using a shadow mask having a set of circular holes with 0.2 mm dim.  $\text{In}_2\text{O}_3/\text{SnO}_2$  (90%/10%) pellets with a diameter of 1 mm or 2 mm were used as sputtering targets. An oxygen flux was maintained in the growth chamber during deposition cycle to prevent the formation of oxygen defects in the transparent conducting layer, which would cause EL from ITO. The ITO thickness is 200 nm. The  $\text{SiO}_x\text{N}_y$ : Ce/ITO structure was heated with a ramp rate of  $15^\circ\text{C}/\text{min}$  to  $600^\circ\text{C}$  and for 1h under nitrogen atmosphere. The bottom aluminum metal contact, a 200-nm-thick Al layer is deposited at room temperature at the bottom of the silicon substrate.

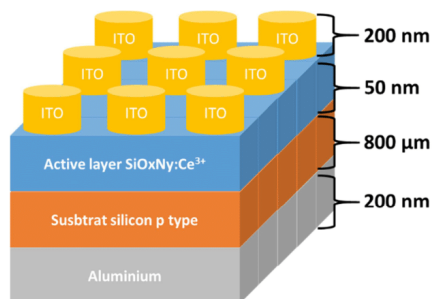


Figure 1. Schematic layout of fabricated Al/p-Si/ $\text{SiO}_x\text{N}_y$ :Ce/ITO device.

### Chemical, Optical and Electrical Characterization

The as-deposited film thicknesses was measured with a UVISEL VIS-FGMS Ellipsometer at 70° incident angle. A Lot-Oriel, 1 kW Xenon lamp having 50 nm wide excitation optical beam, connected to an OMNI300 monochromator was used to excite the samples at 325 nm for the photoluminescence (PL) measurements. The detection system was locked-in with a SR830 amplifier referenced at the excitation light beam chopped frequency. The chemical composition of the SiO<sub>x</sub>N<sub>y</sub>: Ce films was determined by Rutherford Backscattering Spectroscopy (RBS) measurements carried out with a 4.5 MV tandem accelerator in the Edwards Accelerator Laboratory, Ohio University. More details are available elsewhere (10). *I-V* curves were measured at room temperature by means of an Agilent B1500 semiconductor device analyzer connected to a Microtech Summit 11000 probe station. The EL spectra were acquired using a Princeton Instrument LN<sub>2</sub>-cooled CCD coupled to a monochromator. Three sets of samples were deposited and are described in detail below.

### Set Description

For the first set, the nitrogen flux was varied from 1 to 2 sccm, the argon flux was fixed at 8 sccm and the pressure was 3 mTorr. A power density of 2.1 W/cm<sup>2</sup> was applied on the CeO<sub>2</sub> target. The Table I summarizes the different parameters used as well as the thickness of the layers.

**TABLE I.** Growth parameters used for Ce doped SiO<sub>x</sub>N<sub>y</sub> layers corresponding to set 1

Nitrogen flux (sccm)	Thickness (nm)	Ce concentration (at. %)	Al concentration (at. %)
1	47	6	0
1.5	49.7	6	0
2	50.8	6	0

For the second set, all samples were growth under a 2 sccm nitrogen flux and 8 sccm argon flux at room temperature. The power density on the CeO<sub>2</sub> target was varied in order to obtain doping of 2 at. %, 4 at. % and 6 at. % Ce. The Table II summarizes the different growth parameters.

**TABLE II.** Growth parameters used for Ce doped SiO<sub>x</sub>N<sub>y</sub> layers corresponding to set 2

Nitrogen flux (sccm)	Thickness (nm)	Ce concentration (at. %)*	Al concentration (at. %)
2	49	2	0
2	48	4	0
2	51	6	0

For the third set, all samples were then grown under a 2 sccm nitrogen flux and 8 sccm argon flux with a 6 at. % Ce doping. The power density on the Al target was varied in order to obtain doping of 3 at. % and 8.5 at. % Al. The Table III summarizes the different growth parameters.

### 3. Si-Based Materials for Optoelectronics and Resistive Switching

ECS Transactions, 85 (3) 9-21 (2018)

**TABLE III.** Growth parameters used for Ce doped  $\text{SiAlO}_x\text{N}_y$  layers corresponding to set 3

Nitrogen flux (sccm)	Thickness (nm)	Ce concentration (at. %)	Al concentration (at. %)
2	51	6	0
2	54	6	3.0
2	45	6	8.5

#### Results and Discussion

##### Rutherford Back Scattering

The compositions of  $\text{SiO}_x\text{N}_y$ : Ce films having various contents of Si, O, and N were reported previously (10). In that study the Ce content in the  $\text{SiO}_x\text{N}_y$  was constant. Table IV summarizes the concentrations of selected  $\text{SiO}_x\text{N}_y$ : Ce films grown with different Ce concentrations when varying the nitrogen flux from 1 to 2 sccm. In the case of the Ce-doped  $\text{SiAlO}_x\text{N}_y$  layers the Al content was deduced from the kinetic deposition.

**TABLE IV.** Si, O, N and Ce concentrations obtained by RBS

Density of power ( $\text{W}/\text{cm}^2$ )	Nitrogen flux (sccm)	Si (at. %)	O (at. %)	N (at. %)	Ce (at. %)
1.05	2	38.7	18.9	39.7	2
1.5	2	37.6	19.3	38.6	4
2.1	2	31.3	31.3	31.3	6

##### Photoluminescence

Before depositing the electrical contacts, PL spectra were obtained to confirm the  $\text{Ce}^{3+}$  ion optical activity in the Ce-doped  $\text{SiO}_x\text{N}_y$  layers.

**Nitrogen variation (Set 1).** The nitrogen flux applied during the growth was found to be a dominant factor for  $\text{Ce}^{3+}$  emission in  $\text{SiO}_x\text{N}_y$  as well as the silicon concentration (10). Figure 2 shows the PL spectra obtained for three Ce-doped  $\text{SiO}_x\text{N}_y$  films grown with different nitrogen fluxes (1, 1.5 and 2 sccm) and a power density of  $2.1 \text{ W}/\text{cm}^2$  on the  $\text{CeO}_2$  target when excited at 340 nm wavelength.

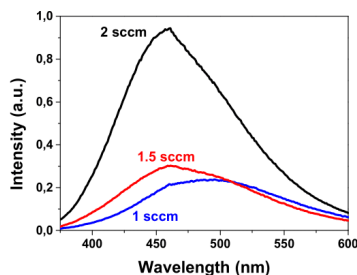


Figure 2. PL spectra of 6 at. % Ce doped  $\text{SiO}_x\text{N}_y$  layer grown under 1, 1.5 and 2 sccm nitrogen fluxes for an excitation wavelength of 340 nm

For nitrogen fluxes of 1 and 1.5 sccm, a wide emission peak is observed from 400 to 600 nm corresponding to  $\text{Ce}^{3+}$  emission. For the highest nitrogen flux (2 sccm), a three times stronger emission is obtained. A previous study in this same system, with lower oxygen concentrations, shows the same  $\text{Ce}^{3+}$  emission (10) but there was no emission for fluxes under 2 sccm. The emergence of an emission for lower nitrogen flux here comes from the oxygen presence which favors the cerium emission.

Ce concentration variation (Set 2). Figure 3 shows the PL spectra of Ce-doped  $\text{SiO}_x\text{N}_y$  layers containing  $\text{Ce}^{3+}$  ions with Ce concentrations between 2, 4 and 6 at.%, all grown with the same nitrogen flux of 2 sccm. The PL intensity increases by an order of magnitude when Ce content increased to 6 at. %.

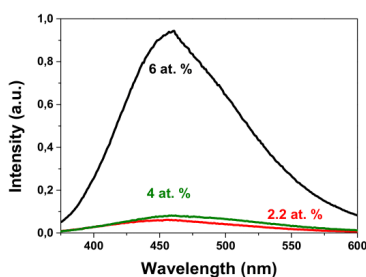


Figure 3. PL spectra of Ce-doped  $\text{SiO}_x\text{N}_y$  layers grown with 2, 4 and 6 at. % of Ce under 2 sccm nitrogen flux when excited at 340 nm wavelength.

Al concentration variation (Set 3). To increase the RE solubility (11), optimized samples were co-doped with Aluminum.

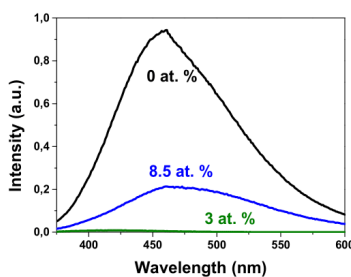


Figure 4. PL spectra of Ce-doped  $\text{SiAlO}_x\text{N}_y$  layers grown with 0, 3 and 8.5 at. % of Al and with 6 at. % of Ce under 2 sccm nitrogen flux excited at 340 nm wavelength.

Figure 4 shows PL spectra of Ce-doped  $\text{SiO}_x\text{N}_y$  samples with 6 at. % of Ce after co-doping with Al. It is seen that visible emission intensity decreases when Al content increases up to 3 at.% and then increases from samples having up to 8.5 at.% of Al. Further studies are required to investigate this behavior, however the Al doping seem to reduce the PL activity.

### 3. Si-Based Materials for Optoelectronics and Resistive Switching

ECS Transactions, 85 (3) 9-21 (2018)

After demonstrating that visible emission from  $Ce^{3+}$  ions in Ce-doped  $SiO_xN_y$  samples could be optically excited, electrical contacts to the samples were fabricated as described in the experimental section. The rest of this article will focus on the electrical excitation of  $Ce^{3+}$  ions in  $SiO_xN_y$  matrices growth with different nitrogen fluxes, then in  $SiO_xN_y$  matrices grown with different Ce ions concentrations and in Al-doped  $SiAlO_xN_y$  matrices.

#### Electroluminescence

**Nitrogen Concentration Variation (Set 1).** All samples have an active thickness of about 50 nm. This thickness implies a low potential barrier height favoring the electrical conduction. A preliminary  $I$ - $V$  characterization was performed on the devices with a voltage bias between 0 V to  $\sim -40$  V. The plots of current density vs. electric field are shown in Figure 5. The  $J(E)$  plot is represented with  $J = I/\pi r^2$  and  $E = V/e$ , respectively, where  $I$  is the measured current,  $r$  is the surface contact radius,  $V$  is the voltage and  $e$  is the layer thickness. The silicon wafers used for the substrates are  $p$ -doped, the current conduction across the structure is more efficient when negatively biased; therefore only this case will be discussed further.

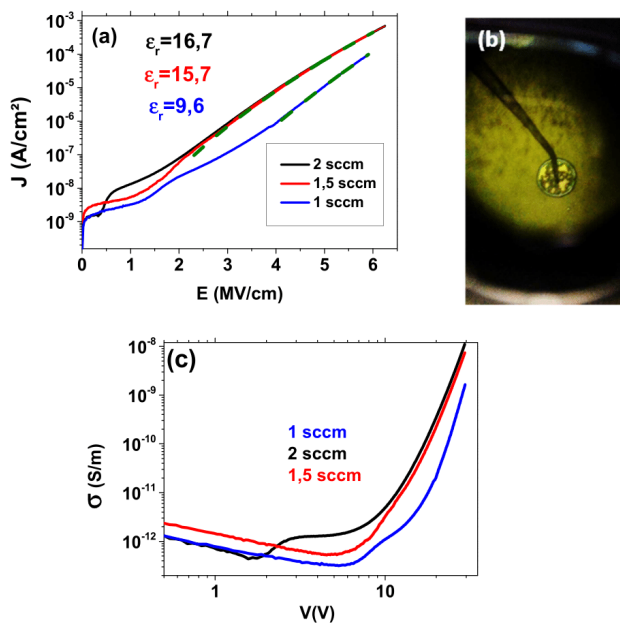


Figure 5. (a) Current density of Ce-doped  $SiO_xN_y$  layers grown with different nitrogen fluxes as a function of the applied electric field (negative polarization) and the corresponding fitting to the Poole-Frenkel conduction mechanism model (dash line). (b) Optical image of a broken electroluminescence device surface. (c) Conductivity  $\sigma$  ( $J/E$ ) vs. external voltage applied.

The Fig 5(a) displays the  $J$ - $E$  curves for three Ce-doped  $\text{SiO}_x\text{N}_y$  layers grown with nitrogen fluxes of 1, 1.5 and 2 sccm, respectively. The  $J$ - $E$  curves are homogenous with a slight increase of the current density starting at 1.6 MV/cm for the samples grown with lower nitrogen fluxes whereas for a strong current density increase is observed at 0.5 MV/cm for the sample grown with a nitrogen flux of 2 sccm. The  $J$ - $E$  curve corresponding to a layer grown with 1.5 sccm nitrogen flux shows an intermediary behavior, namely, for a low electric field, the increase of current density follows the behavior of the lowest flux and after a field of 2 MV/cm, its behavior follows the curve corresponding to a 2 sccm nitrogen flux. All devices breakdown when the electric field applied reached 6 MV/cm, as shown in the Fig 5(b).

In Si based matrices, the conduction mechanisms usually observed are Fowler Nordheim Tunneling (FNT) (12), Trap Assisted Tunneling (TAT) (13,14) or Pool-Frenkel (PF) (15). Their current density ( $J_{FN}$ ,  $J_{TAT}$  and  $J_{PF}$ , respectively) as a function of the electric field ( $E$ ) are expressed by the following equation:

$$J_{FN} = \left( \frac{q^3}{16 \pi^2 \hbar m_{ox} \phi_b} \right) E^2 \exp \left( - \frac{4\sqrt{2m^*} \phi_b^{3/2}}{3\hbar q} \frac{1}{E} \right) \quad [1]$$

With  $m_{ox}$  the electron effective mass in the dielectric,  $\phi_b$  the potential barrier between the electrode and the conduction band and  $m^*$  the electron effective mass.

$$J_{TAT} = \left( \frac{qn_t}{2T} \right) E^2 \exp \left( - \frac{4\sqrt{2m^*} \phi_t^{3/2}}{3\hbar q} \frac{1}{E} \right) \quad [2]$$

Whit  $n_t$  the trap surface density,  $T$  the relaxation time between 2 tunnel effects (capture and emission) and  $\phi_t$  the energy of the trap in comparison to the conduction band.

$$J_{PF} = q \mu N_c E \exp \left( - \frac{q \left( \phi_B - \sqrt{\frac{qE}{\pi \epsilon_0 \epsilon_r}} \right)}{K_b T} \right) \quad [3]$$

Where  $\mu$  is the carrier mobility,  $\phi_B$  the electrode-dielectric barrier,  $K_b$  Boltzmann's constant,  $\epsilon_r$  the relative permittivity,  $T$  the temperature et  $N_c$  the density of states.

By conducting theoretical modeling using Eqs. 1-3 we have concluded that for active layers grown with the higher nitrogen fluxes (1.5 and 2 sccm) the conduction mechanism obeys the PF model (see Fig. 5(a)). For this mechanism, the carrier transport is done by electrons in localized states, by electrons trapping and un-trapping until they reach the dielectric conduction band (15). In this case, the temperature plays an important role as the thermal energy allows electrons to acquire sufficient energy to reach the conduction band. We believe that PF model can be applied satisfactorily to a material with defects similar to those observed in a nitride matrix and that limit the probability of the current tunneling effect. In Table V is shown the dielectric constant,  $\epsilon_r$ , for the 6 at. % Ce sample obtained from the PF fit to the data. Ramirez *et al.* has reported similar effect in Ce-doped oxynitride silicon (8). It was found that for a very similar  $\text{SiO}_x\text{N}_y$  layer

### 3. Si-Based Materials for Optoelectronics and Resistive Switching

ECS Transactions, 85 (3) 9-21 (2018)

composition having 1 at. % of Ce, the  $\epsilon_r$  parameter was between 8 and 13. In contrast, in this study, the  $\text{SiO}_x\text{N}_y$  layers having 6 times larger Ce concentration, have  $\epsilon_r$  slightly larger along better sensitivity to the RE concentration. As reported in the Ref. (8), the large disparity between the dielectric constant values reported is attributed to the simplicity of the devices fabrication. Nevertheless, the average of these measurements seems to highlight an increasing trend with the total amount of RE incorporated. Thus, one can conclude that the RE doping seems to affect the dielectric constants of an active layer; however this hypothesis requires further confirmation.

To validate our theoretical approach we have compared the dielectric constant obtained for a reference device with undoped active layer with one reported by Haji *et al.* (16) for a similar  $\text{SiO}_x\text{N}_y$  composition as shown in Table V. In short, Ref. 16 demonstrates that the PF conduction mechanism applied to the  $\text{SiO}_x\text{N}_y$  system that relative permittivity is lower than reported here for Ce-doped  $\text{SiO}_x\text{N}_y$  layers. The reported  $\epsilon_r$  values are similar to the relative permittivity of the undoped  $\text{SiO}_2$  ( $\epsilon_r \approx 4$ ) and  $\text{Si}_3\text{N}_4$  ( $\epsilon_r \approx 4$ ) matrices (8) rather than to the Ce-doped  $\text{SiO}_x\text{N}_y$  samples.

Ref.	$\text{SiO}_x\text{N}_y$ Undoped	$\text{SiO}_x\text{N}_y$ Doped Ce	
	Hajji <i>et al.</i> (16)		Ramirez <i>et al.</i> (17) $\text{SiO}_x\text{N}_y$ dopé Ce 1 % at.
$\epsilon_r$	6.2-8.8*	8-13	9.6-16.7

\* The Relative permittivity ( $\epsilon_r$ ) values deduced from the Eq. 7 and Fig. 4 reported in Ref.(16)

Figure 5(c) shows electrical conductivity ( $\sigma$ ) through the Ce-doped  $\text{SiO}_x\text{N}_y$  active layer measured at 300 K. It can be seen that the conductivity curves obtained for layers grown with different nitrogen fluxes show two distinct effects when bias voltage increases. First, the lowest voltage threshold (2 V) is observed for the 2 sccm nitrogen flux as compared to the two other nitrogen fluxes (8 V). Secondly, the conductivity rapidly increases for the higher nitrogen flux. We believe, that these two effects can be explained by the nitrogen introduction to the  $\text{SiO}_x\text{N}_y$  matrix resulting in a decrease of the oxygen concentration. Indeed, one can expect that with less oxygen in the  $\text{SiO}_x\text{N}_y$  layer, the matrix properties become similar to  $\text{SiN}_x$  rather than to  $\text{SiO}_2$ , thus the observed conductivity increase.

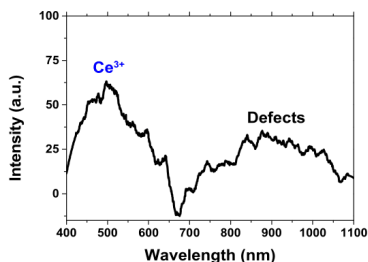


Figure 6. EL spectrum of 6 at. % Ce doped  $\text{SiO}_x\text{N}_y$  layer growth under a 2 sccm nitrogen flux measured at 300 K.

Figure 6 shows the EL spectrum of Ce-doped  $\text{SiO}_x\text{N}_y$  layer grown with a 2 sccm nitrogen flux. A relatively low intensity emission band centered at 500 nm due to  $4f-5d$  transitions in the  $\text{Ce}^{3+}$  ion was detected at 300 K. Nevertheless, this EL peak is similar to the one observed in PL spectra (see Fig.2), thus we believe that in both cases the same optically active center is involved. It should be note, that no EL was detected from the Ce-doped  $\text{SiO}_x\text{N}_y$  layers growth with 1 and 1.5 sccm nitrogen flux because the conduction current has not reached excitation threshold.

Cerium Concentration Variation (Set 2). As seen in Fig. 6, the EL intensity related to  $\text{Ce}^{3+}$  ion is low. One of the reasons for this low intensity emission could come from a high doping concentration. Figure 7(a) displays the  $J$ - $E$  curves of Ce-doped  $\text{SiO}_x\text{N}_y$  layers with three different Ce concentrations. In all cases the  $J$ - $E$  curves are similar and can be modelled by the PF mechanism. We have extracted the dielectric constants ( $\epsilon_r$ ) for each tested Ce-doped  $\text{SiO}_x\text{N}_y$  layer by fitting to the PF model. The  $\epsilon_r$  values are between 14.5 to 16.7 and are higher than the one reported in the literature (17). The  $\epsilon_r$  value increases with the Ce dopant content increase, however the observed  $\epsilon_r$  increase of  $\sim 7\%$  is not significant when compared to the value obtained for the undoped  $\text{SiO}_x\text{N}_y$  layer (see Table V). Figure 7(b) shows the evolution of the conductivity ( $\sigma$ ) as a function of Ce-doping content. It is see that the  $\sigma$  does not depend significantly on the  $\text{Ce}^{3+}$  ions concentration. The Ce dopant seems to not play a significant role on Ce-doped  $\text{SiO}_x\text{N}_y$  active layer conductivity, as opposed to the relative permittivity.

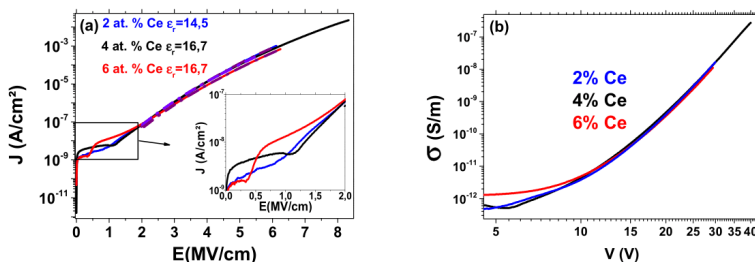


Figure 7. (a) Current density vs. applied field (negative polarization) in Ce-doped  $\text{SiO}_x\text{N}_y$  active layers grown with different Ce contents (negative polarization). Please note that devices with active layers having 2 and 6 at. % of cerium brokedown when field exceeded 6 MV/cm. The dashed line corresponds to the PF fitting. Insert shows initial sections of  $J$ - $E$  curves. (b) Conductivity  $\sigma$  parameter vs. applied voltage for the same active layers as in (a).

The higher current observed in Ce-doped  $\text{SiO}_x\text{N}_y$  sample with 4 at. % Ce content is due to the fact that only this active layer could tolerate an electric field higher than 6 MV/cm. We have recorded EL from devices with active layers doped with 4 and 6 at. % of Ce, however these devices brokedown at higher electric field. Figure 8 shows comparison between EL spectra recorded under the same excitation conditions before catastrophic breakdown of the device occurred and the representative PL spectrum from a Ce-doped  $\text{SiO}_x\text{N}_y$  layer with Ce content of 4 at.%. We speculate that the breakdown in devices with active layers containing high cerium content is possibly due to the contact failure as the selected tested electroluminescent devices failed before achieving sufficient current to generate strong EL signal.



### 3. Si-Based Materials for Optoelectronics and Resistive Switching

ECS Transactions, 85 (3) 9-21 (2018)

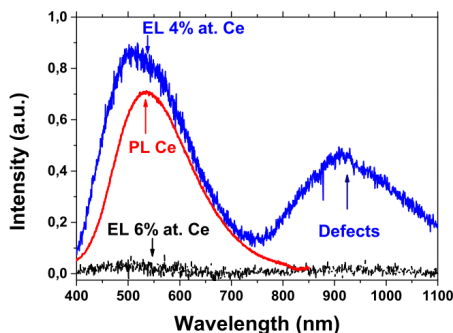


Figure 8. Comparison between EL spectra of 4 and 6 at. % Ce-doped  $\text{SiO}_x\text{N}_y$  active layers grown under a 2 sccm nitrogen flux and PL spectrum from Ce-doped  $\text{SiO}_x\text{N}_y$  layer with 4 at. % of Ce excited at 340 nm wavelength.

It is seen in Fig. 8 that active layer with 6 at. % Ce generates a very low intensity EL, in contrast to the active layer with 4 at. % Ce. The observed EL spectrum is 200 nm wide with maximum peak intensity at 500 nm. This dominant EL spectrum band shape is similar to the PL spectrum obtained for the same active layer confirming that the observed emission originates from  $\text{Ce}^{3+}$  ion. It is seen that the EL peak maximum is redshifted ( $\sim 50$  nm) as compared to the EL spectra reported for similar devices by Ramirez *et al.* (8) and Skopura *et al.* (2). We believe that the observed shift is due to the nephelauxetic effect (18) (10) resulting from the introduction of nitrogen to  $\text{SiO}_x\text{N}_y$  matrix inducing a  $\text{Ce}^{3+}$  ion emission band maximum redshift.

Al Concentration Variation (Set 3) Figure 9 shows the  $J$ - $E$  curves of Ce-doped  $\text{SiAlO}_x\text{N}_y$  active layers doped with Al at 0, 3.0 and 8.5 at. % concentration. It is seen that the current density starts to increase as soon as the electric field is applied. This observation is in direct contrast to the behavior of Al-free active layers where current density increased when the applied electric field exceeded 0.5 MV/cm (see Fig. 5). We believe that by incorporating Al dopants in the active layers the breakdown occurs for electric fields of 7.5 MV/cm and 9 MV/cm for samples doped with Al content at 3.0 at % and 8.5 at.%, respectively. It is clear that incorporating Al increases the conductivity of an active layer at lower bias voltages between 0 to 4 V as seen in Fig. 9(b). For higher bias voltage (up to 40 V), the conductivity of active layers is significantly reduced. Thus, by Al doping one can achieve a device breakdown threshold to occur at higher bias voltage, however at the same time Al doping doesn't increase the overall active layer conductivity.

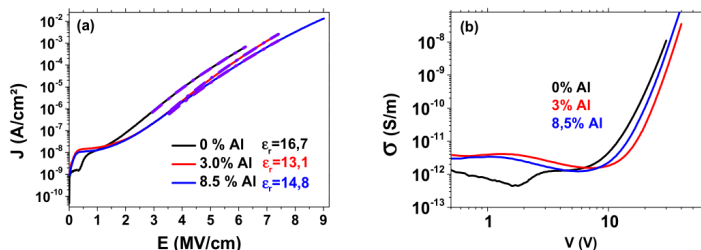


Figure 9. (a) Current density vs. applied electric field (negative polarization) for Ce-doped SiAlO<sub>x</sub>N<sub>y</sub> layers grown with different Al contents. Dashed lines are fits to individual  $J$ - $E$  curves using the PF model. (b) Conductivity  $\sigma$  ( $J/E$ ) vs. applied voltage for the same active layers as in (a).

As seen in Fig. 9(a), all  $J$ - $E$  curves show the same behavior that can be simulated by the PF mechanism. The dielectric constant ( $\epsilon_r$ ) values of 16.7, 13.1 and 14.8 were extracted from use of the PF model for different Ce-doped SiAlO<sub>x</sub>N<sub>y</sub> layers doped with Al at 0, 3 and 8.5 at. % respectively. We have concluded that Al co-dopant to Ce-doped SiO<sub>x</sub>N<sub>y</sub> layers has a direct impact on the  $\epsilon_r$  parameter value.

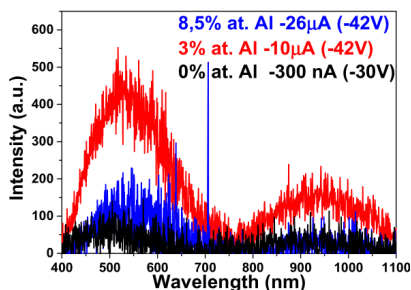


Figure 10. EL spectra of Ce-doped SiAlO<sub>x</sub>N<sub>y</sub> active layers containing 0, 3 and 8.5 at. % of Al grown under a 2 sccm nitrogen flux obtained under excitation condition listed in insert. The EL band peaking at 950 nm corresponds to the Si substrate.

Figure 10 displays the EL spectra of Al co-doped SiO<sub>x</sub>N<sub>y</sub>: Ce<sup>3+</sup> active layers along with a reference Al-free counterpart. It is seen that the most intense EL spectrum is from the SiO<sub>x</sub>N<sub>y</sub>: Ce<sup>3+</sup> active layer co-doped with Al at 3 at. %. There is three times more current passing through this sample as compared to the sample containing 8.5 at. % of Al. We explain this difference in the observed current magnitude by the fact that these two samples have different thickness. We speculate that the thicker the active layer is, the weaker is the electrical field in the active layer and this directly affects the current.

### Conclusions

All studied samples have been tested for their optical activity under optical excitation. Concerning the influence of nitrogen flow, no EL signal was observed for layers grown under 1 and 1.5 sccm nitrogen fluxes. However, a weak EL signal was observed for the

### 3. Si-Based Materials for Optoelectronics and Resistive Switching

ECS Transactions, 85 (3) 9-21 (2018)

sample grown under a 2 sccm nitrogen flux. A well-defined EL signal was obtained for a 4 at. % Ce-doped sample, this demonstrates the potential for blue LED emission with Ce doping. Adding Al on the layers permits an increase in the EL signal compared to the Al free sample, and increases the breakdown voltage. With Al, the EL signal was increased by a factor 5.

The conductivity of the samples was fitted best by a Poole-Frenkel model. Hot carriers jump from defect to defect until they reach the conduction band (with carriers being trapped in localized states). The relative permittivity evolution was found to be in adequacy with the dopants concentration but further study will require confirmation since the conductivity is dependent only on the matrix composition and not the dopant concentration. EL spectroscopy measurements tested the emission of our different Si(Al)O<sub>x</sub>N<sub>y</sub>:Ce<sup>3+</sup> samples. Among all layers tested, only the samples deposited under a 2 sccm nitrogen flux SiO<sub>x</sub>N<sub>y</sub>:Ce<sup>3+</sup> (4 at. %), SiAlON:Ce<sup>3+</sup> (6 at. % Ce, 3 at. % Al and 8.5 at. % Al) present an EL signal. One of the main reasons for the efficiency of those layers is their high breakdown strength enabling the device to reach sufficient current for EL emission. Especially adding Al tends to increase the breakdown threshold in order to obtain an EL signal.

Those results pave the way for enabling blue LED fabrication based on SiO<sub>x</sub>N<sub>y</sub>: Ce<sup>3+</sup> layers. The growth parameters can be optimized as well as the fabrication methods for contacts.

#### Acknowledgments

The authors would like to thank Mr Cédric Frilay from CIMAP Laboratory (Caen, France) for his great help on sample growth. This work was financially supported by the French Research National Agency through the GENESE project (N° ANR-13-BS09-0020-01). W.M.J. acknowledges the support from the NSF CAREER Award no. DMR-1056493.

#### References

1. Suyama M, Laming RI, Payne DN. *Electron Lett.* **26**(21), 1756–1758 (1990).
2. Skorupa W, Sun JM, Prucnal S, Rebohle L, Gebel T, Nazarov AN, et al. *Solid State Phenom.* 108-109,755-60 (2005).
3. Miniscalco WJ. *J Light Technol.* **9**(2), 234–250 (1991).
4. Quimby RS, Miniscalco WJ, Thompson B. *J Appl Phys.* **76**(8), 4472-8 15 oct (1994).
5. Yerci S, Li R, Dal Negro L. *Appl Phys Lett.* **97**(8), 081109 (2010).
6. Xu L, Li S, Jin L, Li D, Yang D. *Nanoscale Res Lett.* **9**(1), 1–6 (2014).
7. DiMaria DJ, Abernathy JR. *J Appl Phys.* **60**(5), 1727 (1986).
8. Ramírez JM, Ruiz-Caridad A, Wojcik J, Gutierrez AM, Estradé S, Peiró F, et al. *J Appl Phys.* **119**(11), 113108 (2016).
9. Koao L, Swart HC, Dejene FB. *J Rare Earths.* 28,206-210 (2010).
10. Ehre F, Labbe C, Dufour C, Wojciech J, Weimmerskirch-Aubatin J, Portier X, et al. *Nanoscale.* **10**(8), 3823-3837 (2018).
11. Nie ZR, Jin T, Fu J, Xu G, Yang J, Zhou JX, et al. *Mater Sci Forum.* 396-402, 1731-0 (2002).
12. Weinberg ZA. *J Appl Phys.* (53), 552 (1982).

**ECS Transactions, 85 (3) 9-21 (2018)**

13. Houg MP, Wang YH, Chang WJ. *J Appl Phys.* **86**(3), 1488-91 (1999).
14. DiMaria DJ, Cartier E. *J Appl Phys.* **78**(6), 3883-3894 (1995).
15. De Graaff HC, Huybers M, de Groot JG. *Solid-State Electron.* **25**(1):67 - 71 (1982).
16. Hajji B, Temple-Boyer P, Olivie F, Martinez A. *Thin Solid Films.* **354**(1):9-12 (1999).
17. Ramirez JM. Thesis (2015).
18. Tchougréeff AL, Dronskowski R. *Int J Quantum Chem.* **109**(11):2606-21 (2009).



# Memristive behaviour of Si-Al oxynitride thin films: the role of oxygen and nitrogen vacancies in the electroforming process

O Blázquez<sup>1,2,6</sup> , G Martín<sup>1,2</sup> , I Camps<sup>3,4</sup>, A Mariscal<sup>3</sup>, J López-Vidrier<sup>5</sup>, J M Ramírez<sup>1,2</sup>, S Hernández<sup>1,2</sup>, S Estradé<sup>1,2</sup>, F Peiró<sup>1,2</sup>, R Serna<sup>3</sup> and B Garrido<sup>1,2</sup>

<sup>1</sup>MIND, Department of Engineering: Electronics, Universitat de Barcelona, Martí i Franquès 1, E-08028 Barcelona, Spain

<sup>2</sup>Institute of Nanoscience and Nanotechnology (IN<sup>2</sup>UB), Universitat de Barcelona, Av. Joan XXIII S/N, E-08028 Barcelona, Spain

<sup>3</sup>Laser Processing Group, Instituto de Óptica 'Daza de Valdés', IO, CSIC, Serrano 121, E-28006 Madrid, Spain

<sup>4</sup>Instituto de Ciencias Físicas, UNAM, Av. Universidad s/n, Col. Chamilpa, Cuernavaca, Morelos, 62210, Mexico

<sup>5</sup>Laboratory for Nanotechnology, Dept. of Microsystems Engineering (IMTEK), University of Freiburg, Albert-Ludwigs-University Freiburg, Georges-Köhler-Allee 103, D-79110 Freiburg, Germany

E-mail: [oblazquez@el.uib.edu](mailto:oblazquez@el.uib.edu)

Received 25 January 2018, revised 6 March 2018

Accepted for publication 16 March 2018

Published 10 April 2018



CrossMark

## Abstract

The resistive switching properties of silicon-aluminium oxynitride (SiAlON) based devices have been studied. Electrical transport mechanisms in both resistance states were determined, exhibiting an ohmic behaviour at low resistance and a defect-related Poole–Frenkel mechanism at high resistance. Nevertheless, some features of the Al top-electrode are generated during the initial electroforming, suggesting some material modifications. An in-depth microscopic study at the nanoscale has been performed after the electroforming process, by acquiring scanning electron microscopy and transmission electron microscopy images. The direct observation of the devices confirmed features on the top electrode with bubble-like appearance, as well as some precipitates within the SiAlON. Chemical analysis by electron energy loss spectroscopy has demonstrated that there is an out-diffusion of oxygen and nitrogen ions from the SiAlON layer towards the electrode, thus forming silicon-rich paths within the dielectric layer and indicating vacancy change to be the main mechanism in the resistive switching.

Keywords: resistive switching, chemical composition, SiAlON thin films, charge transport

(Some figures may appear in colour only in the online journal)

## 1. Introduction

The low energy efficiency of Complementary Metal–Oxide–Semiconductor (CMOS) transistors is a strong limitation for the design of ultra-low power distributed devices for the new era of the Internet of Things and big data. A new generation of energy-efficient, scalable, miniature switching devices and/or novel computer paradigms are expected to deal with these

challenges—such as reconfigurable switching resistors and neuromorphic computing, respectively [1, 2]. In fact, they represent a new bioinspired approach to the hardware implementation of brain neurons and synapses. A switching resistor (commonly known as a memristor) is a device that exhibits a resistance that depends on the voltage applied, keeping its value in the absence of any voltage. This effect is exploited, for example, in resistive random-access memory (ReRAM) devices, which are expected to play a leading role in future applications [3–5].

<sup>6</sup> Author to whom any correspondence should be addressed.

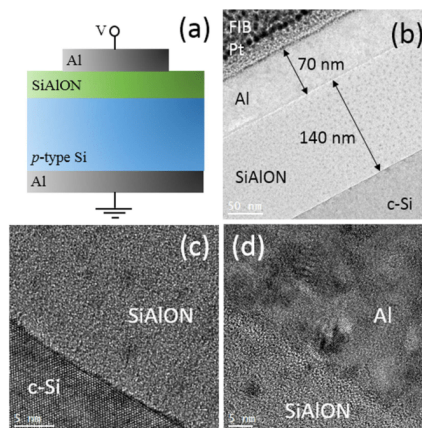
### 3. Si-Based Materials for Optoelectronics and Resistive Switching

There are many different binary compounds currently under study for their use as resistive switches (RS), such as transition metal oxides and refractory materials like  $\text{TiO}_2$ ,  $\text{SnO}_2$ ,  $\text{HfO}_2$ ,  $\text{Ta}_2\text{O}_5$  and  $\text{ZnO}$ , among others. They have shown resistive switching response by forming Metal–Insulator–Metal (MIM) structures, where the metals are typically Ni, Al, Cu, Ag or Ti [6–14]. In these structures, resistive switching properties are usually promoted by the formation and destruction of conductive nanofilaments (conductive paths) between the metal electrodes. Nanofilament formation can proceed in several ways; the most common of these are: (i) the valence change mechanism (VCM), where the rearrangement of oxygen ions leaving their equilibrium sites leads to the formation of metallic nanofilaments (oxygen vacancies), and (ii) electro-chemical metallization (ECM), where the nanofilament is created due to the diffusion of metallic atoms from the contacts into the oxide layer.

As-deposited VCM materials do not usually show memristive properties until an electroforming process is carried out. The electroforming is a curing process which consists of applying a relatively high voltage for some time. During this process, the applied electric field promotes the rearrangement of oxygen ions, thus stimulating local structural modifications which result in the formation of filamentary conducting structures, many of them interrupted by insulating gaps [15]. Once the filamentary structure is preformed, the further application of voltage and/or current leads to the formation or destruction of conducting paths between the electrodes. In the case that a conductive filament is created by the application of a set voltage (usually much lower than for electroforming), there is an abrupt resistance decrease in the device (changing from OFF to ON state). The structure stays in the low resistance state (LRS), ON, until a negative reset voltage and/or a high current is applied and the filaments are destroyed (from ON to OFF), increasing their resistance and changing to the high resistance state (HRS), OFF [16–19].

Although transition metal oxides are the most commonly reported materials with memristive properties, their compatibility with CMOS technology is also an important issue for their implementation in mass production processes. In the past, some of the co-authors of the present work have already demonstrated memristance in  $\text{SiO}_x$  with polysilicon electrodes, with remarkable results [20]. Some aspects require further improvement, like more abrupt switching, reduction of voltage variability, improvement of endurance and increase in writing or erasing speeds [21–24]. The introduction into the oxide of additional elements compatible with CMOS technology (e.g. N and Al) has contributed to an optical and mechanical enhancement [25, 26]—this is a promising route to enhance the optoelectronic performance of these materials, given their implementation in the electronics industry as a resistive switching element.

In this work, we explore the resistive switching properties of silicon-aluminium oxynitride (SiAlON) thin films using an Al-electrode as contact. The electroforming process for activating the resistive switching and the writing and erasing cycles are described in detail. In addition, the



**Figure 1.** (a) Cross-section sketch of the MIS devices under study, containing a SiAlON layer onto a *p*-type c-Si substrate. (b) Detailed image corresponding to a TEM image of the cross-section of a pristine device. (c) and (d) High resolution TEM images of the Si-substrate/SiAlON and SiAlON/Al-electrode interfaces, respectively.

structural and chemical modifications at the nanoscale have revealed an out-diffusion of O and N ions, forming either bubbles or SiAlON precipitates below the Al-electrode, whereas no Al diffusion from the electrode into the SiAlON layer has been observed. These results suggest that the VCM is the most probable mechanism responsible for the resistive switching properties of SiAlON-based ReRAM devices.

#### 2. Experimental details

SiAlON thin films (140 nm-thick) were grown onto *p*-type (100)-Si substrates ( $4\text{--}70\ \Omega\text{cm}$ ) by means of pulsed laser deposition. The ablation of the SiAlON target was carried out at room temperature with a base pressure of  $1 \times 10^{-6}$  mbar, using a 193 nm ArF-excimer laser with a pulse duration of 20 ns and at an energy density of  $4.1\ \text{J cm}^{-2}$  per pulse. After deposition, the films were submitted to an annealing process at  $700\ ^\circ\text{C}$  in air. X-ray photoelectron spectroscopy measurements determined a SiAlON composition of Si (45 at.%), Al (3 at.%), N (40 at.%) and O (12 at.%) [25]. The device structure was completed by fabricating a vertical Metal–Insulator–Semiconductor (MIS) structure, the metal, insulator and semiconductor materials being Al, SiAlON and the Si substrate, respectively. The top and bottom electrode metallization was done via electron beam evaporation of Al, in which the top electrode was properly patterned in the form of  $150\ \mu\text{m}$ -diameter circular dots by using a chromium shadow mask, whereas a full-area Al deposition was applied on

the rear side of the Si substrate. A sketch of the device structure is shown in Figure 1(a).

The device structure was assessed by observing the cross section of the device with a Jeol 2010F transmission electron microscope (TEM), operated at 200 kV, coupled to a GIF Gatan filter. Chemical analysis was performed by means of electron energy loss spectroscopy (EELS), co-acquired with high angular annular dark field (HAADF) in scanning TEM (STEM) mode. The accurate selection of specific regions over the wafer has been made possible by using a Zeiss 1560XB Cross Beam focus ion beam (FIB) and scanning electron microscopy (SEM), and reducing the region thickness down to about 50 nm (up to electron transparency).

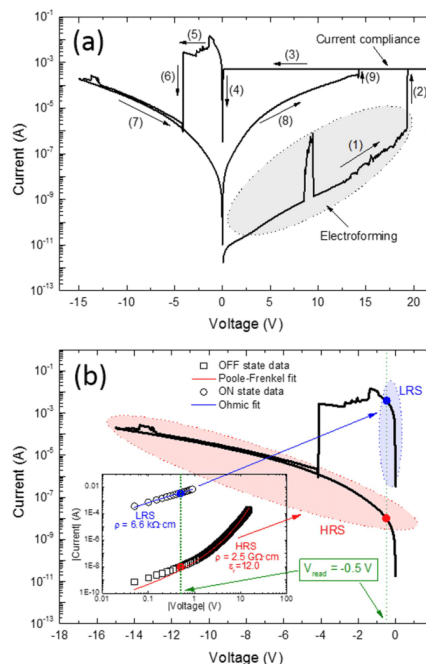
TEM images were acquired in a cross-section configuration from a pristine device. These images show the Al and SiAlON layers on top of the Si-substrate, presenting good uniformity, with layer thicknesses of 70 nm and 140 nm, for the Al and SiAlON, respectively (see figure 1(b)). A Pt-layer on top, necessary for the FIB sample preparation, can also be observed in the images. A high-resolution analysis revealed an atomically-sharp interface between the crystalline Si substrate and the amorphous SiAlON layer with roughness of about three monolayers (see figure 1(c)), whereas the interface between SiAlON and the Al electrode exhibits enhanced roughness.

The electric characterization of the devices was performed by means of an Agilent B1500 semiconductor device analyser and a Cascade Microtech Summit 11000 probe station, wherein the devices under study are screened from external electromagnetic fields by a Faraday cage. This combined hardware–software system is suitable for switching characterization thanks to the possibility to set a protocol using the current–voltage [ $I(V)$ ] sweep mode, with a compliance current when necessary.

### 3. Results and discussion

#### 3.1. Electrical assessment of resistive switching effect in SiAlON

We have performed an in-depth study of the electric properties of the devices under different switching protocols. To elicit the memristive behaviour, first of all the devices must undergo an electroforming process, after which the two resistive states can be obtained using voltage ramps at different polarizations. Figure 2(a) shows the electroforming process in our device, which exhibits characteristic ramps due to the switching between the high and low resistance states. Note that the current is represented in logarithmic scale due to the huge resistance ratio between the states. The switching between the two resistive states describes a cycle in which the following regions can be defined and are labelled in the figure: (1) the pristine device is submitted to a positive increasing ramp up to 20 V, exhibiting a highly resistive conduction. At voltages close to 20 V, (2) there is a sudden increase in the current, which subsequently reaches the current compliance limited at 0.5 mA, whereupon the device



**Figure 2.** (a) Complete cycle of a typical  $I(V)$  curve, showing the two different resistance states. The cycle steps as described in the text are written down as numbers in the graph. Voltage bias is applied at the top electrode, whereas the back contact is grounded. (b) RESET representation where the two states, HRS and LRS, are highlighted in red and blue, respectively. The inset shows these curves in log–log representation, with their corresponding fits (ohmic for LRS and Poole–Frenkel for HRS). The data obtained from fits (resistivity and dielectric constant) are also plotted in the graph. All current values are in absolute value.

switches from the HRS to the LRS. Since at this point we are limiting the current through the device by using a variable resistor in series (to prevent the irreversible breakdown of the device), the resistance in the LRS can only be determined once the voltage is lowered to obtain currents well below this limit, recovering the real  $I(V)$  curve in the LRS. This behaviour is observed in the region labelled as (3), where the current is constant at the current compliance, reducing the voltage. At voltages below 0.1 V, (4) a linear relation between the applied voltage and the obtained current can be observed, with a large slope that indicates the creation of conductive paths between the two electrodes; the device remains in this LRS under low negative bias. At large enough negative voltages without the limitation of the current compliance, (5) the current rapidly increases and remains independent of the applied voltage until (6) it is abruptly reduced from mA to a



### 3. Si-Based Materials for Optoelectronics and Resistive Switching

few  $\mu\text{A}$ . This behaviour suggests that the conductive paths have been interrupted and the device has switched back to the HRS. At this point, (7) the  $I(V)$  curve remains in this HRS, with a conduction behaviour typical from insulating materials. To complete a memristive cycle, (8) the voltage is positively increased again following an insulating  $I(V)$  curve, but far more conductive than for the pristine device. Finally, (9) there is a sudden current increase for voltages around 15 V, again achieving the LRS. The cycle resumes at point (3) and is repeated in the following cycles. Therefore, the switching to the LRS is obtained by applying a write voltage of  $V_{\text{SET}} > 15\text{ V}$  (keeping the current compliance active), and the HRS is attained after  $V_{\text{RESET}} < -5\text{ V}$  is applied (without current compliance).

So far, studies performed in  $\text{SiO}_x$ -based devices have revealed a movement of oxygen ions during the electroforming process as a consequence of the electro-reduction under an external electric field [17]. Actually, regions with oxygen vacancies are locally more conductive, thus inducing an abrupt reduction in its resistance, which is typically ascribed to the formation of conductive nanofilaments through the oxide film [15]. In our  $\text{SiAlON}$ -based devices, the  $I(V)$  curve sometimes exhibits a sudden current increase during the forming process (as observed at 9 V in figure 2(a)), which indicates an attempt of state switching which is not completed, the system thus returning to the original state. In addition, the  $I(V)$  characteristics present irregular behaviour just before the switching (from 12 V). This last feature has been observed in all the studied  $\text{SiAlON}$ -based devices just before finishing the electroforming process, and could be attributed to a gradual, structural material modification before the generation of conductive nanofilaments. The need for a current compliance to attain the LRS is due to the high conductivity that this state exhibits. Indeed, our devices show a conductivity enhancement with respect to other published works on Al-free Si-based materials which present similar memristive behaviour [20]. This occurrence of increased conductivity may be a consequence of the presence of Al, in analogy with the work of Choi *et al*, who presented a resistive switching device based on aluminium nitride in which a current compliance was required for LRS because of the high current this state presents [27].

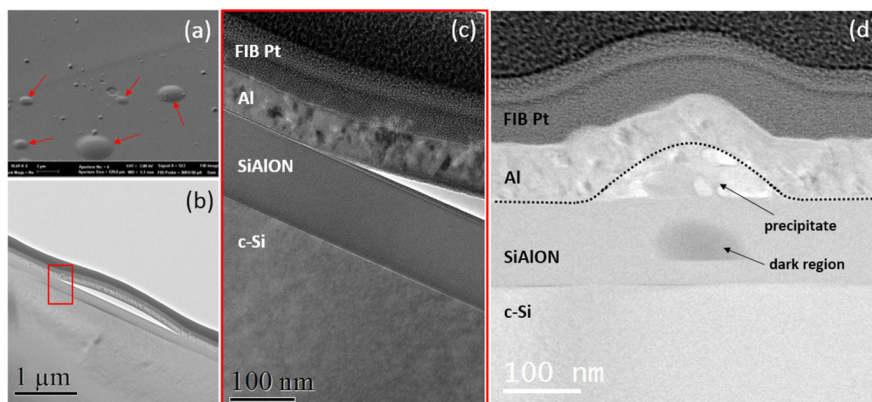
Once the nanofilaments are created after the electroforming process [step (2)], the conductive paths can be interrupted by oxygen migration from the local environment to the nanofilaments due to increased redox oxidation process, thanks to local heating induced by the Joule effect and consequent increase of the local temperature [28]. To generate the conductive paths again and switch from the HRS to the LRS, a much lower voltage is necessary than in the electroforming process, indicating that once conductive paths are created and break, they are more prone to be created again in successive cycles. This fact is further corroborated by the lower resistivity in the HRS [step (8)] compared to the pristine state [step (1)], attributed to the lack of conduction paths through the  $\text{SiAlON}$  layer, which behaves as an insulator. So far, the results indicate that devices based on  $\text{SiAlON}$  with Al-electrodes behave as memristive devices, in agreement with

previous reports of resistive switching in  $\text{SiO}_x$ - and  $\text{SiN}_x$ -based memristors [17, 27].

The electric transport mechanisms dominating in both states have been analysed in the accumulation regime ( $V < 0$ ). This analysis was carried out under these conditions because not only is the reading of the state done in this regime, but also the substrate does not limit the current injection towards the  $\text{SiAlON}$  layer. Figure 2(b) displays, for the sake of simplicity, the accumulation region of the  $I(V)$  curve in figure 2(a), where the studied range for the LRS is marked in blue, and that for the HRS in red. Keeping in mind their electrical characteristics, the two different states can be read by simply monitoring the current at  $V_{\text{read}} = -0.5\text{ V}$  (green dotted vertical line in figure 2(b)), which has been intentionally selected to provide a large resistance difference between the two states (see blue and red points in figure 2(b)). On one hand, there is a linear dependence in the LRS, indicating an ohmic behaviour. Using the thickness and the diameter of the devices as taken from electron microscopy images, a resistivity value of  $\rho_{\text{LRS}} = 6.6\text{ k}\Omega\text{ cm}$  is found at  $V_{\text{read}}$ . It is important to note that this resistivity value has been obtained by considering the full device area. It is likely that current only flows through narrow (nm-thick) conductive paths, whose section could be orders of magnitude lower; therefore, the conductivity of the material might even be locally higher in this state. On the other hand, the HRS exhibits a non-linear  $I(V)$  curve for more than five orders of magnitude in current, with a resistivity of  $\rho_{\text{HRS}} = 2.5\text{ G}\Omega\text{ cm}$  at  $V_{\text{read}}$ . The defective nature of the  $\text{SiAlON}$  layer suggests a (trap-assisted) Poole–Frenkel mechanism, in which the current dependence on the applied voltage follows the expression [29–31]

$$I = \frac{q\mu N_t A}{d} V \exp\left(\frac{-\phi_t + \sqrt{q^3 V / (\pi\epsilon_0 \epsilon_r d)}}{k_B T}\right),$$

where  $q$  is the elementary charge,  $\mu$  the electron drift mobility,  $N_t$  the density of trapping states,  $A$  and  $d$  the area of the device and the thickness of the  $\text{SiAlON}$  layer, respectively,  $\phi_t$  the energy barrier of the defect-generated trap level with respect to the  $\text{SiAlON}$  conduction band,  $\epsilon_r$  and  $\epsilon_0$  the relative and vacuum dielectric permittivity, respectively,  $k_B$  the Boltzmann constant, and  $T$  the temperature. By fitting this expression to the experimental data, a relative permittivity of  $\epsilon_r = 12.0$  was obtained, which approaches the value corresponding to pure Si ( $\epsilon_r = 11.9$ ) [32]. However, it should be noted that this value may differ from what we would obtain by means of other techniques, since the most general Poole–Frenkel technique also takes into account the trapping and detrapping ratio of electrons within the localized states [33–35], which would result in a reduced effective  $\epsilon_r$ . Indeed, the necessary presence of these trap states is in agreement with the layer containing partially conductive paths with some oxygen vacancies, which results in the abovementioned fact that the devices are more conductive at HRS than before the electroforming process.



**Figure 3.** (a) SEM image of the top electrode of a device after the electroforming process, where surface features are marked with red arrows. (b) Cross-section TEM image of a bubble. (c) Detailed image at the edge of the bubble, i.e. the red framed region in (b). (d) TEM image of the cross section of a different region, showing a precipitate beneath the Al electrode and a dark region within the SiAlON layer.

### 3.2. Compositional analysis after the electroforming process

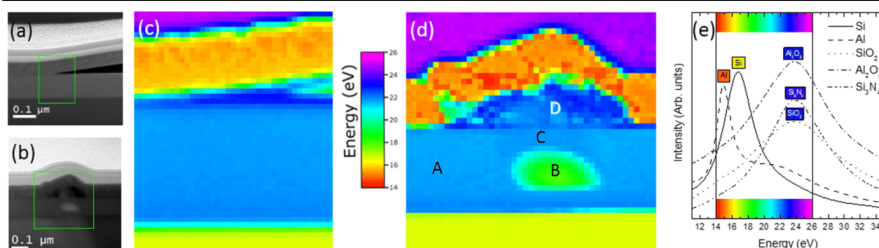
In order to shed light on the structural modifications that drive the two different conduction mechanisms, we have performed an in-depth microscopic study at the nanoscale after the electroforming process, by acquiring SEM and TEM images. Figure 3(a) shows a SEM image of the surface of a device after the electroforming process. Some irregularities can be seen on the surface, randomly distributed, with lateral sizes that range from some hundreds of nanometres to a few micrometres, which is in contrast to the smooth and homogeneous surface in pristine devices (see figure 1). The formation of some of these irregularities with a circular shape is of special interest because they could even be observed *in situ* during the electroforming process by an optical microscope; based on this, we have tentatively ascribed them to structural modifications during the electroforming process; they could, therefore, be of interest in explaining the resistive switching properties of SiAlON-based devices.

Samples were prepared for TEM observation in cross-section configuration by using FIB, in order to explore the structure underneath those circular shapes (see figures 3(b)–(d)). Figure 3(b) clearly shows that the Al-electrode is locally bent and separated from the SiAlON layer, whereas the latter layer is perfectly stacked on top of the substrate, forming a bubble. In figure 3(c), a magnified view of the selected part of figure 3(b) is displayed, in which the different layers of the devices can be clearly observed at the edge of the bubble, all of them continuously and perfectly stacked. However, when moving to the centre of the bubble there is a clear detachment of the Al top electrode from the SiAlON layer, thus causing a physical deformation that can be observed from the top of the devices (the detachment is around 200 nm in height). In fact, the contrast of the region between the electrode and the

SiAlON layer indicates that there is total electron transparency in this region, i.e. a void region, suggesting that this surface inhomogeneity has a bubble-like structure, which was presumably filled by gas during the electroforming process. Considering the chemical reduction of the active layer during the electroforming process reported in the literature and the atomic species of our SiAlON layer, the only possible gases that can produce those bubbles are  $O_2$  and  $N_2$ . Thus, the positive bias applied to the top electrode should induce the migration of negatively-charged O or N ionic species from the SiAlON layer towards the top electrode. Whereas some authors have reported  $O_2$  release during both the electroforming process and for the formation of new conductive filaments in oxides [36, 37], devices based on nitrides have been observed to release  $N_2$  during the resistive switching process, which would also promote the formation of gas bubbles [27].

Nevertheless, the creation of bubble-like features is not the only mechanism that governs the formation of topological irregularities in the surface. In figure 3(d), we show a cross-section TEM image corresponding to another feature in the surface. It is evident from the figure that in this region there is a local thickness increase of the layer beneath the Al-electrode, with a non-uniform contrast. In fact, the image reveals a precipitate on top of the SiAlON layer, which bends the Al contact (see the dotted-framed region of figure 3(d)). The precipitate presents a width of 250 nm and a height of 130 nm, showing an irregular shape. Immediately under this precipitate there is a darker region within the SiAlON layer, suggesting a compositional modification of this active layer that is presumably related to the formation of the precipitate on top of it. It is important to note that this feature is not observed underneath the bubbles, where the SiAlON layer seems to remain unaltered.

### 3. Si-Based Materials for Optoelectronics and Resistive Switching



**Figure 4.** STEM (dark-field) images corresponding to (a) an edge of a bubble and (b) a precipitate; (c) and (d) show the colour-coded plasmon energy maps of the corresponding green square-framed regions in (a) and (b), respectively. (e) Low energy-loss spectra of Si, Al, SiO<sub>2</sub>, Al<sub>2</sub>O<sub>3</sub> and Si<sub>3</sub>N<sub>4</sub>, showing the plasmon of Si (~16.7 eV), SiO<sub>2</sub> (~23 eV), Si<sub>3</sub>N<sub>4</sub> (~24 eV), Al (~15 eV) and Al<sub>2</sub>O<sub>3</sub> (23.8 eV), where the colour scale employed in (c) and (d) is also included and correlated to the chemical composition according to the convoluted plasmon energy.

In order to analyse the composition of these regions, low-loss EELS analyses of these regions were carried out in STEM mode. Figures 4(a) and (b) correspond to the STEM-HAADF images of the analysed regions (a bubble and a precipitate). Figures 4(c) and (d) show the colour-coded maps corresponding to the energy value of the bulk plasmon peak observed in the low energy loss region of the spectra in the considered areas [the colour scale ranges from 14 eV (red) to 26 eV (purple)]. The low-loss region of the spectra of the elements and compounds of relevance for this analysis are displayed in figure 4(e) [plasmon of Si (~16.7 eV), SiO<sub>2</sub> (~23 eV), Si<sub>3</sub>N<sub>4</sub> (~24 eV), Al (~15 eV) and Al<sub>2</sub>O<sub>3</sub> (23.8 eV)] [38, 39], together with their colour correspondence.

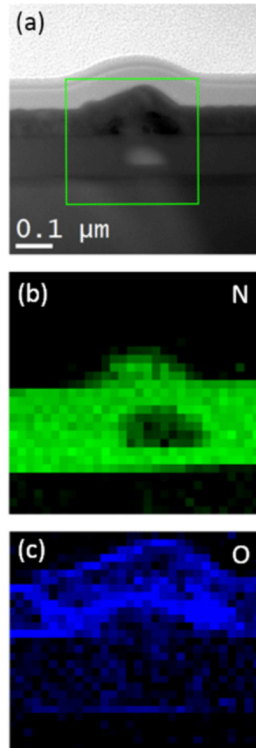
In figure 4(c), a homogeneous contrast can be observed for all the layers, both at the edge and in the middle of the bubble, which indicates that there is no modification of the plasmon energy of the different layers (SiAlON and Al), i.e. no modification of their stoichiometry. Moreover, there is a clear shift to higher energies of the plasmon peak at the interfaces that can be attributed to partial oxidation because of their exposure to the atmosphere during the different steps of the device fabrication. However, the interface between the SiAlON and Al layers presents higher plasmon energies than for both materials, pointing to a higher content of O and/or N. Due to the facts that the composition is homogeneous around this region and that the bubble must be filled with gas (O<sub>2</sub> and/or N<sub>2</sub>), the compositional variation at the SiAlON/Al interface could be related to O or N migration from other regions of the device, forming SiO<sub>2</sub> and/or Si<sub>3</sub>N<sub>4</sub> or Al<sub>2</sub>O<sub>3</sub> and resulting in an effective plasmon shift to a higher energy.

The same analysis was carried out in the region where a precipitate is observed (figures 4(b) and (d)). The region labelled as A in figure 4(d) presents a plasmon peak at 21.8 eV, corresponding to the SiAlON layer, whose energy is substantially lower than the plasmon peak for SiO<sub>2</sub> or Si<sub>3</sub>N<sub>4</sub>, but larger than the one corresponding to pure crystalline Si. In addition, energy-dispersive x-ray spectroscopy measurements in the same region assessed the presence of Si, Al, O and N within the SiAlON layers (not shown here). The SiAlON region labelled as B in figure 4(d) presents a different

plasmon energy, centred around 18.0 eV (green colour in the image), which indicates that this region has a different composition than the rest of the SiAlON layer. The fact that the plasmon energy of this region has decreased with respect to its surroundings indicates a larger concentration of Si and/or Al, with some degree of oxidation or nitridation (i.e. formation of silicon-rich oxynitride). Therefore, these results suggest that there has been some out-diffusion of O (and probably N) from this region towards other parts of the structure (for instance, towards the top electrode as suggested by figure 4(c)), which takes place during the electroforming process.

The region situated just above B, labelled C, displays a plasmon peak around 22.2 eV, close but with a slightly larger energy than the one corresponding to the SiAlON layer, which can be attributed to a higher presence of O and N. Finally, the region labelled D in figure 4(d) presents a plasmon peak around 23 eV, which indicates a region rich in O or N between the SiAlON and Al layers. In addition, the Al contact presents a less regularly coloured distribution, indicating a component modification probably caused by the precipitate.

In order to determine whether the shift of the plasmon peak is due to the interdiffusion of N, O or both, further EELS experiments were carried out. Figure 5 shows the composition density maps of the precipitate obtained from core-loss EEL spectrum images before and after removing the background signal, integrating the area under the K edge of N at 401 eV (figure 5(b)) and the K edge of O at 532 eV (figure 5(c)). The results of the core-loss EELS study clearly show that the shift of the plasmon peak is due to the diffusion of both oxygen and nitrogen through the SiAlON layer. In addition to their presence in the precipitate, the region just below (labelled B in figure 4(d)) shows a lower concentration of these two elements. The fact that the Al-electrode exhibits more intense oxygen signal than the SiAlON layer could be ascribed to the different probabilities of electron-matter interaction in Al and SiAlON. The results displayed in figure 4(d), where the Al-electrode presents a plasmon peak closer to that of metallic Al than of Al<sub>2</sub>O<sub>3</sub>, are in agreement with this assumption. Nevertheless, the high concentration of oxygen observed in



**Figure 5** (a) STEM (dark-field) image corresponding to the precipitate under analysis; (b) and (c) show the composition density maps obtained from the core-loss EEL spectrum of the green square-framed region. Compositional maps are obtained from the areal density of the K edge of N at 401 eV (green) and the K edge of O at 532 eV (blue).

the external part of the electrode can be ascribed to the ambient oxidation, whereas oxygen diffusion from SiAlON into the Al-electrode is responsible for the O presence at the precipitate/electrode interface.

Due to the fact that both oxygen and nitrogen ions are negatively charged, the composition results presented so far suggest that these ions drift towards the top electrode when polarized under positive bias. During the upward diffusion of  $O^{2-}$  and  $N^{3-}$  ions, a non-negligible concentration of these ions is partially trapped in the intermediate region (label C in figure 4(d)), as demonstrated by a subtle shift to higher energies observed when analysing the latter. Some of the remaining (i.e. still diffusing) ions arrive at the precipitate (label D), again inducing a plasmon blue-shift in this region due to enhanced  $SiO_2$  and  $Si_3N_4$  formation. If the diffusing

$O^{2-}$  and  $N^{3-}$  ion concentration is higher than what the precipitate can absorb, these ions may actually reach the SiAlON/Al interface, where they are discharged, forming  $O_2$  and  $N_2$  gas, which is in turn further diffused through the interface and accumulated in random areas. After certain gas pressure is reached, the top electrode will mechanically stress the weakest part of the layer, resulting in a layer bending that gives rise to the observed bubble-like structure on top of the devices. From the analysis of both features it is thus plausible to assume the bubble-like structures to be the final step of the proto-precipitate feature, in a process that started with ion migration from the SiAlON layer and ended up stressing (and bending) the Al contact layer through  $O_2$  and  $N_2$  gas saturation at the Al/SiAlON interface.

The compositional analysis at the nanoscale made so far has shown a clear out-diffusion after the electroforming process of both N and O atomic species. Similar results were obtained in other silicon-based memristors, where it was shown that the electroforming and switching processes are ruled by actual movement of these species under the presence of an external electric field [17]. In our devices, this out-diffusion suggests the formation of conductive nanofilaments made of Si–Al alloy as the responsible process for attaining the LRS. Assuming that our nanofilaments exhibit a similar relative stoichiometry of Si and Al to the SiAlON layer, they are probably mostly composed of Si, with some minor Al incorporation. Taking into account the area of the devices, the difference in conductivity between LRS and HRS in our device ( $\sigma_{LRS}^{SiAlON} = 1.5 \times 10^{-4} \Omega^{-1} \text{cm}^{-1}$ ,  $\sigma_{HRS}^{SiAlON} = 4 \times 10^{-10} \Omega^{-1} \text{cm}^{-1}$ ) is some orders of magnitude larger than in similar devices made of either  $SiO_x$  ( $\sigma_{LRS}^{SiO_x} = 1.6 \times 10^{-5} \Omega^{-1} \text{cm}^{-1}$ ,  $\sigma_{HRS}^{SiO_x} = 4.6 \times 10^{-9} \Omega^{-1} \text{cm}^{-1}$ ) [15], or SiON ( $\sigma_{LRS}^{SiON} = 2.5 \times 10^{-9} \Omega^{-1} \text{cm}^{-1}$ ,  $\sigma_{HRS}^{SiON} = 2.5 \times 10^{-10} \Omega^{-1} \text{cm}^{-1}$ ) [40]—which, together with the structural observation at the nanoscale, suggests that Al plays an important role in the nanofilament creation, thus enhancing the overall conductivity of the devices. Finally, since aluminium can easily be oxidized (and also nitrized) [27, 41], it should contribute to the fast capture of either O or N atoms in the reset process [27], as suggested by the low reset voltage in comparison to the set one.

In summary, the described observations of the device cross-section morphology under external polarization, as well as the chemical composition analysis of the regions under study, give evidence of the diffusion of  $O^{2-}$  and  $N^{3-}$  ions through the SiAlON layer. In fact, the structural modification observed may be responsible for the creation of conductive paths, and thereby for the generation of memristive behaviour, as corroborated by the electrical characterization. The combination of electrical and structural results thus demonstrate that SiAlON exhibits similar memristive properties to metal oxides or nitrides, where the presence of oxygen and nitrogen vacancies plays a key role in the switching between the distinct resistance states—the VCM mechanism being responsible for their memristive properties.

#### 4. Conclusion

SiAlON-based MIS devices were fabricated, showing a memristive behaviour with a current density variation of more than five orders of magnitude at  $V_{\text{read}} = -0.5$  V. Electrical transport mechanisms in both resistance states were determined, the devices exhibiting an ohmic behaviour at LRS and defect-related Poole–Frenkel mechanism at HRS. The electroforming process was found to generate some bubble-like features in the Al top electrode, the observation of which by TEM suggests gas eruption from the SiAlON layer. In addition, a smaller feature was also observed under the Al electrode, promoted by a precipitate at the Al/SiAlON interface. EELS analysis determined that the precipitate corresponds to SiAlON, with its stoichiometry slightly modified—attributable in principle to  $O^{2-}$  and/or  $N^{3-}$  ion rearrangement. In order to determine which species—oxygen or nitrogen—is responsible for the blue-shift of the plasmon peak of the SiAlON precipitate with respect to the rest of the layer, core-loss EEL spectra were analysed, indicating that both oxygen and nitrogen are involved in the diffusion process. In summary, we have been able to observe directly, via electron microscopy, how the resistive switching cycle applied on SiAlON-based devices modifies the structure of the latter dielectric, demonstrating that a VCM-type memristive mechanism takes place, which in turn makes this material an attractive alternative to the exhaustively-studied metal oxides due to its potential adaptability through modification of its composition.

#### Acknowledgments

This work was financially supported by the Spanish Ministry of Economy and Competitiveness (Project Nos. TEC2012-38540-C02-01, TEC2016-76849-C2-1-R, MAT2013-41506-P, MAT2016-79455-P and MINECO/FEDER TEC2015-69916-C2-1-R). O B also acknowledges the subprogram ‘Ayudas para Contratos Predoctorales para la Formación de Doctores’ from the Spanish Ministry of Economy and Competitiveness for economical support. A M acknowledges financial support from BES-2013-062593.

#### ORCID iDs

O Blázquez  <https://orcid.org/0000-0002-0921-2793>

G Martín  <https://orcid.org/0000-0001-6741-2577>

#### References

- [1] Baek I G et al 2004 *IEDM Tech. Dig. IEEE Int. Electron Devices Meet.* 2004 IEEE pp 587–90
- [2] Waser R and Aono M 2007 *Nat Mater.* **6** 833
- [3] Kaeriyama S, Sakamoto T, Sunamura H, Mizuno M, Kawaura H, Hasegawa T, Terabe K, Nakayama T and Aono M 2005 *IEEE J. Solid-State Circuits* **40** 168
- [4] Strukov D B and Likharev K K 2005 *Nanotechnology* **16** 888
- [5] Folling S, Turel O and Likharev K 2001 *JCNN'01. Int. Jt. Conf. Neural Networks. Proc. (Cat. No. 01CH37222)* vol 1
- [6] Pickett M D, Medeiros-Ribeiro G and Williams R S 2012 *Nat. Mater.* **12** 114
- [7] Jo S H, Chang T, Ebong I, Bhadviya B B, Mazumder P and Lu W 2010 *Nano Lett.* **10** 1297
- [8] Ohno T, Hasegawa T, Tsuruoka T, Terabe K, Gimzewski J K and Aono M 2011 *Nat. Mater.* **10** 591
- [9] Torrezan A C, Strachan J P, Medeiros-Ribeiro G and Williams R S 2011 *Nanotechnology* **22** 485203
- [10] Hasegawa T, Terabe K, Tsuruoka T and Aono M 2012 *Adv. Mater.* **24** 252
- [11] Valov I, Waser R, Jameson J R and Koziicki M N 2011 *Nanotechnology* **22** 289502
- [12] Valov I 2014 *ChemElectroChem* **1** 26
- [13] Vescio G, Crespo-Yepes A, Alonso D, Claramunt S, Porti M, Rodriguez R, Cornet A, Cirera A, Nafria M and Aymerich X 2017 *IEEE Electron Device Lett.* **38** 457
- [14] Martín G, González M B, Campabadal F, Peiró F, Cornet A and Estradé S 2018 *Appl. Phys. Express* **11** 14101
- [15] Mehonic A, Munde M S, Ng W H, Buckwell M, Montesi L, Bosman M, Shluger A L and Kenyon A J 2017 *Microelectron. Eng.* **178** 98
- [16] Mehonic A et al 2012 *J. Appl. Phys.* **111** 74507
- [17] Mehonic A et al 2016 *Adv. Mater.* **28** 7486
- [18] Chang Y-F, Fowler B, Chen Y-C, Chen Y-T, Wang Y, Xue F, Zhou Y and Lee J C 2014 *J. Appl. Phys.* **116** 43708
- [19] Sawa A 2008 *Mater. Today* **11** 28
- [20] Mehonic A, Cuff S, Wojdak M, Hudziak S, Jambois O, Labbé C, Garrido B, Rizk R and Kenyon A J 2012 *J. Appl. Phys.* **111** 74507
- [21] Waser R, Dittmann R, Staikov G and Szot K 2009 *Adv. Mater.* **21** 2632–2663
- [22] Yang J J, Strukov D B and Stewart D R 2012 *Nat. Nanotechnol.* **8** 13
- [23] Linn E, Rosezin R, Kügeler C and Waser R 2010 *Nat. Mater.* **9** 403
- [24] Lv H et al 2009 *Appl. Phys. Lett.* **94** 213502
- [25] Camps I, Ramírez J M, Mariscal A, Serna R, Garrido B, Perálvarez M, Carreras J, Barradas N P, Alves L C and Alves E 2015 *Appl. Surf. Sci.* **336** 274
- [26] da Silva C R M, de Melo F C L and de Macedo Silva O M 1996 *Mater. Sci. Eng. A* **209** 175
- [27] Choi B J, Torrezan A C, Strachan J P, Kotula P G, Lohn A J, Marinella M J, Li Z, Williams R S and Yang J J 2016 *Adv. Funct. Mater.* **26** 5290
- [28] Waser R, Dittmann R, Staikov G and Szot K 2009 *Adv. Mater.* **21** 2632
- [29] Frenkel J 1930 *Phys. Rev.* **36** 1604
- [30] Blázquez O, López-Vidrier J, Hernández S, Montserrat J and Garrido B 2014 *Energy Procedia* **44** 145
- [31] Berencén Y, Wutzler R, Rebohle L, Hiller D, Ramírez J M, Rodríguez J A, Skorupa W and Garrido B 2013 *Appl. Phys. Lett.* **103** 111102
- [32] Sze S M and Ng K K 2007 *Physics of Semiconductor Devices* 3rd edn (New York: Wiley)
- [33] Harrell W R and Frey J 1999 *Thin Solid Films* **352** 195
- [34] Osinniy V, Lysgaard S, Kolkovsky V, Pankratov V and Larsen A N 2009 *Nanotechnology* **20** 195201
- [35] López-Vidrier J et al 2013 *J. Appl. Phys.* **114** 163701
- [36] Mehonic A, Buckwell M, Montesi L, Garnett L, Hudziak S, Fearn S, Chater R, McPhail D and Kenyon A J 2015 *J. Appl. Phys.* **117** 124505
- [37] Chen C, Gao S, Zeng F, Tang G S, Li S Z, Song C, Fu H D and Pan F 2013 *J. Appl. Phys.* **114** 014502
- [38] EELS Atlas <http://eels.info/atlas> (accessed November 07, 2017)
- [39] EELS Data Base <https://eelsdb.eu> (accessed November 07, 2017)
- [40] Chen D, Huang S and He L 2017 *J. Semicond.* **38** 43002
- [41] Maiti N, Biswas A, Tokas R B, Bhattacharyya D, Jha S N, Deshpande U P, Barve U D, Bhatia M S and Das A K 2010 *Vacuum* **85** 214

## Luminescence yield in Al and Tb<sup>3+</sup> delta-doped oxide thin films fabricated by electron beam evaporation

O. Blázquez,<sup>(a)</sup> J. M. Ramírez,<sup>(a)</sup> J. López-Vidrier,<sup>(a)</sup> Y. Berencén,<sup>(a)</sup> S. Hernández,<sup>(a)</sup> P. Sanchis<sup>(b)</sup> and B. Garrido<sup>(a)</sup>

<sup>(a)</sup>MIND-IN<sup>2</sup>UB, Electronics Department, Universitat de Barcelona, Martí i Franquès 1, E-08028 Barcelona (Spain)

<sup>(b)</sup>Nanophotonics Technology Center, Universitat Politècnica de València, Camino de Vera s/n, E-46022 València (Spain)

### Abstract

Electron beam evaporation was employed in order to fabricate Al- and Tb-codoped Si oxide multilayers via the delta-doping approach. This methodology permits the control of the rare-earth (RE) separation along the growth direction with nanometric resolution. To investigate the control of the RE separation in the growth direction, different SiO<sub>2</sub> thicknesses were studied. After deposition, the samples were submitted to different annealing processes for 1 h in N<sub>2</sub>, at temperatures ranging from 700 to 1100 °C. Photoluminescence experiments reveal narrow emissions ascribed to Tb<sup>3+</sup> ions in all samples, with an intensity variation depending on the oxide thickness and annealing temperature. In addition, the incorporation of Al under different spatial configurations produced an enhancement of more than one order of magnitude in the photoluminescence intensity, in respect to the best sample without Al. Finally, time-resolved measurements were carried out in order to determine the <sup>5</sup>D<sub>4</sub>→<sup>7</sup>F<sub>5</sub> transition dynamics, obtaining a decay time of ~1.6 ms ascribed to the Tb<sup>3+</sup> ions.

### I. Introduction

During the last two decades, rare earth (RE)-doped oxides have been studied due to its narrow and intense luminescence, becoming a good candidate for novel light-emitting silicon-based materials for optoelectronic applications [1]. Many works have been reported on RE-doped SiO<sub>2</sub> or Si-rich silicon oxide [2-4]. A wide variety of deposition techniques, such as implantation [5] or thermal evaporation in effusion cells [6], have been employed to fabricate these doped materials. Chemical synthesis-based techniques like sol-gel have also shown a good optical performance [7]; however, the deposition control and the incompatibility with planar technology suppose a drawback towards its integration into electronics and photonics [8]. In addition, as it is well known, inter-RE ion distance is one of the most important parameters in order to avoid clustering, which quenches the optical emission [9]. As a consequence, most research is focused on deposition techniques that allow the inter-RE separation control. In this work, we present the fabrication of Al- and Tb-codoped Si oxide multilayers by means of electron beam evaporation (EBE). Via the delta-doping approach, an alternated deposition of nanometric Tb (the dopant) and silicon oxide layers was achieved, thus obtaining a multilayer (ML) structure. This permitted the study of the system luminescence yield as a function of the Tb layer separation along the growth direction. Besides, the introduction of Al in the system was found to conveniently modify the Tb<sup>3+</sup> environment, thus inducing a notorious enhancement in the system's luminescence emission.

### II. Experimental details

The electron beam evaporation technique was used to fabricate Tb-doped silicon oxide (TSO) samples onto crystalline (100)-Si substrate. The employed system was a PFEIFFER VACUUM Classic 500 with a

### 3. Si-Based Materials for Optoelectronics and Resistive Switching

Ferrotec GENIUS electron beam controller and a Ferrotec CARRERA high-voltage power supply. Prior to deposition, the substrates were successively cleaned with acetone, isopropyl alcohol, ethanol and distilled water, being agitated ultrasonically during each process. The delta-doping approach was used in order to dope the SiO<sub>2</sub> matrix initially only with Tb<sup>3+</sup> ions, alternatively depositing SiO<sub>2</sub> and Tb nanometric layers. In this case, the multilayer (ML) consists of 15 × [Tb(0.4 nm)/SiO<sub>2</sub>(*d*)], being *d* the nominal SiO<sub>2</sub> layer thickness, ranging from 1.0 nm to 3.0 nm. In order to protect the ML, two 10-nm thick SiO<sub>2</sub> layers were deposited on the bottom and top of the ML (see Fig. 1).

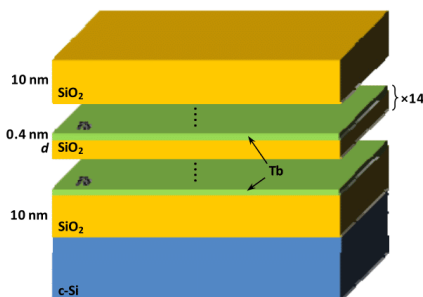


Fig. 1. Tb-doped SiO<sub>2</sub> (TSO) ML structure of samples, where *d* ranges from 1.0 to 3.0 nm.

The base pressure of the chamber was  $1.6 \times 10^{-6}$  mbar and the substrate temperature was heated at 100 °C. During the deposition, the nominal rates were 1.0 Å/s and 0.2 Å/s for SiO<sub>2</sub> and Tb respectively, being the acceleration voltage 6 kV. Finally, annealing process was carried out at 700, 900 and 1100 °C in a N<sub>2</sub> atmosphere for 1 h.

In order to study the influence of Al in the optical properties of Tb<sup>3+</sup>, new samples were fabricated by co-doping the SiO<sub>2</sub> with Tb and Al (TASO). The Al was evaporated using an acceleration voltage of 10 kV and keeping the other deposition parameters used for the Tb doping unchanged. Different layer configurations were studied in order to find the best structure that results in the maximum Tb<sup>3+</sup> emission. These configurations consisted in depositing 0.8-nm-thick Al and 0.4-nm-thick Tb layers, either separated by oxide (TASO1) or adjacent (TASO2). Two new samples were fabricated, doubling the Al concentration by either depositing 1.6 nm of Al in a TASO1 configuration (TASO3) or sandwiching Tb layer between two 0.8-nm-thick Al layers (TASO4). The oxide spacer was fixed at 3.0 nm for TASO1 and TASO3, and reduced to 1.5 nm for TASO2 and TASO4, in order to keep a similar total inter-Tb layer separation. Table 1 shows the four described configurations, repeated through the ML and keeping the same number and thickness of Tb layers as in TSO samples for comparison.

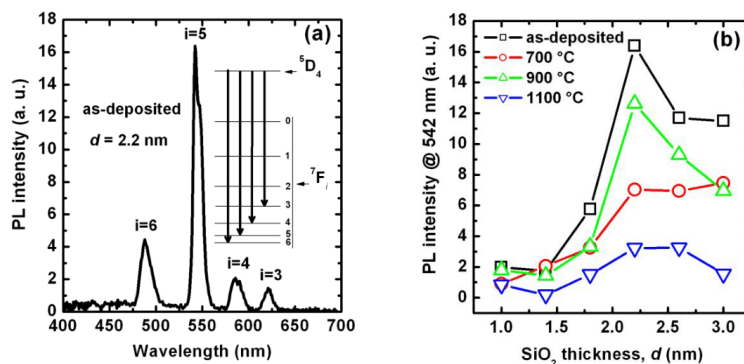
Table 1. Summary of different unit ML structures for Tb- and Al- codoped samples and their thicknesses. Samples consist of 15 unit ML structures.

Sample	TASO1	TASO2	TASO3	TASO4
Unit ML structure	SiO <sub>2</sub> /Tb/SiO <sub>2</sub> /Al	SiO <sub>2</sub> /Tb/Al	SiO <sub>2</sub> /Tb/ SiO <sub>2</sub> /Al	SiO <sub>2</sub> /Al/Tb/Al
Nominal thickness (nm)	1.5/0.4/1.5/0.8	3.0/0.4/0.8	1.5/0.4/1.5/1.6	3.0/0.8/0.4/0.8

Photoluminescence (PL) spectra were acquired exciting the samples with the 325-nm line of a He-Cd laser, the resulting emission being collected in the visible range from 400 to 700 nm using a photomultiplier tube coupled to a monochromator, and amplified with a standard lock-in system. The laser excitation beam was mechanically chopped to determine the  $\text{Tb}^{3+}$  radiative lifetime, being the signal processed using an Agilent infinium DSO8064A oscilloscope.

### III. Results and discussion

PL spectra were acquired exciting the samples with the 325-nm line of a He-Cd laser and collecting the emission in the visible range from 400 to 700 nm. Typical  $\text{Tb}^{3+}$  spectra were observed coming from all samples, with and without Al, which corresponds to the electronic  $^5\text{D}_4 \rightarrow ^7\text{F}_i$  transitions ( $i = 3, 4, 5$  and  $6$ ). In particular, Fig. 3(a) shows the PL spectrum of the as-deposited TSO sample with  $d = 2.2$  nm, where the four  $\text{Tb}^{3+}$  transitions are clearly observed. In the case of the annealed samples, an additional wide emission was observed that increases the background of the total emission throughout the visible range (not shown in this figure). Depending on the annealing temperature, this broad emission is centered at different wavelengths and presents different intensities. Fig. 3(b) summarizes the PL intensity of the  $^5\text{D}_4 \rightarrow ^7\text{F}_5$  transition peak (542 nm) as a function of  $d$ , for all TSO samples and at different annealing temperatures, without considering the background emission. Poor emission intensity is observed for samples with  $d \leq 1.4$  nm. However, a clear increase of  $\text{Tb}^{3+}$  emission intensity appears in the range between  $d = 1.4$  and  $2.2$  nm for all TSO samples. In the case of samples with a thicker spacing layer than  $2.2$  nm, the emission intensity is kept or softly decreases depending on the annealing temperature. It is important to note that the annealing process basically increases the broad background emission, which is related to the defects inside the oxide matrix [5], being the  $\text{Tb}^{3+}$  emission of annealed samples substantially lower than as-deposited ones.





### 3. Si-Based Materials for Optoelectronics and Resistive Switching

Fig. 3. (a) PL spectrum corresponding to the TSO sample with SiO<sub>2</sub> thickness of  $d = 2.2$  nm in as-deposited conditions. A diagram corresponding to the different  $^5D_4 \rightarrow ^7F_i$  (where  $i$  spans from 0 to 6) transitions is also displayed. (b) PL intensity of the  $^5D_4 \rightarrow ^7F_5$  transition peak (542 nm) as a function of  $d$  and at different annealing temperatures.

The abrupt variation of the PL intensity as a function of the SiO<sub>2</sub> spacing layer thickness could be related to the Tb separation along the growth direction, which becomes a critical parameter to avoid clustering [9]. The possibility to control this separation is one of the key factor in order to improve the number of activated luminescent centers and, thus, to increase the efficiency of light emission. The broad PL band observed in the annealed samples is typically ascribed to SiO<sub>2</sub> defects (oxygen vacancies and/or non-bridging chemical bonds in Si-O) [2, 3, 5]. To be optically active, Tb<sup>3+</sup> requires a C<sub>4v</sub> symmetry (TbO<sub>6</sub> conformation), similar to other RE ions in the same oxidation state (such as Er<sup>3+</sup> or Yb<sup>3+</sup>) [10, 11]. Therefore, Tb<sup>3+</sup> ions are very sensitive to the presence of surrounding defects, which constitutes a drawback for their emission. In addition, the central position of this broad background emission varies depending on the annealing temperature, which may indicate the activation of different defect populations. The fact that the annealing treatment does not improve the activation of more Tb ions as luminescent centers, being these already optically activated during the deposition process, confirms their poor diffusion within the oxide and the role of matrix defects avoiding their optical activation.

The introduction of thin Al layers into the oxide matrix (TASO) was found to directly affect the Tb<sup>3+</sup> ions environment, leading to an increase of luminescence intensity and an improvement at high annealing temperatures. Fig. 4 shows the visible spectra of TSO with  $d = 3$  nm and TASO4 samples, both annealed at 900 °C. A strong RE emission is observed for the co-doped sample compared to Tb-doped one, being the enhancement of more than one order of magnitude. The broad background is also observed, confirming the generation of defects when the active layers are thermally treated. However, this emission is much weaker in comparison with the Tb<sup>3+</sup> electronic transitions. The study of the different layer configurations of Al layers is summarized in the inset of Fig. 4, where the PL peak intensity at 542 nm is represented as a function of all different TASO configurations, for as-deposited and annealed at 900 °C samples. As it is shown in the inset of the figure, for TSO samples the annealing process does not improve the RE emission, as previously mentioned. However, all TASO samples present a clear improvement of luminescence once an annealing process at 900 °C is carried out. The best configuration (in terms of PL emission yield) corresponds to TASO4, which consists of a Tb layer sandwiched between two Al layers. This fact confirms that Al ions modify the surrounding environment of Tb<sup>3+</sup> ions, generating non-bridging oxygen atoms (Al-O) and consequently enhancing the RE optical emission [12].

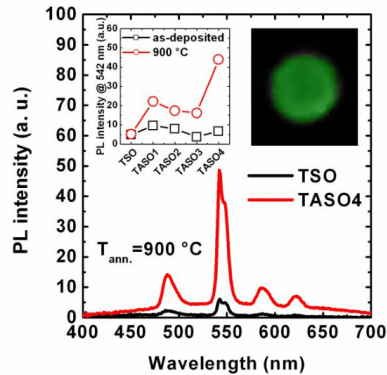


Fig. 4. Comparison between PL spectra obtained from TSO and TSO4 with  $d = 3$  nm, both annealed at 900 °C. The inset shows the 542-nm Tb peak intensity of as-deposited (black squares) and annealed at 900 °C (red circles) samples for the different layer configurations. The inset image corresponds to a photograph of the emission of TSO4 sample annealed at 900 °C, also observed with the naked eye.

In order to study the PL dynamics of the  ${}^5D_4 \rightarrow {}^7F_5$  transition, time-resolved measurements were performed by using the same excitation wavelength and mechanically chopping the excitation beam. Fig. 5 shows the time-resolved emission of the TSO and TSO4 samples annealed at 900 °C, once the laser excitation is switched off. Both measurements reveal two single exponential decay times, suggesting more than one optical centers are excited. The slow decay time ( $\tau_1 \sim 1.6$  ms) is the same for both samples, which could be attributed to the decay time of Tb $^{3+}$  ions in a proper  $C_{4V}$  configuration. On the other hand, the other faster decay times ( $\tau_2 \sim 1.2$  ms and  $\tau_3 \sim 0.6$  ms) could be ascribed to cross-relaxation processes, as observed under high RE ion concentration conditions [12, 13]. This effect is more evident for TSO samples than in the case of TSO samples, as the samples without Al present a larger number of Tb neighbors, which contributes to quench the emission. Moreover, the addition of Al ions also contributes to have the Tb ion in a more favorable bonding configuration, making them optically active centers.

### 3. Si-Based Materials for Optoelectronics and Resistive Switching

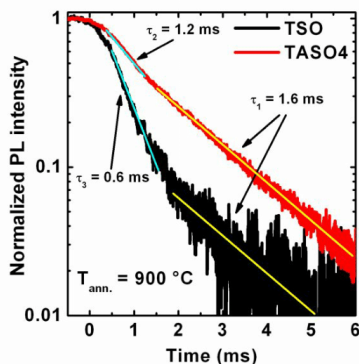


Fig. 5. Time-resolved PL signal corresponding to TSO and TAsO4 samples annealed at 900 °C.

#### IV. Conclusions

Tb-doped SiO<sub>2</sub> samples were fabricated by means of the electron beam evaporation technique using the delta-doping approach. A multilayer structure was achieved by alternatively depositing SiO<sub>2</sub> and Tb nanometric layers. Al was also introduced to co-dope the samples, using different ML stack configurations. An optimal SiO<sub>2</sub> thickness of 2.2 nm was found to avoid PL quenching effects in the growth direction. A wide defect emission was observed for annealed samples, which is mainly attributed to oxygen vacancies and non-bridging chemical bonds in Si-O. In contrast of Tb-doped samples, Al-Tb-co-doped samples generate Al-O bonds when the samples are annealed at 900 °C, thus eliminating the bridging oxygens and consequently enhancing the Tb<sup>3+</sup> emission intensity about one order of magnitude. Time-resolved PL measurements reveal a slow Tb<sup>3+</sup> decay time of ~1.6 ms. However, slightly faster decay times were also observed, especially in samples without Al, that were ascribed to cross-relaxation processes. The introduction of Al decreases this effect, tending to generate one single Tb-related optical center.

#### Acknowledgments

This work was financially supported by the Spanish Ministry of Economy and Competitiveness (Project TEC2012-38540-C02-01). O. B. also acknowledges the subprogram “Ayudas para Contratos Predoctorales para la Formación de Doctores” for economical support.

#### References

- [1] A. J. Kenyon, Progress in Quantum Electronics **26**, 225-284 (2002).
- [2] M. Kulacki and R. Turan, J. Lumin., **137**, 37 (2013).
- [3] A. Podhorodecki, L. W. Golacki, G. Zatryb, J. Misiewicz, J. Wang, W. Jadwisieniczak, K. Fedus, J. Wojcik, P. R. J. Wilson, P. Mascher, J. Appl. Phys. **115**, 143510 (2014).
- [4] A. Podhorodecki, G. Zatryb, J. Misiewicz, J. Wojcik, P. R. J. Wilson, P. Mascher, Nanotechnology **23**, 475707 (2012).

- [5] L. Rebohle and W. Skorupa, “*Rare-Earth Implanted MOS Devices for Silicon Photonics*”, Springer Series in Materials Science (Springer, 2010).
- [6] A. T. Fromhold JR., W. D. Foster, *Electrocomponent Science and Technology* **3**, 51-62 (1976).
- [7] E.M. Yeatman, M.M. Ahmad, O. McCarthy, A. Martucci, M. Guglielmi, *Journal of Sol-Gel Science and Technology* December 2000, Volume 19, Issue 1-3, pp 231-236.
- [8] J. M. Ramírez, Y. Berencén, L. López-Conesa, J. M. Rebled, F. Peiró and B. Garrido, *Appl. Phys. Lett.* **103**, 081102 (2013).
- [9] R. Serna, *et al.*, *Appl. Phys. Lett.* **75**, 4073 (1999).
- [10] M. Ishii, S. Komuro, T. Morikawa, Y. Aoyagi, *J. Appl. Phys.* **89**, 3679 (2001)
- [11] M. Llusçà, J. López-Vidrier, A. Antony, S. Hernández, B. Garrido, J. Bertomeu, *Thin Solid Films* **562**, 456 (2014).
- [12] C. Armellini, M. Ferrari, M. Montagna, G. Pucker, C. Bernard, A. Monteil, *Journal of Non-Crystalline Solids* **245**, 115-121 (1999).
- [13] V. H. Romero, E. De la Rosa, T. López-Luke, P. Salas, C. Angeles-Chavez, *J. Phys. D: Appl. Phys.* **43**, 465105 (2010).

### 3. Si-Based Materials for Optoelectronics and Resistive Switching



## Structural and optical properties of Al-Tb/SiO<sub>2</sub> multilayers fabricated by electron beam evaporation

O. Blázquez,<sup>a)</sup> J. López-Vidrier,<sup>b)</sup> L. López-Conesa, M. Busquets-Masó, S. Estradé, F. Peiró, S. Hernández, and B. Garrido

*MIND-IN<sup>2</sup>UB, Department of Engineering: Electronics, Universitat de Barcelona, Martí i Franquès 1, E-08028 Barcelona, Spain*

(Received 28 June 2016; accepted 20 September 2016; published online 4 October 2016)

Light emitting Al-Tb/SiO<sub>2</sub> nanomultilayers (NMLs) for optoelectronic applications have been produced and characterized. The active layers were deposited by electron beam evaporation onto crystalline silicon substrates, by alternatively evaporating nanometric layers of Al, Tb, and SiO<sub>2</sub>. After deposition, all samples were submitted to an annealing treatment for 1 h in N<sub>2</sub> atmosphere at different temperatures, ranging from 700 to 1100 °C. Transmission electron microscopy confirmed the NML structure quality, and by complementing the measurements with electron energy-loss spectroscopy, the chemical composition of the multilayers was determined at the nanoscopic level. The average composition was also measured by X-ray photoelectron spectroscopy (XPS), revealing that samples containing Al are highly oxidized. Photoluminescence experiments exhibit narrow emission lines ascribed to Tb<sup>3+</sup> ions in all samples (both as-deposited and annealed ones), together with a broadband related to SiO<sub>2</sub> defects. The Tb-related emission intensity in the sample annealed at 1100 °C is more than one order of magnitude higher than identical samples without Al. These effects have been ascribed to the higher matrix quality, less SiO<sub>2</sub> defects emitting, and a better Tb<sup>3+</sup> configuration in the SiO<sub>2</sub> matrix thanks to the higher oxygen content favored by the incorporation of Al atoms, as revealed by XPS experiments. *Published by AIP Publishing.*  
[\[http://dx.doi.org/10.1063/1.4964110\]](http://dx.doi.org/10.1063/1.4964110)

### I. INTRODUCTION

The production of efficient light emitting devices based on silicon is of primary interest for the optoelectronic industry, especially for application in optical sensors, panel, displays, and even for indicators and illumination.<sup>1–4</sup> In order to achieve this goal, novel strategies have been employed. Such is the case of the semiconductor materials doped with rare earth (RE) ions, which have been widely studied due to the narrow and intense luminescence they yield, aiming at a wealth of applications.<sup>5–8</sup> Recently, excellent electro-optical properties have been reported on III–V semiconductors as host matrix for different RE ions, allowing for a suitable performance as light-emitting devices.<sup>5,9</sup> In addition, REs have been employed to develop light-emitting silicon-based materials for optoelectronic applications.<sup>10,11</sup> With this aim, several works have reported on RE-doped oxides such as SiO<sub>2</sub>, Si-rich silicon oxide,<sup>12–14</sup> or Si-rich silicon oxynitride<sup>15</sup> matrices as potential candidates to become active layers in light-emitting devices. The interest in determining the optical and electronic properties of the different RE species lies in the particular electronic structure they present, which allows engineering the desired emission spectra of the active layer. Among the different RE elements, erbium is one of the most studied elements, given that its Er<sup>3+</sup> oxidation state presents a characteristic emission at 1.55 μm, which is suitable for

telecom applications.<sup>16</sup> As well, terbium and europium are interesting for their emission in the visible range, being green and red emissions typically reported for, respectively, Tb<sup>3+</sup> and Eu<sup>3+</sup> ions.<sup>17</sup> Nevertheless, clustering of RE induces the ions to become optically inactive, which notably drops their emission efficiency. In the literature, and in combination with SiO<sub>2</sub>, aluminum has been widely employed for dispersing RE ions and thus allows for a higher RE incorporation without clustering.<sup>18,19</sup>

Different methods have been employed to combine these materials, being ion implantation,<sup>16</sup> thermal evaporation in effusion cells,<sup>20</sup> or plasma-enhanced chemical-vapor deposition<sup>21</sup> the most used ones. In a previous publication, some of the current authors reported the fabrication of Tb doped SiO<sub>2</sub> by means of chemical vapor deposition.<sup>22</sup> Other techniques such as sol-gel have shown a good optical performance,<sup>23,24</sup> but the difficulties for a controlled deposition and the incompatibility with planar technology constitute important drawbacks for the integration of RE in electronic and photonic devices.<sup>25</sup> In this work, we focus on electron beam evaporation (EBE), a physical deposition method widely employed to metalize devices, but also to grow layers from a wide range of materials, which include semiconductors. The possibility to directly evaporate pure elements and simple compounds without the need of complex chemical reactions allows also for achieving controlled deposition of thin films and reduces (or even eliminates) their contamination. The most widely used method based on EBE to combine different materials within a single thin film is by using targets with mixed compounds and under a

<sup>a)</sup>Author to whom correspondence should be addressed. Electronic mail: oblazquez@el.ub.edu. Tel.: (+34) 93 4039176.

<sup>b)</sup>Now at IMTEK, Faculty of Engineering, Albert-Ludwigs-University Freiburg, Georges-Köhler-Allee 103, D-79110 Freiburg, Germany.

### 3. Si-Based Materials for Optoelectronics and Resistive Switching

particular atmosphere. However, the electrical current needed to properly evaporate the compounds can differ substantially and, therefore, their respective evaporation rates are difficult to control. Despite this drawback, another way to control the overall amount of the different elements takes advantage of the sequential evaporation of different materials from different targets, thus depositing consecutive nanometric layers of each of them (i.e., using the so-called nanomultilayer (NML) approach), instead of trying to do it during one single evaporation process. Therefore, this approach can be used to combine RE layers of a few nanometers with a matrix material, hence allowing for a controlled inter-ion distance in the growth direction. Finally, a post-deposition thermal treatment is then required to induce the optical activation of the ionic species, and thus making the films luminescent.

In this work, we describe the fabrication and present the structural and optical characterization of Al-Tb/SiO<sub>2</sub> nanomultilayered thin films. To obtain this structure, Al, Tb, and SiO<sub>2</sub> nanomultilayers (NMLs) were deposited using the EBE technique on a Si substrate. Different electron microscopy and high-energy spectroscopic techniques were used to characterize the multilayer structure at the nanoscale, from which the spatial distribution and binding structure of the different involved species were obtained. The overall composition of the NML structure has been determined by X-ray photoelectron spectroscopy (XPS) measurements, which also allowed gathering information about the Al effect on the Tb environment. The influence of the annealing temperature and the presence of Al atoms on the emission properties of Tb<sup>3+</sup> ions were studied by means of photoluminescence (PL). Finally, the study of the PL emission lifetime of the different samples is discussed in terms of the Tb<sup>3+</sup> ions atomic environment, as corroborated by structural techniques. Overall, the study highlights the possibility of employing the EBE technique, using the multilayer approach, to deposit optically active rare earth-based thin films that can lead to several optoelectronic applications.

#### II. EXPERIMENTAL DETAILS

Thin films of Al-Tb/SiO<sub>2</sub> nanomultilayers were fabricated by means of EBE technique onto crystalline (100)-Si substrate, using a PFEIFFER VACUUM Classic 500 instrument with a Ferrotec GENIUS electron beam controller and a Ferrotec CARRERA high-voltage power supply. Before deposition, substrates were cleaned with acetone, isopropyl alcohol, ethanol, and de-ionized water, and agitated ultrasonically during each process. Nanometric layers of SiO<sub>2</sub>, Tb, and Al were alternatively deposited. In this case, the NML consists of 15 periods of Al/Tb/Al/SiO<sub>2</sub> layers with nominal thicknesses of 0.8, 0.4, 0.8, and 3 nm, respectively, being this configuration optimum for the optical activation of Tb<sup>3+</sup> ions, as experimentally observed in a previous study.<sup>26</sup> In order to protect the stack from the following thermal annealing, two 10-nm SiO<sub>2</sub> layers were deposited at the bottom and on top of the NML structure. To elucidate the role of Al, an identical set of samples was also deposited with no Al in the NML structure (Tb/SiO<sub>2</sub>), keeping constant the thickness of

the Tb and SiO<sub>2</sub> layers (nominally, 0.4 and 3 nm, respectively). In Fig. 1, the cross-section schemes corresponding to both described structures are drawn.

Before the evaporation process, the base pressure in the chamber was  $1.6 \times 10^{-6}$  mbar and the temperature of the substrate was kept at 100 °C. The nominal deposition rates were 0.2, 0.2, and 1.0 Å/s for Al, Tb, and SiO<sub>2</sub>, respectively, using an electron beam acceleration voltage of either 10 kV for Al or 6 kV for Tb and SiO<sub>2</sub>. Once the deposition process was completed, the layers were submitted to an annealing treatment at temperatures of  $T_{\text{ann}} = 700, 900, \text{ or } 1100$  °C in a N<sub>2</sub> atmosphere for 1 h in a conventional tubular furnace.

A structural characterization of the cross-section NML structure was carried out on the as-deposited Al-Tb/SiO<sub>2</sub> sample by means of transmission electron microscopy (TEM). The sample was prepared for TEM observation by conventional mechanical polishing methods up to electron transparency. Data were acquired using a JEOL 2010F microscope, equipped with a Schottky field emission gun and coupled to a Gatan imaging filter with 0.8 eV energy resolution. Chemical information was obtained from spatially localized electron energy-loss (EEL) spectra acquired along three periods of the NML (spectrum imaging). These spectra were co-acquired with a high angular annular dark field (HAADF) image in scanning mode (scanning-TEM, STEM), which presents a contrast corresponding to different atomic numbers. The energy-loss range was selected to be from 1000 to 2000 eV, thus covering the core-loss edges for the three elements of interest (Tb M4 and M5 edges, Al K edge, and Si K edge). No information regarding the location of oxygen could be attained due to the limitation in the energy loss of the employed energy window (O K-edge is placed around 532 keV). Areal density maps for these edges were obtained as an elemental distribution map of the multilayer. XPS measurements were also carried out using a PHI 5500 Multitechnique System, to study the overall composition and obtain information regarding the Al influence on the Tb-related binding formation, in the annealed samples at the highest temperature, with and without Al.

The optical emission properties of the NMLs were studied by means of PL spectra, exciting the samples with the

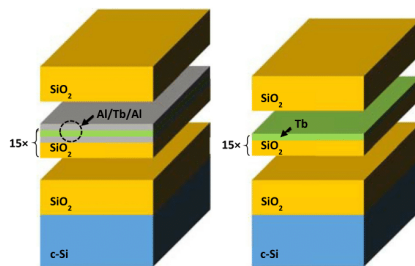


FIG. 1. Sketch of the multilayer structures employed in the present work, corresponding to 15 periods of (left) Al/Tb/Al/SiO<sub>2</sub> and (right) Tb/SiO<sub>2</sub> layers, plus the 10-nm SiO<sub>2</sub> protecting layers at the bottom and on top of the NML.

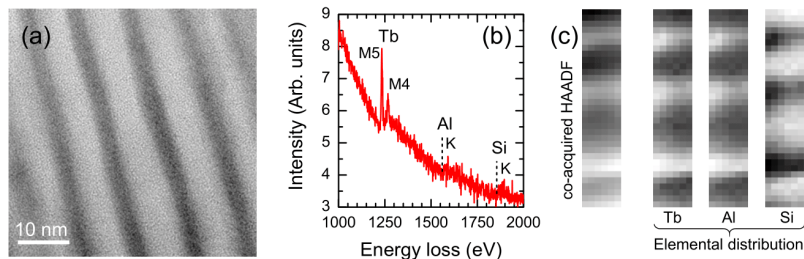


FIG. 2. (a) HRTEM image of the as-deposited Al-Tb/SiO<sub>2</sub> sample. (b) EEL spectrum of an area along three periods of the multilayer. (c) Co-acquired HAADF image of the same area and elemental distribution maps corresponding to each element of interest (Tb, Al, and Si) obtained from the spatially-resolved spectra.

325-nm line of a He-Cd laser. The resulting emission was collected in the visible range from 400 to 700 nm using a GaAs photomultiplier tube (PMT) coupled to a monochromator in a lock-in configuration. In order to study the Tb<sup>3+</sup> radiative lifetime, the laser excitation beam was mechanically square-pulsed with a period of 20 ms and 50% duty cycle (resulting in a rise/fall time of  $\sim 300 \mu\text{s}$ ). The obtained PL signal from the PMT was analyzed by a digital oscilloscope.

### III. RESULTS AND DISCUSSION

#### A. Structural characterization

To inspect the correct deposition and fabrication of the NML samples under study, their structure and composition were determined by high resolution TEM (HRTEM) and STEM-electron energy-loss spectroscopy (EELS) imaging, respectively. The HRTEM image from the as-deposited Al-Tb/SiO<sub>2</sub> sample exhibits an atomically-sharp interface of the Si substrate with the deposited layer. Moreover, no crystalline domains are observed in any of the regions, which implies that all layers are amorphous. In Fig. 2(a), a HRTEM image is presented, which shows the correct deposition of a nanomultilayer structure (different contrast corresponding to different material phases), with a small degree of waviness.

The as-deposited sample was further analyzed by means of HAADF and EELS spectrum imaging, in order to investigate the chemical composition of the NML stack. In Fig. 2(b), an EEL spectrum for the sample under study along three periods is presented. The spectrum clearly exhibits core-loss edges of the three interesting elements (Tb M4 and M5 edges, Al K edge, and Si K edge). An HAADF image of the same region was also taken, showing a clear difference in contrast between adjacent layers. Since HAADF contrast is sensitive to the atomic mass of the involved species, this result reveals that different atomic species are preferentially located within the NML stack, thus indicating their presence in the NML structure. Actually, the brightest contrast, corresponding to the heaviest atoms, is consistent with the spatial localization of the Tb ions within the stack. The distribution of the other present species, however, cannot be deduced from the HAADF analysis; for this reason, an EEL spectrum was co-acquired at each pixel in scanning mode. By mapping

the energy-loss intensity corresponding to each element (after background subtraction), elemental distribution maps of the different species were built from the spectrum image. Fig. 2(c) shows the co-acquired HAADF image and the elemental distribution map of the three elements of interest (Tb, Al, and Si). It is clearly observed that the Si signal is spatially isolated from the Tb and Al signals. This means that Si is only located in the nominal SiO<sub>2</sub> layers, whereas Tb and Al signals were found to come from the same region, homogeneously distributed in an Al/Tb/Al stack and with no evidence of the nominal sandwiched structure, which implies a certain degree of intermixing of this stack and, thus, minimizing the possible Tb clustering. The overall result from the structural characterization is the presence of two distinct regions within our samples: one composed only by SiO<sub>2</sub> and the other one containing a mixture of Tb and Al. The

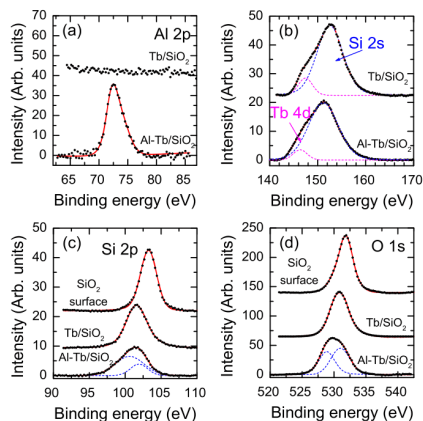


FIG. 3. XPS spectra corresponding to the NML samples with and without Al, acquired around the binding energies corresponding to Al 2p, Tb 4d, Si 2s, Si 2p, and O 1s bonds. (a) and (b) compare the presence of Al and Tb in both samples, whereas (c) and (d) focus on the stoichiometry of the present SiO<sub>2</sub> on the capping layer (on top of the NMLs) and within the NML stack.



### 3. Si-Based Materials for Optoelectronics and Resistive Switching

measured thicknesses from both regions, as obtained from the HRTEM images [see Fig. 2(a)], are 5 and 3 nm, respectively for the SiO<sub>2</sub> and the Al-Tb layers, both thicker than the nominal values (3 and 2 nm, respectively).

In order to accurately determine the composition of the Al-Tb/SiO<sub>2</sub> structure and obtain information regarding the Al effect on the binding formation around Tb ions, XPS measurements at different depths were carried out on samples with and without Al and annealed at 1100 °C, by sputtering the layer with Ar<sup>+</sup> ions. As the depth resolution is around 5–10 nm, an average value of the total composition of the NMLs can be obtained. Fig. 3 exhibits the photoemission spectra obtained from the different elements within the multilayers: Si, O, Tb, and Al. In addition, Figs. 3(c) and 3(d) also present the photoemission spectra of O and Si from the top SiO<sub>2</sub> capping layer (the composition and stoichiometry of this SiO<sub>2</sub> layer could therefore be analyzed without being influenced by the rest of the nanometric layers).

The photoemission spectra corresponding to energies around the bound energy of Al 2p are displayed in Fig. 3(a). A flat spectrum (i.e., no signal) is obtained from the Tb/SiO<sub>2</sub> NMLs, whereas a clear contribution from Al is observed in the spectrum from the Al-Tb/SiO<sub>2</sub> NMLs, evidencing that Al is present only in the latter. Looking at the energy around the Tb 4d bonds, between 140 and 165 eV [see Fig. 3(b)], there is a broadband that can be deconvoluted into two different contributions: one from Tb 4d (≈147 eV) and another from Si 2s bonds (≈152 eV). Their relative intensity is almost constant in the two samples, although there are small changes in their mean energy, probably associated with the influence of Al to the NML structure, which specially affect the Tb bonds. The energy window around Si 2p bonds (between 95 and 105 eV) displays one peak at ≈102 eV [see Fig. 3(c)], which broadens under the presence of Tb and Al-Tb.

The most interesting analysis, however, corresponds to binding energies near 530 eV, related to O 1s bonds [see Fig. 3(d)]. Indeed, Fig. 3 displays the photoemission spectra of the samples under study (Al-Tb/SiO<sub>2</sub> and Tb/SiO<sub>2</sub> samples) around the mentioned binding energies well within the NML structure (where Tb and Al ions are present), together with the spectrum obtained at the first surface (which corresponds to the SiO<sub>2</sub> capping layer, equivalent in both samples). On one hand, the O 1s peak at the surface oxide is narrow and very well defined, peaking at around 532 eV. On the other hand, the O 1s peak from the NMLs is clearly shifted to lower energies and broadened, as the presence of Tb ions influences the oxygen binding energy. Although we do not

rule out the possibility of having Tb-O bonds, which are non-dominant and probably located only at the SiO<sub>2</sub>-Tb interface, the Si-O binding energy is definitely affected by the neighboring layers. Furthermore, the effect of Al can also be highlighted within the NML, which induces a more pronounced shift to lower energies and a larger broadening of the O 1s peak. In fact, this larger broadening can be ascribed to another contribution [see the deconvolution of the bottom spectrum in Fig. 3(d)], which could be related to Al-O, Tb-O, or a combination of both bonds (in agreement with EEL results that point to an intermixing of Al and Tb at the nanoscale).

Considering the cross-section ratio from each atomic element, we have evaluated the average composition of the layers from the relative areas. The deconvolution of the binding energy contributions was performed by fitting each of them to one or two pseudo-Voigt functions. In Table I, we present the values obtained for the two samples (with and without Al), together with the values from the top SiO<sub>2</sub> capping layer as a reference. It is interesting to notice that the SiO<sub>2</sub> on the surface (identical for both samples) is stoichiometric, within the uncertainty of our measurements (below 1%). The situation for the silicon oxide within the NMLs in the sample with Al is much different: the oxygen to silicon ratio is 2.7 (see Table I), which implies an oxygen excess of 23%. Due to the fact that the same process was employed for depositing SiO<sub>2</sub> both on the surface and within the multilayers, a stoichiometric composition of the layers is expected there also. Therefore, the layers containing Al and Tb might have captured this extra oxygen, in agreement with the observation of Al-O or Tb-O bonds in the photoemission spectra around the O 1s binding energy. Since aluminum is easily oxidized,<sup>27</sup> the most probable situation is having all the Al atoms in the form of alumina (Al<sub>2</sub>O<sub>3</sub>). In that case, and considering that the rest of the oxygen atoms are bound to Tb ones, we estimate that there will be a minimum of 45% of Tb atoms in the form of Tb<sub>2</sub>O<sub>3</sub>. Even though the possibility of having Al-Tb-O ternary compounds cannot be ruled out<sup>18,19</sup> because Al and Tb atoms are homogeneously distributed in the Al/Tb/Al stack (as observed by TEM measurements). For the sample with no Al, the situation is much different: the oxygen-to-silicon ratio is exactly 2.0, indicating that no extra oxygen is added to the Tb layers. Actually, Tb atoms are much less chemically reactive than aluminum, which makes their oxidation difficult, taking into account the low pressure employed during deposition. Thus, in this sample, only the Tb atoms at the interface might be bound to

TABLE I. XPS peak positions, integrated areas under the curves, and evaluated atomic compositions of the top SiO<sub>2</sub> layer, and the Tb/SiO<sub>2</sub> and Al-Tb/SiO<sub>2</sub> NMLs.

	SiO <sub>2</sub>		Tb/SiO <sub>2</sub>			Al-Tb/SiO <sub>2</sub>			
	Si 2p	O 1s	Si 2p	O 1s	Tb 4d	Si 2p	O 1s	Tb 4d	Al 2p
Peak position (eV)	103.3	531.8	101.5	530.8	147.4	100.7	528.8	146.2	72.5
Integrated area (a.u.)	2.46	31.94	5.76	29.01	2.22	102.0	531.0	4.46	30.20
Atomic content (%)	33	67	33	66	2	24	65	1	10

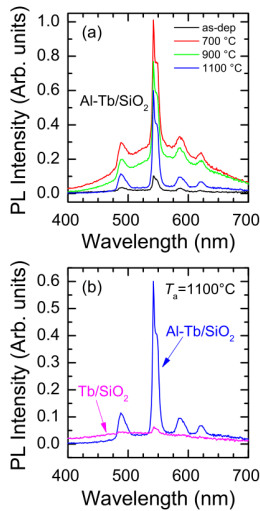


FIG. 4. (a) PL spectra corresponding to Al-Tb/SiO<sub>2</sub> NML samples, submitted to different annealing temperatures and excited at  $\lambda_{exc} = 325$  nm. (b) Comparison of the PL spectra acquired from the NML samples with and without the presence of Al, both annealed at 1100 °C. All the spectra have been normalized to the maximum PL emission (corresponding to sample Al-Tb/SiO<sub>2</sub> annealed at 700 °C), thus keeping their relative intensity.

oxygen atoms from the adjacent SiO<sub>2</sub> layers. In conclusion, the use of Al in the Al/Tb/Al stack favors the oxidation of the Tb ions, which may have an important impact on their emission properties.

### B. Optical emission of Al-Tb/SiO<sub>2</sub> films

The optical emission properties of the samples containing Al and submitted to different annealing temperatures were studied by means of PL by exciting the films with the  $\lambda = 325$  nm line of a continuous-wave He-Cd laser [see Fig. 4(a)]. For comparison purposes, we have also analyzed the samples with no Al content [see Fig. 4(b)]. Please note that the intensity from each sample has been normalized to the one with maximum emission (the sample with Al and annealed at 700 °C). There are some identical features that can be observed in all the spectra that evolve with the annealing temperature: four narrow and weak emissions and a broadband centered around 550 nm. On one hand, the former features, i.e., the narrow emission peaks, have their origin in the electronic transitions of the discrete energy levels from the Tb<sup>3+</sup> ions. In particular, the observed peak positions at 488, 542, 586, and 622 nm correspond to the <sup>5</sup>D<sub>4</sub>→<sup>7</sup>F<sub>*i*</sub> electronic transitions with *i* = 6, 5, 4, and 3, respectively (see for instance Ref. 28). On the other hand, the additional broadband contribution is ascribed to SiO<sub>2</sub> defects (oxygen vacancies and/or non-bridging chemical Si-O

bonds).<sup>12,13,16</sup> It is interesting to follow the intensity evolution of these two different contributions, as observed in Fig. 4(a): the spectra show a sudden increase of the Tb-related emission after the annealing treatment, together with the increase of the defects band emission, favoring the optical activation of both Tb<sup>3+</sup> ions and matrix defects. This latter emission reaches its maximum at 700 °C and decreases again for higher  $T_{ann}$ , whereas the emission from the Tb<sup>3+</sup> ions is kept almost constant for the three different annealing treatments. This evolution is linked to the nature of these two contributions to the PL spectra, and both the absorption and emission processes should be taken into account.

As we demonstrated by XPS, our SiO<sub>2</sub> films are stoichiometric, but most likely they do not reach the quality levels of thermal SiO<sub>2</sub>. Therefore, we expect deep defect levels in our material, an assumption that is supported by the observed broad emission in the spectra. This emission is coming from the absorption (and thus excitation) and subsequent relaxation of defect states, and provides no emission when the amount of non-radiative paths is too large (as happens in the as-deposited sample); on the contrary, the emission enhancement at higher temperatures is due to a reduction of non-radiative defects while activating radiative ones (which, as observed by PL, requires high annealing temperatures), reaching a maximum emission at 700 °C; higher annealing temperatures improve the long-range atomic ordering of the oxide matrix (i.e., its structural arrangement),<sup>14</sup> consequently reducing the overall presence of defects and thus decreasing their emission. The situation is slightly different for Tb<sup>3+</sup> ions emission: in this case, in order to excite optically active Tb<sup>3+</sup> ions, the excitation energy must match the transition energy involving the <sup>3</sup>D<sub>4</sub> electronic level (i.e., resonant conditions). When the exact matching by incident radiation is not possible, the latter may still be absorbed by the matrix and partially transferred to the Tb<sup>3+</sup> ions (into the <sup>5</sup>D<sub>4</sub> electronic level) with the consequent radiative decay to the <sup>7</sup>F<sub>*i*</sub> levels that gives rise to the observed PL. As no apparent energy level is found in Tb<sup>3+</sup> species (see Ref. 29), the simple observation of those narrow emissions evidences that the 325 nm excitation (~3.8 eV) accomplishes the second case, i.e., a SiO<sub>2</sub> matrix absorption followed by energy transfer to Tb<sup>3+</sup> ions, and a consequent radiative decay. Therefore, the incoming photons on such a material structure are expected to excite the intra-band gap (defects-induced) electronic levels within the host SiO<sub>2</sub> matrix and transfer that energy to Tb<sup>3+</sup> ions.<sup>30</sup> Regarding the temperature evolution of the Tb-related PL emission intensity, annealing properly rearranges the local environment of Tb, so that the REs become optically active; indeed, this is the reason why a huge emission increase is observed after annealing at 700 °C. Higher annealing temperatures do not substantially improve the O environment of Tb, and hence no further Tb-related PL intensity increase takes place, although, as already discussed, they contribute to the reduction of the emission from SiO<sub>2</sub> defects.

When comparing the emission of samples annealed at 1100 °C with and without Al [see Fig. 4(b)], one can observe a dramatic intensity reduction from Tb-related emission, which evidences that Al doping induces a higher optical activation of Tb<sup>3+</sup> ions. Indeed, this pattern is repeated under all

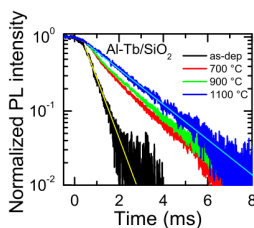


FIG. 5. Normalized time-resolved PL of Al-Tb/SiO<sub>2</sub> samples at 542 nm, both as-deposited and annealed at different temperatures.

other annealing conditions (not shown). Actually, XPS analysis has demonstrated that the presence of Al precipitates the NML oxidation, having an extra 23% of O atoms inside the Al-Tb layers. Thus, the inclusion of Al atoms contributes to the oxidation of the Tb atoms environment, some of them easily reaching the 3+ oxidation state while at the same time contributing to improve the stoichiometry (and the quality) of the deposited SiO<sub>2</sub>. These facts are supported by the PL observations, which evidence that the presence of Al contributes to improve the optical activation of Tb<sup>3+</sup> ions, whereas a high  $T_{\text{ann}}$  notably reduces the emission from the matrix defects (also compatible with a better SiO<sub>2</sub> quality).

To complement the information provided by the spectrally resolved PL measurements, the emission dynamics of the samples was also investigated by analyzing the PL emission decay, monitoring the  ${}^3\text{D}_4 \rightarrow {}^7\text{F}_5$  transition ( $\lambda = 542$  nm). For this, the He-Cd laser was mechanically square-pulsed with a period of 20 ms, allowing for a time resolution of around 0.3 ms. In Fig. 5, the PL emission decay curves of the Al-Tb/SiO<sub>2</sub> samples are displayed just after the laser excitation is cut, for the different annealing temperatures. Please note that the monitored wavelength presents a high contribution of defects to PL emission; however, since defects in SiO<sub>2</sub> typically exhibit decay times faster than 100 ns (because of high population of non-radiative centers),<sup>31</sup> the following analysis on the (slower-lifetime) Tb-related PL decay is not affected by this occurrence. In the case of the as-deposited sample, a single exponential function was employed to adjust the data, obtaining a good fit that revealed a decay time of  $\tau_{\text{decay}} = 0.5$  ms. This value, although in good agreement with reported values in the literature on similar systems, is still too close to the time resolution of the setup, so that further conclusions are prevented in this work. After the annealing process, the measurements exhibit a different behavior consisting of two different decay times, a first fast decay ( $\tau_f$ ) followed by a slower one ( $\tau_s$ ), as can be observed for the samples with  $T_{\text{ann}} = 700$  and  $900$  °C. A two-exponential fit was used to estimate both lifetime values, thus obtaining values slightly longer than for the as-deposited sample (and markedly longer than the setup time resolution),  $\tau_f = 1.2$  ms and  $\tau_s = 1.7$  ms. Finally, emission corresponding to the sample annealed at the highest temperature,  $T_{\text{ann}} = 1100$  °C, exhibits only one decay time, which corresponds to the longest ( $\tau_s$ ) one observed in the intermediate-temperature annealed samples. It should be

mentioned here that the sample without Al (not shown in the figure) presented a decay time of around 0.6 ms, similar to the as-deposited sample; this indicates that the contribution of Al to Tb<sup>3+</sup> emission only takes place after the annealing treatment.

The two different decay times revealed at low annealing temperatures (700 and 900 °C), associated with the recombination lifetime within the rare earth ions, indicate that there are Tb<sup>3+</sup> ions in two different optically active spatial configurations.<sup>24,32</sup> As the annealing temperature increases, the faster decay time becomes longer until it reaches the slower one and only one decay time is observed ( $\tau_s \approx 1.7$  ms). In fact, different recombination lifetimes are ascribed to a different combination of radiative and non-radiative processes taking place within the material system (Tb ions and matrix defects); in this frame, the increase of  $\tau_{\text{decay}}$  after increasing the annealing temperature can be associated with a reduction of non-radiative processes.<sup>33</sup> Actually, Tb<sup>3+</sup> requires a C<sub>4v</sub> symmetry (a TbO<sub>6</sub> conformation) to be optically active, as in the case of other RE ions in the same oxidation state (such as Er<sup>3+</sup> or Yb<sup>3+</sup>).<sup>34–36</sup> This occurrence, bearing in mind the multilayer structure, can take place at the interfaces between the Al/Tb mixed stack and the SiO<sub>2</sub> sublayers, although the possible diffusion of oxygen from the SiO<sub>2</sub> sublayers to the Al/Tb stack cannot be discarded; this argument also holds for the samples containing no Al. The fact that Tb<sup>3+</sup> ions are very sensitive to the presence of surrounding defects constitutes a drawback for their emission. Both the high temperature annealing and the introduction of Al in the samples modify the environment of Tb<sup>3+</sup> ions by eliminating defects (mainly oxygen vacancies), generating non-bridging oxygen bonds (Al-O), and reducing the Tb-Tb cross-relaxation processes,<sup>28</sup> similarly to the case of Eu<sup>3+</sup> in Al<sub>2</sub>O<sub>3</sub>-SiO<sub>2</sub> systems,<sup>37</sup> consequently increasing the luminescence lifetime and thus the total emission yield from Tb<sup>3+</sup> ions. This frame is also in agreement with the higher rate of active RE under the presence of Al, as suggested by the larger excitation cross-section of the Al-Tb/SiO<sub>2</sub> multilayers. Indeed, the latter statement can be correlated to the binding structure modification undergone by Tb-doped NML when introducing Al, as supported by the XPS analysis.

The discussion and stated hypotheses within the present work, although in reasonable agreement with the presented experimental results, should be supported by a further analysis focusing on the local environment of Tb<sup>3+</sup> ions. Nevertheless, we have shown here that, by using the EBE technique to directly deposit Tb and SiO<sub>2</sub> multilayers, we can achieve active Tb<sup>3+</sup> ions within a SiO<sub>2</sub> matrix, and that we can strongly enhance their emission yield by introducing Al atoms in a controlled manner within the multilayer system. As a consequence, this system can be considered for future optoelectronic applications requiring visible light emission (such as light-emitting devices) or discrete and coherent emission energies (RE-based lasing systems).

#### IV. CONCLUSIONS

Al-Tb/SiO<sub>2</sub> multilayers were fabricated by means of electron beam evaporation by alternatively evaporating

nanometric SiO<sub>2</sub> and sandwiching the Tb layer between two Al layers. The resulting nanostructures were submitted to different annealing temperatures. A structural characterization of the samples was carried out via TEM, which confirmed the deposited NML structure. A chemical analysis of the composition at the nanoscale by means of HAADF and EELS showed that Tb and Al thin layers are homogeneously mixed and adequately separated by the SiO<sub>2</sub> layers. XPS measurements were also performed on samples with and without Al, indicating that the presence of Al modifies the binding structure of O 1s orbitals, probably inducing a rearrangement of the Tb oxygen environment. The PL spectra of all samples exhibit narrow Tb<sup>3+</sup> ions- and broad defects-related emission, whose relative yield varies with the temperature of the post-deposition annealing treatment and the presence of Al. A study of the PL decay time showed two different values in annealed samples containing Al,  $\tau_f = 1.2$  ms and  $\tau_s = 1.7$  ms, which evidences that two different atomic arrangements might exist surrounding the RE ions. The above mentioned results were discussed in terms of the environment of the REs under different conditions: the introduction of Al generates Al-O bonds when the NML is annealed, eliminating the bridging oxygen atoms and enhancing the Tb<sup>3+</sup> optical activation, consequently improving the PL emission intensity of REs by more than one order of magnitude. The above discussed experimental results evidence that the combination of electron beam evaporation with a multilayer approach becomes an appropriate method for the fabrication of luminescent Al-Tb/SiO<sub>2</sub> NMLs, which can be applied in the field of visible-light emission optoelectronics and lasing.

#### ACKNOWLEDGMENTS

This work was financially supported by the Spanish Ministry of Economy and Competitiveness (Project Nos. TEC2012-38540-C02-01, CSD2009-2013, MAT-2010-16407, and MAT2013-41506). O.B. also acknowledges the subprogram “Ayudas para Contratos Predoctorales para la Formación de Doctores” from the Spanish Ministry of Economy and Competitiveness for economical support.

<sup>1</sup>O. Boyraz and B. Jalali, *Opt. Express* **12**, 5269–5273 (2004).

<sup>2</sup>G. T. Reed, G. Mashanovich, F. Y. Gardes, and D. J. Thomson, *Nat. Photonics* **4**, 518–526 (2010).

<sup>3</sup>D. J. Moss, R. Morandotti, A. L. Gaeta, and M. Lipson, *Nat. Photonics* **7**, 597–607 (2013).

<sup>4</sup>A. Rickman, *Nat. Photonics* **8**, 579–582 (2014).

<sup>5</sup>A. J. Steckl and R. Birkhahn, *Appl. Phys. Lett.* **73**, 1700 (1998).

<sup>6</sup>A. J. Steckl, M. Garter, D. S. Lee, J. Heikenfeld, and R. Birkhahn, *Appl. Phys. Lett.* **75**, 2184 (1999).

<sup>7</sup>J. Heikenfeld, M. Garter, D. S. Lee, R. Birkhahn, and A. J. Steckl, *Appl. Phys. Lett.* **75**, 1189 (1999).

<sup>8</sup>Q. Wang and A. J. Steckl, *Appl. Phys. Lett.* **82**, 502 (2003).

<sup>9</sup>*Rare-Earth Doped III-Nitrides for Optoelectronic and Spintronic Applications*, Series: Topics in Applied Physics, Vol. 124, edited by K. P. O'Donnell and W. Dierolf (Springer, Dordrecht, The Netherlands, 2010).

<sup>10</sup>A. J. Kenyon, *Prog. Quantum Electron.* **26**, 225–284 (2002).

<sup>11</sup>S. Yerci, R. Li, and L. Dal Negro, *Appl. Phys. Lett.* **97**, 081109 (2010).

<sup>12</sup>M. Kulakci and R. Turan, *J. Lumin.* **137**, 37 (2013).

<sup>13</sup>A. Podhorodecki, L. W. Golacki, G. Zatoryb, J. Misiewicz, J. Wang, W. Jadwisieniczak, K. Fedus, J. Wojcik, P. R. J. Wilson, and P. Mascher, *J. Appl. Phys.* **115**, 143510 (2014).

<sup>14</sup>A. Podhorodecki, G. Zatoryb, J. Misiewicz, J. Wojcik, P. R. J. Wilson, and P. Mascher, *Nanotechnology* **23**, 475707 (2012).

<sup>15</sup>Y. Berencén, R. Wutzler, L. Rebolle, D. Hiller, J. M. Ramírez, J. A. Rodríguez, W. Skorupa, and B. Garrido, *Appl. Phys. Lett.* **103**, 111102 (2013).

<sup>16</sup>L. Rebolle and W. Skorupa, *Rare-Earth Implanted MOS Devices for Silicon Photonics*, Springer Series in Materials Science (Springer, 2010).

<sup>17</sup>W. Chen, R. Samynaiken, and Y. Huang, *J. Appl. Phys.* **88**, 1424 (2000).

<sup>18</sup>G. G. Vienne, W. S. Brocklesby, R. S. Brown, Z. J. Chen, J. D. Minelly, J. E. Roman, and D. N. Payne, *Opt. Fiber Technol.* **2**, 387 (1996).

<sup>19</sup>G. Alombert-Goget, N. Gaumer, J. Obriot, A. Rammal, S. Chausseant, A. Monteil, H. Portales, A. Chiasera, and M. Ferrari, *J. Non-Cryst. Solids* **351**, 1754 (2005).

<sup>20</sup>A. T. Fromhold, Jr. and W. D. Foster, *Electrocomponent Sci. Technol.* **3**, 51–62 (1976).

<sup>21</sup>M. Yoshihara, A. Sekiya, T. Morita, K. Ishii, S. Shimoto, S. Sakai, and Y. Ohki, *J. Phys. D: Appl. Phys.* **30**, 1908–1912 (1997).

<sup>22</sup>J. M. Ramírez, J. Wojcik, Y. Berencén, A. Ruiz-Cardad, S. Estradé, F. Peiró, P. Mascher, and B. Garrido, *Nanotechnology* **26**, 085203 (2015).

<sup>23</sup>E. M. Yeatman, M. M. Ahmad, O. McCarthy, A. Martucci, and M. Guglielmi, *J. Sol-Gel Sci. Technol.* **19**(1–3), 231–236 (2000).

<sup>24</sup>A. J. Silversmith, N. T. T. Nguyen, B. W. Sullivan, D. M. Boye, C. Ortiz, and K. R. Hoffman, *J. Lumin.* **128**, 931–933 (2008).

<sup>25</sup>J. M. Ramírez, Y. Berencén, L. López-Conesa, J. M. Rebled, F. Peiró, and B. Garrido, *Appl. Phys. Lett.* **103**, 081102 (2013).

<sup>26</sup>O. Blázquez, J. M. Ramírez, J. López-Vidrier, Y. Berencén, S. Hernández, P. Sanchis, and B. Garrido, *Proc. SPIE* **9520**, 95200K-1 (2015).

<sup>27</sup>N. Mañti, A. Biswas, R. B. Tokas, D. Bhattacharyya, S. N. Jha, U. P. Deshpande, U. D. Barve, M. S. Bhatia, and A. K. Das, *Vacuum* **85**, 214 (2010).

<sup>28</sup>F. S. Richardson, *Chem. Rev.* **82**, 541 (1982).

<sup>29</sup>J. Vuojola and T. Soukka, *Methods Appl. Fluoresc.* **2**, 012001 (2014).

<sup>30</sup>C. Armellini, M. Ferrari, M. Montagna, G. Pucker, C. Bernard, and A. Monteil, *J. Non-Cryst. Solids* **245**, 115–121 (1999).

<sup>31</sup>K. S. Min, K. V. Shcheglov, C. M. Yang, H. A. Atwater, M. L. Brongersma, and A. Polman, *Appl. Phys. Lett.* **69**, 2033 (1996).

<sup>32</sup>V. H. Romero, E. De la Rosa, T. López-Luke, P. Salas, and C. Angeles-Chavez, *J. Phys. D: Appl. Phys.* **43**, 465105 (2010).

<sup>33</sup>K. S. Seol, T. Karasawa, Y. Ohki, H. Nishikawa, and M. Takiyama, *Microelectron. Eng.* **36**, 193 (1997).

<sup>34</sup>A. J. Steckl, J. Heikenfeld, D. S. Lee, and M. Garter, *Mater. Sci. Eng. B* **81**, 97–101 (2001).

<sup>35</sup>M. Ishii, S. Komuro, T. Morikawa, and Y. Aoyagi, *J. Appl. Phys.* **89**, 3679 (2001).

<sup>36</sup>M. Llusà, J. López-Vidrier, A. Antony, S. Hernández, B. Garrido, and J. Bertomeu, *Thin Solid Films* **562**, 456 (2014).

<sup>37</sup>M. Nogami and Y. Abe, *J. Non-Cryst. Solids* **197**, 73 (1996).



ISSN 1862-6300  
 Phys. Status Solidi A  
 215 - No. 3 February 7  
 (2018)

**physica**  
**status**  
**solidi**  
**a**

www.pss-a.com

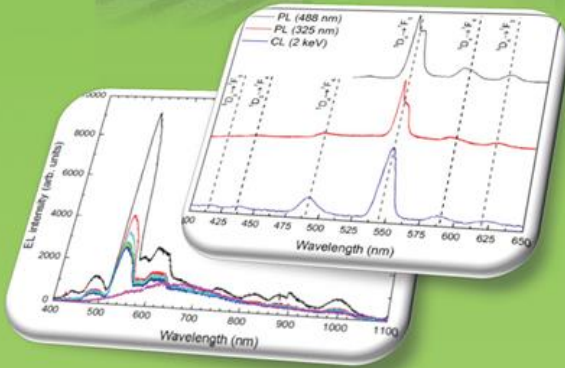
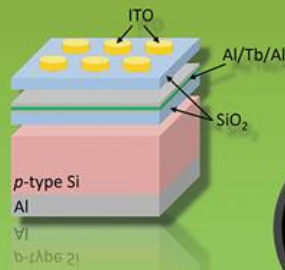
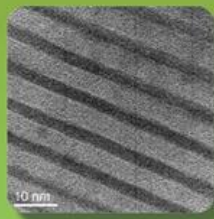
applications and materials science

**3**  
**2018**

Special Issue:

Nanoparticles in Dielectric Matrix: From Synthesis to Device  
 Applications for Photonics, Electronics, and Biosensing

Guest-edited by Simona Boninelli



WILEY-VCH

## Green Electroluminescence of Al/Tb/Al/SiO<sub>2</sub> Devices Fabricated by Electron Beam Evaporation

Juan Luis Friero, Oriol Blázquez, Julian López-Vidrier, Lluís López-Conesa, Sònia Estradé, Francesca Peiró, Jordi Ibáñez, Sergi Hernández,\* and Blas Garrido

In this work, the fabrication and the structural, optical and electrical properties of Al-Tb/SiO<sub>2</sub> nanomultilayers have been studied. The nanomultilayers were deposited by means of electron beam evaporation on top of p-type Si substrates. Optical characterization shows a narrow and strong emission in the green spectral range, indicating the optical activation of Tb<sup>3+</sup> ions. The electrical characterization revealed conduction limited by the electrode, although trapped-assisted mechanisms can also contribute to transport. The electroluminescence analysis revealed also emission from Tb<sup>3+</sup> ions, a promising result to include this material in future optoelectronics applications as integrated light-emitting devices.

have been widely studied in the last two decades due to their narrow and intense luminescence, as a potential alternative for more efficient devices than LEDs.<sup>[4–6]</sup>

Rare earth elements have their 4f electronic shell partially filled, and when they are optically active, they usually have an oxidation state +3 due to the loss of one 4f electron and the two 6s electrons. These elements have luminescent properties resulting from the intra-4f transitions (almost independent of the matrix) or 5d-to-4f ones (sensitive to the matrix).<sup>[7]</sup>

Erbium has been studied as dopant of different films like silica (SiO<sub>2</sub>), yielding emissions in the infrared part of the spectrum (≈1535 nm) when in an Er<sup>3+</sup> oxidation state, which makes it very useful for optical fiber telecommunication systems.<sup>[8,9]</sup> Other REs have been researched for their emission in the visible range, such as Ce<sup>3+</sup>,<sup>[8]</sup> Tb<sup>3+</sup>,<sup>[10–11]</sup> and Eu<sup>3+</sup>,<sup>[12]</sup> in the blue (460 nm), green (543 nm), and red (615 nm) parts of the spectra, respectively. In the **Figure 1**, the electronic levels, energies and transitions for a particular RE species (Tb<sup>3+</sup> ions as it will be later studied in this work<sup>[13]</sup>) are presented.

Fabrication of these materials has been exploited through many different techniques, such as plasma-enhanced chemical vapor deposition,<sup>[11]</sup> ion implantation,<sup>[14]</sup> liquid source chemical vapor deposition,<sup>[15]</sup> magnetron sputtering,<sup>[16]</sup> and sol-gel.<sup>[17]</sup> Some other techniques have also been attempted, but are less commonly employed, like atomic layer deposition.<sup>[18]</sup>

Following the approach to new RE light emitters, in this work it is described the fabrication and characterization of nanomultilayered (NML) structures composed of SiO<sub>2</sub>, Al and Tb<sup>3+</sup> ions, by means of electron beam evaporation (EBE). In a previous work, different combinations of these layers have been tested aiming at the best layer configuration that exhibits stronger emission.<sup>[19]</sup> The optical properties of the chosen configuration were studied by photoluminescence (PL) in samples annealed at different temperatures.<sup>[20]</sup>

The films employed in this work were deposited by using EBE, considering the optimum nanomultilayered structure as Al-Tb/SiO<sub>2</sub>, on top of a p-type Si substrate. The films used for the structural and optical characterization consist of 15 × Al/Tb/Al/SiO<sub>2</sub> layers, ending with a SiO<sub>2</sub> layer that serves as protection. For the electrical characterization, 5 × Al/Tb/Al/SiO<sub>2</sub> layers were fabricated, also on a p-type Si substrate, adding a full area bottom electrode of Al and top contact of indium tin oxide (ITO). The ITO contact also allows for electro-optical characterization, as it is a

### 1. Introduction

The invention of LEDs has opened the door for the field of optoelectronics, as the use of semiconductors allows scaling these light sources to the sizes of microelectronic devices employed today. Optoelectronic devices are designed to employ light in combination with (or instead of) electric currents, which introduces many advantages: separation of electronic devices (thus enabling the optimization of the chip layout), reduction of electromagnetic interference, cable length and weight, sustenance of precise signal timing, reduction of interconnect densities and energy saving (thanks to lower heat losses).<sup>[1–3]</sup>

These new devices need to be able to operate in concert with current electronic devices based on silicon technology, which requires of Si-based light collectors, transducers between electric and optical signals, light waveguides, and light emitters. For the latter, semiconductor materials doped with rare earth (RE) ions

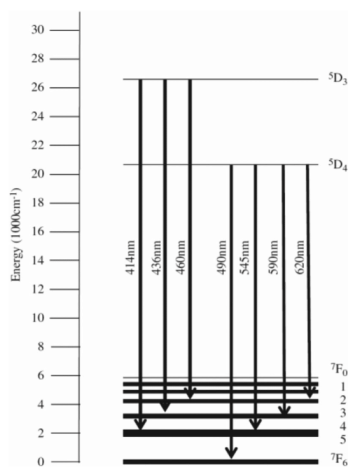
J. L. Friero, O. Blázquez, Dr. J. López-Vidrier, Dr. L. López-Conesa, Dr. S. Estradé, Prof. F. Peiró, Dr. J. Ibáñez, Dr. S. Hernández, Prof. B. Garrido  
MIND-IN<sup>2</sup>UB, Department of Engineering: Electronics Universitat de Barcelona, Martí i Franquès 1, E-08028 Barcelona, Spain  
E-mail: shernandez@ub.edu

Dr. J. López-Vidrier  
IMTEK, Faculty of Engineering, Albert-Ludwigs-University, Georges-Köhler-Allee 103, D-79110 Freiburg, Germany

Dr. J. Ibáñez  
Institute of Earth Sciences Jaume Almera ICTJA-CSIC, Lluís Soler i Sabarís s/n, E-08028 Barcelona, Catalonia, Spain

The ORCID identification number(s) for the author(s) of this article can be found under <https://doi.org/10.1002/pssa.201700451>.

DOI: 10.1002/pssa.201700451



**Figure 1.** Electronic transitions of  $\text{Tb}^{3+}$ , taken from Ref. [13].

transparent conducting oxide (TCO). The average composition of the nanomultilayers was assessed by using X-ray photoelectron spectroscopy (XPS). Different techniques were employed to determine the optical properties of the Tb-films, such as PL and cathodoluminescence (CL). The electrical properties were studied through the different  $I(V)$  curves obtained. Finally, the electroluminescence (EL) of the NMLs was also measured in the accumulation regime. The results suggest the possibility of employing EBE for the fabrication of RE-doped materials that can be introduced into devices for optoelectronic applications in the future.

## 2. Experimental Section

Different combinations in nanomultilayer structures for  $\text{SiO}_2$ , Al and Tb were tested in a previous study, in order to achieve the optimal configuration for the optical activation of the  $\text{Tb}^{3+}$  ions.<sup>[19,20]</sup> All test samples and the ones here employed were fabricated by electron beam evaporation, and deposited on top of p-type Si substrates, which were cleaned with acetone, isopropyl alcohol, ethanol, and de-ionized water, and agitated ultrasonically during each process, before being introduced into the chamber.

The equipment employed for the deposition is a PFEIFFER VACUUM Classic 500 chamber with a Ferrotec GENIUS electron beam controller and a Ferrotec CARRERA high-voltage power supply. The base pressure in the chamber was  $1.6 \times 10^{-6}$  mbar and the temperature of the substrate was kept at  $100^\circ\text{C}$ . Acceleration voltages were 6 kV for  $\text{SiO}_2$  and Tb, and 10 kV for Al, with deposition rates of 1.0, 0.2, and  $0.2 \text{ \AA s}^{-1}$ , respectively.

The samples for the structural and optical characterization consisted of 15 stacks of Al/Tb/Al/ $\text{SiO}_2$ , with two 10-nm layers of  $\text{SiO}_2$  before and after them to prevent any atomic diffusion from or to the nanomultilayers. The nominal thickness of the Al, Tb,

and  $\text{SiO}_2$  layers were 0.8, 0.4, and 3 nm, respectively (see Figure 2 (a)). After deposition, the samples were submitted to an annealing process at  $1100^\circ\text{C}$  in  $\text{N}_2$  atmosphere for 1 h. An identical sample was also fabricated but with no Al, in order to observe the influence of this element. In the Figure 2(b) the cross-section of the nanomultilayers acquired by transmission electron microscopy (TEM) is shown, where the nanometric structure can be clearly seen: the bright layers with a thickness of 5 nm correspond to  $\text{SiO}_2$ , whereas the dark ones, with a thickness of 3 nm, are a stack of Al-Tb, as demonstrated by electron energy loss spectroscopy.<sup>[20]</sup> As revealed by the TEM image, this stack serves as delta doping system of Tb in a  $\text{SiO}_2$  matrix, allowing for obtaining nanometric separation between the different Tb layers, while isolating them in the growth direction and thus reducing possible clustering effects.

For the electrical and electro-optical characterization, new samples were fabricated consisting of 5 stacks of Al/Tb/Al/ $\text{SiO}_2$ , also annealed at  $1100^\circ\text{C}$  in  $\text{N}_2$  atmosphere for 1 h. After annealing, indium tin oxide (ITO) electrodes were deposited on top of the multilayers using a shadow mask, with circular shape with a radius of  $200 \mu\text{m}$ , and subsequently annealed at  $600^\circ\text{C}$  in  $\text{N}_2$  atmosphere for 1 h. Finally, a full area Al metallization was performed on the backside of the Si substrate for defining the bottom contact. This structure is schematically shown in Figure 2(c).

To determine the overall composition of the deposited films, XPS measurements were carried out using a PHI 5500 Multitechnique System, thus obtaining information regarding the Al influence on the Tb-related binding formation.

Photoluminescence measurements with two different excitation energies were employed for determining the optically active emission from  $\text{Tb}^{3+}$  ions. The 325-nm line from a HeCd laser or the 488-nm line from an  $\text{Ar}^+$  laser were used for the excitation of the  $\text{Tb}^{3+}$  ions. In the case of the HeCd laser, the spectra were analyzed using a Horiba Jobin Yvon LabRAM HR spectrometer, whereas the spectral analysis exciting with the  $\text{Ar}^+$  laser was done using a GaAs photomultiplier tube (PMT) coupled to a monochromator in a lock-in configuration. For the acquisition of CL spectra, a JEOL JSM-7100F scanning electron microscope coupled to a monochromator and a GaAs PMT was employed. In order to avoid damage on the surface, a defocused electron beam of  $80 \mu\text{A}$ , accelerated at 2 keV, was used for the measurements.

Electrical characterization of the samples was done by two contact measurements with an Agilent B1500 semiconductor device analyzer and a Cascade Microtech Summit 11000 probe station using a Faraday cage. The back-contact was grounded through the chuck, whereas the top ITO-contact was swept from  $-15$  to  $15 \text{ V}$ , with steps of  $50 \text{ mV s}^{-1}$ .

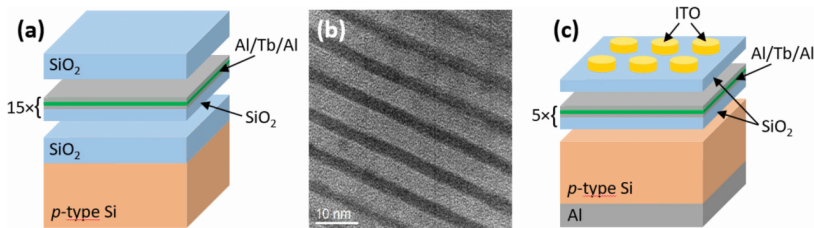
Emission from the sample obtained through electroluminescence (EL) was collected with a Seiva 888 L microscope. Whereas the integrated emission was recorded using the same GaAs PMT employed in the PL measurements, the spectral emission was captured by means of Princeton Instruments LN-cooled charge-coupled device via a 1/4m Oriel monochromator.

## 3. Results and Discussion

Measurements performed by XPS allowed determining the composition and the effect of the presence of Al atoms



### 3. Si-Based Materials for Optoelectronics and Resistive Switching



**Figure 2.** a) Sketch of the nominal deposited structure for structural and optical characterization purposes. b) HRTEM image of the deposited nanomultilayer structure. c) Sketch of the nominal deposited devices employed in the electrical and electro-optical characterization.

surrounding the Tb ions. In **Table 1** we have summarized the obtained results. Whereas the sample with no Al showed stoichiometric  $\text{SiO}_2$ , the sample containing Al showed an increase of the oxygen content. Thus, this observation implies that, on one hand, the Tb ions in the sample with no Al may be bound to other Tb ions or dangling bonds from  $\text{SiO}_2$ , and, on the other hand, the sample with Al exhibits an oxygen excess that should be located in the Al/Tb/Al stack (the  $\text{SiO}_2$  in the whole sample is stoichiometric). As aluminium is much more chemically reactive than terbium, the oxygen excess in the sample with Al is more likely to be bound to Al forming alumina ( $\text{Al}_2\text{O}_3$ ). In order to have a minimum quote of the amount of Tb which is oxidized (i.e., prompt to be optically active), we considered that: (i) all the Si atoms are bound to O atoms, thus forming  $\text{SiO}_2$ ; (ii) all the Al atoms are in the form of alumina ( $\text{Al}_2\text{O}_3$ ); and (iii) the remaining O content is bound to Tb atoms. Under these assumptions, and considering the atomic content in the Al/Tb/Al/ $\text{SiO}_2$  sample (considering the whole film), we found that at least 45% of the Tb ions are in the form of  $\text{Tb}_2\text{O}_3$ . Thus, the addition of Al contributes to the oxidation of Tb ions, which should also influence their emission properties.<sup>[20]</sup>

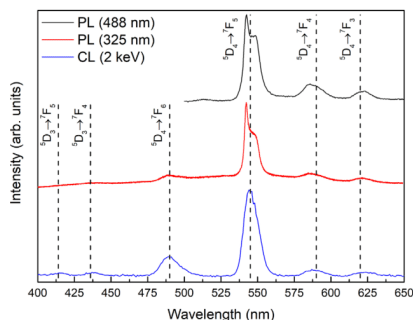
Optical emission of the Al/Tb/Al/ $\text{SiO}_2$  structure was first characterized by means of PL. Two different excitation lines were employed: a non-resonant excitation using  $\lambda = 325$  nm and a resonant excitation with  $\lambda = 488$  nm (see **Figure 3**).<sup>[12]</sup> The spectrum acquired under non-resonant conditions shows peaks at 489, 542, 584, and 621 nm; under resonant excitation, the same emission features were detected but the one at 489 nm, as it is close to the excitation wavelength. These emission bands are a consequence of the intra-4f electronic radiative transitions within  $\text{Tb}^{3+}$  ions ( $^3\text{D}_4 \rightarrow ^7\text{F}_j$ , with  $J = 6, 5, 4,$  and  $3$ ).<sup>[7,12]</sup>

Similar emission to the PL one was obtained when performing CL measurements by exciting the sample with an electron

beam of 2 keV, which allows an effective direct excitation of the Tb species by impact excitation. **Figure 3** shows the emission spectrum collected with the characteristic peaks of  $\text{Tb}^{3+}$  at 489, 544, 587, and 624 nm. These emission bands correspond to the  $^5\text{D}_4 \rightarrow ^7\text{F}_j$  transitions as previously described. Blue emission bands also appear in the CL spectrum, corresponding to  $^5\text{D}_3 \rightarrow ^7\text{F}_j$  ( $J = 5$  and  $4$ ) transitions, with peaks at 415 and 437 nm. All these results are in good agreement with others found in the literature (see Ref. [21]).

The most intense emission at 544 nm in both PL and CL spectra corresponds to the green visible range, and it is split into two peaks, as a consequence of the Stark effect due to the local electric field.<sup>[7]</sup> These results evidence that the employed deposition technique and methodology, that takes advantage of the nanomultilayered deposition of different materials, produce optically active  $\text{Tb}^{3+}$  species, emitting in the green spectral region.

The electrical properties of the fabricated devices were analyzed by acquiring the  $I(V)$  curves, grounding the Al bottom electrode through the chuck whereas the ITO contact on top was swept in two regimes: accumulation (negative bias) and inversion (positive bias). The obtained curves for each regime



**Figure 3.** Normalized PL and CL measurements of the Al/Tb/Al/ $\text{SiO}_2$  structure.

**Table 1.** XPS evaluated atomic compositions for the Tb/ $\text{SiO}_2$  and Al/Tb/Al/ $\text{SiO}_2$  NMLs.

	Atomic content (%)			
	Si	O	Tb	Al
Tb/ $\text{SiO}_2$	33	65	2	–
Al/Tb/Al/ $\text{SiO}_2$	24	65	1	10

are displayed in **Figure 4**. The devices can reach intensities in the order of  $10^3 \mu\text{A}$  at  $-15 \text{ V}$  applied voltage. Higher voltages were not sustained by the ITO contacts as the current increased to mA. The curves show an almost symmetric behavior for both regimes, indicating non-rectifying characteristics.

As shown by structural characterization, the device is composed by layers of  $\text{SiO}_2$  and  $\text{Al}_2\text{O}_3$ , for which an insulating behavior, that is, limited movement of charges, is expected. Thus, considering the different transport mechanisms taking place in dielectric materials, we have assessed the electrical conduction of our devices. We found that the best agreement to the experimental data was obtained when considering an electrode-limited conduction mechanism based on Schottky emission. Thermionic emission of electrons is achieved when a potential barrier formed at a metal-insulator (or semiconductor-insulator) interface is overcome. Applying an external electric field the barrier can be lowered, easing the emission. This process can be modeled as:

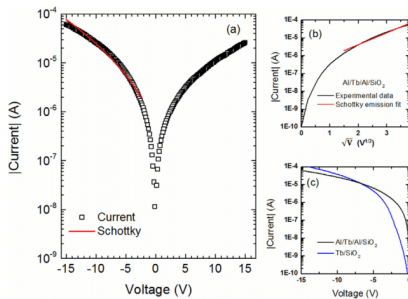
$$J_{\text{Schottky}} = \frac{4\pi m^* q}{h^3} k_B^2 T^2 \exp\left(-\frac{\phi_B}{k_B T}\right) \exp\left(\frac{\beta}{k_B T} E^{1/2}\right), \quad (1)$$

where  $\phi_B$  is the potential barrier height (in eV),  $q$  the elementary charge,  $E$  the applied electric field,  $k_B T$  the thermal energy,  $h$  the Planck's constant,  $m^*$  the effective mass of electrons, and  $\beta$  is defined as:

$$\beta = \sqrt{\frac{q^3}{4\pi\epsilon_0\epsilon_r}}, \quad (2)$$

where  $\epsilon_0$  and  $\epsilon_r$  are the absolute and relative permittivity, respectively.<sup>[22]</sup>

The fitting of the experimental  $I(V)$  curve to the Schottky emission model yields a relative dielectric constant of the dielectric layer of  $\epsilon_r = 18.86$ . However, in general, the obtained



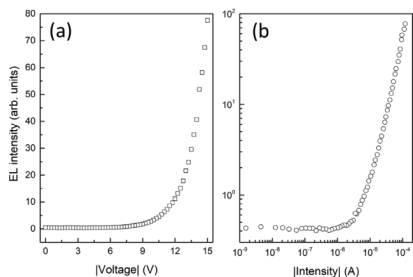
**Figure 4.** a)  $I(V)$  curve of a device containing Al/Tb/Al/SiO<sub>2</sub> multilayers, fit taking into account a Schottky-type conduction mechanism. b) Linearization for Schottky model in the range from  $-2.25$  to  $-15 \text{ V}$  for the device containing Al/Tb/Al/SiO<sub>2</sub> multilayers. c) Comparison of the  $I(V)$  curves of a devices containing Al/Tb/Al/SiO<sub>2</sub> and containing Tb/SiO<sub>2</sub> multilayers.

permittivity value may differ from the experimentally determined values by means of other optical techniques, due to the heterogeneity of our samples. Actually, Poole–Frenkel mechanism is also in good agreement to the experimental data, however with a large dielectric constant ( $\epsilon_r > 300$ ). The presence of Al in the structure is the probable cause for the Schottky emission fitting best the data, because electrons must overcome the potential barrier generated by the AlO<sub>x</sub> layers, as it has been previously reported.<sup>[23]</sup>

The  $I(V)$  characteristic of an identical device but without Al (Tb/SiO<sub>2</sub> multilayers) has also been analyzed. In **Figure 4(c)** there is a comparison of the current evolution at different voltages for both kinds of devices, with and without Al. It is evident that similar currents can be achieved for both devices, with and without Al in them, which implies that Al is not strongly influencing the electrical characteristic. Nevertheless, the sample with Al is slightly more resistive than the one with no Al (at high voltages), which could be due to either an increase of the total thickness or the fact that Al layers are presumably fully oxidized and thus become insulating (as we stated before). Another interesting feature is the fact that the slope of the two curves is also slightly different. Checking the conduction mechanisms, both curves follow a Schottky emission model at large voltages, but with a different dielectric constant: the sample without Al presents a dielectric constant of about 8.8, almost half of the one with Al. Consequently, Al is only slightly modifying the  $I(V)$  characteristic. Actually, the electrical conduction through the SiO<sub>2</sub> barriers should be identical for both devices, just being different through the Al/Tb/Al or Tb layers, which modifies the effective dielectric constant while keeping the conduction mechanism.

The application of an electrical current to the device can also produce the excitation of Tb<sup>3+</sup> ions, which can be de-excited by emitting their excess of energy in the form of light. No emission (or very weak) was found for the devices with no Al, which is in good agreement with PL measurements (see Refs. [19] and [20]). The total integrated emission collected by the PMT is shown in **Figure 5 (a)** and **5(b)** as a function of the applied voltage and current circulating through the device, respectively. We observed that the threshold voltage for emission to take place is 8.5 V, whereas higher voltages produce an almost exponential increase of the integrated EL. Looking at the behavior of the EL with the injected current, we observe that it increases linearly with a threshold current for emission at  $\approx 2 \mu\text{A}$ , which establishes a direct relation between impinging electrons and resulting emitted photons. Thus, the linearity of the EL with the injected current at high voltage and injection (i.e., above the excitation threshold) is suggesting that electrons with high kinetic energy are responsible for the excitation of the Tb optical centers. In fact, such electro-optical characteristics are typical of an excitation mechanism governed mainly by direct impact excitation; however, energy transfer mechanisms from the matrix can also be contributing.<sup>[22]</sup>

The spectral analysis of the EL is displayed in **Figure 6**. The spectra were acquired for 30 s, applying  $-100 \mu\text{A}$  at  $-18 \text{ V}$ , in the range of 400–1100 nm. The spectra exhibit peaks at 437, 483, 531, and 576 nm, over a broad low-intensity background. Whereas the former features correspond to  $^7\text{D}_4 \rightarrow ^7\text{F}_J$  transitions (with  $J = 6, 5, 4$ , and 3) from Tb<sup>3+</sup> ions, in good agreement to PL and CL measurements (see **Figure 3**), the latter band is probably

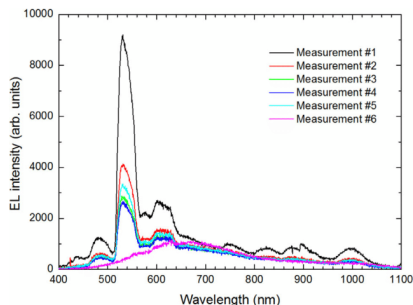


**Figure 5.** Integrated emission of the Al/Tb/Al/SiO<sub>2</sub> structure, obtained in accumulation, as a function of a) voltage and b) current, represented in absolute value.

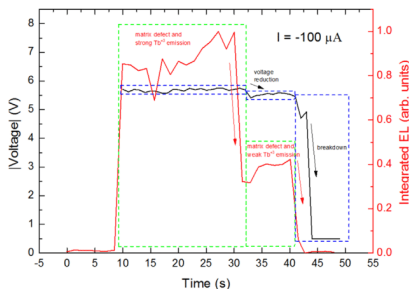
originated in the deep defects in either the SiO<sub>2</sub> or the ITO contact.

Another interesting observation is the fact that there is an intensity reduction of the Tb emission at successive measurements, reaching total quenching of Tb emission beyond the fifth one (please see spectrum labeled as measurement #6 in Figure 6, where only the background contribution is observed). In order to study this effect, the time evolution of the EL and the applied voltage has been simultaneously monitored at a constant current, this time using a different (i.e., pristine) device (but virtually identical). The results of this particular device are presented in Figure 7. One can observe that the EL emission starts practically simultaneously with the current injection, within the employed time resolution (voltage also increases). Both EL and applied voltage remain constant for about 30 s, immediately after which there is a slight reduction in the voltage, together with a sudden reduction of the EL emission. For longer times, the device becomes even more conductive, inducing the total quenching of the device EL emission.

This EL quenching and voltage reduction could be related to some atomic rearrangement after high electron flux is injected.



**Figure 6.** EL spectra successively acquired from the device at  $-100 \mu\text{A}$  and 30 s.



**Figure 7.** Evolution of voltage and EL as function of time for a device containing Al/Tb/Al/SiO<sub>2</sub> multilayers, at a constant current of 100  $\mu\text{A}$ .

Indeed, it has been observed in oxide matrices that, under certain excitation conditions, a displacement of oxygen atoms takes place.<sup>[24,25]</sup> This, in turn, induces both the creation of alternative (oxygen vacancies-related) conduction paths and the probable reduction of Tb-O bonds, the latter reducing the concentration of optically active centers. In this frame, an increase of the thermal budget could improve the stability of the Tb<sub>2</sub>O<sub>3</sub> phase, making this material a potential candidate for future optoelectronics applications, in particular as integrated light-emitting devices.

**4. Conclusions**

Al/Tb/Al/SiO<sub>2</sub> nanomultilayers have been fabricated by electron beam evaporation, alternatively depositing each layer. Optical characterization by means of PL and CL showed that Tb<sup>3+</sup> ions are optically active. Electrical characterization allowed inferring that the conduction mechanism governing the structure is a Schottky emission model, although thermal activated mechanisms cannot be discarded. The threshold voltage and current for EL to take place were determined by integrated EL measurement. As well, the spectral distribution of EL is related to a combination between Tb<sup>3+</sup> ions and matrix defect-related emission. The hereby presented results prove that the combination of electron beam evaporation and nanomultilayer structures are useful to obtain luminescent Al/Tb/Al/SiO<sub>2</sub> light-emitting systems.

**Acknowledgements**

This work was financially supported by the Spanish Ministry of Economy and Competitiveness (TEC2016-76849-C2-1-R and MAT2015-71035-R). O.B. also acknowledges the subprogram "Ayudas para Contratos Predoctorales para la Formación de Doctores" from the Spanish Ministry of Economy and Competitiveness for economical support.

**Conflict of Interest**

The authors declare no conflict of interest.

### Keywords

electron beam evaporation, luminescence, nanomultilayers, rare earth ions, terbium

Received: June 30, 2017

Revised: September 1, 2017

Published online:

- [1] Efficient blue light-emitting diodes leading to bright and energy-saving white light sources, The Nobel Prize in Physics 2014 – Advanced Information, [online], Nobel Media AB, Available: [http://www.nobelprize.org/nobel\\_prizes/physics/laureates/2014/advanced.html](http://www.nobelprize.org/nobel_prizes/physics/laureates/2014/advanced.html), 2014; Accessed: 10/06/2017.
- [2] K. D. Hirschman, L. Tsybeskov, S. P. Dutttagupta, P. Fauchet, *Nature Photonics* **2010**, *4*, 518.
- [3] G. T. Reed, G. Mashanovich, F. Y. Gardes, D. J. Thomson, *Nat. Photonics* **2010**, *4*, 518.
- [4] S. Yerci, R. Li, L. Dal Negro, *App. Phys. Lett.* **2010**, *97*, 081109.
- [5] A. J. Kenyon, *Prog. Quantum Electron.* **2002**, *26*, 225.
- [6] S. Jiang (Ed.), Proceedings of the SPIE VII Conference on Rare-Earth Doped Materials and Devices, 4990, **2003**.
- [7] J. Li, O. H. Zalloum, T. Roschuk, C. L. Heng, J. Wojcik, P. Mascher, *Adv. Opt. Technol.* **2008**. Article ID 295601.
- [8] A. J. Kenyon, P. F. Trwoga, M. Federighi, C. W. Pitt, *J. Phys.: Condens. Matter* **1994**, *6*, L319.
- [9] J. M. Ramirez, Y. Berencén, L. López-Conesa, J. M. Rebled, F. Peiró, B. Garrido, *Appl. Phys. Lett.* **2013**, *103*, 081102.
- [10] Y. Berencén, R. Wutzler, L. Rebohle, D. Hiller, J. M. Ramirez, J. A. Rodríguez, W. Skorupa, B. Garrido, *Appl. Phys. Lett.* **2013**, *103*, 111102.
- [11] S. Boninelli, G. Bellocchi, G. Franzò, M. Miritello, F. Iacona, *J. Appl. Phys.* **2013**, *113*, 143503.
- [12] H. Jeong, S.-Y. Seo, J.-H. Shin, *Appl. Phys. Lett.* **2006**, *88*, 161910.
- [13] A. J. Silversmith, D. M. Boye, K. S. Brewer, C. E. Gillespie, Y. Lu, D. L. Campbell, *J. Lumin.* **2006**, *121*, 14.
- [14] P. Ruterana, M. P. Chauvat, K. Lorenz, *Semicond. Sci. Technol.* **2015**, *30*, 044004.
- [15] J. L. Deschanvres, W. Meffre, J. C. Joubert, J. P. Senateur, F. Robaut, J. E. Broquin, R. Rimet, *J. Alloys Compd.* **1998**, *275*, 742.
- [16] T. Minami, T. Yamamoto, T. Miyata, *Thin Solid Films* **2000**, *366*, 63.
- [17] X. P. Zhao, J. B. Yin, *Chem. Mat.* **2002**, *14*, 2258.
- [18] L. Norin, E. Vanin, P. Soininen, M. Putkonen, in Conference on Lasers and Electro-Optics, Optical Society of America, May **2007**.
- [19] O. Blázquez, J. M. Ramirez, J. López-Vidrier, Y. Berencén, S. Hernández, P. Sanchis, B. Garrido, in SPIE Microtechnologies, pp. 95200K-95200 K, International Society for Optics and Photonics, June **2015**.
- [20] O. Blázquez, J. López-Vidrier, L. López-Conesa, M. Busquets-Masó, S. Estradé, F. Peiró, S. Hernández, B. Garrido, *J. Appl. Phys.* **2016**, *120*, 135302.
- [21] H. S. Ahmed, O. M. Ntwaeaborwa, M. A. Gusowski, J. R. Botha, R. E. Kroon, *Physica B: Condensed Matter* **2012**, *407*, 1653.
- [22] J. M. Ramirez, Ph.D. thesis, Dept. d'Electrònica, University de Barcelona, Barcelona, Spain, June **2015**.
- [23] C. J. Li, S. Jou, W. L. Chen, *Jap. J. App. Phys.* **2011**, *50*, 01BG08.
- [24] I. Valov, *ChemElectroChem* **2014**, *1*, 26.
- [25] E. W. Lim, R. Ismail, *Electronics* **2015**, *4*, 586.



## 4. Materials for Optoelectronics and Resistive Switching

---

*“The difference between stupidity and genius is that genius has its limits”*

*Albert Einstein*

---

Beyond Si-based materials, which have demonstrated good electro-optical properties, other materials have been explored to be employed in optoelectronics, being metal oxides among the most interesting ones. One of the most studied metal oxides is ZnO, which presents excellent electrical and optical properties due to its high versatility. Depending on the growth condition, ZnO can become intrinsic, *p*-type or *n*-type. This possibility, together with its non-toxicity and abundance, opens its applicability as RE host matrix or electrical contact. Moreover, the optical transparency that presents in the visible range is suitable to be employed as TCO as well. Similar to Si-based materials, described in the Chapter 3, the resistive switching properties of ZnO are presented, completing the characterization of the material. In this Thesis, ZnO layers have been employed as both host matrix of RE luminescent centers and as TCO for the EL of Si-NCs embedded in SiO<sub>2</sub> matrix. Therefore, this chapter is divided into two subsections, depending on the function of the ZnO layer. In both cases, electro-optical and resistive switching properties are presented, being some results published in international peer-reviewed journals.

### 4.1. Tb- and Eu-doped ZnO

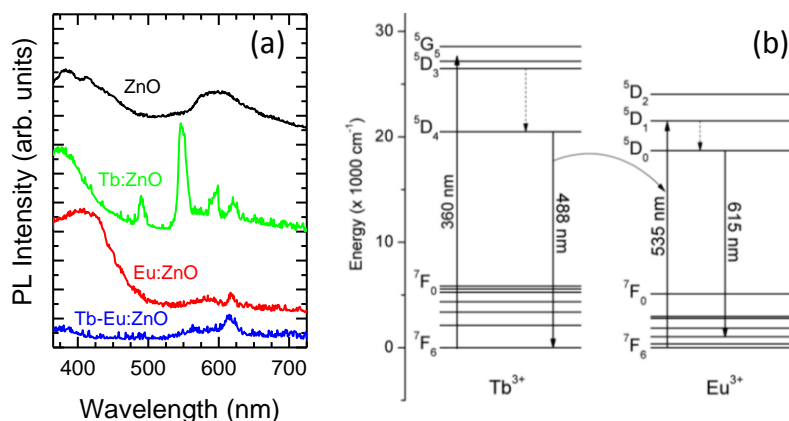
In this subsection, the study of ZnO doped with different REs has been presented as result of a collaboration with *UNICAEN*. In order to achieve device structure with well-insulated devices, SiO<sub>2</sub> windows were initially opened onto the *p*-type Si wafers at *CNM*. After this process, active layers were deposited at *UNICAEN*, consisting of ZnO, Tb-doped ZnO, Eu-doped ZnO and Tb:Eu-doped ZnO. These layers

were grown by means of RF sputtering, using  $Tb_4O_7$  and  $Eu_2O_3$  targets as dopants, and a ZnO target for the host matrix. After the deposition, samples were annealed at 450 °C for 1 h in an argon atmosphere. Finally, ITO was deposited (at *CNM*) as top electrode and aluminum in the rear side of the substrate.

The optical characterization via PL was carried out at *UNICAEN*, exciting the samples with a 450-W Xenon lamp and collecting the resulting PL emission using a *Horiba Spectrofluorometer Fluorolog*. The electro-optical characterization was performed in the EL laboratory of the research group in Barcelona, using the system described in the *Section 2.5.1. Electroluminescence Spectroscopy*.

### 4.1.1. Optical and Electro-Optical Properties

The first study consisted of the optical characterization of the material, analyzing the PL spectra of samples. In the Figure 4.1(a), the spectra of all samples are represented. Undoped ZnO presented two features related to the band-to-band emission around 380 nm and defects of the ZnO around 590 nm, as expected. In the case of Tb-doped ZnO samples, four narrow features appear, which can be attributed to the  ${}^5D_4 \rightarrow {}^7F_i$  ( $i = 3, 4, 5$  and  $6$ ) electronic transitions of the  $Tb^{3+}$  ions. Similar results were obtained for Eu-doped ZnO, but presenting a peak around 615 nm, ascribed to the  ${}^5D_0 \rightarrow {}^7F_2$  electronic transition of  $Eu^{3+}$  ions. The RE emission observed in both cases confirms that REs are optically active, presenting a decrease of the defect-related emission. In the case of the co-doped sample with both Tb and Eu ions, no emission of  $Tb^{3+}$  is obtained, being the peak at 620 nm the only feature, which is related to the  $Eu^{3+}$  emission. However, an enhancement of this  $Eu^{3+}$  emission is observed when the sample is co-doped with Tb ions as well. Other similar studies, reported in the literature, have determined the origin of this behavior. Park *et al.* observed energy transfer from  $Tb^{3+}$  to  $Eu^{3+}$  ions in gadolinium aluminate garnet ( $Gd_3Al_5O_{12}$ , GAG) doped with different REs, being the probability of this transfer strongly dependent on the concentration of  $Eu^{3+}$  [121]. These results agree with the ones observed in the hereby presented work. The excited  ${}^5D_4$  electronic level of  $Tb^{3+}$  can transfer the energy to  $Eu^{3+}$  via the  ${}^5D_4 \rightarrow {}^7F_6$  relaxation ( $\sim 2.5$  eV). This energy is close to the corresponding energy of the  ${}^7F_6 \rightarrow {}^5D_1$  electronic transition of the  $Eu^{3+}$  ( $\sim 2.3$  eV), being the energy transfer very



**Figure 4.1.** PL spectra of undoped ZnO, Tb-doped ZnO, Eu-doped ZnO and Tb- and Eu-codoped ZnO. (b) Scheme of the energy transfer mechanism from Tb<sup>3+</sup> ions to Eu<sup>3+</sup> ions. Solid arrows represent the radiative transitions, while dashed ones the non-radiative transition [37].

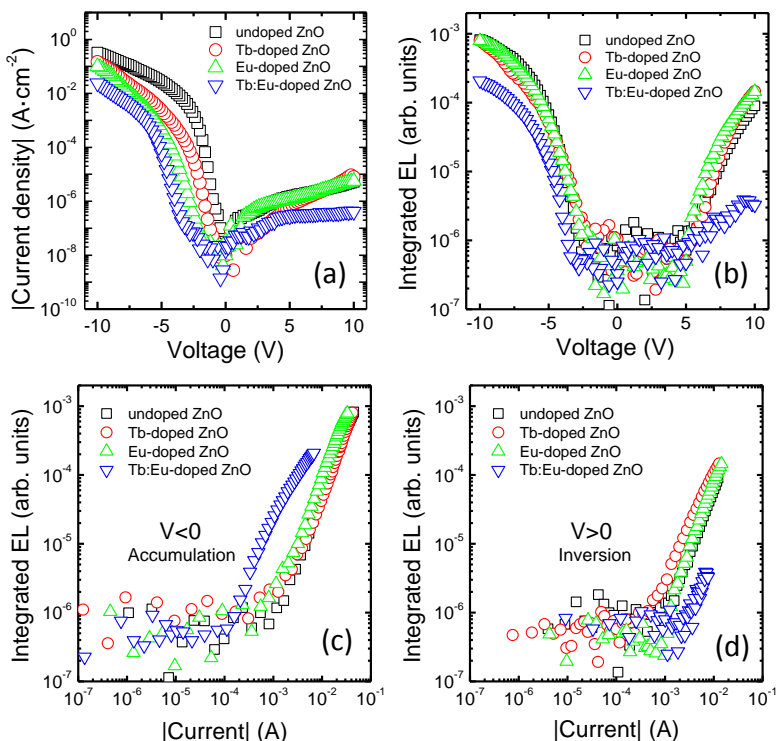
efficient. After the non-radiative relaxation to the  $^5D_0$  electronic level, the radiative  $^5D_0 \rightarrow ^7F_2$  relaxation takes place [see Figure 4.1 (b)][37].

These results motivated the further exploration of the electro-optical properties of the RE-doped ZnO. First of all, the  $I(V)$  characteristics were analyzed, obtaining similar curves for all samples. The Figure 4.2(a) represents the current density as a function of the applied voltage. A clear rectifying behavior can be observed in all devices, due to the  $N-I-P$  design. In accumulation regime ( $V < 0$ ), undoped ZnO exhibits more conductivity than doped samples, being the ZnO codoped with both REs the least conductive. As it is well known, the introduction of REs into a semiconductor reduces its conductivity; in the case of ZnO, the presence of REs influences directly on the grain boundaries, tending to form aggregates and thus destroying the grain boundary structure [37].

The next study consisted of the EL analysis. In this case, the largest devices (area of  $0.92 \text{ mm}^2$ ) were employed to maximize the acquired emission signal. The Figure 4.2(b) plots the integrated EL intensities

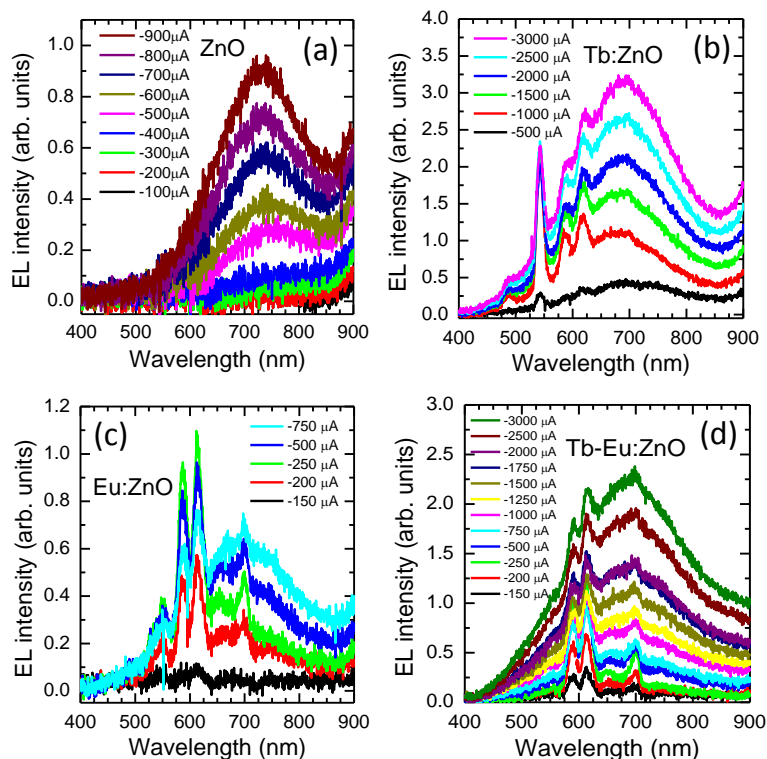


#### 4. Materials for Optoelectronics and Resistive Switching



**Figure 4.2.** (a)  $J(V)$  characteristics of undoped ZnO and doped ZnO with Tb, Eu, and both REs. (b) Integrated EL of samples versus applied voltage. (c) and (d) represent in log-log the integrated EL intensity as a function of current intensity in accumulation and inversion, respectively ion.

of devices as a function of the applied voltage. The threshold voltage is observed in both regimes, showing a lower absolute value in accumulation regime ( $-3$  V) than in inversion one ( $+5$  V). In the case of the sample co-doped with both Tb and Eu, an important reduction in EL intensity is observed. This could be attributed to a poorer excitation of the luminescent centers when a larger concentration of RE ions is present, this EL quenching being due to either a larger amount of induced defects or to enhanced clustering. In Figure 4.2(c) and Figure 4.2(d), this integrated EL intensities are plotted as a function of the injected current in accumulation and inversion regimes, respectively. Similar EL yield was found for undoped ZnO, Tb-doped ZnO and Eu-doped ZnO devices in both accumulation and inversion regimes, presenting threshold currents for EL around  $10^{-3}$  A. However, the case of the codoped sample is particular, since it

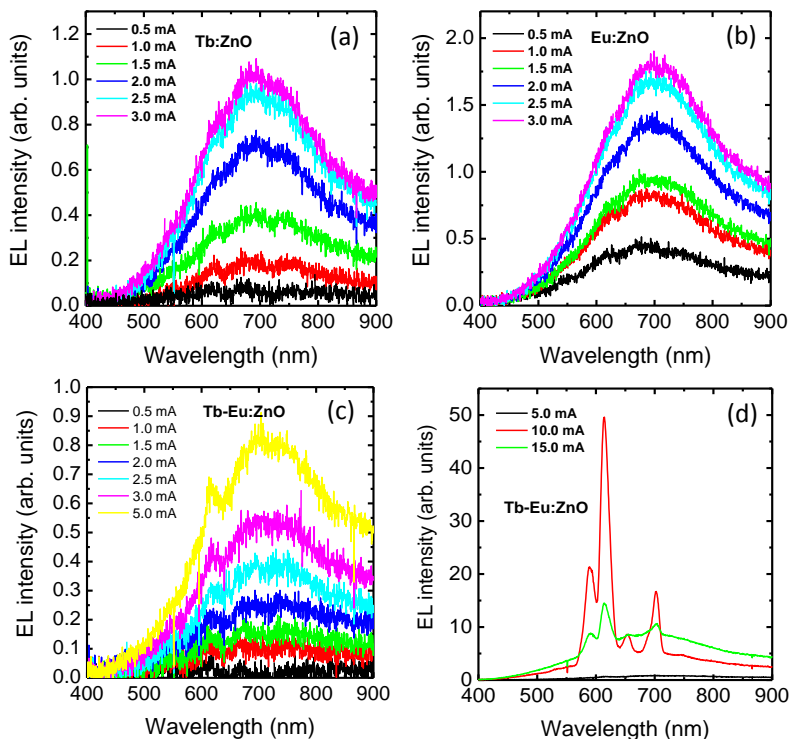


**Figure 4.3.** EL spectra of (a) undoped ZnO, (b) Tb-doped ZnO, (c) Eu-doped ZnO and (d) Tb- and Eu-codoped ZnO at different injected current in accumulation regime ( $V < 0$ ). Whereas narrow peaks are related to the RE emission, the broad ones are ascribed to the emission of the defects of ZnO.

presents a lower threshold current ( $10^{-4}$  A) for EL in accumulation regime, but a lower one ( $2 \times 10^{-3}$  A) in inversion regime.

In order to better determine the origin of these EL emissions, spectra were acquired with a CCD for 30 s and under different injected currents (see Figure 4.3). In all samples, a broad emission background was detected, ascribed to the optically-active defects within the ZnO, be it intrinsic defects or induced by RE ions doping. Different behaviors were observed depending on the current injection regime. In all cases, the defects-related matrix emission intensity increases with current, being the dominant emission. It is important to note that Eu-doped device requires less current to activate the RE emission than Tb-doped one, thus exhibiting a higher EL efficiency. As well, and

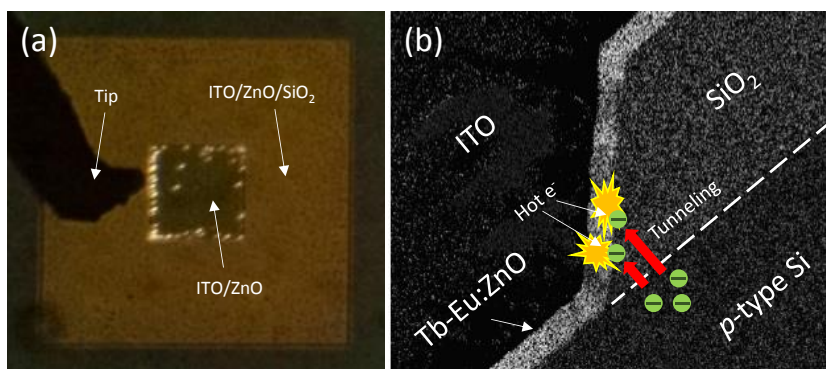
#### 4. Materials for Optoelectronics and Resistive Switching



**Figure 4.4.** EL spectra of (a) Tb-doped ZnO, (b) Eu-doped ZnO and (c) Tb- and Eu-codoped ZnO at different injected current in inversion regime ( $V > 0$ ). (d) Strong enhancement of EL emission of co-doped ZnO sample, showing a degradation of the RE emission at higher injected current.

analogous to what was observed in PL, the co-doped sample presents no  $\text{Tb}^{3+}$  emission.

In general, RE emission could only be observed in accumulation regime, increasing its EL emission when the current increases (until being quenched at large enough currents). In Figure 4.4(a,b,c), the spectra in inversion regime of Tb-doped ZnO, Eu-doped ZnO and Tb:Eu-doped ZnO are represented, respectively. As it can be seen, no presence of RE emission is observed in the two first samples, being the defects-related emission of ZnO the only contribution. However, in the case of the co-doped sample [Figure 4.4(c)], a feature around 615 nm can be observed, which increases with the injected current. This peak could be ascribed to the typical radiative  ${}^5\text{D}_0 \rightarrow {}^7\text{F}_2$  transition of  $\text{Eu}^{3+}$  ions, similar to the one observed in PL. This sample also



**Figure 4.5.** (a) Photography of co-doped devices under high injection current, where an intense dotted-shape EL can be observed close to the edges of the device. (b). EDX map of Zn corresponding to the co-doped samples. The image shows the non-abrupt edge of the device responsible of the generation of hot electrons via tunneling the  $\text{SiO}_2$  toward the RE-doped ZnO active layer, exiting efficiently the luminescent centers.

exhibits the emission of the ZnO defects, scaling with the injected current. Remarkable results were obtained when the injection current increased to 10 mA. Figure 4.4(d) shows the EL spectra of the same devices, presented in Figure 4.4(c), corresponding to injected current of 5 mA, 10 mA and 15 mA. A clear increase of two orders of magnitude in EL emission was observed at 10 mA with respect to the corresponding one at 5 mA, being the  $\text{Eu}^{3+}$  emission the main contribution. This abrupt enhancement corresponds to an increase of the EL emission efficiency and confirms that the excitation mechanism takes place via electron impact. However, further increasing the injected current, until 15 mA, the  $\text{Eu}^{3+}$  emission decreases, despite the broad emission related to ZnO defects keeps increasing. This behavior suggested a degradation of the luminescent centers. To corroborate this assumption, successive spectra were measured keeping the same injected current, confirming that the  $\text{Eu}^{3+}$  emission is progressively quenched (not shown). In addition, this decrease of the RE signal was also correlated to a voltage decrease, suggesting that the device becomes more conductive.

Another interesting result is the EL distribution along the device. In Figure 4.5(a), a photography of the smaller device working at this high injected current is presented. The fact that the strong emission (visible

to the naked eye) appears in the form of dots at the edge of the devices suggests two hypothesis. The first one is related to the device structure, inducing more efficient excitation of the RE ions at the edges of the device. Observing TEM images, non-abrupt shape can be seen in this region, presenting thinner SiO<sub>2</sub> layers close to the device [see Figure 4.5(b)]. The fact that the main emission takes place at the edges could be ascribed to the hot electron injection through the thinnest part of the SiO<sub>2</sub> via tunneling from the Si substrate to the Tb-Eu:ZnO active layer. These hot electrons have enough energy to excite the REs by electron impact mechanism, strongly increasing the EL efficiency with respect to the rest of the device area. The other hypothesis is related to the dotted-shaped emission. This feature only appears under high injected current, increasing sometimes the number of emitting dots with time. This behavior can be correlated with the decrease of the applied voltage in the successive measured spectra mentioned before. Overall, the possible formation of conductive paths when the device is submitted to enough voltage can explain both the dotted emission and the voltage decrease.

### **4.1.2. Resistive Switching Properties**

The electro-optical properties of these devices suggested the formation of conductive paths, which opens the possibility to employ them as resistive switching devices. Moreover, they exhibited EL emission under high injection current, which could be used as optical read as well. Hence, the resistive switching properties of these samples were analyzed in detail, and they are presented in the following sections.

#### **4.1.2.1. ITO/ZnO/*p*-Si structure as resistive switching device**

First of all, the undoped ZnO sample was explored in order to determine the resistive switching properties of the ITO/ZnO/*p*-Si structure. In this case, the electroforming was carried out supplying a positive voltage ramp at the ITO top contact and setting the current compliance at 5 mA, achieving the LRS at 12.5 V. After this electroforming, the device was submitted to 100 cycles between -1 V and +1 V, presenting Set and Reset processes around +0.4 V and -0.4 V, respectively, working in self-compliance mode. A current contrast

of more than 5 orders of magnitude was observed between both HRS and LRS at the  $V_{\text{read}} = -0.2$  V, being  $10^{-11}$  A and  $2 \times 10^{-6}$  A the corresponding currents, respectively.

In the next step, the device was submitted to a specific pulse-voltage pattern, which consists of four pulses corresponding to: (i) inducing the Set at +2 V, (ii) reading within the LRS at  $-0.2$  V, (iii) inducing the Reset at  $-1$  V and (iv) reading within the HRS at  $-0.2$  V. Whereas the duration of the Set and Reset was kept at 50 ms to achieve correctly the resistive switching behavior, the lectures were set only at 0.1 ms (system limitation). Working at these conditions, the device presented an endurance of  $10^3$  cycles with 99.5% of success. In this case, the LRS current fits well with the measured by voltage ramps ( $2 \times 10^{-6}$  A). However, the HRS presented currents around  $10^{-9}$  A, being two order of magnitude larger than using voltage ramps. This difference could be attributed to the short duration of the pulse during the Reset, affecting the atomic arrangement.

In order to understand better the physics that governs the current through the conductive filaments, the charge transport mechanisms of the three different resistive states (pristine, HRS and LRS) were determined in accumulation regime. The pristine state presented trap-assisted tunneling (TAT) along 7 orders of magnitude in current, which was expected due to the intrinsic intra-band electronic states ascribed to the defective nature of the undoped ZnO. In contrast, a space-charge limited current (SCLC) was observed when the device was in LRS. These results are in agreement with the large amount of injected carriers through the conduction filaments, exhibiting a quadratic dependence on the voltage. Finally, the  $I(V)$  curve corresponding to the HRS showed clearly two different trends. Initially, the curve presented TAT transport mechanism at low voltages, similar to the pristine state. However, for voltages larger than 0.7 V, the trend of the curve changes following the Fowler-Nordheim (FN) tunneling transport mechanism.

Taking into account the obtained parameters from the fits and assuming that the re-oxidized region recovers the stoichiometry of the pristine state, some structural parameters were estimated like the reduction of the effective surface of the device and the thickness of the gap between the electrode and the interrupted conductive path. In

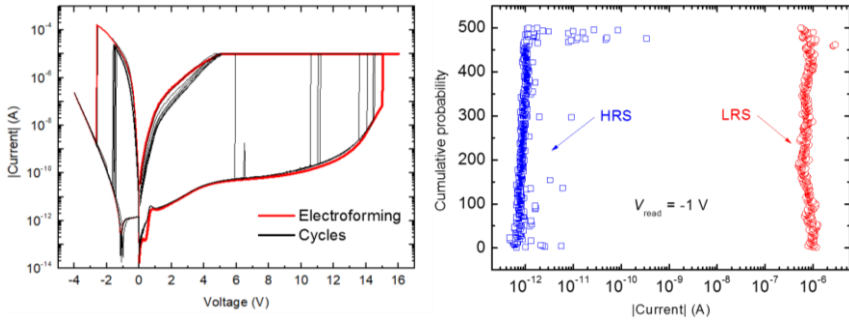
this case, the effective surface of the device in LRS was reduced from  $2.1 \times 10^{-3} \text{ cm}^2$  to  $1.4 \times 10^{-10} \text{ cm}^2$ , which corresponds to around 20 nanofilaments, assuming their reported diameter (10–50 nm) in the literature. Regarding the thickness of the gap corresponding to the re-oxidized region, the parameters extracted from the fits permitted to determine a thickness around 9 nm, leading to an electric field of  $0.8 \text{ MVcm}^{-1}$  at 0.7 V. This reduction can explain the change from TAT to FN mechanism at 0.7 V, being it ascribed to the enhancement of the electric field due to the reduction of the effective thickness and the boundary effect at the tip of the nanofilaments.

This work has just been submitted in *Applied Physics Letters* (2018) [see Section A.1. *List of Articles* (VI)].

##### **4.1.2.2. Effect of RE ions on the resistive switching properties**

Following the resistive switching characterization of the ITO/ZnO/*p*-type Si devices, the next step consisted of analyzing the effect of the REs on the resistive switching properties. In order to carry out this study, the Tb-doped ZnO sample was submitted to the same analysis than the undoped one. First of all, different current compliances were explored from 1  $\mu\text{A}$  to 5 mA, observing that the introduction of the RE permitted to reduce this value some orders of magnitude. In contrast to the undoped sample, whose optimum current compliance was 5 mA, Tb-doped ZnO allows reducing this value down to 10  $\mu\text{A}$ , thus keeping stable the LRS. However, a clear increase of the Set and Reset voltages was required to induce the resistive switching, as it can be observed in the Figure 4.6(a). Similar to the case of undoped ZnO, both HRS and LRS are well defined, their corresponding curves matching each other, and exhibiting a current difference of 6 orders of magnitude at voltage values around  $-1 \text{ V}$ . The  $I(V)$  characteristics shows higher voltage dispersion in Set than in Reset, which matches perfectly after the two first cycles.

When the device was submitted to pulse-voltage pattern, similar results were obtained. In this case, the voltages consisted of 12 V and  $-5 \text{ V}$  to induce the Set and Reset, respectively, reading the current of each resistive states at  $-1 \text{ V}$ . The duration of each pulsed voltage was initially the same than undoped ZnO (50 ms to induce the Set and

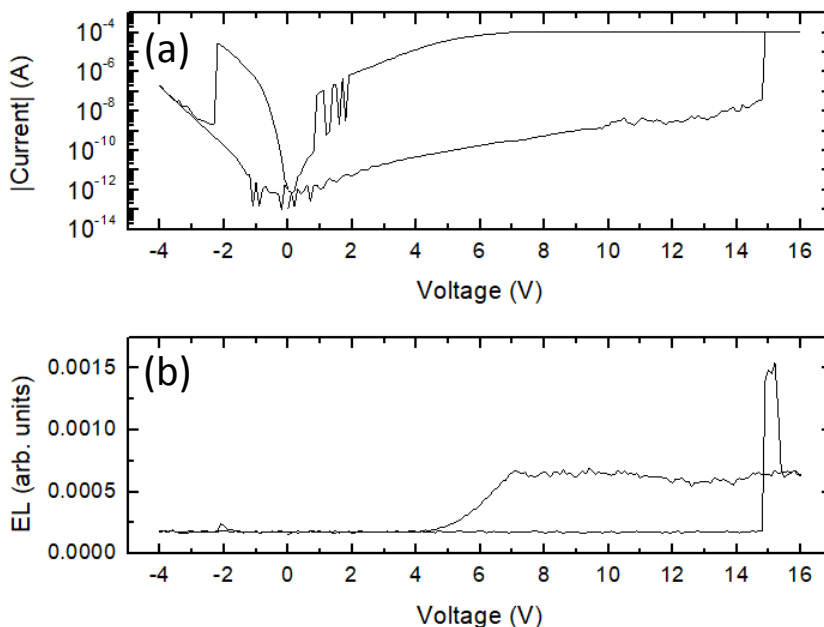


**Figure 4.6.** (a)  $I(V)$  characteristics of Tb-doped ZnO sample, showing a resistive switching behavior. The red line indicates the first cycle corresponding to the Electroforming process. (b) Cumulative probability of HRS and LRS current measured at  $-1$  V along 500 cycles.

Reset and 0.1 ms for the reading), obtaining similar results. In Figure 4.6(b), the cumulative probability of the HRS and LRS current under these conditions along 500 cycles is displayed. In contrast to the undoped sample, no variation of the current at HRS was observed with respect to using voltage ramps. This fact indicates that the Reset process is totally completed, using the same time. This effect can be explained from the point of view of the role of the Tb ions. The REs near the conductive paths could trap part of the out-diffused oxygen ions, being easier the re-oxidation of these nanofilaments by filling their oxygen vacancies.

Finally, the electro-optical properties of the Tb-doped ZnO were carried out analyzing the electroluminescence of the device by means of the system described in the section 2.5. *Electro-Optical Characterization*. The integrated EL signal was detected along the whole resistive switching cycle in order to study the emission in both HRS and LRS. The Figure 4.7(a) shows the  $I(V)$  characteristics of a resistive switching cycle, where Set and Reset take place around 15 V and  $-2$  V, respectively. Observing the corresponding integrated EL emission [Figure 4.7(b)], one can observe that the device does not exhibit EL emission in the HRS. Just at the moment when Set occurs, a sudden increase of the light emission is observed, showing an overshoot. After that, the integrated EL signal remains constant during all the time that the current compliance is active. Around 7 V, the  $I(V)$  curve recovers its own shape decreasing its value and consequently, the integrated EL emission also decreases, quenching the emission

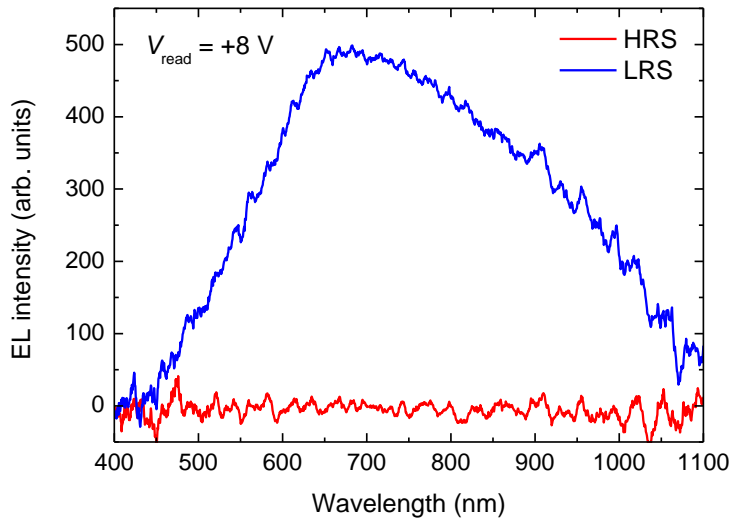




**Figure 4.7.** (a)  $I(V)$  characteristics of Tb-doped ZnO sample, showing a resistive switching behavior. (b) Integrated EL emission corresponding to the  $I(V)$  curve of (a).

about 4 V. Applying negative voltages to induce the Reset process, slight EL signal was observed around  $-2$  V in the LRS; however, the Reset process, which takes place immediately, quenches this emission. After that, no EL emission was observed along the rest of the curve in the HRS. The fact that the device does not present EL emission in HRS can be explained by the low current that flows through the device, which is not enough to induce EL emission. Nevertheless, the current around  $10^{-6}$  A that the device presents at voltages larger than 3 V allows for light emission.

In order to identify the origin of this integrated EL emission, emission spectra were acquired at  $+8$  V in both resistive states. The Figure 4.8 shows these spectra between 400 nm and 1100 nm. In accordance to what was observed in integrated EL, the HRS does not present EL emission along this range, as not high enough current flows through the device. However, a broad spectrum was observed applying the same voltage ( $+8$  V) in the LRS. Analyzing the shape of this spectrum, no emission from  $Tb^{3+}$  ions is observed, whose narrow peaks should



**Figure 4.8.** (a)  $I(V)$  characteristics of Tb-doped ZnO sample, showing a resistive switching behavior. (b) Integrated EL emission corresponding to the  $I(V)$  curve of (a).

appear between 488 nm and 620 nm [see Figure 4.3(b)]. Therefore, only emission ascribed to the ZnO defects is observed, arising probably from the conductive paths with high density of oxygen vacancies. This issue is in agreement with the observed in Figure 4.5(a), where bright spots appears under high injection current.

In conclusion, the introduction of REs into the ZnO layer clearly changes the resistive switching properties, increasing the required voltages to induce the Set and Reset processes. However, it seems that this chemical modification limits the out-diffusion of oxygen atoms, easing their reincorporation during the Reset process. In addition, both the defective nature of ZnO and the results obtained analyzing the EL emission, open the possibility to read optically the resistive state as well.

## 4.2. ZnO/Si-NCs/p-Si Light Emitter

In the case that ZnO presents  $n$ -type properties, this material can be employed as TCO. This kind of electrode is required in devices whose active layer needs to absorb or emit light (solar cells or light-emitting

diodes, respectively). In this subsection, ZnO plays the role of TCO in devices containing Si-NCs embedded into silicon oxynitride host matrix. As mentioned in the section *1.3 Silicon Nanocrystals*, the optical properties of these nanostructures present interesting properties due to the possibility to tune their emission depending on their size.

Samples were fabricated depositing multilayered silicon-rich oxynitride (SRON)/SiO<sub>2</sub> structure onto *p*-type Si substrate. This deposit was carried out by means of PECVD at 375 °C alternating both materials. After the deposition, the samples were annealed at 1150 °C for 1 h in N<sub>2</sub> ambient to induce the precipitation of the silicon excess in SRON in form of Si-NCs. The device structure was achieved after depositing a 100-nm thick ZnO layer on top of the multilayers by means of ALD at 200 °C, which was photolithography patterned obtaining circular-shaped contacts. Finally, the rear side was full-area evaporated with Al as bottom electrode.

### **4.2.1. Optical and Electro-Optical Properties**

The optical and electro-optical characterization of these devices is divided into two studies. The first one consists of the modulation of the defects-related EL emission of the ZnO layer via AC excitation. In the second one, an additional 2-nm-thick Si<sub>3</sub>N<sub>4</sub> interlayer at the Si-NCs-substrate interface and 10-nm-thick SiO<sub>2</sub> capping layer on top of the multilayers were introduced. The analysis of the injected current and how these layers affect the EL emission was carried out.

#### **4.2.1.1. Modulation of ZnO emission via pulsed excitation**

The EL emission was acquired using the system described in the section *2.5. Electro-Optical Characterization* in Barcelona. Both spectra and integrated EL were analyzed under symmetric square voltage pulses with 50 μm of period, obtaining an enhancement of the EL emission about one order of magnitude compared to DC electrical excitation. Applying constant DC excitation of -7 V, which corresponds to the accumulation regime, the corresponding EL spectra exhibits a broad emission ranging from 400 nm to 1100 nm. Taking into account the nature of the device, this emission was

deconvolved into two contribution, Si-NCs emission (~900 nm) and ZnO defects emission (~700 nm). The first one well agrees with the obtained emission in similar devices, but using ITO as top electrode, only presenting this contribution due to the no emission of the ITO top electrode.

Once both contributions were identified, pulsed excitation was carried out using symmetric square voltage pulses between  $-7$  V and  $7$  V. In this case, 50% duty cycle was selected over a period of  $50$   $\mu$ s, thus staying  $25$   $\mu$ s in accumulation regime and  $25$   $\mu$ s in inversion one. Under this AC electrical excitation, an enhancement of almost one order of magnitude was observed, attributed to the sequential injection of carriers from Si substrate towards the Si-NCs. Varying the duty cycle of this electrical excitation, but keeping the  $50$ - $\mu$ s period, a quenching of the defective emission of ZnO was observed. The shorter the time in accumulation regime, the lower the EL emission of ZnO defects. This behavior suggests that the recombination dynamics of the different luminescent centers play an important role. The analysis of the time-resolved EL was carried out collecting the integrated signal with the PMT and displayed using the oscilloscope. A symmetric square voltage pulsed of  $500$   $\mu$ s with 50% duty cycle was employed as electrical excitation. This larger period was selected to be sure that luminescent centers, especially Si-NCs, completed their excitation. Different dynamics was observed depending on the charge injection regime. In accumulation regime, EL emission increases up to the DC-like emission level with a rise time of  $\sim 18$   $\mu$ s. During the voltage pulse in inversion regime, the deep depletion regime is achieved and, consequently, an EL overshoot takes place with a rise time of  $\sim 17$   $\mu$ s, followed by a slower decay of the EL with decay time of  $\sim 76$   $\mu$ s. In order to understand better the excitation process that occurs in both ZnO and Si-NCs luminescent layers, the mechanism was analyzed in terms of the energy band diagram. Whereas in accumulation regime holes are injected into Si-NCs from the *p*-type Si substrate and electrons from the ZnO top electrode, in inversion regime only electrons (minority carriers) of the *p*-type substrate tunnel into Si-NCs. In both cases, the generation of electron-hole pairs within the quantum-confined Si-NCs takes place, whose recombination induces the EL emission of the Si-NCs. However, the injection asymmetry between electrons and holes, due to their mobility difference in SiO<sub>2</sub>, suggests that this generation of electron-hole pair

likely occurs via electron impact, the electrons tunneling the SiO<sub>2</sub> host matrix from the ZnO to Si-NCs. On the other hand, the ZnO EL emission can be explained by electron-hole generation as a consequence of hole injection from Si-NCs to the ZnO top electrode, which presents high concentration of electrons (as ZnO is naturally *n*-type). Typically, ZnO does not allow the injection of holes into it, but the defect-related deep-level states permit this process. Indeed, the fact that no presence of the band-to-band recombination is observed in EL supports this assumption. The presence of these holes in the Si-NC layer could be induced as a result of the electron-hole generation due to the band-to-band excitation of Si-NCs and the hole injection from the *p*-type Si, being accumulated at the ZnO/Si-NCs interface. The fact that electrons cannot compensate this positive charge in accumulation regime could explain that the injection, in inversion regime, of electrons from *p*-type Si into the positive charge of Si-NCs generates electron-hole pairs, resulting in the EL emission overshoot observed. Once this charge is compensated, the EL emission decays because the unlikely hole injection from ZnO and the low electron injection from the *p*-type Si in inversion regime are not enough to observe EL in DC excitation. Therefore, ZnO defects-related EL emission can be modulated by AC excitation, while simultaneously enhancing the EL intensity of the Si-NCs. In conclusion, this study demonstrated that ZnO EL emission can be totally quenched, and therefore the device EL emission spectral lineshape modulated through the visible range, by controlling the duty cycle of the pulse excitation.

This work was presented in the international conference of the *European Materials Research Society (EMRS) Spring Meeting* celebrated in Strasbourg (France) in 2017, as oral communication [see Section B.3. Conference Contributions (28)]. In addition, it finally was published in *Applied Physics Letters Vol. 110, 203104 (2017)* [see Section A.1. *List of Articles (VII)*].

##### **4.2.1.2. Effect of Si<sub>3</sub>N<sub>4</sub> inversion layer on Si-NCs emission**

As observed in the previous study, the injection of electrons from *p*-type Si substrate can play an important role for the Si-NCs EL emission. However, the low concentration of electrons that this layer presents is the main drawback to achieve high carrier injection in

inversion regime. In order to overcome this problem, an additional thin film of  $\text{Si}_3\text{N}_4$  was deposited onto the *p*-type Si substrate, before the multilayered structure of Si-NCs. Three different samples were fabricated, containing all of them  $5 \times (\text{Si-NCs}/\text{SiO}_2)$  bilayers with nominal thicknesses of 4.5 nm and 1.0 nm, respectively. The first one, consists only of the Si-NC/SiO<sub>2</sub> multilayers. In the second one, a 2-nm thick  $\text{Si}_3\text{N}_4$  inversion layer was located between the Si substrate and the first Si-NC/SiO<sub>2</sub> bilayer. Additional 10-nm thick SiO<sub>2</sub> layer was deposited on top of the Si-NC/SiO<sub>2</sub> multilayers in the third sample as carrier injection blocking layer. Finally, device structure was achieved after depositing ZnO as TCO as top electrode and Al in the rear side of the substrate. The multilayered structure containing Si-NCs and the additional  $\text{Si}_3\text{N}_4$  and SiO<sub>2</sub> layers was confirmed by TEM images.

The optical characterization of the samples was carried out by PL analysis, showing the typical Gaussian-like spectra ascribed to the radiative excitonic recombination of Si-NCs. The sample containing SiO<sub>2</sub> top layer presented a slight PL redshift, probably caused by a modulation (due to internal reflections) generated by this top layer. However, no evident spectrum variation was observed due to the presence of the  $\text{Si}_3\text{N}_4$  inversion layer, indicating that it does not play a relevant role in the PL emission.

Regarding the electrical properties, the  $I(V)$  curves of the three samples were analyzed in accumulation regime. The device containing only Si-NCs presents more conductivity than the others, being the least conductive the sample containing the SiO<sub>2</sub> additional capping layer, as expected. The capacitance versus voltage [ $C(V)$ ] curves, obtained at 300 kHz and sweeping between +6 V and -6 V, show a flat band voltage around -0.3 V and the overall capacitance about  $\sim 120 \text{ nF cm}^{-2}$  for the sample with only Si-NCs. However, the sample with the additional  $\text{Si}_3\text{N}_4$  layer presents larger capacitance of  $\sim 140 \text{ nF cm}^{-2}$  due to its lower AC conductivity, and lower flat band voltage around -2.0 V ascribed to the positive fixed charge within the  $\text{Si}_3\text{N}_4$  interlayer. The introduction of the oxide blocking barrier induces the largest capacitance about  $\sim 143 \text{ nF cm}^{-2}$  because of this oxide barrier and exhibits a negative threshold voltage shift.

The electro-optical properties were determined by studying the EL emission of the three devices in both DC and AC electrical excitation. In DC, EL spectra were observed only in the samples without the SiO<sub>2</sub> layer, due to the limit of current injection that this layer performs. Comparing to PL, broader spectra were determined, which is ascribed to the excitation of smaller Si-NCs, which are not efficiently excited by photons due to their low cross-section. In this DC conditions, the introduction of the Si<sub>3</sub>N<sub>4</sub> layer reduces the carrier injection, and consequently the EL emission. However, a clear enhancement of the EL emission was observed in all device working in AC and using the same electric field than DC and setting a period of 50 μs with a duty cycle of 50% (accumulation and inversion times of 25 μs). This increase of the EL emission is attributed to the sequential injection of carriers after alternate polarization switching. Moreover, devices containing the additional Si<sub>3</sub>N<sub>4</sub> layer exhibited a greater enhancement when working in AC. The narrower and red-shifted spectra that the samples exhibit under pulsed excitation with respect to the PL emission were attributed to the modulation of the high- and low-energy EL emission contributions, depending on the duty cycle of the pulsed excitation (see 4.2.1.1. *Modulation of ZnO emission via pulsed excitation*).

In order to understand better this injection process, time-resolved EL study was carried out by applying square voltage pulses of ±7 V with a period of 1 ms with duty cycle of 50%. This larger period was selected to give enough time to complete the decay time in both regimes. An emission overshoot was observed immediately after each polarization switch, recovering the DC-like emission level when the device worked in accumulation regime. This effect was only observed in the devices containing the additional Si<sub>3</sub>N<sub>4</sub> layer. However, when devices switched from accumulation regime to inversion one, the overshoot was observed in all devices followed by an EL decay until EL was totally quenched. In accumulation regime, some holes are confined in Si-NCs within the layer immediately on top of the substrate which might not be recombined with electrons due to the asymmetry between electron and hole mobilities in SiO<sub>2</sub>. When the device switches from accumulation to inversion, this positively charged Si-NCs attract electrons from the substrate, reaching the overshoot peak. After this process, very low injected current is

expected because of the fact that electrons are the minority carriers in the *p*-type Si substrate.

This work was published in *Advanced Electronic Materials*, 1700666 (2018) [see Section A.1. *List of Articles (VIII)*].

## 4.2.2. Resistive Switching Properties

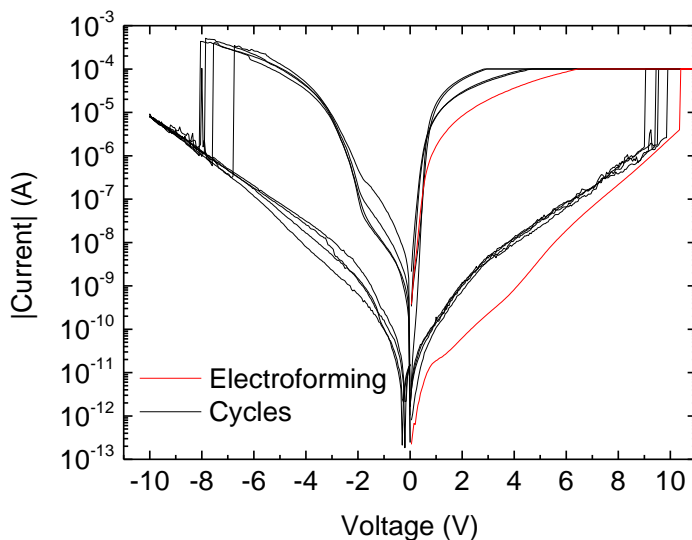
Analogously to section 4.1.2.1. *ITO/ZnO/p-Si structure as resistive switching device*, the study of the resistive switching properties of these of these ZnO/Si-NCs/*p*-Si devices containing the Si<sub>3</sub>N<sub>4</sub> inversion was also carried out. The employed experimental system was the one described section 2.4. *Electrical Characterization*. In addition, the EL emitted in each resistive state was explored by collecting the emitted light using the PMT and the CCD described in section 2.5 *Electro-Optical Characterization*.

### 4.2.2.1. ZnO/Si-NCs/*p*-Si as resistive switching device

First of all, and similar to the other studies, different current compliances were explored, observing that keeping this current limitation at 100  $\mu$ A permitted to complete some cycles with well-defined resistive states. In Figure 4.9, the  $I(V)$  characteristics of the device is presented, showing the electroforming and four completed cycles. As observed in other cases, the curve corresponding to the electroforming process (i.e., the pristine state) presents less current than in following cycles at HRS. This fact is ascribed to residual oxygen vacancies still present after the Reset process, which increase the effective conductivity of the device. This electroforming process took place around 10 V, achieving the LRS limited by the current compliance. When negative current was supplied, the HRS was recovered between  $-7$  V and  $-8$  V depending on the cycle. Despite the fact that the devices only present some cycles before obtaining a permanent resistive state, well defined states were observed with a current difference about 6 orders of magnitude.

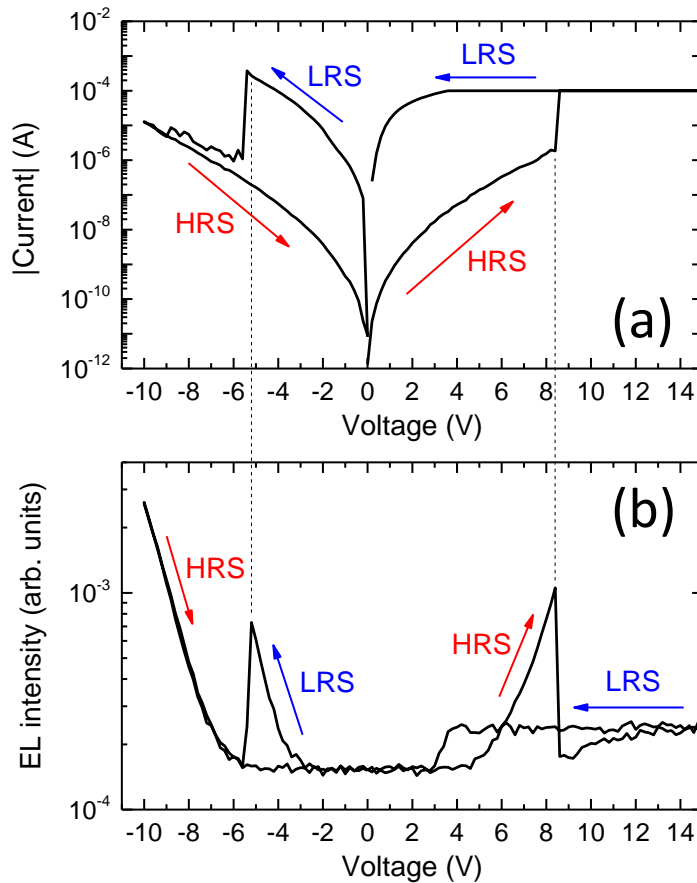
Following the measurement protocol used for the other studied resistive switching devices, the EL emission of this device was analyzed. The integrated light emission was initially collected by the PMT while simultaneously acquiring an  $I(V)$  curve. In Figure 4.10(a)





**Figure 4.9.** (a)  $I(V)$  characteristics of Tb-doped ZnO sample, showing a resistive switching behavior. (b) Integrated EL emission corresponding to the  $I(V)$  curve of (a).

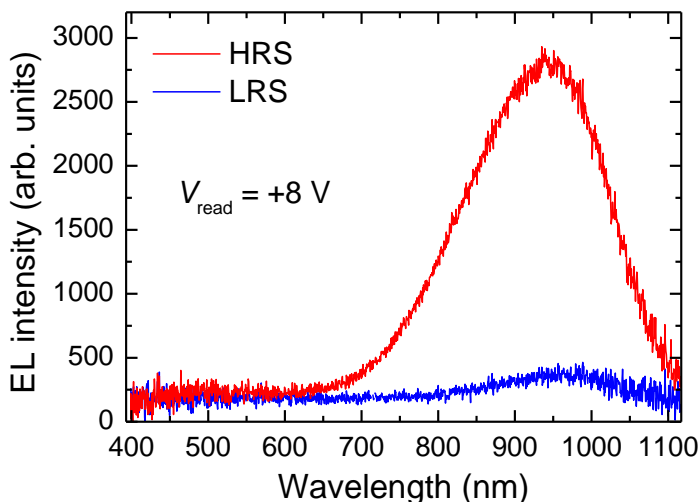
a single cycle is presented, where the Set and Reset processes take place around 8 V and  $-7$  V, respectively. Observing the corresponding EL emission along the whole cycle, which is shown in Figure 4.10(b), one can see that the device exhibits EL emission depending on the applied voltage and the resistive state. First of all, the device was submitted to a positive voltage ramp in the HRS, not yielding EL emission at low voltages. The threshold voltage for light emission is around 5 V, beyond which EL intensity progressively increases. When the Set process takes place, the EL emission suddenly decreases, keeping the value constant while the current compliance is active and being totally quenched around 3 V. Applying negative voltages without current compliance, the device presents again EL emission with a threshold voltage of  $-3$  V, being totally quenched immediately after the Reset process occurs. After that, the EL emission is recovered with a higher threshold voltage around  $-6$  V. This behavior is totally different than the one observed in ITO/Tb:ZnO/ $p$ -Si, where no EL emission was observed in the HRS. This occurrence can be explained by taking into account that, in the case of the device containing Si-NCs, the HRS presents enough current in positive voltage, and before the Set process, to induce EL emission. Regarding the LRS, the device presents more electrical conductivity and, therefore, EL emission can



**Figure 4.10.** (a)  $I(V)$  characteristics of Tb-doped ZnO sample, showing a resistive switching behavior. (b) Integrated EL emission corresponding to the  $I(V)$  curve of (a).

take place at low voltages, high enough to induce the excitation of the luminescent centers but not to force resistive switching

The analysis of the spectra corresponding to this EL emission was carried out to determine the origin of the luminescent centers. In this case, the CCD was used, such as previously described. Observing the Figure 4.10(b), two spectra were acquired at 8 V, because both HRS and LRS present EL emission at this applied voltage. In the Figure 4.11, these spectra are displayed in a range between 400 nm and 1100 nm. As it can be observed, both spectra present a broad spectrum centered around 950 nm, being the EL intensity in HRS higher than



**Figure 4.11.** (a)  $I(V)$  characteristics of Tb-doped ZnO sample, showing a resistive switching behavior. (b) Integrated EL emission corresponding to the  $I(V)$  curve of (a).

in LRS, which is in agreement with the integrated EL measurements [see Figure 4.10(b)]. The position of these peaks suggest that EL emission yields from Si-NCs, as previously discussed in this Thesis. In addition, the spectrum corresponding to the HRS fits perfectly with the obtained one in the electro-optical study just above and published in the Paper VIII. In particular, the fact that the EL spectrum in HRS is more intense than in LRS can be explained in terms of the effective area through which the current flows. Once the conductive path is formed, the current flows only through it, being the effective area reduced. In this case, the LRS presents slight EL emission of Si-NCs, which could indicate that some Si-NCs remain optically active in the way of these conductive paths. However, in the HRS the Si-NCs EL emission is clearly more intense, which suggests two hypothesis. The first one consists of a greater amount of optically active Si-NCs in the re-oxidized region, between the remnant conductive path and the electrode; in this frame, the structural and chemical modification of the active layer in the LRS induces the optical deactivation of these Si-NCs. The second hypothesis suggests that the conductive paths are totally or almost totally re-oxidized, inducing the current flow through the same or similar area than in the pristine state.

These results are very interesting since they not only demonstrate the viability of employing Si-NCs in resistive switching applications, but also the light emission from these nanostructures can be used to read optically. Moreover, the study of this light emission can help more in-depth understanding the physics that governs the resistive switching mechanism and how this electrical characteristics can affect the electro-optical properties of the device.

These results are very interesting because not only demonstrate the viability of employing Si-NCs in resistive switching application, but also the light emission form these nanostructures can be used to read optically. Moreover, the study of this light emission can help to understand better the physics that governs the resistive switching mechanism and how this electrical characteristics can affect the electro-optical properties of the device.



**Resistive switching and charge transport mechanisms in ITO/ZnO/p-Si devices**

O. Blázquez,<sup>1,2</sup> J. L. Frieiro,<sup>1,2</sup> J. López-Vidrier,<sup>3</sup> C. Guillaume,<sup>4</sup> X. Portier,<sup>4</sup> C. Labbé,<sup>4</sup> P. Sanchis,<sup>5</sup> S. Hernández,<sup>1,2</sup> B. Garrido<sup>1,2</sup>

<sup>1</sup>MIND, Department of Electronics and Biomedical Engineering, Universitat de Barcelona, Martí i Franquès 1, E-08028 Barcelona (Spain)

<sup>2</sup>Institute of Nanoscience and Nanotechnology (IN<sup>2</sup>UB), Universitat de Barcelona, Av. Joan XXIII S/N, E-08028 Barcelona (Spain)

<sup>3</sup>Laboratory of Nanotechnology, Department of Microsystems Engineering (IMTEK), Albert-Ludwigs-Universität Freiburg, Georges-Köhler-Allee 103, D-79110 Freiburg (Germany)

<sup>4</sup>CIMAP Normandie Univ, ENSICAEN, UNICAEN, CEA, CNRS, 14050 Caen (France)

<sup>5</sup>Nanophotonics Technology Center, Universitat Politècnica de València, Camino de Vera s/n, E-46022 Valencia (Spain)

**Abstract**

The resistive switching properties of ITO/ZnO/p-Si devices have been studied, which present well defined resistive states with more than five orders of magnitude of difference in current. Both high resistance state (HRS) and low resistance state (LRS) were induced by either sweeping or pulsing the voltage, observing some differences in the high resistance state. Finally, the charge transport mechanisms dominating the pristine, HRS and LRS states have been analyzed in depth, which suggests a partial re-oxidation of the conductive nanofilaments and a reduction of the effective conductive area.

The poor energy efficiency of CMOS transistors and the fast scaling in memories are considered a serious drawback within the new era of big data and Internet of Things, which leads to the search of a new generation of ultra-low-power nanodevices to overcome this important challenge that the electronics industry faces. Resistive switching (RS) memories or resistance random access memories (ReRAM) have become a solution for the next generation of nonvolatile memories thanks to their low-power operation, high switching speed and compatibility with the CMOS technology.<sup>1-4</sup> In these devices, the

## 4. Materials for Optoelectronics and Resistive Switching

switching between the low resistance state (LRS) and the high resistance state (HRS), when an external electric field is applied, is due to either ionic movement leading to atomic rearrangement inside the active layer (valence change mechanism, VCM) or metallic diffusion from the electrode (electro-chemical metallization, ECM), thus inducing the formation and destruction of conductive nanofilaments (CNFs).<sup>5,6</sup> Different oxide compounds have been explored, such as TiO<sub>2</sub>, HfO<sub>2</sub>, SnO<sub>2</sub> or ZnO, which have demonstrated promising results.<sup>7-12</sup> Among these metal oxides, ZnO has since long attracted a great deal of attention because of its abundance and non-toxicity, arising special interest also in gas sensing<sup>13,14</sup> or as transparent conductive oxide (TCO) in light-emitting and photovoltaic devices. Hence, this broad range of applications of ZnO makes it a potential candidate for a new family of transparent ReRAM devices. Here, we report on the RS properties of sputtered ZnO within an indium tin oxide (ITO)/ZnO/*p*-Si device configuration. The selection of ITO as top contact provides also advantages over the control of the switching mechanisms, as no metal diffusion from the electrodes should occur.<sup>15</sup> More than five orders of magnitude difference in current has been observed between LRS and HRS, with stable switching, taking place at low voltages ( $\pm 1$  V) and with free current compliance. A cycling endurance beyond 1000 cycles has been demonstrated using pulse trains for performing the reading and the changes between the two resistivity states. Finally, the obtained results are explained according to the charge transport mechanisms underlying the three different conduction states (pristine, LRS and HRS), which sheds light to the CNF formation and destruction processes within ZnO.

Devices consisting in ITO/ZnO/*p*-type Si have been fabricated using a metal-oxide-semiconductor (MOS) configuration. The ZnO layer consists of a 60-nm-thick layer deposited by means of 4 inches radiofrequency magnetron sputtering system from a pure ZnO target. The ZnO layer was grown on a *p*-type (100)-oriented silicon substrate using a power density value of 0.97 Wcm<sup>-2</sup>, a 15  $\mu$ bar Ar pressure and a substrate temperature of 400 °C. An annealing process at 450 °C for 1 h was carried out in a conventional furnace and under Ar atmosphere. The top contact was achieved by deposition of ITO by electron-beam evaporation with a subsequent annealing at 200 °C in air for 1 h. By using photolithography, devices with an effective area of 460×460  $\mu$ m<sup>2</sup> were successfully fabricated. The electric characterization of the MOS devices was performed by means of an Agilent B1500 semiconductor device analyzer.

The  $I(V)$  characteristics of the devices were studied by applying a voltage on the top electrode while grounding the bottom contact, sweeping the voltage from  $V = -1$  V to  $V = +1$  V, thus performing RS cycles. In FIG. 1(a), we show a representative  $I(V)$  curve out of more than 100 cycles, where the change from LRS to HRS is achieved at negative voltages, while the reverse change takes place at positive ones. Prior to it, an electroforming process was carried out by applying positive ramp voltage and setting a current compliance at 5 mA. The voltage at which this electroforming process takes place lies around 12.5 V, leading the device to the LRS, as shown in the inset of FIG. 1(a). This state exhibits a much higher current than the pristine state, but without the need of using a limiting current compliance of the measuring system considering the explored range of voltages ( $\pm 1$  V): this state can thus be considered as a self-compliant LRS. The following step consists of applying a negative ramp voltage until  $-1$  V in order to switch from LRS to HRS, leading to a considerable reduction in the current passing through the device, but being larger than the one observed in the pristine state. After applying another voltage sweep up to 1 V, the LRS state is again recovered. In this cycle, the *set* and *reset* processes occur around  $+0.4$  V and  $-0.4$  V, respectively. At this point, the device was submitted to 100 consecutive self-compliant cycles by means of positive and negative ramp voltages in the range from  $-1$  V to  $+1$  V for *set* and *reset* steps, respectively [see inset of FIG. 1(a)]. A current contrast of more than 5 orders of magnitude is observed between both states at a reading voltage of  $V_{\text{read}} = -0.2$  V (LRS is plotted in blue, HRS in red). In order to analyze better these parameters along the 100 cycles, FIG. 1(b) shows the cumulative probability of the currents at  $V_{\text{read}}$  for HRS and LRS. This plot confirms that both states are well defined and stable, with mean current values of  $\sim 10^{-11}$  A and  $\sim 2 \times 10^{-6}$  A for HRS and LRS, respectively. The cumulative probabilities of the switching voltages between both states ( $V_{\text{set}}$  and  $V_{\text{reset}}$ ) are shown in FIG. 1(c), which shows a clear variation between  $V_{\text{set}} = +0.1$  V and  $+0.6$  V (though always a positive voltage well below 1 V is required), whereas  $V_{\text{reset}}$  presents a small variation always taking negative values between  $-0.4$  V and  $-0.5$  V.



#### 4. Materials for Optoelectronics and Resistive Switching

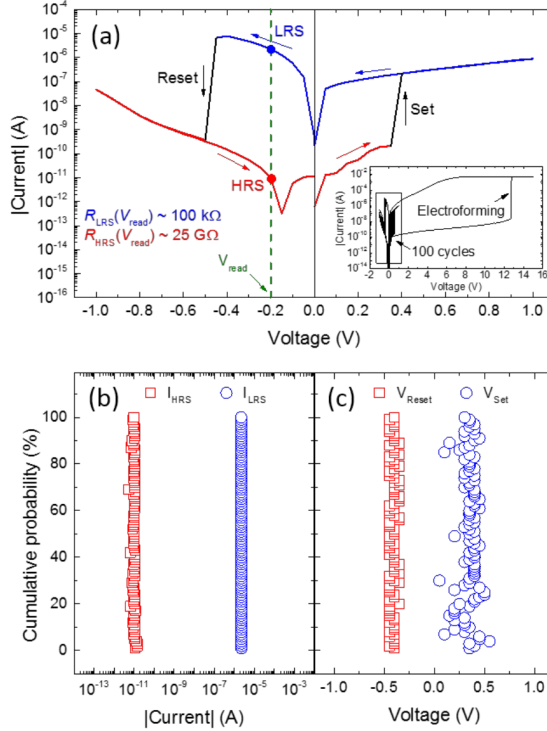


FIG. 1. (a)  $I(V)$  characteristics of one RS cycle, where the voltage sweep direction of each cycle is indicated by arrows. HRS and LRS are colored in red and blue, respectively, whereas the *set* and *reset* processes are displayed in black. The vertical green dashed line indicates the read voltage ( $V_{\text{read}}$ ) where the current is analyzed. In the inset, the electroforming process is shown, followed by the 100 cycles, as scale reference. (b) and (c) represent the cumulative probability of the HRS and LRS currents at  $V_{\text{read}}$ , and the cumulative probability of the  $V_{\text{set}}$  and  $V_{\text{reset}}$ , respectively, averaged over the 100 cycles.

Taking into account the maximum  $V_{\text{set}}$  and  $V_{\text{reset}}$  values observed along the 100 cycles (in absolute value), the device was submitted to a specific pulse-voltage pattern, as shown in FIG. 2(a). In brief, the first pulse forces the *set* by applying +2 V, followed by a second pulse at  $V_{\text{read}} = -0.2$  V to read the current of the LRS. The third pulse, at -1 V, induces

the *reset* towards HRS. Finally, the current at  $V_{\text{read}} = -0.2$  V is again monitored within this state. The duration of the *set* and *reset* pulses was kept at 50 ms, long enough to promote switching, as observed experimentally; instead, reading times were set to a much faster value, 0.1 ms, limited by the experimental setup. The device presented an endurance of more than 1000 periods with 99.5% of success, whose cumulative probability is represented in FIG. 2(b). In this case, LRS presents the same current values than the observed ones when the device was submitted to voltage ramps via  $I(V)$  curves [see FIG. 1(a)], taking values centered again around  $\sim 2 \times 10^{-6}$  A. This confirms that the LRS is well-defined under both excitation conditions. In contrast, HRS presents a larger current than the one obtained using  $I(V)$  curves. Whereas voltage ramps induced stable current intensity around  $\sim 10^{-11}$  A, pulsed excitation increases current intensity up to  $\sim 10^{-9}$  A. This difference in the current values within HRS could be related to the short duration of the pulse during the *reset* process, which affects the atomic arrangement, as suggested by Marchewka *et al.* in TaO<sub>x</sub>-based ReRAMs.<sup>16</sup>

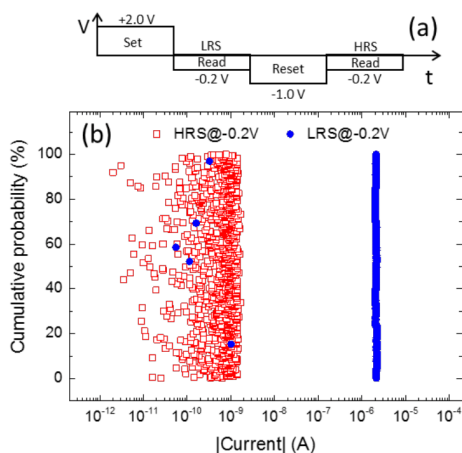


FIG. 2. (a) Scheme of the pulse-voltage pattern employed in the study. (b) Cumulative probability plot of HRS and LRS currents at  $V_{\text{read}}$  under the pulse schematics in (a), after more than 1000 periods.

In order to shed light on the physics underlying the memristive behavior of the ZnO-based device under study, the charge transport mechanisms governing the different states

#### 4. Materials for Optoelectronics and Resistive Switching

(pristine, HRS and LRS) were determined in the substrate accumulation regime ( $V < 0$  range). FIG. 3(a) represents the isolated  $I(V)$  curves corresponding to each of these three states in log-log representation. The three states present differentiated trends: the current intensity in the LRS exhibits a polynomial dependence on the applied voltage, whereas this dependence is exponential in the pristine state; in the HRS the situation is more complex and a combination of at least two mechanisms takes place.

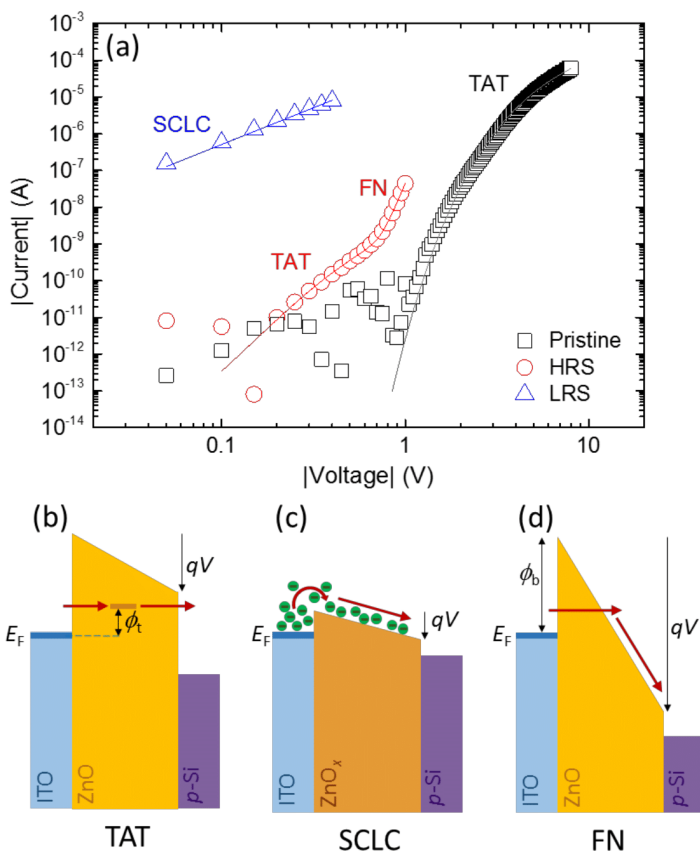


FIG. 3. (a) Log-log representation of the  $I(V)$  characteristics of pristine (black squares), HRS (red circles) and LRS (blue triangles) states with their respective charge transport

mechanism fits. All curves were acquired in substrate accumulation conditions ( $V < 0$ ). Sketches of the energy band diagram of TAT, SCLC and FN charge transport mechanisms are depicted in (b), (c) and (d), respectively. Whereas TAT and FN mechanisms take place in the ZnO (HRS), SCLC mechanism occurs in ZnO<sub>x</sub> (LRS).

In the pristine state, trap-assisted tunneling (TAT) mechanism might presumably be the dominant conduction mechanism in our devices, as ZnO is an undoped material with intrinsic intra-band electronic states (due to its defective nature);<sup>17</sup> a sketch of the energy band diagram for the TAT mechanism is depicted in FIG. 3(b). Under these conditions, the electrical current depends exponentially on the applied voltage, following the expression:<sup>17</sup>

$$I = \frac{qn_t S}{2\tau} \exp\left(-\frac{8\pi\sqrt{2m^*}d\phi_t^{3/2}}{3hqV}\right), \quad (1)$$

being  $q$  the elementary charge,  $n_t$  the trap areal density,  $S$  the area of the device,  $\tau$  the relaxation time between subsequent tunneling events,  $m^*$  the effective mass of electrons,  $d$  the thickness through which the electric field is applied,  $\phi_t$  the offset energy between the electrode Fermi level and the trap level, and  $h$  the Planck's constant.

Regarding the LRS, the observed high current intensity suggests a large amount of injected carriers, which is compatible with the space charge-limited current (SCLC) theory [see FIG. 3(c)], exhibiting a quadratic dependence on the voltage:<sup>18</sup>

$$I = \frac{9}{8} \mu \epsilon_0 \epsilon_r S \frac{V^2}{d^3}, \quad (2)$$

where  $\mu$  is the electron drift mobility, and  $\epsilon_0$  and  $\epsilon_r$  are the vacuum and relative permittivities, respectively. Finally, in the *reset* process, the conductivity of the devices dramatically decreases, reaching the HRS. Thus, the ZnO active layer becomes highly resistive and the intrinsic intra-band states are again relevant for the conduction. We observed that the current intensity dependence on the applied voltage exhibits two different trends, separated at a threshold voltage around 0.7 V [see FIG. 3(a)]. At voltages below this threshold, TAT mechanism should again dominate charge transport, whereas Fowler-Nordheim<sup>19</sup> (FN) could be the main conduction mechanism at higher electric fields, due to the further lowering of the potential barrier. Therefore, a combination of both mechanisms can be considered, following the expression:

$$I = \frac{qn_t S}{2\tau} \exp\left(-\frac{8\pi\sqrt{2m^*}d\phi_t^{3/2}}{3hqV}\right) + \frac{q^2 S}{8\pi^2 h d^2 \phi_b} V^2 \exp\left(-\frac{8\pi\sqrt{2m^*}d\phi_b^{3/2}}{3hqV}\right), \quad (3)$$

## 4. Materials for Optoelectronics and Resistive Switching

where the first and second terms of the right side of the equation correspond to TAT and FN models, respectively, being  $\phi_b$  the energy offset between the ITO electrode Fermi level and the ZnO conduction band [see FIG. 3(b,d)].

Under these considerations, we have fitted the experimental  $I(V)$  curves of the pristine, LRS and HRS states with the expressions from EQ. (1), EQ. (2) and EQ. (3), respectively. This procedure allows us extracting physical parameters from the devices which are relevant to understand the RS mechanism within.

For the pristine state, we have fitted the experimental data using EQ. (1) taking into account that the current flows over the full device area through the 60-nm thick ZnO layer, and using an electron effective mass for ZnO of  $0.3m_e$ ,<sup>20</sup> which results in  $\phi_t$  to be around 0.20 eV. Considering this mechanism, current is properly adjusted along more than six orders of magnitude, although some deviations are observed at voltages lower than 2 V. In fact, some other effects such as charge trapping can occur and, thus, the parameters that could be obtained from the pre-exponential factor are subjected to a large error.

Using EQ. 2, we have fitted the experimental data from LRS, obtaining an excellent agreement with the space charge-limited current (SCLC) conduction mechanism. From the fit, and assuming that for a substoichiometric  $\text{ZnO}_x$  the electron drift mobility ranges between 18 and 140  $\text{cm}^2\text{V}^{-1}\text{s}^{-1}$  and the relative permittivity is above 8.3,<sup>21,22</sup> we have found that the effective device area that is contributing to the conduction should be equal to or below  $1.4 \times 10^{-10} \text{ cm}^2$ , much lower than the actual top ITO contact area ( $2.1 \times 10^{-3} \text{ cm}^2$ ). This result suggests that the high current intensity observed in the LRS flows through filaments along the ZnO semiconductor layer. Taking into account the maximum active surface evidenced by the conduction mechanism, the current density along the CNFs can be evaluated, obtaining a lower limit of  $J = 1.6 \times 10^4 \text{ Acm}^{-2}$  at  $V_{\text{read}} = -0.2 \text{ V}$ . This current density is indeed excessively high, but still lower than the one observed in  $\text{TaO}_x/\text{TiO}_2/\text{TaO}_x$  structure, where values over  $10^7 \text{ Acm}^{-2}$  were achieved.<sup>23</sup> Further assuming that, in the *set* process, out-diffusion of oxygen ions is forming CNFs with diameters of about 25 nm (typical diameters reported in the literature lay between 10 and 50 nm<sup>11,12,24,25</sup>), the found active surface corresponds to 20 CNFs. Thus, this result suggests the formation of a limited number of conduction paths, with nanoscale dimensions.

Finally, we could successfully fit the HRS  $I(V)$  curve to EQ. 3. Actually, the experimental current intensity for voltages below  $V = 0.7$  V is properly reproduced by considering only the TAT contribution. The fact that the TAT mechanism is dominant at low voltages suggests a conduction through the ZnO defective states, in a similar way than in the pristine state. This assumption points out to CNFs being interrupted, presumably due to their partial re-oxidation. The overall current through the ZnO layer is limited by this gap region, which contributes to the HRS. Assuming that the current flows through a ZnO layer with similar structural and chemical composition than the one in the pristine state ( $\phi_t = 0.20 \pm 0.02$  eV), we found an effective thickness reduction of about 85 % (effective thickness of  $9 \pm 1$  nm). The electric field along the gap of the interrupted CNFs is enhanced by, at least, this thickness variation, leading to a value of  $\sim 0.8$  MVcm<sup>-1</sup> at  $V = 0.7$  V (see for instance Ref. 26, where there is an enhancement of the electric field in Ga:ZnO nanofibers due to boundary effects). This electric field is enough to inject carriers with high kinetic energy to overcome the ITO-ZnO band offset ( $\phi_b$ ), making dominant the FN mechanism. Actually, the experimental data is well reproduced by the FN model, with a band offset energy of  $\phi_b = 0.57 \pm 0.04$  eV, which is below the energy that carriers have at voltages above 0.7 V. The application of voltages larger than 1 V will produce again the *set* process, presumably by promoting out-diffusion of oxygen atoms towards the electrode.

The modeling of the pristine state, LRS and HRS in ZnO-based devices has allowed determining the mechanism responsible for the conduction in each of them, as well as important structural parameters. In the literature, these three states have also been analyzed: (i) the pristine shows trap-assisted conduction typical of dielectric materials, like Poole-Frenkel or TAT, in good agreement with our observations.<sup>27,28</sup> On the other hand, (ii) the LRS typically exhibits a high conductance with an Ohmic or SCLC behavior; considering the effective areas reported so far,<sup>12</sup> the current density reaches values compatible with ZnO with a high density of oxygen vacancies, indicating that the CNF formation is due to the out-diffusion of O atoms and/or oxygen deficiency in the film grown by magnetron sputtering. Finally, (iii) the HRS at low voltages presents again conduction typical of dielectric materials assisted by traps, suggesting that the conductive paths are partially re-oxidized, thus inducing the interruption of the CNFs along 9 nm. At larger voltages (above 0.7 V), injected carriers from the ITO contact present enough energy to overcome the ITO-ZnO potential barrier, exhibiting a FN behavior. The correlation between the charge transport mechanisms through ZnO and its structural

## 4. Materials for Optoelectronics and Resistive Switching

modification under external electrical stress helps anticipating the optimum operation conditions of ZnO-based memristors. In addition, subsequent cycles between positive and negative voltages can promote stable switching between the two states (HRS and LRS), maintaining the previously observed mechanisms.

Here, we have demonstrated the RS properties of ITO/ZnO/*p*-type Si devices. A difference in current of more than 5 orders of magnitude is observed between LRS and HRS, with endurance beyond  $10^3$  cycles, while working at low voltages. The analysis of the intensity-voltages curves has shown the formation of CNFs at the *set* process due to out-diffusion of O atoms, which is responsible for the LRS. In the *reset* process, these CNFs are interrupted along 9 nm by their re-oxidation, recovering the ZnO defective layer in this region. The fact that this region is in the range of some nanometers propitiated the observed high stability of the RS cycle in these devices. Overall, ZnO, when combined with *p*-type Si substrate and an ITO top electrode, is demonstrated as an excellent candidate for a future generation of RS memories, whose combination with other Si-based devices provides a large range of applications in transparent electronics.

### Acknowledgements

This work was financially supported by the Spanish Ministry of Economy and Competitiveness (Project Nos. TEC2012-38540-C02-01 and TEC2016-76849-C2-1-R). O.B. also acknowledges the subprogram “Ayudas para Contratos Predoctorales para la Formación de Doctores” from the Spanish Ministry of Economy and Competitiveness for economical support. X.P., C.L. and C.G. are grateful to C. Frilay for his expertise in the maintenance of the sputtering kit used for the growth of the ZnO films.

### References

- <sup>1</sup> I.G. Baek, M.S. Lee, S. Sco, M.J. Lee, D.H. Seo, D.-S. Suh, J.C. Park, S.O. Park, H.S. Kim, I.K. Yoo, U.-I. Chung, and J.T. Moon, in *IEDM Tech. Dig. IEEE Int. Electron Devices Meet. 2004*. (IEEE, 2004), pp. 587–590.
- <sup>2</sup> R. Waser and M. Aono, *Nat. Mater.* **6**, 833 (2007).
- <sup>3</sup> S. Kaeriyama, T. Sakamoto, H. Sunamura, M. Mizuno, H. Kawaura, T. Hasegawa, K. Terabe, T. Nakayama, and M. Aono, *IEEE J. Solid-State Circuits* **40**, 168 (2005).

- <sup>4</sup> D.B. Strukov and K.K. Likharev, *Nanotechnology* **16**, 888 (2005).
- <sup>5</sup> A. Mehonic, S. Cuff, M. Wojdak, S. Hudziak, O. Jambois, C. Labbé, B. Garrido, R. Rizk, and A.J. Kenyon, *J. Appl. Phys.* **111**, 074507 (2012).
- <sup>6</sup> A. Mehonic, A. Vrajitoarea, S. Cuff, S. Hudziak, H. Howe, C. Labbé, R. Rizk, M. Pepper, and A.J. Kenyon, *Sci. Rep.* **3**, 2708 (2013).
- <sup>7</sup> M.D. Pickett, G. Medeiros-Ribeiro, and R.S. Williams, *Nat. Mater.* **12**, 114 (2012).
- <sup>8</sup> S.H. Jo, T. Chang, I. Ebong, B.B. Bhadviya, P. Mazumder, and W. Lu, *Nano Lett.* **10**, 1297 (2010).
- <sup>9</sup> G. Vescio, A. Crespo-Yepes, D. Alonso, S. Claramunt, M. Porti, R. Rodriguez, A. Cornet, A. Cirera, M. Nafria, and X. Aymerich, *IEEE Electron Device Lett.* **38**, 457 (2017).
- <sup>10</sup> I. Valov, *ChemElectroChem* **1**, 26 (2014).
- <sup>11</sup> G. Martín, M.B. González, F. Campabadal, F. Peiró, A. Cornet, and S. Estradé, *Appl. Phys. Express* **11**, 014101 (2018).
- <sup>12</sup> F.M. Simanjuntak, D. Panda, K.-H. Wei, and T.-Y. Tseng, *Nanoscale Res. Lett.* **11**, 368 (2016).
- <sup>13</sup> J. Kim and K. Yong, *J. Phys. Chem. C* **115**, 7218 (2011).
- <sup>14</sup> Q. Yuan, Y. Zhao, L. Li, and T. Wang, *J. Phys. Chem. C* **113**, 6107 (2009).
- <sup>15</sup> S.Z. Rahaman, S. Maikap, H.-C. Chiu, C.-H. Lin, T.-Y. Wu, Y.-S. Chen, P.-J. Tzeng, F. Chen, M.-J. Kao, and M.-J. Tsai, *Electrochem. Solid-State Lett.* **13**, H159 (2010).
- <sup>16</sup> A. Marchewka, B. Roesgen, K. Skaja, H. Du, C.-L. Jia, J. Mayer, V. Rana, R. Waser, and S. Menzel, *Adv. Electron. Mater.* **2**, 1500233 (2016).
- <sup>17</sup> M. Krzywiecki, L. Grządziel, A. Sarfraz, D. Iqbal, A. Szwajca, and A. Erbe, *Phys. Chem. Chem. Phys.* **17**, 10004 (2015).
- <sup>18</sup> P.N. Murgatroyd, *J. Phys. D. Appl. Phys.* **3**, 151 (1970).
- <sup>19</sup> R.H. Fowler and L. Nordheim, *Proc. R. Soc. A Math. Phys. Eng. Sci.* **119**, 173 (1928).
- <sup>20</sup> Ü. Özgür, Y.I. Alivov, C. Liu, A. Teke, M.A. Reshchikov, S. Doğan, V. Avrutin, S.-J. Cho, and H. Morkoç, *J. Appl. Phys.* **98**, 041301 (2005).



## 4. Materials for Optoelectronics and Resistive Switching

- <sup>21</sup> E.M. Kaidashev, M. Lorenz, H. von Wenckstern, A. Rahm, H.-C. Semmelhack, K.-H. Han, G. Benndorf, C. Bundesmann, H. Hochmuth, and M. Grundmann, *Appl. Phys. Lett.* **82**, 3901 (2003).
- <sup>22</sup> D. Gall, *J. Appl. Phys.* **119**, 1 (2016).
- <sup>23</sup> W. Lee, J. Park, S. Kim, J. Woo, J. Shin, G. Choi, S. Park, D. Lee, E. Cha, B.H. Lee, and H. Hwang, *ACS Nano* **6**, 8166 (2012).
- <sup>24</sup> D.-H. Kwon, K.M. Kim, J.H. Jang, J.M. Jeon, M.H. Lee, G.H. Kim, X.-S. Li, G.-S. Park, B. Lee, S. Han, M. Kim, and C.S. Hwang, *Nat. Nanotechnol.* **5**, 148 (2010).
- <sup>25</sup> B.J. Choi, A.C. Torrezan, J.P. Strachan, P.G. Kotula, A.J. Lohn, M.J. Marinella, Z. Li, R.S. Williams, and J.J. Yang, *Adv. Funct. Mater.* **26**, 5290 (2016).
- <sup>26</sup> X. Sun, *SPIE Newsroom* **82**, 1096 (2006).
- <sup>27</sup> C. Hu, Q. Wang, S. Bai, M. Xu, D. He, D. Lyu, and J. Qi, *Appl. Phys. Lett.* **110**, 073501 (2017).
- <sup>28</sup> F. Gul and H. Efeoglu, *Superlattices Microstruct.* **101**, 172 (2017).



## Modulation of the electroluminescence emission from ZnO/Si NCs/*p*-Si light-emitting devices via pulsed excitation

J. López-Vidrier,<sup>1(a)</sup> S. Gutsch,<sup>1</sup> O. Blázquez,<sup>2</sup> D. Hiller,<sup>1</sup> J. Laube,<sup>1</sup> R. Kaur,<sup>1</sup> S. Hernández,<sup>2</sup> B. Garrido,<sup>2</sup> and M. Zacharias<sup>1</sup>

<sup>1</sup>Laboratory for Nanotechnology, IMTEK, Faculty of Engineering, University of Freiburg, Georges Köhler Allee 103, D-79110 Freiburg, Germany

<sup>2</sup>Departament d'Enginyeries: Electrònica, MIND-IN<sup>2</sup>UB, Universitat de Barcelona, Martí i Franquès 1, E-08028 Barcelona, Spain

(Received 31 March 2017; accepted 5 May 2017; published online 19 May 2017)

In this work, the electroluminescence (EL) emission of zinc oxide (ZnO)/Si nanocrystals (NCs)-based light-emitting devices was studied under pulsed electrical excitation. Both Si NCs and deep-level ZnO defects were found to contribute to the observed EL. Symmetric square voltage pulses (50- $\mu$ s period) were found to notably enhance EL emission by about one order of magnitude. In addition, the control of the pulse parameters (accumulation and inversion times) was found to modify the emission lineshape, long inversion times (i.e., short accumulation times) suppressing ZnO defects contribution. The EL results were discussed in terms of the recombination dynamics taking place within the ZnO/Si NCs heterostructure, suggesting the excitation mechanism of the luminescence centers via a combination of electron impact, bipolar injection, and sequential carrier injection within their respective conduction regimes. *Published by AIP Publishing.*  
<http://dx.doi.org/10.1063/1.4983722>

The potential of silicon nanocrystals (Si NCs) for optoelectronics has arisen the interest of the research community since the discovery of the quantum confinement effect,<sup>1</sup> which leads not only to a discretization of the allowed electronic states within the energy bands but also to an increase in the band gap energy of the bulk material.<sup>2,3</sup> In particular, the control of the NC size allows for Si band gap engineering,<sup>4</sup> which can be exploited towards tunable-light emission Si-based devices. For this reason, exhaustive efforts are dedicated to understand the charge injection mechanisms that yield electroluminescence (EL) emission from SiO<sub>2</sub>-embedded Si NCs-based light-emitting diodes (LEDs). Some reported works suggest bipolar injection to be the dominant excitation mechanism under DC conditions,<sup>5,6</sup> where simultaneous injection of electrons and holes into the NCs results in efficient exciton formation. Notwithstanding, the asymmetry of electrons and holes in tunneling through SiO<sub>2</sub> barriers often leads to a less efficient excitation via impact ionization.<sup>7,8</sup> To overcome limitations of DC excitation, pulsed emission was proposed that relies on the efficient sequential injection of electrons and holes into NCs,<sup>9–12</sup> effectively lowering operation voltages and hence increasing device stability.<sup>13</sup>

Considering the top contact, *n*-type poly-Si is typically employed for Si NC-based capacitors or field-effect transistors,<sup>5,6,9</sup> because it provides excellent charge injection and can be deposited and implanted via standard microelectronics techniques. Nevertheless, its absorption in the visible range overlaps with the Si NCs emission spectrum.<sup>14</sup> Therefore, wide-band gap *n*-type transparent conductive oxides (TCOs) such as indium tin oxide (ITO) are increasingly being used in these light-emitting systems.<sup>7,8</sup> In the present work, atomic

layer deposition (ALD) of zinc oxide (ZnO) was used for the top contact, which is a robust alternative for Si NCs-based LEDs.<sup>15,16</sup> In addition, ALD-ZnO presents luminescence properties under certain fabrication conditions and device design,<sup>16,17</sup> which could be used to complement the red-infrared NCs-based emission towards higher energies within the visible spectrum.

In this work, devices containing Si NCs/SiO<sub>2</sub> multilayers (MLs) as active luminescent layer were employed. A total number of five SiO<sub>0.93</sub>N<sub>0.23</sub> (SRON)/SiO<sub>2</sub> bilayers were deposited on top of (100) Si substrate (*p*-type, base resistivity of 1–20  $\Omega$ cm) by means of plasma-enhanced chemical-vapor deposition. The SRON and SiO<sub>2</sub> layer thicknesses were kept constant at 4.5 nm and 1 nm, respectively. A subsequent high-temperature annealing treatment was carried out at 1150 °C for 1 h in N<sub>2</sub> ambient, to induce phase separation resulting in the excess Si precipitation and crystallization in the form of Si NCs, followed by H<sub>2</sub> defect passivation at 450 °C for 1 h. The material properties of analogous Si NC/SiO<sub>2</sub> MLs concerning NC size, crystalline quality and optical absorption and emission have been reported in the past.<sup>18–23</sup> Finally, a 200-nm-thick ZnO film was deposited by ALD at 200 °C (Refs. 15 and 16) and patterned by conventional photolithography, followed by full-area Al metallization of the rear side. A cross-section sketch of the studied devices is shown in the inset of Fig. 1. Further details on the multilayers deposition and device fabrication can be found elsewhere.<sup>7,24,25</sup>

Current-voltage [*I*(*V*)] characterization was carried out in dark and at room temperature using an Agilent B1500 semiconductor device analyzer connected to a Microtech Summit 11000 probe station. Integrated electroluminescence was measured at room temperature by collecting the devices emission under DC electrical excitation with a Seiwa 888L

<sup>a</sup>Electronic mail: julia.lopez.vidrier@imtek.uni-freiburg.de

## 4. Materials for Optoelectronics and Resistive Switching

203104-2 López-Vidrier et al.

Appl. Phys. Lett. 110, 203104 (2017)

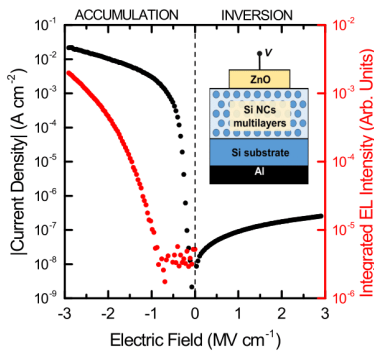


FIG. 1. Current density (black) and integrated EL emission intensity (red) as a function of the applied electric field. The inset shows a cross-section scheme of the devices under study.

microscope using a long working distance  $20\times$  objective (NA = 0.4), coupled to a calibrated Hamamatsu GaAs R928 photomultiplier tube. The EL spectra were acquired by a Princeton Instruments LN<sub>2</sub>-cooled CCD coupled to a monochromator, under either DC or pulsed excitation. Time-resolved EL measurements were performed by collecting the resulting integrated EL emission using a high-time resolution Agilent Infinium DSO 8064A oscilloscope.

The current density vs. electric field [ $J(E)$ ] characteristic of the device is presented in Fig. 1. As expected from the device design, the  $J(E)$  curve exhibits a strong rectifying behavior. At substrate accumulation ( $E < 0$ ) bipolar injection is possible, whereas in substrate inversion ( $E > 0$ ), the current is strongly limited by the  $p$ -Si depletion layer. Integrated EL intensity (red curve in Fig. 1) was measured over the whole scanned voltage range, although the actual signal was observed only in accumulation (see Ref. 8 for a detailed study on the power efficiency from devices containing analogous MLs). The onset for EL was found to be remarkably low, around  $-0.84 \text{ MV cm}^{-1}$  ( $\sim -2.3 \text{ V}$ ), corresponding to a minimum injection current density of  $\sim 10^{-3} \text{ A cm}^{-2}$  required to excite the luminescent centers within the device. This onset voltage is indeed comparable to previous reported works on similar structures.<sup>6</sup>

A further inspection of the EL emission properties of the device was performed by spectrally resolving the acquired signal, under a constant DC excitation of  $-7 \text{ V}$  (accumulation, equivalent to  $-2.55 \text{ MV cm}^{-1}$  and corresponding to  $J \sim 2 \times 10^{-2} \text{ A cm}^{-2}$ ). The resulting spectrum is displayed in Fig. 2(a), which exhibits a broad lineshape ranging from 400 nm to 1100 nm. Indeed, all acquired spectra could be deconvoluted into two well-defined contributions, as observed in Fig. 2(a), peaking around 700 nm and 850 nm. The origin of the low-energy contribution is typically ascribed to the excitonic recombination at the fundamental quantum-confined electronic states of Si NCs.<sup>20</sup> For the sake of direct comparison, Fig. 2(b) presents an EL spectrum from a previous publication, corresponding to a Si NC MLs-based sample with the

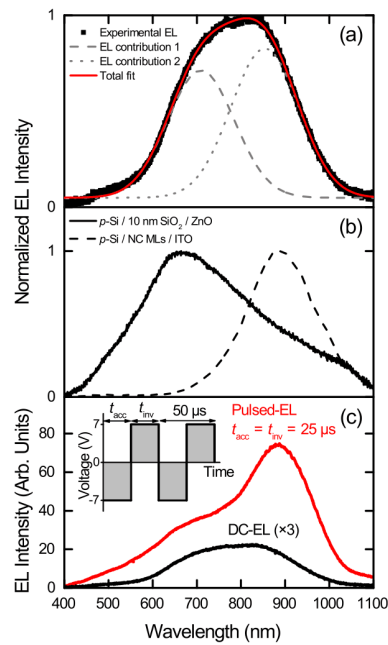


FIG. 2. (a) Normalized experimental EL spectrum acquired from the device under study (black points), fitted according to two different contributions (dashed and dotted grey lines), whose sum (solid red line) is in excellent agreement with the experimental data. (b) Normalized EL spectra corresponding to a reference sample containing a 10-nm-thick SiO<sub>2</sub> layer instead of NC MLs and ZnO electrode (solid line) and to an analogous NC ML sample with ITO instead of ZnO as top electrode, dashed line) taken from Ref. 7. (c) Direct comparison between spectra acquired under DC (black) and pulsed (red) excitation. The inset shows the pulse schematics.

same structural parameters but with ITO instead of ZnO as top TCO electrode.<sup>7</sup> In fact, the fundamental difference between both samples, i.e., the different TCO, highlights the possibility that the high-energy EL contribution in Fig. 2(a) is related to ZnO. Again, Fig. 2(b) may shed light to the origin of this contribution by displaying the EL spectrum acquired on a reference sample containing a 10-nm-thick SiO<sub>2</sub> layer instead of Si NC MLs and with the same ALD-deposited ZnO on top. Note that in this case larger electric fields are required to achieve permanent current flow in the Fowler-Nordheim regime. This emission is centered around 700 nm, and its broadness indicates the excitation of luminescent centers within a wide range of electronic level energies, as usually obtained from deep-level defect states in ZnO (donor-acceptor pairs generated by O vacancies and Zn interstitials);<sup>27</sup> the fact that no near-band gap excitonic recombination of ZnO is observed around 380 nm (and thus no emission tail is detected)<sup>28</sup> can be due either to a lower excitation energy than the ZnO band gap or to no additional annealing treatment being carried out on the ZnO-deposited samples.<sup>17</sup> Actually,

the hypothesis of emission coming from ZnO intra-band gap defect states is supported by the observation of ZnO-related contribution broadening towards higher energies when increasing the DC excitation current density (not shown here), which promotes electron-hole pair generation in higher-energy defect states within the ZnO band gap.

Once the different contributions to EL were identified, efforts were focused on the effect of pulsed excitation on the emission. For this, a square voltage pulse, symmetric between  $-7$  V and  $7$  V (well within the accumulation and the substrate inversion regimes, respectively), was employed [see inset of Fig. 2(c)], whose result is displayed in Fig. 2(c) in comparison to the spectrum resulting from DC excitation at  $-7$  V [see Fig. 2(a)]. A pulse period of  $50$   $\mu$ s was selected (equivalent to a driving frequency of  $20$  kHz), which showed the maximum emission yield in our samples, in good agreement with previous reported works on analogous systems and methodologies.<sup>9,10,13</sup> In addition, we selected a 50% duty cycle, i.e., accumulation ( $t_{acc}$ ) and inversion ( $t_{inv}$ ) pulse times of  $25$   $\mu$ s, as schematized in the inset of Fig. 2(c). We observe a huge enhancement of the EL intensity under applied pulsed excitation, estimated as a factor  $\sim 9$  from the ratio between the EL integrated areas. This behavior was first observed by Walters *et al.*<sup>9</sup> and was attributed to the sequential injection of carriers from the Si substrate towards the active layer under alternate accumulation and inversion cycles. Provided that the system response to this type of excitation is tightly related to the carrier injection characteristics, the duty cycle of the pulse is expected to play an important role on the EL emission of the system. Under this assumption, we modified the duty cycle by applying different accumulation and inversion times, while keeping fixed the  $50$ - $\mu$ s pulse period. The limiting cases are displayed in Fig. 3. As can be observed, the spectral lineshape drastically evolves, shorter  $t_{acc}$  (and thus longer  $t_{inv}$ ) inducing the progressive quenching of the ZnO defects-related contribution, and consequently leaving Si NCs as the only active luminescent centers.

To understand the effect of the different pulsed excitation characteristics on the EL emission output, it is necessary to analyze the recombination dynamics taking place within the system. Fig. 4(a) displays the EL emission dynamics on a whole excitation period of  $1$  ms ( $t_{acc} = t_{inv} = 500$   $\mu$ s). This period was intentionally selected to provide complete charging of the luminescent species and corresponding EL decay. Please note that, since radiative recombination in ZnO defects emission typically takes place in the nanosecond range,<sup>29</sup> the observed slow EL decay in the figure (microsecond range) must necessarily be dominated by processes taking place within the Si NC MLs. Indeed, the dynamics pattern is similar to the ones reported in Ref. 8, where analogous Si NC MLs-based devices were analyzed that contained ITO electrode instead of ZnO, again evidencing that processes taking place in ZnO are not reflected in the observed dynamics. Focusing again on Fig. 4(a), markedly different phenomena occur under opposite charging regimes. In accumulation, EL emission increases up to a constant DC-like emission level, being the rise time estimated as  $\sim 18$   $\mu$ s. Once the pulse voltage is switched from  $-7$  V to  $7$  V, i.e., the deep depletion regime is reached, an EL overshoot (rise

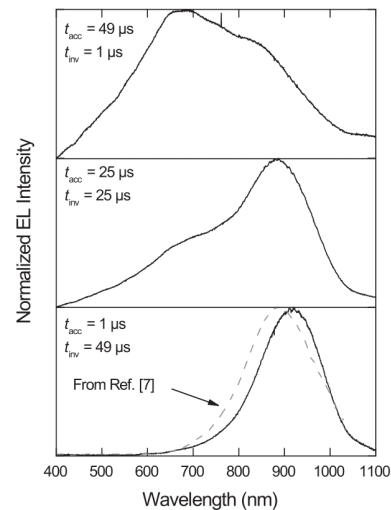


FIG. 3. Normalized EL spectra acquired under pulsed excitation, using a symmetric square-voltage pulse of  $-7/7$  V and different accumulation and inversion times, while holding a fixed period of  $50$   $\mu$ s. The EL spectrum from an analogous sample from Ref. 7 is also displayed (grey dashed line).

time  $\sim 17$   $\mu$ s) takes place followed by a slow decay, whose single-exponential fit resulted in a decay time of  $\sim 76$   $\mu$ s. The estimated characteristic times are in good agreement with expected values for Si NCs.<sup>30–32</sup>

The EL recombination dynamics of the system sheds light on the carrier injection and excitation processes taking place within the device structure. These mechanisms are illustrated by the energy band diagrams displayed in Fig. 4(b). In accumulation, holes are injected into the Si NC MLs from the valence band of the  $p$ -type Si substrate, while electrons are injected from the ZnO top electrode. The observed emission of ZnO can only be explained by electron-hole generation as a consequence of hole injection from the Si NC MLs into the ZnO electrode, where a high concentration of electrons exists ( $\sim 5 \times 10^{19}$   $\text{cm}^{-3}$ ). Due to the large band offset between the ZnO and the Si NCs valence bands, ZnO is essentially a hole-blocking contact. However, defects-related deep-level states are possibly excited by holes, which is the reason of the missing observation of ZnO band gap transition in the EL spectra. Regarding the observed Si NCs-related EL emission, it must be a consequence of electron-hole pair generation within the quantum-confined NC states. Note that, because of injection asymmetry between electrons and holes (hole mobility is several orders of magnitude lower than that of electrons),<sup>33</sup> and although bipolar excitation of opposite electrode-injected carriers cannot be entirely ruled out, generation of electron-hole pairs in Si NCs most likely occurs via electron impact of tunneling electrons from the ZnO electrode.<sup>34</sup> However, it was recently shown that defect states at Si NC interfaces may allow for band-to-band

## 4. Materials for Optoelectronics and Resistive Switching

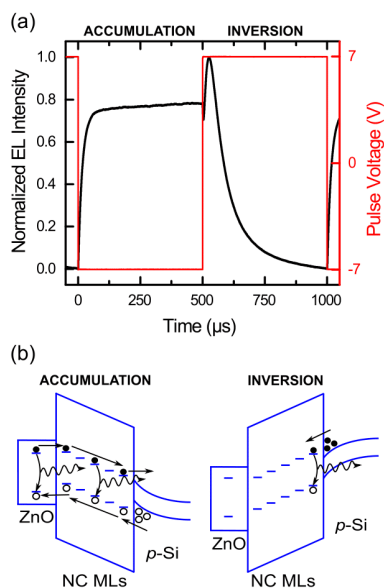


FIG. 4. (a) EL emission dynamics (black) over a period of 1 ms (50% duty cycle), corresponding to the device under study (the employed voltage pulse in red). (b) Energy band diagrams corresponding to the ZnO/NC MLs/p-Si system under the respective conduction regimes.

excitation at electric fields below  $1 \text{ MV cm}^{-1}$ ,<sup>25</sup> effectively generating massive amounts of holes that accumulate at the ZnO-MLs interface (mechanism not shown in the band diagrams). Both mechanisms are feasible in the present structure, and support the observed constant EL emission level. In this process, hole injection and defect-related hole generation within the Si NC MLs, as well as the higher electron mobility leading to more efficient electron transport through the MLs, may result in non-compensated (i.e., non-recombined) positively charged Si NCs. Under inversion, minority carriers from the substrate (electrons in the formed inversion layer at the substrate-MLs interface) are injected into these positively charged NCs via Coulomb field-enhanced tunneling, the so-called sequential carrier injection,<sup>9,10</sup> which induces electron-hole pair formation resulting in the EL emission overshoot observed in Fig. 4(a). This exciton formation is maximized when all positively charged NCs are neutralized, after which EL decays. Under this regime, excitation of the luminescent centers is not achieved because of both the unlikely hole injection from ZnO (*n*-type) and the low electron injection rate from the *p*-type substrate, so that neither bipolar nor impact excitation are possible; as a consequence, no EL emission is observed in conventional (DC-excited) spectra.

Recovering again the results displayed in Fig. 3, the proposed frame for excitation may explain the quenching of ZnO defects-related emission. When the pulse is governed

by the accumulation regime (i.e., longer  $t_{\text{acc}}$  is employed), hole injection into ZnO defects and electron impact of (or electron-hole bipolar injection into) Si NCs are achieved. In this case,  $t_{\text{inv}} = 1 \mu\text{s}$  is notably shorter than the inversion decay time ( $\sim 6 \mu\text{s}$ ), and thus complete discharge of the Si NCs is not fulfilled. As  $t_{\text{inv}}$  increases, exciton generation within ZnO and Si NCs still takes place, whereas the efficiency of Coulomb field-enhanced electron-hole pair formation is increased; this is translated into an enhancement of the Si NC-related EL with respect to ZnO. These findings are further supported by an enhanced Si NC-related EL emission observed when increasing the voltage (not shown), where a more efficient electron injection from the inversion layer is achieved. Finally, when decreasing  $t_{\text{acc}}$  to  $1 \mu\text{s}$ , electron and hole injection is not efficient throughout the device, and thus no holes can be injected from the MLs into ZnO, which totally quenches ZnO emission. In contrast, this accumulation time is long enough to positively charge the Si NCs next to the substrate-ML interface, which favors recombination by neutralization within this region and results in the sole presence of Si NCs-related emission in the acquired spectra.

So far, this work has revealed that, in ZnO/Si NC MLs/*p*-Si LEDs, EL emission results from a complex charge injection and excitation pattern. On one hand, DC excitation in accumulation regime leads to emission by impact excitation of Si NCs and by electron-hole pair generation in ZnO after hole injection into deep-level intra-band gap defects. On the other hand, the recombination dynamics becomes far less intuitive when a pulsed excitation is employed, where a sequential Coulomb field-enhanced electron-hole generation adds to impact excitation, resulting in an enhanced EL emission with respect to the DC case. In addition, the relative emission from the different luminescent centers can be modified by controlling the pulse parameters ( $t_{\text{acc}}$  and  $t_{\text{inv}}$ ), which can be exploited towards particular optoelectronic applications requiring whole-visible range emission. Overall, these observations shed light to the sequential charging of Si NCs, a promising field for Si NCs EL. It is foreseen that the modification of NC-based LED design will lead to enhanced sequential bipolar excitation in detriment to inefficient impact ionization, which will notably improve the performance of Si NC-based devices.

This work was financially supported by the German Research Foundation (ZA191/27-3 and ZA191/33-1) and the Spanish Ministry of Economy and Competitiveness (TEC2016-76849-C2-1-R).

<sup>1</sup>L. T. Canham, *Appl. Phys. Lett.* **57**, 1046 (1990).

<sup>2</sup>F. Iacona, G. Franzò, and C. Spinella, *J. Appl. Phys.* **87**, 1295 (2000).

<sup>3</sup>F. Iacona, G. Franzò, V. Vinciguerra, A. Irrera, and F. Priolo, *Opt. Mater.* **17**, 51 (2001).

<sup>4</sup>M. Zacharias, J. Heitmann, R. Scholz, U. Kahler, M. Schmidt, and J. Bläsing, *Appl. Phys. Lett.* **80**, 661 (2002).

<sup>5</sup>A. Marconi, A. Anopchenko, M. Wang, G. Pucker, P. Bellutti, and L. Pavesi, *Appl. Phys. Lett.* **94**, 221110 (2009).

<sup>6</sup>A. Anopchenko, A. Marconi, E. Moser, S. Prezioso, M. Wang, L. Pavesi, G. Pucker, and P. Bellutti, *J. Appl. Phys.* **106**, 033104 (2009).

<sup>7</sup>J. López-Vidrier, Y. Berencén, S. Hernández, O. Blázquez, S. Gutsch, J. Laube, D. Hiller, P. López, M. Schnabel, S. Janz, M. Zacharias, and B. Garrido, *J. Appl. Phys.* **114**, 163701 (2013).

- <sup>8</sup>J. López-Vidrier, Y. Berencén, S. Hernández, B. Mundet, S. Gutsch, J. Laube, D. Hiller, P. Löper, M. Schnabel, S. Janz, M. Zacharias, and B. Garrido, *Nanotechnology* **26**, 185704 (2015).
- <sup>9</sup>R. J. Walters, G. I. Bourianoff, and H. A. Atwater, *Nat. Mater.* **4**, 143 (2005).
- <sup>10</sup>R. J. Walters, J. Carreras, T. Feng, L. D. Bell, and H. A. Atwater, *IEEE J. Sel. Top. Quantum Electron.* **12**, 1647 (2006).
- <sup>11</sup>M. Perálvarez, C. García, M. López, B. Garrido, J. Barreto, C. Domínguez, and J. A. Rodríguez, *Appl. Phys. Lett.* **89**, 051112 (2006).
- <sup>12</sup>J. Barreto, M. Perálvarez, J. A. Rodríguez, A. Morales, M. Riera, M. López, B. Garrido, L. Lechuga, and C. Domínguez, *Physica E* **38**, 193 (2007).
- <sup>13</sup>T. Creazzo, B. Redding, E. Marchena, J. Murakowski, and D. W. Prather, *Opt. Express* **18**, 10924 (2010).
- <sup>14</sup>O. Blázquez, J. López-Vidrier, S. Hernández, J. Montserrat, and B. Garrido, *Energy Procedia* **44**, 145 (2014).
- <sup>15</sup>J. Laube, D. Nübling, H. Beh, S. Gutsch, D. Hiller, and M. Zacharias, *Thin Solid Films* **603**, 377 (2016).
- <sup>16</sup>H. Beh, D. Hiller, J. Laube, S. Gutsch, and M. Zacharias, *J. Vac. Sci. Technol. A* **35**, 01B127 (2017).
- <sup>17</sup>R. Könenkamp, R. C. Word, and M. Godinez, *Nano Lett.* **5**, 2005 (2005).
- <sup>18</sup>S. Gutsch, D. Hiller, J. Laube, M. Zacharias, and C. Kübel, *Beilstein J. Nanotechnol.* **6**, 964 (2015).
- <sup>19</sup>J. López-Vidrier, S. Hernández, D. Hiller, S. Gutsch, L. López-Conesa, S. Estradé, F. Peiró, M. Zacharias, and B. Garrido, *J. Appl. Phys.* **116**, 133505 (2014).
- <sup>20</sup>H. Gnaser, S. Gutsch, M. Wahl, R. Schiller, M. Kopnarski, D. Hiller, and M. Zacharias, *J. Appl. Phys.* **115**, 034304 (2014).
- <sup>21</sup>S. Hernández, J. López-Vidrier, L. López-Conesa, D. Hiller, S. Gutsch, J. Ibáñez, S. Estradé, F. Peiró, M. Zacharias, and B. Garrido, *J. Appl. Phys.* **115**, 203504 (2014).
- <sup>22</sup>J. Valenta, M. Greben, Z. Remeš, S. Gutsch, D. Hiller, and M. Zacharias, *Appl. Phys. Lett.* **108**, 023102 (2016).
- <sup>23</sup>J. Ibáñez, S. Hernández, J. López-Vidrier, D. Hiller, S. Gutsch, M. Zacharias, A. Segura, J. Valenta, and B. Garrido, *Phys. Rev. B* **92**, 035432 (2015).
- <sup>24</sup>A. M. Hartel, D. Hiller, S. Gutsch, P. Löper, S. Estradé, F. Peiró, B. Garrido, and M. Zacharias, *Thin Solid Films* **520**, 121 (2011).
- <sup>25</sup>S. Gutsch, J. Laube, A. M. Hartel, D. Hiller, N. Zakharov, P. Werner, and M. Zacharias, *J. Appl. Phys.* **113**, 133703 (2013).
- <sup>26</sup>J. Valenta, N. Lalic, and J. Linnros, *Opt. Mater.* **17**, 45 (2001).
- <sup>27</sup>Y. Chen, D. M. Bagnall, H. Koh, K. Park, K. Hiraga, Z. Zhu, and T. Yao, *J. Appl. Phys.* **84**, 3912 (1998).
- <sup>28</sup>Y. X. Liu, Y. C. Liu, C. L. Shao, and R. Mu, *J. Phys. D: Appl. Phys.* **37**, 3025 (2004).
- <sup>29</sup>A. J. Morfa, B. C. Gibson, M. Karg, T. J. Karle, A. D. Greentree, P. Mulvaney, and S. Tomljenovic-Hanic, *Nano Lett.* **12**, 949 (2012).
- <sup>30</sup>N. Lalic and J. Linnros, *J. Appl. Phys.* **80**, 5971 (1996).
- <sup>31</sup>J. Linnros, N. Lalic, A. Galeckas, and V. Grivickas, *J. Appl. Phys.* **86**, 6128 (1999).
- <sup>32</sup>M. Dovrat, Y. Goshen, J. Jedrzejewski, I. Balberg, and A. Sa'ar, *Phys. Rev. B* **69**, 155311 (2004).
- <sup>33</sup>J. F. Verwey, E. A. Amerasekera, and J. Bischoff, *Rep. Prog. Phys.* **53**, 1297 (1990).
- <sup>34</sup>Z. Liu, J. Huang, P. C. Joshi, A. T. Voutsas, J. Hartzell, F. Capasso, and J. Bao, *Appl. Phys. Lett.* **97**, 071112 (2010).



# Effect of Si<sub>3</sub>N<sub>4</sub>-Mediated Inversion Layer on the Electroluminescence Properties of Silicon Nanocrystal Superlattices

Julian López-Vidrier,\* Sebastian Gutsch, Oriol Blázquez, Jan Valenta, Daniel Hiller, Jan Laube, Javier Blanco-Portals, Lluís López-Conesa, Sònia Estradé, Francesca Peiró, Blas Garrido, Sergi Hernández, and Margit Zacharias

The achievement of an efficient all-Si electrically-pumped light emitter is a major milestone in present optoelectronics still to be fulfilled. Silicon nanocrystals (Si NCs) are an attractive material which, by means of the quantum confinement effect, allow attaining engineered bandgap visible emission from Si by controlling the NC size. In this work, SiO<sub>2</sub>-embedded Si NCs are employed as an active layer within a light-emitting device structure. It is demonstrated that the use of an additional thin Si<sub>3</sub>N<sub>4</sub> interlayer within the metal–insulator–semiconductor device design induces an enhanced minority carrier injection from the substrate, which in turn increases the efficiency of sequential carrier injection under pulsed electrical excitation. This results in a substantial increase in the electroluminescence efficiency of the device. Here, the effect of this Si<sub>3</sub>N<sub>4</sub> interlayer on the structural, optical, electrical, and electro-optical properties of a Si NC-based light emitter is reported, and the physics underlying these results is discussed.

## 1. Introduction

Given the huge impact of quantum confinement on the electronic properties of silicon nanocrystals (Si NCs), namely the band structure modification as a function of the NC size,<sup>[1–4]</sup> in-depth studies have been carried out on the physical mechanisms involved in the optical<sup>[5–7]</sup> and electrical<sup>[8–10]</sup> performance of SiO<sub>2</sub>-embedded Si NCs, and their potential to become active material candidates in optoelectronic applications such as light-emitting devices (LEDs).<sup>[11–13]</sup> Light emission from Si NCs has recently become a very promising field, which can set a basis for novel fully Si-based optoelectronics and photonics. Indeed, the photoluminescence (PL) quantum yield (QY) of Si NCs in SiO<sub>2</sub>, i.e., the ratio between the photons

that are absorbed in and emitted from Si NCs, has been estimated by several groups, and QY efficiencies exceeding even 30% have been reported.<sup>[14,15]</sup> Nevertheless, the case of electron-to-photon conversion is not so straightforward in SiO<sub>2</sub>-embedded Si NCs, because carrier injection is strongly limited by the high band offset between the Si NC and the dielectric host, which can only be overcome under certain tunneling conditions.<sup>[16]</sup> In this respect, some works have addressed the excitation mechanisms that govern the electroluminescence (EL) emitted by size-controlled Si NCs in SiO<sub>2</sub>. Among the most accepted hypotheses, electron–hole pairs are believed to be formed within Si NCs after bipolar carrier injection and/or impact ionization via high-kinetic-energy electrons; while the former approach claims that electrons and holes are injected from the electrodes to the NC system at a similar rate,<sup>[17,18]</sup> the latter takes into account the asymmetry of injection efficiency due to the mobility difference between both carriers in the oxide.<sup>[19,20]</sup> In any case, the overall power efficiency (PE) of these systems, i.e., the ratio between the optical output and the electrical input, is low.

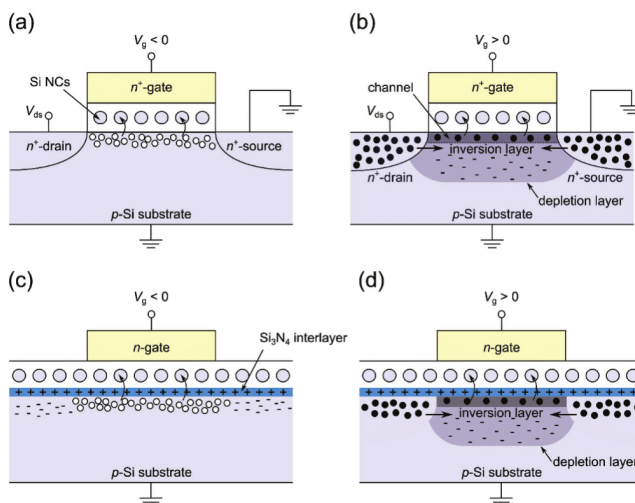
Aiming to increase the power efficiency of Si NCs/SiO<sub>2</sub>-based light-emitting devices, different strategies have been conceived. Such is the case of the pulsed electrical excitation of Si NC-based LEDs, which was found to substantially

Dr. J. López-Vidrier, Dr. S. Gutsch, Dr. D. Hiller, Dr. J. Laube, Prof. M. Zacharias  
Laboratory of Nanotechnology  
IMTEK  
Faculty of Engineering  
Albert-Ludwigs Universität Freiburg  
Georges-Köhler-Allee 103, 79110 Freiburg, Germany  
E-mail: julia.lopez.vidrier@imtek.uni-freiburg.de  
O. Blázquez, J. Blanco-Portals, Dr. L. López-Conesa, Dr. S. Estradé,  
Prof. F. Peiró, Prof. B. Garrido, Dr. S. Hernández  
MIND-IN<sup>2</sup>UB  
Departament d'Enginyeries: Electrònica  
Universitat de Barcelona  
C/Martí i Franquès 1, 08028 Barcelona, Spain  
Prof. J. Valenta  
Faculty of Mathematics and Physics  
Charles University  
Ke Karlovu 3, 121 16 Prague 2, Czech Republic  
Dr. L. López-Conesa  
Unitat TEM-MAT  
Centres Científics i Tecnològics de la Universitat de Barcelona (CCiTUB)  
Lluís Solé i Sabarís 1, 08028 Barcelona, Spain

 The ORCID identification number(s) for the author(s) of this article can be found under <https://doi.org/10.1002/aelm.201700666>.

DOI: 10.1002/aelm.201700666



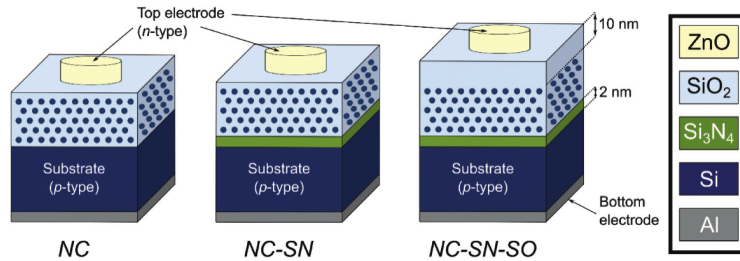


**Figure 1.** Cross-sectional schematic of the Si NC-based MOSFET device employed by Walters et al.<sup>[21]</sup> in either substrate a) accumulation or b) inversion regimes, where sequential carrier injection from the substrate, respectively holes (open circles) and electrons (full circles), is fostered.  $V_{ds}$  and  $V_g$  are, respectively, the drain–source and gate voltages. c,d) The sketch corresponding to the proposed MOS device design that includes an intrinsically high positively charged interlayer (in blue), respectively in substrate accumulation and inversion regimes. Such an interlayer will present fixed positive charges (+), whereas fixed negative charges (–) are found within the substrate. The shaded regions in panels (b) and (d) indicate the inversion layer (dark gray) and depletion zone (light gray) formed below the NC-based layer.

enhance their EL emission yield by more than one order of magnitude, apart from reducing device degradation and power consumption.<sup>[21–26]</sup> This approach takes advantage of the sequential carrier injection within the NCs, which improves the poor bipolar injection efficiency shown by hot-carrier-based conventional DC excitation mechanisms. In particular, the work by Walters et al. reported a metal-oxide–semiconductor field-effect transistor (MOSFET) structure. Here, the channel created between the heavily doped drain and source terminals acts as a selective carrier injection layer that allows for “charge programming” the Si NCs embedded in a bulk  $\text{SiO}_2$  layer, with holes in accumulation and electrons in inversion, as illustrated in Figure 1a and Figure 1b, respectively.<sup>[21,22]</sup> The key point of this device design takes place in inversion conditions, where an *n*-type channel is created between drain and source that provides additional electrons to the substrate ones. In another approach, Creazzo et al. opted for a MOS capacitor structure, much simpler in terms of a design than a transistor device, where the active oxide material consisted of several Si NC superlattices.<sup>[26]</sup> Learning from these structures, we propose here an alternative NC-based device design that allows for an improved sequential injection while preserving the simplicity of the MOS design. Specifically, we employ the intrinsically high positive charge density of  $\text{Si}_3\text{N}_4$ ,<sup>[27]</sup> which we place between the Si substrate and the NC-based active layer. In substrate accumulation conditions

(Figure 1c), holes from the substrate are normally accumulated at the substrate/interlayer interface, thus being injected into the NC-based layer. The real advantage of this structure is found in substrate inversion regime, where a permanent inversion layer underneath the interlayer region surrounding the gate contact can supply large amounts of electrons for the region underneath the gate. This structure mimics Walters et al.’s *n*-type MOSFET channel by injecting additional electrons from the substrate into the NCs (Figure 1d). Therefore, this interlayer is expected to enhance the injection of both carriers into the NC-based active layer under the corresponding polarization regimes.

We will demonstrate here that the controlled generation of an inversion layer through the above-described interlayer approach results in a significant enhancement of the EL efficiency of Si NC-based MOS capacitors under pulsed electrical excitation. For this, we designed three different samples allowing us to compare the obtained results not only with our previous works but also with those reported in the literature. With this objective, a careful structural, optical, electrical, and electro-optical characterization is carried out, from which the carrier injection and Si NC excitation mechanisms that take place within our devices can be assessed. It is the aim of this work to study, in detail, the effect of the hereby selected different device configurations on the EL performance of Si NC-based LEDs.



**Figure 2.** Sketch of the device structures under study. They essentially consist of  $5 \times \text{Si NC/SiO}_2$  superlattices deposited on top of  $p$ -type Si substrate, with a circular ALD–ZnO top electrode and a backside full-area Al metallization (device NC). Device NC-SN contains an extra 2 nm  $\text{Si}_3\text{N}_4$  interlayer between the Si substrate and the Si NC SLs. Device NC-SN-SO was designed as device NC-SN, but containing an additional 10 nm  $\text{SiO}_2$  layer between the Si NC SLs and the top ZnO electrode. On the right-hand side, a legend is provided with the color correspondence to each material. Thicknesses are not to scale.

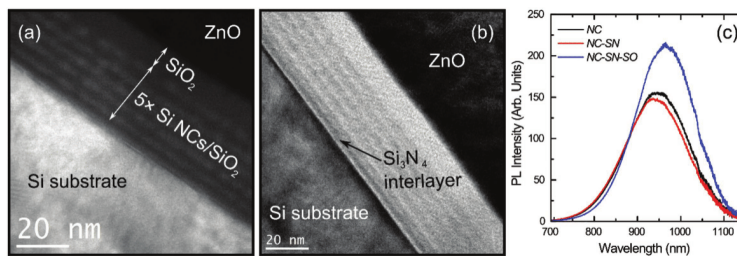
## 2. Results

### 2.1. Material Structure Inspection

The employed approach makes use of an engineered inversion layer, which allows tuning the carrier injection mechanism into the Si NCs and, as a result, allows modifying their EL emission in a controlled manner. To inspect this effect, three different samples were fabricated. The basic structure (labeled as “NC”) contains a stack of  $5 \times \text{Si NC/SiO}_2$  superlattices (SLs, nominal layer thicknesses of 4.5 and 1 nm, respectively, and a total active layer nominal thickness of 27.5 nm) deposited on top of a  $p$ -type Si substrate. This number of SLs was selected according to general EL performance criteria, since thicker SL stacks exhibit poor carrier injection (and thus higher EL onset voltage) and thinner ones release a barely observable luminescence. Top and bottom contacts were made by transparent and intrinsically conductive ( $n$ -type) ZnO and Al contacts, respectively. The inversion layer is achieved by the inclusion of a 2 nm  $\text{Si}_3\text{N}_4$  interlayer between the Si substrate and the first Si NC/ $\text{SiO}_2$  bilayer, which constitutes the device labeled as “NC-SN” (total nominal thickness of 29.5 nm). This interlayer thickness was found to be optimum for our investigation

purposes, since slightly thicker layers do not affect the superlattices PL, whereas they clearly decrease the current density through the device. Finally, the additional effect of blocking the carrier injection from the top electrode is analyzed by embedding a 10 nm  $\text{SiO}_2$  layer between the last NC layer and the atomic layer deposition (ALD)–ZnO top electrode, in the device labeled as “NC-SN-SO” (total nominal thickness of 39.5 nm). In **Figure 2**, the schematics corresponding to the three device designs are displayed.

The cross section of the devices was directly imaged by means of transmission electron microscopy (TEM). In particular, **Figure 3a** displays an energy-filtered TEM (EFTEM) image from the cross section of device NC-SN-SO. This particular sample was selected since it presents all the distinct characteristics under study, namely the Si NC/ $\text{SiO}_2$  SLs, the  $\text{Si}_3\text{N}_4$  interlayer, and the additional  $\text{SiO}_2$  capping layer. By filtering around the Si plasmon energy ( $E_{\text{Si}} = 16.7$  eV), the contrast of the regions containing high Si content is highlighted (bright regions). This analysis allows the observation of the Si NCs, properly arranged in five ordered layers conveniently separated by  $\approx 1$  nm lower-Si-content barriers (i.e., the  $\text{SiO}_2$  layers), with a total stack thickness of  $\approx 30$  nm (from the substrate to the last Si NC layer). This microscopy observation is consistent with cross-sectional



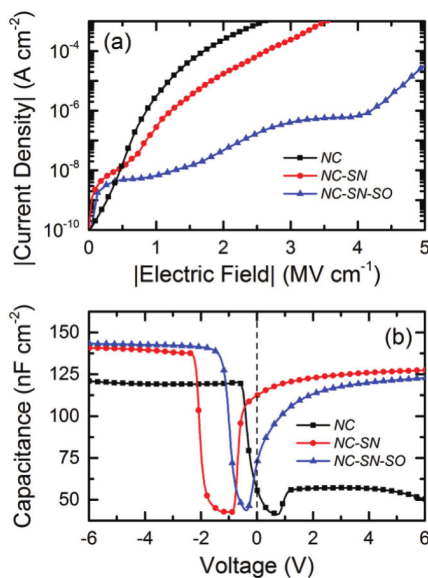
**Figure 3.** a) Energy-filtered and b) unfiltered bright-field transmission electron microscopy images from the cross section of device NC-SN-SO. The different observed layers are highlighted. c) Photoluminescence spectra corresponding to the three samples under study.

Si NC sizes around  $\approx 4$  nm, as previously reported on equivalent samples.<sup>[28,29]</sup> In addition, an  $\approx 9$  nm layer is found between the Si NC superlattices and the ALD-ZnO gate electrode which, because of its identical contrast to the inter-NC barriers in EFTEM images filtering around the SiO<sub>2</sub> plasmon energy (image not presented), must also be composed by SiO<sub>2</sub>. EFTEM imaging, however, gives no clear evidence of the presence of a nitride layer between the Si substrate and the Si NC SLs, which is due to the proximity between the plasmon energies of SiO<sub>2</sub> ( $\approx 22.5$  eV) and Si<sub>3</sub>N<sub>4</sub> ( $\approx 23.7$  eV).<sup>[30]</sup> This drawback is solved by unfiltered bright-field TEM, as shown in Figure 3b, where the brightness contrast allows observing an  $\approx 2$  nm layer on top of the crystalline Si substrate, which can be attributed to the Si<sub>3</sub>N<sub>4</sub> interlayer.

PL spectra were acquired from each sample, whose results are displayed in Figure 3c. All samples exhibit a Gaussian-like spectrum ranging from 600 to 1150 nm. This kind of emission is typically ascribed to the radiative excitonic recombination within the Si NCs, with a full-width at half-maximum (FWHM) of  $\approx 160$ – $170$  nm observed for all samples, attributed to the NC size distribution and phonon contributions due to the indirect transition.<sup>[31]</sup> The PL emission peaks around  $\approx 940$ – $945$  nm for samples NC and NC-SN, whereas it is slightly redshifted ( $\approx 965$  nm) for sample NC-SN-SO. The occurrence of a small PL shift to longer wavelength in sample NC-SN-SO is likely to be caused by a modulation effect of the SiO<sub>2</sub> capping layer on the spectral emission properties of the Si NCs because of the internal distribution of the optical excitation field, affecting in turn the PL emission intensity.<sup>[32,33]</sup> It is interesting to note that, within the uncertainty attributed to measurement reproducibility and surface homogeneity, samples NC and NC-SN yield a virtually identical emission spectrum, which indicates that the 2 nm Si<sub>3</sub>N<sub>4</sub> interlayer does not play a relevant role in the PL properties of the sample.

## 2.2. Electrical Characterization

Figure 4a displays the current density versus electric field ( $J(E)$ ), both in absolute values) characteristics corresponding to the three devices under study in accumulation regime, i.e., under negative applied voltage on the top ALD-ZnO electrode. Indeed, these curves already state a signature for each device structure. In particular, device NC shows an increase of current density of several orders of magnitude, as expected from continuous charge transport within NC-related states and no blocking layer impeding charge injection through the electrodes.<sup>[20,34]</sup> Device NC-SN exhibits an analogous trend to device NC, which reveals similar carrier injection conditions. However, in this case the curve is clearly shifted to higher voltages, which can be attributed to the fixed charges induced by the Si<sub>3</sub>N<sub>4</sub> interlayer because of its highly defective nature.<sup>[27]</sup> The  $J(E)$  curve corresponding to device NC-SN-SO presents, in contrast to the other devices, an almost flat region at low and medium electric fields. Within this electric field regime, the current is transient and governed by charge injection.<sup>[35]</sup> The current is purely capacitive as no charge traverses the SiO<sub>2</sub> blocking layer. At higher electric fields, persistent Fowler–Nordheim injection becomes the dominating charge transport mechanism.<sup>[34]</sup>



**Figure 4.** a) Current density versus electric field curves (both in absolute value) obtained from the three devices under study in accumulation regime. b) Capacitance versus voltage curves corresponding to the same devices.

The electrical characterization of the devices under study was complemented by the investigation of the capacitance versus voltage ( $C(V)$ ) curves, obtained at 300 kHz in a fast +6 to  $-6$  V sweep, which are plotted in Figure 4b. Device NC presents the typical behavior expected from Si NC SLs,<sup>[34]</sup> showing a flat band voltage,  $V_{FB,NC} \approx -0.3$  V, as well as the generation of a depletion region at slightly positive voltages, always exhibiting a marked difference between charge accumulation ( $V < 0$ ) and inversion ( $V > 0$ ) regimes. The overall capacitance value in accumulation is low ( $\approx 120$  nF cm<sup>-2</sup>), which is attributed to the high conductivity of the Si NC SLs under fast AC excitation. Addition of the thin nitride layer (device NC-SN) increases the observed capacitance ( $\approx 140$  nF cm<sup>-2</sup>) due to a lower AC conductivity, and leads to a notably lower flat band voltage ( $V_{FB,NC-SN} \approx -2.0$  V) due to the positive fixed charges within the Si<sub>3</sub>N<sub>4</sub> interlayer. The effect is similar to the recently reported work by Tondini et al.,<sup>[36]</sup> where nonpassivated defective field oxide provides a similar threshold voltage shift. Finally, device NC-SN-SO (with the largest capacitance,  $\approx 143$  nF cm<sup>-2</sup>, due to the presence of the oxide blocking barrier) also exhibits a negative threshold voltage shift. The  $V_{FB}$  decrease for this device with respect to device NC-SN is due to the presence of the blocking oxide, thus indicating that the effect of the fixed positive charge is reduced.

### 2.3. Electroluminescence Emission

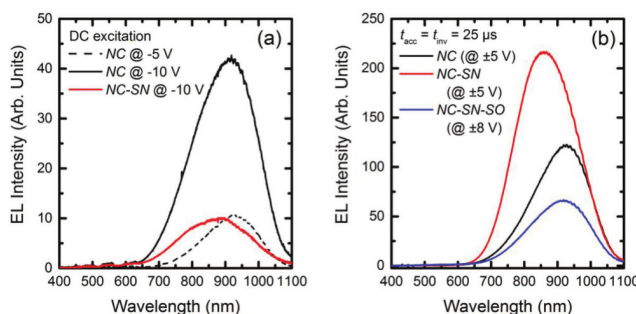
The electrical properties have shown so far that an introduced thin  $\text{Si}_3\text{N}_4$  layer into the NC-based LED provides an inversion layer underneath the whole superlattice structure. Therefore, minority carriers are provided to the active region from the inverted areas around the gate. This is expected to have a notable impact in the EL generation within our devices. In Figure 5a, the EL spectra corresponding to devices NC and NC-SN obtained under DC electrical excitation at  $-5$  and  $-10$  V are displayed. In this regime, defect-induced field ionization between neighboring Si NCs already takes place in both devices.<sup>[34]</sup> The current density of device NC is about one order of magnitude higher than in device NC-SN, which might be the reason for not observing the EL emission of the latter at  $-5$  V. With  $-10$  V DC excitation ( $\approx 3.4$ – $3.6$  MV  $\text{cm}^{-1}$ ), however, the EL signal from both devices could be observed. Indeed, under these conditions, the EL emission yield corresponding to device NC is larger than when the  $\text{Si}_3\text{N}_4$  interlayer is present. In addition, since this voltage corresponds to an electric field ( $\approx 2.5$  MV  $\text{cm}^{-1}$ ) well within the blocked region of device NC-SN-SO, no emission was observed from the latter device.

The spectral line shape of the EL of the devices can also be analyzed. As can be observed, devices NC and NC-SN exhibit a clear emission at low energies, within the 600–1000 nm range. When comparing these spectra with the plotted PL in Figure 3c, we can attribute the low-energy part of the EL spectra to the excitonic recombination within Si NCs, as has been reported before.<sup>[37,38]</sup> However, the increase in width of EL spectra ( $\text{FWHM}_{\text{NC}} \approx 230$  nm;  $\text{FWHM}_{\text{NC-SN}} \approx 250$  nm) with respect to PL can be understood as follows: smaller NC sizes are excited more efficiently via carrier injection (compared to PL, where the absorption cross section decreases rapidly with decreasing NC size),<sup>[37,39]</sup> thus broadening the spectra toward higher energies. Please note that, although quantum-confined Stark effect (i.e., the effective reduction of the Si NC bandgap, and therefore a peak redshift, due to the presence of an external electric field)<sup>[40]</sup> could also take part in our NC-based devices, our

observations indicate that excitation of the small NC population dominates the EL behavior. In the case of device NC-SN-SO, no EL was observed before the onset of the permanent Fowler–Nordheim current at significantly higher electric fields, as was already expected for this device. Finally, it is interesting to note that, under DC excitation, the presence of the  $\text{Si}_3\text{N}_4$  interlayer is clearly reducing the carrier injection and NC excitation within the SLs, which results in a decreased EL emission.

Following the main aim of this work, i.e., to improve the EL emission under pulsed excitation, we measured EL with an excitation of square pulses of  $\pm 5$  V, thus keeping the same amplitude as for DC excitation measurements. We used a period of 50  $\mu\text{s}$  and a duty cycle of 50%, which implies accumulation and inversion times of, respectively,  $t_{\text{acc}} = t_{\text{inv}} = 25$   $\mu\text{s}$  (the respective results are displayed in Figure 5b). Please note that, for the sake of comparison, we had to apply  $\pm 8$  V to device NC-SN-SO, which corresponds to an electric field equivalent to the one in devices NC and NC-SN, due to the additional  $\text{SiO}_2$  blocking barrier. The most immediate result from this approach is the enhanced EL intensity in all devices with respect to DC excitation, even when a similar voltage difference of 10 V was applied. Such an excitation scheme was first reported for MOSFET devices by Walters et al.,<sup>[21]</sup> and it was attributed to the sequential injection of carriers after alternate polarization switching. The enhancement is also significant for our MOS-based devices containing the  $\text{Si}_3\text{N}_4$  interlayer, NC-SN and NC-SN-SO, with respect to the NC device: the EL signal has doubled, reversing the situation that was observed under DC excitation (Figure 5b). This demonstrates that the nitride interlayer plays a decisive role on the sequential injection and excitation mechanisms that take place under pulsed excitation.

It can also be observed from Figure 5b that the NC and NC-SN devices exhibit a narrower emission in pulsed excitation than under DC excitation conditions, and centered at lower energies (in respect to NC quantum confinement-related PL emission). In our previous work, we reported on the modulation of the high- and low-energy EL emission contributions on an analogous device to NC, showing that shorter  $t_{\text{acc}}$  induces



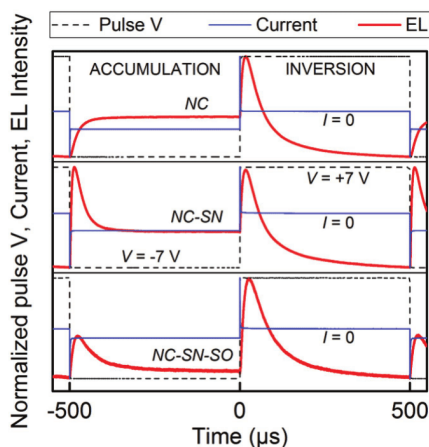
**Figure 5.** EL spectra corresponding to different devices, after applying a) DC electrical excitation at  $-5$  V on device NC and  $-10$  V on both devices NC and NC-SN, and b) 50  $\mu\text{s}$  period and 50% duty cycle square voltage pulses on the three devices. The intensity scales in both graphs are directly comparable. Please note that, in panel (b), a higher voltage excitation at  $\pm 8$  V was required for device NC-SN-SO in order to attain a comparable signal level to the other devices.

a high-energy (defect-related) emission quenching, which was ascribed to the insufficient time for efficient hole injection from the Si substrate into the SLs and thus the ALD-ZnO gate.<sup>[41]</sup> Additionally, we observe a narrowing ( $\text{FWHM}_{\text{NC}} \approx 200 \text{ nm}$ ,  $\text{FWHM}_{\text{NC-SN}} \approx 220 \text{ nm}$ ,  $\text{FWHM}_{\text{NC-SN-SO}} \approx 220 \text{ nm}$ ) and redshift of the EL emission in Figure 5b with respect to the DC excitation in Figure 5a. Nevertheless, these spectra still exhibit a peak blueshift and broadening with respect to the PL spectra displayed in Figure 3c, which confirms that the excitation of smaller NCs still prevails.

At this point, it is worth analyzing in more detail the total luminescence output from the samples. For this, the EL power efficiency of devices NC and NC-SN was estimated by exciting them with square pulses of  $\pm 5 \text{ V}$ , using a pulse period of  $80 \mu\text{s}$  and a duty cycle of 40% (which yielded the most efficient integrated EL), and collecting the whole EL emission in a 10 cm diameter integrating sphere. The reader is kindly directed to ref. [42] for further details on the experimental equipment and mathematical analysis of the outcoming luminescence from the devices. For evaluating the PE, we took into account the ratio between the optical power output,  $P_{\text{opt}}$ , and the electrical power input,  $I \times V$  [ $\text{PE} = P_{\text{opt}}/(I \times V)$ ]. In the case of our device NC, the mentioned voltage pulse conditions led to the estimation of  $\text{PE}_{\text{NC}} = 6 \times 10^{-3}\%$ , whereas the utilization of the  $\text{Si}_3\text{N}_4$  inversion layer (i.e., device NC-SN) induced an emission enhancement up to  $\text{PE}_{\text{NC-SN}} \approx 2.6 \times 10^{-2}\%$ , i.e., of a factor  $\approx 4$ . This result is so far the maximum efficiency reached by our Si NC-based devices.<sup>[20]</sup> Please note that the PE enhancement after  $\text{Si}_3\text{N}_4$  inversion layer incorporation is notably larger than the one observed in the EL spectra (by a factor of  $\approx 2$ ). This occurrence is due, first, to the PE normalization by the applied voltage and current (whereas voltage was fixed at  $-10 \text{ V}$ , current is different in devices NC and NC-SN according to Figure 4a), and second, to the fact that the integrating sphere collects all EL emitted by the device, whereas a small solid angle reaches the entrance slit of the spectrometer when spectrally analyzing EL.

#### 2.4. Recombination Dynamics and Excitation Mechanisms

The substantial enhancement of EL emission intensity from the particular device designs under study, after pulsed electrical excitation is employed, must necessarily be related to the charge injection mechanisms taking place within the devices. With the aim of understanding such injection processes, time-resolved EL studies were performed by applying controlled square voltage pulses, of  $\pm 7 \text{ V}$  (well within the substrate accumulation and deep inversion regimes), and with a total period of 1 ms and 50% duty cycle (i.e.,  $t_{\text{acc}} = t_{\text{inv}} = 500 \mu\text{s}$ ), whose results are given in Figure 6. Such a long period was selected so that the whole luminescence decay, in both accumulation and inversion regimes, be complete. Again, distinct features govern the rise/decay EL pattern of the devices under test, namely the emission overshoot immediately after each polarity switch (in both polarization regimes) and the DC-like emission level reached after decay (only in accumulation). The observation of these effects is very clear in this figure. When switching from inversion ( $V > 0$ ) to accumulation ( $V < 0$ ), a sudden increase in EL takes place in devices containing a  $\text{Si}_3\text{N}_4$  interlayer (NC-SN),



**Figure 6.** Normalized time-resolved EL emission (in red) from the devices under study during one voltage-pulse electrical excitation period (1 ms and 50% duty cycle). The pulse voltage ( $\pm 7 \text{ V}$ , in black dashed lines) and the current (in blue) are also indicated. For the sake of clarity, accumulation and inversion regimes are highlighted, as well as the  $I = 0$  level (no current is observed in inversion).

whereas device NC directly reaches a constant emission after switching to accumulation. Devices NC-SN and NC-SN-SO also reach a DC emission after decay from the overshoot; the device with  $\text{SiO}_2$  blocking barrier exhibits a much lower intensity level. After switching from accumulation to inversion, an EL overshoot is observed in all devices, followed by a decay until EL is totally quenched. Please note that the EL's rise and decay times in all three devices lie in the range of  $5\text{--}25 \mu\text{s}$  (rise time) and  $30\text{--}75 \mu\text{s}$  (decay time), obtained by a single-exponential decay fitting, which is in agreement with usual characteristic times for luminescence excitation and decay processes, respectively, taking place in Si NCs.<sup>[43–45]</sup> This indicates that we are effectively dealing with the recombination dynamics of the Si NCs/ $\text{SiO}_2$  system, and no contribution from either the  $\text{SiO}_2$  matrix or the ALD-ZnO electrode is observed (characterized by much faster kinetics of the order of nanoseconds).<sup>[46]</sup>

The time-resolved EL signal corresponding to device NC was already reported in ref. [41] on an analogous device. In that work, the constant EL was attributed to continuous formation of electron-hole pairs within Si NCs due to bipolar injection of holes from the *p*-type substrate and electrons from the ALD-ZnO gate electrode. Because of the mobility asymmetry between electrons and holes within  $\text{SiO}_2$ ,<sup>[47]</sup> some injected holes are confined in Si NCs within the layer immediately on top of the substrate which might not be recombined with electrons. During the accumulation-to-inversion switch, the positively charged Si NCs attract electrons from the substrate until total neutralization (reaching the overshoot peak), after which EL decays. In this case, since electrons are minority carriers

in the *p*-type Si substrate, no continuous electron injection is expected, because the minority carriers have to be generated thermally in the substrate. This slow process limits the current during inversion, as shown by the time-resolved current pattern (blue curves in Figure 6) being zero in the inversion regime.

The case of the devices containing a Si<sub>3</sub>N<sub>4</sub> interlayer is different: devices NC-SN and NC-SN-SO present an additional EL overshoot after the inversion-to-accumulation switch, an effect observed in other published works in the literature, too.<sup>[21,26]</sup> As already described for device NC, the inversion cycle totally quenches EL emission, as expected from the complete compensation of positively charged Si NCs with substrate-injected electrons. In this case, however, the inversion layer around the gate induced by the Si<sub>3</sub>N<sub>4</sub> layer promotes additional electron supply to the SLs. The lower DC level found in device NC-SN-SO must be necessarily attributed to the presence of the blocking barrier. It essentially obstructs electron injection from the ALD-ZnO gate electrode. Apparently, electrons injected from the top electrode play a decisive role in the recombination dynamics and efficiency. Finally, the difference in accumulation-to-inversion and inversion-to-accumulation EL overshoot intensity is due to the asymmetry between electron and hole Si NCs' charging. As an example, in the particular case of sample NC-SN-SO, electron injection from the ALD-ZnO gate is strongly quenched in accumulation, which results in only hole trapping from the substrate.

### 3. Discussion

So far, numerous studies have demonstrated that the EL emission from matrix-embedded Si NCs can be strongly enhanced by means of pulsed electrical excitation.<sup>[21–23,26]</sup> This frame clearly favors the occurrence of bipolar injection being the main mechanism governing the excitation of the NCs, followed by the consequent photon emission after electron–hole pair recombination. In their work, Walters et al. described the sequential programming of alternately charged Si NCs by using a field-effect-transistor-like structure (a simple schematic of such structure is displayed in Figure 1a,b).<sup>[21,22]</sup> This design presented two remarkable features: (i) the channel generated between highly *n*-doped drain and source, which acts as an electron reservoir under alternate polarization conditions, and (ii) a SiO<sub>2</sub> layer between the Si NCs active layer and the poly-Si gate, which provides adequate insulation against injection of carriers from the top electrode. Indeed, the device structure NC-SN-SO was intentionally designed to mimic Walters et al.'s field-effect transistor: it contains a Si<sub>3</sub>N<sub>4</sub> interlayer between substrate and SLs, which has proved to act as an inversion layer that provides the adjacent Si NCs with minority carriers from the substrate under alternate polarization conditions similar to case (i), plus an additional 10 nm SiO<sub>2</sub> blocking barrier that minimizes carrier injection from the ALD-ZnO gate, analogous to case (ii). The recombination dynamics displayed in Figure 6 show how this device exhibits hole and electron carrier injection from the substrate immediately after switching to accumulation and inversion regimes, respectively (as demonstrated by the EL overshoots after each polarity change). In our case, however, an EL DC component is still observed in accumulation, which indicates that, at the high voltages employed ( $\pm 7$  V), the

blocking barrier is not totally quenching the constant injection of high-kinetic-energy electrons from the gate electrode.

The role of a controlled inversion layer on the bipolar injection of carriers on the Si NC-based active layer was recently studied by Tondini et al.<sup>[36]</sup> They showed that the inversion layer generated after nonpassivation of the field oxide surrounding the NC SLs became a source of minority electrons and holes that increased the efficiency of NC charging. This was proved by *C*(*V*) measurements, which evidenced considerable charging even under strong substrate inversion conditions, which led to a nonrectifying behavior of the overall device. Our investigations on the Si<sub>3</sub>N<sub>4</sub> interlayer approach (device NC-SN) have corroborated these results, as can be seen in Figure 4b, where only device NC exhibits a real substrate inversion behavior, i.e., with negligible or no charging at all. In addition, both works coincide in the determination of the carrier injection nature from the inversion layer, by means of recombination dynamics studies that point out the alternated injection of electrons and holes under different polarization conditions (see Figure 6). In our case, absolute EL intensity measurements have shown a four-fold increase of PE in device NC-SN with respect to device NC, in excellent agreement with the enhancement shown by Tondini et al. The *C*(*V*) characteristics displayed in Figure 4b shed light to this fact, where a clear shift of the curves toward lower *V*<sub>FB</sub> (higher in absolute value) indicates that a similar charging level occurs at low voltages and under both accumulation and inversion regimes, which favors the sequential bipolar injection within the Si NC SLs. Despite the similar results obtained in both works, the strength of our approach lies in the simplicity of our design, where the controlled inclusion of a nitride interlayer (which has no effect on the SL structure according to Figure 3) provides notably higher EL emission yield from Si NCs. Indeed, this is a very promising result, which highlights the advantages of introducing such a thin nitride layer on the performance of Si NC-based LEDs.

The EL emission efficiency of Si NC-based LEDs is limited by both carrier injection into and light extraction from the devices. In this study, we have reported a maximum PE of  $\approx 2.6 \times 10^{-2}\%$ , which corresponds to a quantum efficiency of  $\approx 0.1\%$  when normalized by the number of injected electrons and the number of emitted photons (see ref. [42] for details on this calculation). It is an interesting exercise to contextualize our result within the existing literature on the topic, where different approaches have been employed to improve either the charge injection or the light extraction issues. Perálvarez et al. demonstrated an EL power efficiency on SiO<sub>2</sub> thin-film-embedded Si NCs around  $10^{-3}\%$  when grown via ion implantation, which was notably enhanced by two orders of magnitude when the plasma-enhanced chemical-vapor deposition (PECVD) technique was employed.<sup>[48]</sup> Almost simultaneously, some works on Si NC SLs were reported by Pavesi and co-workers,<sup>[17,18]</sup> where a power efficiency as high as  $\approx 0.2\%$  was demonstrated after DC electrical injection at low current density values.<sup>[17]</sup> In these works, however, a highly *n*-doped poly-Si gate was employed as top electrode, which notably favors tunnel-like injection of carriers within the SLs. As well, an additional 50 nm antireflective Si<sub>3</sub>N<sub>4</sub> layer was employed on top of the poly-Si gate, in order to minimize optical losses.<sup>[18]</sup> In contrast, and despite its high and constant transparency throughout the visible range,<sup>[49,50]</sup>

our ALD–ZnO is not optimized for light extraction. In addition, relevant is the achievement of external quantum efficiencies higher than 1% by means of chemically prepared colloidal Si nanoparticles (NPs).<sup>[51,52]</sup> In these works, the colloidal Si NPs are spin-coated as an emitter layer within a device structure containing polymer-based electron and hole injection and transport layers. This already states a substantial difference with respect to our SiO<sub>2</sub>-embedded Si NCs: although the Si NC/SiO<sub>2</sub> superlattice structure is able to finely control the NC size, the high Si–SiO<sub>2</sub> offset energy for the injection of both electrons and holes strongly limits charge injection into such systems, and therefore the excitation of Si NCs. Notwithstanding, matrix-embedded Si NC-based active layers show long-term operation, in contrast to the less-stable NPs, whose operation times are limited to some tens of hours due to NP migration toward the contacts when high electric fields are applied.<sup>[53]</sup> Finally, some groups have addressed the light extraction efficiency enhancement by taking advantage of a 2D photonic crystal layer deposited as top electrode of Er<sup>3+</sup>-doped Si NC-based devices, which allows for precisely coupling, and thus enhancing, the Er<sup>3+</sup>-ion-related near-infrared emission.<sup>[54–56]</sup> This approach, compatible with Si technology, could be employed to enhance the visible-NIR emission from Si NCs.

In general, the published works so far have demonstrated that slight modifications on the NCs' processing and distribution within the LED active layer, as well as the device design and the excitation conditions, result in different device efficiencies. In this frame, our design-improvement approach consists of depositing a controlled interlayer between substrate and Si NC superlattices, which favors minority carrier injection from the substrate and, consequently, electron–hole pair generation even in deep substrate inversion regime. Within this structure, the use of pulsed electrical excitation was found to increase the efficiency of the sequential carrier injection mechanism. In addition, the novelty of the design approach lies in the simplicity of the additional Si<sub>3</sub>N<sub>4</sub> interlayer deposition step, which not only allows the application of planar technology, thus avoiding complex fabrication steps, but is also compatible with any existing device configuration strategy.

#### 4. Conclusion

Light-emitting devices based on Si NCs have been fabricated via PECVD-deposited Si-rich oxynitride (SRON)/SiO<sub>2</sub> superlattices and a subsequent high-temperature annealing treatment. Our device structure consists in the addition of a 2 nm thick PECVD-deposited Si<sub>3</sub>N<sub>4</sub> layer between the Si substrate and the SLs. The control sample structure contains both the nitride layer and a 10 nm SiO<sub>2</sub> carrier injection-blocking layer. The structural, optical, electrical, and electro-optical properties of these LEDs have been studied. TEM analysis confirms the controlled deposition of the SLs as well as the additional nitride inversion layer and oxide blocking barrier. Electrical measurements revealed that the Si<sub>3</sub>N<sub>4</sub> interlayer contains a high density of fixed positive charges that invert the substrate. Due to continuous supply of electrons from the inversion layer around the electrode, the injection of electrons from the substrate into the SLs is significantly enhanced. This effect induces an enhancement of

EL emission intensity, under pulsed excitation, with respect to the conventional Si NC SL-based devices. In addition, EL yield is notably higher under pulsed electrical excitation, which is correlated to a more efficient sequential carrier injection. The best performance is achieved by devices containing the nitride interlayer under pulsed excitation, with a power efficiency of  $\approx 2.6 \times 10^{-2}\%$ , i.e.,  $\approx 4$  times higher than the conventional device structure. This efficiency increase confirms that our device design, i.e., the addition of a 2 nm Si<sub>3</sub>N<sub>4</sub> interlayer, provides an easy approach to enhance the performance of Si NC-based LEDs, by means of a fast technological process compatible with planar microelectronics. Overall, our hereby presented results pave the way for further improving the performance of light-emitting devices containing a Si NC-based active layer.

#### 5. Experimental Section

**Material Preparation:** The Si NC/SiO<sub>2</sub> SLs were fabricated via the so-called superlattice approach.<sup>[57]</sup> Through this method, alternated SRON (4.5 nm) and SiO<sub>2</sub> (1 nm) layers were deposited on top of *p*-type Si substrate ( $[B] = 10^{16} \text{ cm}^{-3}$ , base resistivity of 1–20  $\Omega \text{ cm}$ ) by means of PECVD (deposition temperature of 375 °C). On top of such a structure, a 10 nm capping SiO<sub>2</sub> layer was also deposited by PECVD, followed by 10 nm amorphous Si and another 5 nm SiO<sub>2</sub> in order to protect the SLs from the subsequent high-temperature annealing treatment. After deposition, the samples were annealed at 1150 °C for 1 h under N<sub>2</sub> ambient in a quartz tube furnace, to induce the SRON Si excess precipitation and crystallization in the form of Si NCs. In addition, the H<sub>2</sub> passivation treatment was carried out at 450 °C for 1 h in pure H<sub>2</sub> gas, to get rid of undesired dangling bonds. After annealing, the 10 nm SiO<sub>2</sub> capping, amorphous Si and 5 nm SiO<sub>2</sub> protecting layers were selectively wet chemically etched. More details on the Si NC SLs' fabrication process are given in ref. [28]. So far, the fabrication of the sample labeled as NC was described. In sample NC-SN, an extra 2 nm Si<sub>3</sub>N<sub>4</sub> layer was deposited between the Si substrate and the first SRON/SiO<sub>2</sub> bilayer via PECVD. In sample NC-SN-SO, additionally to the thin Si<sub>3</sub>N<sub>4</sub> layer, a 10 nm SiO<sub>2</sub> layer was deposited on top of the SLs which was left unetched, to provide a blocking barrier for carriers from the top electrode.<sup>[34]</sup> In Figure 2, the details of the three different material structures can be observed.

**Device Fabrication:** The device structure was achieved by full-area evaporating the Si substrate rear side with Al, and depositing on top of the SLs a 100 nm ALD–ZnO (naturally *n*-type, resistivity < 0.01  $\Omega \text{ cm}$  and  $\approx 75\%$  transparency throughout the whole visible spectrum) using ALD, at a deposition temperature of 200 °C.<sup>[50,58]</sup> The top ALD–ZnO electrode was patterned by conventional photolithography, achieving 500  $\mu\text{m}$  diameter circular-shaped contacts (i.e., a total device area of  $\approx 2 \times 10^{-3} \text{ cm}^2$ ). This way, an N-I-P design was achieved, "N" being the top *n*-type ALD–ZnO electrode, "I" (intrinsic) the Si NC SLs, and "P" the *p*-type Si substrate. Further details on the device preparation can be found elsewhere.<sup>[19,34]</sup>

**Material and Device Characterization:** Direct observation of the sample structure was carried out via EFTEM and high-resolution TEM using a JEOL 2010F instrument (field emission gun operating at 200 keV) equipped with a Gatan Image Filter (with a resolution of 0.8 eV), after preparing the samples by mechanical flat polishing and final low angle Ar<sup>+</sup>-ion milling. In the case of EFTEM, the Si signal contrast was obtained by energetically filtering the electron energy loss spectra around the Si plasmon energy ( $E_{\text{Si}} \approx 16.7 \text{ eV}$ ). PL spectra were acquired at room temperature by means of an LN<sub>2</sub>-cooled CCD camera coupled to a high spectral resolution single-grating monochromator, after exciting the material samples with the 325 nm line of a He–Cd laser. Room temperature current–voltage ( $I(V)$ ) and capacitance–voltage ( $C(V)$ ) measurements, swept at a frequency of 300 kHz, were performed in dark using high-resolution probes in a Microtech Summit 11000 probe station (equipped with a Faraday cage for electrical screening)

- [42] J. Valenta, *Nanosci. Methods* **2014**, 3, 11.
- [43] N. Lalic, J. Linnros, *J. Appl. Phys.* **1996**, 80, 5971.
- [44] J. Linnros, N. Lalic, A. Galeckas, V. Grivickas, *J. Appl. Phys.* **1999**, 86, 6128.
- [45] M. Dovrat, Y. Goshen, J. Jedrzejewski, I. Balberg, A. Sa'ar, *Phys. Rev. B: Condens. Matter Mater. Phys.* **2004**, 69, 155311.
- [46] A. J. Morfa, B. C. Gibson, M. Karg, T. J. Karle, A. D. Greentree, P. Mulvaney, S. Tomljenovic-Hanic, *Nano Lett.* **2012**, 12, 949.
- [47] J. F. Verwey, E. A. Amerasekera, J. Bisschop, *Rep. Prog. Phys.* **1990**, 53, 1297.
- [48] M. Perálvarez, J. Barreto, J. Carreras, A. Morales, D. Navarro-Urrios, Y. Lebour, C. Domínguez, B. Garrido, *Nanotechnology* **2009**, 20, 405201.
- [49] H. Beh, D. Hiller, J. Laube, S. Gutsch, M. Zacharias, *J. Vac. Sci. Technol., A* **2017**, 35, 01B127.
- [50] J. Laube, D. Nübling, H. Beh, S. Gutsch, D. Hiller, M. Zacharias, *Thin Solid Films* **2016**, 603, 377.
- [51] K. Y. Cheng, R. Anthony, U. R. Kortshagen, R. J. Holmes, *Nano Lett.* **2011**, 11, 1952.
- [52] F. Maier-Flaig, J. Rinck, M. Stephan, T. Bockrocker, M. Bruns, C. Kübel, A. K. Powell, G. A. Ozin, U. Lemmer, *Nano Lett.* **2013**, 13, 475.
- [53] F. Maier-Flaig, C. Kübel, J. Rinck, T. Bockrocker, T. Scherer, R. Prang, A. K. Powell, G. A. Ozin, U. Lemmer, *Nano Lett.* **2013**, 13, 3539.
- [54] M. Galli, A. Politi, M. Belotti, D. Gerace, M. Liscidini, M. Patrini, L. C. Andreani, M. Miritello, A. Irrera, F. Priolo, Y. Chen, *Appl. Phys. Lett.* **2006**, 88, 251114.
- [55] L. Ondić, M. Varga, K. Hruška, A. Kromka, K. Herynková, B. Hönerlage, I. Pelant, *Appl. Phys. Lett.* **2013**, 102, 251111.
- [56] R. Lo Savio, M. Galli, M. Liscidini, L. C. Andreani, G. Franzò, F. Iacona, M. Miritello, A. Irrera, D. Sanfilippo, F. Priolo, F. Iacona, M. Miritello, *Appl. Phys. Lett.* **2014**, 104, 121107.
- [57] M. Zacharias, J. Heitmann, R. Scholz, U. Kahler, M. Schmidt, J. Bläsing, *Appl. Phys. Lett.* **2002**, 80, 661.
- [58] H. Beh, D. Hiller, M. Bruns, A. Welle, H. W. Becker, B. Berghoff, C. Sürgers, R. Merz, M. Zacharias, *J. Appl. Phys.* **2017**, 122, 025306.





## 5. Summary and Conclusions

This Thesis has been focused on the fabrication and characterization of different CMOS-compatible materials in order to determine both their electro-optical and resistive switching properties. Basically, two materials have been explored, silicon-aluminum oxynitride (SiAlON) and zinc oxide (ZnO). The first material under study, SiAlON, has been fabricated using three techniques, namely RF-sputtering, pulsed-laser deposition and electron beam evaporation. In this case, different stoichiometries were analyzed in order to obtain excellent optical and electrical properties. The incorporation of different rare earths (REs) was also carried out, using Ce and Eu, which exhibited photoluminescence (PL) emission under laser excitation. The electro-optical characterization was performed after fabricating device structures onto *p*-type silicon substrates. The employed top electrode was selected depending on the characterization technique. To collect the electroluminescence (EL) from the devices a transparent conductive oxide (TCO) was required, using indium tin oxide (ITO) because of its excellent electrical and optical properties. Light emission was obtained from both devices, containing Ce and Eu, suggesting that SiAlON is a great candidate to be employed as RE host matrix. In addition, the resistive switching properties of these devices were analyzed as well, using Al as top electrical contact.

Similar fabrication processes were carried out towards attaining rare earth (RE)-doped SiAlON. This was achieved by depositing a multilayered structure of Tb-Al/SiO<sub>2</sub>, which allowed determining the RE ions inclusion effectivity of the delta-doping approach. The optical characterization demonstrated PL emission from trivalent Tb<sup>3+</sup> ions. Different (Al/Tb/SiO<sub>2</sub>) multilayer configurations were tested to optimize the number of active luminescent centers. Finally, the resistive switching properties of RE-doped SiO<sub>2</sub> were also analyzed and the role of the RE ions within was explored as well.

The second studied material was ZnO. In this case, the material was deposited onto *p*-type silicon via either RF-sputtering or atomic layer deposition (ALD) depending on the role of the deposited layer. While the first one was used to deposit the ZnO as RE host matrix, the second

## 5. Summary and Conclusions

one was employed to attain a ZnO layer acting as TCO top electrode. In the first case, different REs (Tb and Eu) were tested. A clear PL emission of both REs was obtained. The narrow peak-like features in the spectra indicate the optical activation of the trivalent RE ions, being the ZnO an optimum host matrix for this kind of luminescent centers. To carry out the electrical characterization, device structures were attained using ITO as top TCO electrode. The EL from these devices was obtained, achieving similar spectra than the ones observed via PL. However, the luminescent degradation with time suggests the formation of conductive paths which effectively quench the EL emission. Taking into account this behavior, the resistive switching properties of these devices were analyzed, obtaining different cycles. The role of the REs in the resistive switching properties of ZnO was studied as well, allowing for a reduction of the current compliance in the electroforming process, but increasing the required voltages to induce the resistive switching phenomenon. Moreover, the incorporation of the REs into the ZnO host matrix permitted obtaining more stable Reset processes, which suggests that the REs near the conductive paths could trap part of the out-diffused oxygen ions and, consequently, the re-oxidation of these conductive paths becomes easier.

Finally, when using a ZnO layer as top electrical contact, a multilayered  $\text{SiO}_x/\text{SiO}_2$  structure was employed. After deposition, this structure was annealed at high temperature in order to induce the precipitation and crystallization of the silicon excess in the form of silicon nanocrystals (Si-NCs). The optical and electrical properties of these nanostructures are well known and have reported in previous works and doctoral theses of the research group. Therefore, the incorporation of the ZnO as TCO was implemented to determine the EL of the Si-NCs when current is injected under different electrical polarizations. Studies in DC and AC have been carried out, obtaining interesting results related to the modulation of the light emission from ZnO defects and enhancing the EL emission from the Si-NCs. The incorporation of a thin  $\text{Si}_3\text{N}_4$  inversion layer, between the Si substrate and the multilayered Si-NCs, allowed modifying the injected current, thus obtaining an enhancement of the EL emission. These measurements confirmed the good electrical and optical properties of the ZnO working as TCO and permitted to understand the physical mechanisms involved in the EL process of the luminescent centers. In

addition, the resistive switching properties of these devices were determined. In this case, devices presented some cycles with well defined resistive states. Under these resistive switching conditions, devices exhibit EL emission, being the intensity and the threshold voltage dependent on the resistive state.

In conclusion, the results presented in this Thesis demonstrate the correlation between the EL emission and the resistive switching properties. Using these characteristics, the resistive state can be read not only electrically, but also optically from the emission of the luminescent centers through the TCO top electrode contact. Overall, these results pave the way to a new set of memory devices that can be, in a near future, integrated into the Photonics field, dominated by faster interconnections and less dependence to material transmission media.



## 6. Resum en Català

Aquesta Tesi es basa en la fabricació i caracterització de diferents materials compatibles amb al tecnologia CMOS, per tal de poder determinar les seves propietats electró-òptiques i de commutació resistiva. Bàsicament, s'han estudiat dos materials, oxinitrur de silici i alumini (SiAlON) i òxid de zinc (ZnO). En el cas del SiAlON, s'han emprat diferents tècniques de fabricació i s'han tingut en compte diferents estequiometries per tal d'optimitzar-ne les propietats òptiques i elèctriques. Tanmateix, s'ha dut a terme la incorporació de terres rares (Ce i Eu) en aquestes matrius, les quals han presentat emissió de fotoluminescència (PL) sota excitació làser. Les propietats electro-òptiques de dit material s'han pogut estudiar a partir de dispositius bàsics obtinguts després de dipositar òxid d'indi i estany (ITO) com a elèctrode transparent, els quals han mostrat emissió d'electroluminescència (EL) de les terres rares. Dits dispositius també han presentat propietats de commutació resistiva (emprant Al com a contacte superior).

L'ZnO es va utilitzar com a matriu contenidora de terres rares (Tb i Eu), les quals han demostrat ésser òpticament actives tot presentant emissió de PL i d'EL. No obstant, dita luminescència mostra una degradació, possiblement deguda a la formació de camins conductius. Aquest fet va promoure l'estudi de les propietats de commutació resistiva, obtenint resultats interessants depenent de l'existència o no de la terra rara. Per altra banda, l'ZnO es va emprar com a contacte transparent sobre una estructura de multicapes de nanocristalls de Si (Si-NCs). Mitjançant estudis elèctrics en AC, es va poder modular l'emissió d'EL de dit sistema. A més, la incorporació d'una capa fina de nitrur de silici a la interfície entre el substrat de Si i els Si-NCs va permetre també millorar l'eficiència d'emissió EL d'aquestes nanoestructures. Finalment, el sistema ZnO/Si-NCs ha mostrat propietats de commutació resistiva i emissió EL de forma simultània, aquesta última depenent de l'estat resistiu del dispositiu.

En resum, la relació entre les propietats electró-òptiques i les de commutació resistiva en els materials estudiats permet obrir les portes

## 6. Resum en Català

a nous dispositius amb dos estats resistius que puguin ser llegits tant elèctricament com òpticament.

# A. List of Publications Presented in this Thesis

## A.1. List of Articles

- I. Ehré, F.; Dufour, C.; Blázquez, O.; Garrido, B.; Jadwisienczak, M.; Ingram, D.C.; Gourbilleau, F.; Labbé, C., “Enhancing the blue emission in Ce doped silicon oxynitrides thin films for electroluminescence device applications”, *ECS Trans.* **85** (3), 9-21 (2018).  
DOI: <https://doi.org/10.1149/08503.0009ecst>
- II. Blázquez, O.; Martín, G.; Camps, I.; Mariscal, A.; López-Vidrier, J.; Ramírez, J.M.; Hernández, S.; Estradé, S.; Peiró, F.; Serna, R.; Garrido, B., “Memristive behaviour of Si-Al oxynitride thin films: The role of oxygen and nitrogen vacancies in the electroforming process”, *Nanotechnology* **29**, 235702 (2018).  
DOI: <https://doi.org/10.1088/1361-6528/aab744>
- III. Blázquez, O.; Ramírez, J. M.; López-Vidrier, J.; Berencén, Y.; Hernández, S.; Sanchis, P.; Garrido, B., “Luminescence yield in Al and Tb<sup>3+</sup> delta-doped oxide thin films fabricated by electron beam evaporation”, *Proc. SPIE* **9520**, Integrated Photonics: Materials, Devices, and Applications III, 95200K (2015).  
DOI: <http://dx.doi.org/10.1117/12.2178855>
- IV. Blázquez, O.; López-Vidrier, J.; López-Conesa, L.; Busquets-Masó, M.; Estradé, S.; Peiró, F.; Hernández, S.; Garrido, B., “Structural and optical properties of Al-Tb/SiO<sub>2</sub> multilayers fabricated by electron beam evaporation”, *Journal of Applied Physics* **120**, 135302 (2016).  
DOI: <https://doi.org/10.1063/1.4964110>
- V. Friero, J.L.; Blázquez, O.; López-Vidrier, J.; López-Conesa, L.; Estradé, S.; Peiró, F.; Ibáñez, J.; Hernández, S.; Garrido, B., “Green Electroluminescence of Al/Tb/Al/SiO<sub>2</sub> Devices



## A. List of Publications Presented in this Thesis

Fabricated by Electron Beam Evaporation”, *Physica Status Solidi A* 1700451 (2017).

DOI: <https://doi.org/10.1002/pssa.201700451>

- VI. Blázquez, O.; Frieiro, J.L.; López-Vidrier, J.; Guillaume, C.; Portier, X.; Labbé, C.; Sanchis, P.; Hernández, S.; Garrido, B., “Resistive switching and charge transport mechanisms in ITO/ZnO/p-Si devices”, *Applied Physics Letters* submitted and under correction (2018).

DOI: -

- VII. López-Vidrier, J.; Gutsch, S.; Blázquez, O.; Hiller, D.; Laube, J.; Kaur, R.; Hernández, S.; Garrido, B.; Zacharias, M., “Modulation of the electroluminescence emission from ZnO/Si NCs/p-Si light-emitting devices via pulsed excitation”, *Applied Physics Letters* **110**, 203104 (2017).

DOI: <https://doi.org/10.1063/1.4983722>

- VIII. López-Vidrier, J.; Gutsch, S.; Blázquez, O.; Hiller, D.; Laube, J.; Kaur, R.; Hernández, S.; Garrido, B.; Zacharias, M., “Effect of Si<sub>3</sub>N<sub>4</sub>-mediated inversion layer on the electroluminescence properties of silicon nanocrystals superlattices”, *Advanced Electronic Materials*, 1700666 (2018).


















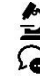
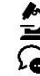
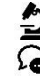


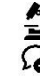
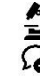
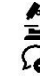


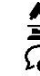
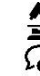
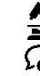


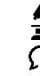
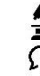
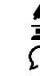
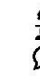
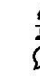
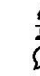





DOI: <https://doi.org/10.1002/aelm.201700666>

## A.2. Paper Contribution Statement

This thesis presents eight published articles (see subsection A.1) as part of the results in sections 3. *Si-Based Materials for Optoelectronics and Resistive Switching* and 4. *ZnO-Based Materials for Optoelectronics and Resistive Switching* and they have been sorted according to the topic and/or the results for better understanding, being non-chronological their publication. Some of them are proceedings presented in conferences, showing previous results. However, this thesis presents at least 4 articles which accomplish the regulation of the Physics Committee of the University of Barcelona (Papers II, IV, VII and VIII). The paper VI has just been submitted to APL and it is under some corrections to be finally accepted. This paper will accomplish this regulation as well. The other ones correspond to proceedings from conferences, which scientific

interest could be taken into account for the Committee. My contribution in all of these papers has been different depending on the publication and it is summarized in Table A.1.

**Table A.1.** Statement of the contribution in the present articles.

<i>Paper</i>	<i>I</i>	<i>II</i>	<i>III</i>	<i>IV</i>	<i>V</i>	<i>VI</i>	<i>VII</i>	<i>VIII</i>
	   	     	     	     	   	     	  	  
 Writing	 Experiments	 Discussion	 Sample Fabrication	 First Author				



## B. Curriculum Vitae

### B.1. Journal Publications

1. Blázquez, O.; López-Vidrier, J.; Hernández, S.; Montserrat, J.; Garrido, B., “Electro-optical properties of non-stoichiometric silicon nitride films for photovoltaic applications”, *Energy Procedia* **44**, 145-150 (2013).  
DOI: <https://doi.org/10.1016/j.egypro.2013.12.021>
2. Blázquez, O.; López-Vidrier, J.; Hernández, S.; Montserrat, J.; Garrido, B., “Investigando las propiedades electró-ópticas de capas delgadas de nitruro de silicio no estequiométrico para aplicaciones fotovoltaicas”, *Óptica Pura y Aplicada* **46-4**, 309-314 (2013).  
DOI: <https://doi.org/10.7149/OPA.46.4.309>
3. López-Vidrier, J.; Berencén, Y.; Hernández, S.; Blázquez, O.; Gutsch, S.; Laube, J.; Hiller, D.; Löper, P.; Schnabel, M.; Janz, S.; Zacharias, M.; Garrido, B., “Charge transport and electroluminescence of silicon nanocrystals/SiO<sub>2</sub> superlattices”, *Journal of Applied Physics* **114**, 163701-163707 (2013).  
DOI: <https://doi.org/10.1063/1.4826898>
4. López-Vidrier, J.; Berencén, Y.; López-Conesa, L.; Blázquez, O.; Ramírez, J.M.; Estradé, S.; Peiró, F.; Hernández, S.; Garrido, B., “Transport and electroluminescence properties of size-controlled silicon nanocrystals embedded in SiO<sub>2</sub> matrix following the superlattice approach”, *ECS Trans.* **61-5**, 133-139 (2014).  
DOI: <http://dx.doi.org/10.1149/06105.0133ecst>
5. Blázquez, O.; Ramírez, J. M.; López-Vidrier, J.; Berencén, Y.; Hernández, S.; Sanchis, P.; Garrido, B., “Luminescence yield in Al and Tb<sup>3+</sup> delta-doped oxide thin films fabricated by electron beam evaporation”, *Proc. SPIE* **9520**, Integrated Photonics: Materials, Devices, and Applications III, 95200K (2015).  
DOI: <http://dx.doi.org/10.1117/12.2178855>
6. Pruna, R.; Palacio, F.; López, M.; Pérez, J.; Mir, M.; Blázquez, O.; Hernández, S.; Garrido, B., “Electrochemical characterization

- of organosilane-functionalized nanostructured ITO surfaces”, *Applied Physics Letters*. **109**, 903270 (2016). DOI: <https://doi.org/10.1063/1.4960734>
7. Blázquez, O.; López-Vidrier, J.; López-Conesa, L.; Busquets-Masó, M.; Estradé, S.; Peiró, F.; Hernández, S.; Garrido, B., “Structural and optical properties of Al-Tb/SiO<sub>2</sub> multilayers fabricated by electron beam evaporation”, *Journal of Applied Physics* **120**, 135302 (2016). DOI: <https://doi.org/10.1063/1.4964110>
  8. Pruna, R., Palacio, F., Martínez, M.; Blázquez, O.; Hernández, S.; Garrido, B.; López, M., “Organosilane-functionalization of nanostructured indium tin oxide films”, *Interface Focus* **6**, 20160056 (2016). DOI: <http://dx.doi.org/10.1098/rsfs.2016.0056>
  9. López-Vidrier, J.; Gutsch, S.; Blázquez, O.; Hiller, D.; Laube, J.; Kaur, R.; Hernández, S.; Garrido, B.; Zacharias, M., “Modulation of the electroluminescence emission from ZnO/Si NCs/p-Si light-emitting devices via pulsed excitation”, *Applied Physics Letters* **110**, 203104 (2017). DOI: <https://doi.org/10.1063/1.4983722>
  10. Frieiro, J.L.; Blázquez, O.; López-Vidrier, J.; López-Conesa, L.; Estradé, S.; Peiró, F.; Ibáñez, J.; Hernández, S.; Garrido, B., “Green Electroluminescence of Al/Tb/Al/SiO<sub>2</sub> Devices Fabricated by Electron Beam Evaporation”, *Physica Status Solidi A* 1700451 (2017). DOI: <https://doi.org/10.1002/pssa.201700451>
  11. Blázquez, O.; Martín, G.; Camps, I.; Mariscal, A.; López-Vidrier, J.; Ramírez, J.M.; Hernández, S.; Estradé, S.; Peiró, F.; Serna, R.; Garrido, B., “Memristive behaviour of Si-Al oxynitride thin films: The role of oxygen and nitrogen vacancies in the electroforming process”, *Nanotechnology* **29**, 235702 (2018). DOI: <https://doi.org/10.1088/1361-6528/aab744>
  12. Ehré, F.; Dufour, C.; Blázquez, O.; Garrido, B.; Jadwisienczak, M.; Ingram, D.C.; Gourbilleau, F.; Labbé, C., “Enhancing the

blue emission in Ce doped silicon oxynitrides thin films for electroluminescence device applications”, *ECS Trans.* **85** (3), 9-21 (2018).

DOI: <https://doi.org/10.1149/08503.0009ecst>

13. Ibáñez, J.; Blázquez, O.; Hernández, S.; Garrido, B.; Rodríguez-Hernández, P.; Muñoz, A.; Velázquez, M.; Vaber, P.; Manjón, F.J., “Lattice dynamics study of cubic  $Tb_2O_3$ ”, *Journal of Raman Spectroscopy*, 5488 (2018).

DOI: <https://doi.org/10.1002/jrs.5488>

## B.2. Book Chapters

1. Garrido, B.; Hernández, S.; Berencén, Y.; López-Vidrier, J.; Ramírez, J.M.; Blázquez, O.; Mundet, B., “*Electrical transport in Si-based nanostructured superlattices*” in “*Nanotechnology and Photovoltaic Devices: Light Energy Harvesting with Group IV Nanostructures*”, edited by Valenta, J. and Mirabella, S., Ed. Pan Stanford (2015).  
ISBN 9789814463638

## B.3. Conference Contributions

1. López-Vidrier, J.; Hernández, S.; Blázquez, O.; Hiller, D.; Gutsch, S.; Schnabel, M.; Löper, P.; López-Conesa, L.; Estradé, S.; Peiró, F.; Janz, S.; Zacharias, M; Garrido, B., “Structural and electro-optical properties of silicon-rich silicon oxide superlattices containing silicon nanocrystals for photovoltaic applications”, **Poster Presentation**, *MRS (Materials Research Society) Fall Meeting*, Boston (United States), 2012.
2. Blázquez, O.; López-Vidrier, J; Hernández, S.; Berencén, Y.; Garrido, B., “Investigating the electro-optical properties of non-stoichiometric silicon nitride thin films for photovoltaic applications”, **Poster Presentation**, *VIII OPTOEL (Reunión española de Optoelectrónica)*, Alcalá de Henares (Spain), 2013.

3. López-Vidrier, J.; Hernández, S.; Blázquez, O.; Hiller, D.; Gutsch, S.; Schnabel, M.; Löper, P.; López-Conesa, L.; Estradé, S.; Peiró, F.; Janz, S.; Zacharias, M.; Garrido, B. “SiO<sub>x</sub>/SiO<sub>2</sub> superlattices for photovoltaic applications: structural and electro-optical properties”. **Poster Presentation**. *9th Spanish Conference on Electronic Devices*, Valladolid (Spain), 2013.
4. Blázquez, O.; López-Vidrier, J.; Hernández, S.; Montserrat, J.; Garrido, B., “Electro-optical properties of non-stoichiometric silicon nitride films for photovoltaic Applications”. **Poster Presentation**. *EMRS (European Materials Research Society) Spring Meeting*, Strasbourg (France), 2013.
5. Ramírez, J. M.; Berencén, Y.; López-Vidrier, J.; Blázquez, O.; Hernández, S.; Garrido, B.; Hurtado, J.; Sánchez, N.; Ivanova, T.; López Royo, F.; Sanchis, P., “Structural and luminescence properties of silicon-rich oxides and nitrides fabricated by PECVD”, **Oral Communication**. *CEN (Conferencia Española de Nanofotonica)*, Santander (Spain), 2014.
6. Ramírez, J. M.; Berencén, Y.; López-Vidrier, J.; Blázquez, O.; Hernández, S.; Garrido, B.; Hurtado, J.; Sánchez, N.; Ivanova, T.; López Royo, F.; Sanchis, P., “Structural and luminescence properties of silicon-rich oxides and nitrides fabricated by PECVD”, **Poster Presentation**. *CEN (Conferencia Española de Nanofotonica)*, Santander (Spain), 2014.
7. Garrido, B.; López-Vidrier, J.; Berencén, Y.; Blázquez, O.; Ramírez, J.M.; Hernández, S.; “Size-controlled silicon nanocrystal superlattices for tandem solar cells”, **Oral Communication**. *Nanospain*, Madrid (Spain) 2014.
8. López-Vidrier, J.; Berencén, Y.; Hernández, S.; Blázquez, O.; Gutsch, S.; Laube, J.; Hiller, D.; Löper, P.; Schnabel, M.; Janz, S.; Zacharias M.; Garrido, B. “On the origin of the electroluminescence of silicon nanocrystals/SiO<sub>2</sub> superlattices”, **Poster Presentation**. *EMRS (European Materials Research Society) Spring Meeting*, Lille (France), 2014.

9. Blázquez, O.; Ramírez, J.M.; López-Vidrier, J.; Busquets-Masó, M.; López-Conesa, L.; Hernández, S.; Estradé, S.; Peiró F.; Garrido, B., “Luminescence of Al<sup>3+</sup> and Tb<sup>3+</sup> delta-doped silicon oxide thin films fabricated by electron beam evaporation”, **Oral Communication**. *EMRS (European Materials Research Society) Spring Meeting*, Lille (France), 2015.
10. Busquets-Masó, M.; López-Vidrier, J.; Hernández, S.; Blázquez, O.; Gutsch, S.; Hiller, D.; Zacharias M.; Garrido, B., “Photoconduction spectroscopy in silicon nanocrystals/SiO<sub>2</sub> superlattices”, **Oral Communication**. *EMRS (European Materials Research Society) Spring Meeting*, Lille (France), 2015.
11. Blázquez, O.; López-Vidrier, J.; Ramírez, J.M.; Busquets-Masó, M.; Hernández, S.; Garrido, B., “Luminescence Tb:SiO<sub>2</sub> and Al:Tb:SiO<sub>2</sub> multilayered structures fabricated by electric bean evaporation”, **Poster Presentation**. *IX OPTOEL (Reunión española de Optoelectrónica)*, Salamanca (Spain), 2015.
12. Blázquez, O.; Ramírez, J.M.; López-Vidrier, J.; Berencén, Y.; Hernández, S.; Sanchis, P.; Garrido, B., “Luminescence yield in Al and Tb<sup>3+</sup> delta-doped oxide thin films fabricated by electron beam evaporation”, **Oral Communication**. *SPIE Microtechnologies*, Barcelona (Spain), 2015.
13. Pruna, R.; Palacio, F.; López, M.; Diéguez, A.; Mir, M.; Pérez, J.; Blázquez, O.; Hernández, S.; Garrido, B., “Development of DNA biosensors based on nanostructured ITO films”, **Oral Communication**. *EMRS (European Materials Research Society) Spring Meeting*, Lille (France), 2016.
14. López-Vidrier, J.; Blázquez, O.; Portier, X.; Busquets-Masó, M.; Hernández, S.; Labbé, C.; Garrido, B., “Intense visible electroluminescence from Eu- and Tb-codoped ZnO thin films”, **Oral Communication**. *EMRS (European Materials Research Society) Spring Meeting*, Lille (France), 2016.
15. Pruna, R.; Palacio, F.; López, M.; Gómez, J. M.; Mir, M.; Pérez, J.; Blázquez, O.; Hernández, S.; Garrido, B., “Characterization



- and functionalization of nanostructured ITO films for biosensing applications”, **Poster Presentation**. *EMRS (European Materials Research Society) Spring Meeting*, Lille (France), 2016.
16. Blázquez, O.; Ramírez, J.M.; Camps, I.; López-Vidrier, J.; Hernández, S.; Serna, R.; Garrido, B., “Si-Al oxynitride thin films for memristive switching Applications”, **Oral Communication**. *EMRS (European Materials Research Society) Spring Meeting*, Lille (France), 2016.
  17. Camps, I.; Mariscal, A.; Ramírez, J.M.; Blázquez, O.; Calvo-Barrio, L.; Garrido, B.; Serna, R., “Evolution of the broad band white emission of Eu doped films based on SiAlON as a function of the excitation”, **Oral Communication**. *EMRS (European Materials Research Society) Spring Meeting*, Lille (France), 2016.
  18. Blázquez, O.; López-Vidrier, J.; Vales, P.; Hernández, S.; Garrido, B., “Structural and electro-optical characterization of ZnO/p-Si light-emitting devices”, **Poster Presentation**. *CDE (Conference on Electron Devices)*, Barcelona (Spain), 2017.
  19. Blázquez, O.; Mariño, E.; Hernández, S.; Garrido, B., “Memristive characterization of SiAlON thin films”, **Poster Presentation**. *CDE (Conference on Electron Devices)*, Barcelona (Spain), 2017.
  20. Pruna, R.; Palacio, F.; Martínez, M.; Blázquez, O.; Hernández, S.; Garrido, B.; López, M., “Optimizing the electrochemical performance of nanostructured ITO electrodes”, **Poster Presentation**. *EMRS (European Materials Research Society) Spring Meeting*, Strasbourg (France), 2017.
  21. Pruna, R.; Palacio, F.; Salvador, J.P.; Martínez, M.; Blázquez, O.; Hernández, S.; Garrido, B.; Marco, M.P.; López, M., “On the potential use of nanostructured ITO electrodes as amperometric biosensors”, **Oral Communication**. *EMRS (European Materials Research Society) Spring Meeting*, Strasbourg (France), 2017.

22. Busquets-Masó, M.; Blázquez, O.; López-Vidrier, J.; Geyer, A.; Oliva, R.; Hiller, D.; Zacharias, M.; Valenta, J.; Garrido, B.; Hernández, S.; Ibáñez, J., “High-pressure optical and vibrational properties of silicon nanocrystals”, **Poster Presentation**. *EMRS (European Materials Research Society) Spring Meeting*, Strasbourg (France), 2017.
23. Blázquez, O.; López-Vidrier, J.; Busquets-Masó, M.; López-Conesa, L.; Estradé, S.; Peiró, F.; Hernández, S.; Ibáñez, J.; Garrido, B., “Green electroluminescence of Al/Tb/Al/SiO<sub>2</sub> devices fabricated by electron beam evaporation”, **Poster Presentation**. *EMRS (European Materials Research Society) Spring Meeting*, Strasbourg (France), 2017.
24. Ehré, F.; Dufour, C.; Gourbilleau, F.; Portier, X.; Cardin, J.; Garrido, B.; Blázquez, O.; Jadwisienczak, W. M.; Richard, A. L.; Ingram, David C.; Labbé, C., “Ce<sup>3+</sup> doped silicon oxynitride thin films for emitting devices”, **Oral Communication**. *EMRS (European Materials Research Society) Spring Meeting*, Strasbourg (France), 2017.
25. López-Vidrier, J.; Hiller, D.; Gutsch, S.; Laube, J.; Blázquez, O.; Hernández, S.; Garrido, B.; Zacharias, M., “Electroluminescence emission of Si NC / SiO<sub>2</sub> multilayers under pulsed electrical excitation”, **Oral Communication**. *EMRS (European Materials Research Society) Spring Meeting*, Strasbourg (France), 2017.
26. Blázquez, O.; Martín, G.; Camps, I.; Ramírez, J.M.; Hernández, S.; Estradé, S.; Peiró, F.; Serna, R.; Cornet, A.; Garrido, B., “Structural and electrical characterization of SiAlON memristors: the role of oxygen vacancies in the electroforming process”, **Oral Communication**. *EMRS (European Materials Research Society) Spring Meeting*, Strasbourg (France), 2017.
27. López-Vidrier, J.; Gutsch, S.; Blázquez, O.; Hiller, D.; Laube, J.; Kaur, R.; Hernández, S.; Garrido, B.; Zacharias, M., “Modulation of the electroluminescence emission from ZnO / Si NCs / p-Si light-emitting devices via pulsed excitation”, **Poster Presentation**. *X OPTOEL (Reunión española de Optoelectrónica)*, Santiago de Compostela (Spain), 2017.

28. López-Vidrier, J.; Hiller, D.; Gutsch, S.; Laube, J.; Blázquez, O.; Hernández, S.; Garrido, B.; Zacharias, M., “Electroluminescence emission enhancement of Si NCs under pulsed electrical excitation and improved device design”, **Oral Communication**. *EMRS (European Materials Research Society) Fall Meeting*, Warsaw (Poland), 2017.
29. Garrido, B.; Blázquez, O.; López-Vidrier, J.; Huguet, A.; Pruna, R.; López, M.; Frieiro, J.L.; Hernández, S., “Materials and devices for integrated optoelectronics, biosensing and human centric lighting”, **Oral Communication**. *2nd Workshop on Photonic Integrated Circuits for Telecom & Bio/Life Sciences*, Castelldefels (Spain), 2017.
30. Ehre, F.; Dufour, C.; Blázquez, O.; Garrido, B.; Jadwisienczak, W.; Ingram, D.C.; Gourbilleau, F.; Labbé, C., “Naked eye blue emission in Ce<sup>3+</sup> codoped SiO<sub>x</sub>N<sub>y</sub>: toward Si-based light-emitting devices”, **Invited Oral Communication**. *233<sup>rd</sup> ECS Meeting*, Seattle (USA), 2018.

## B.4. Seminars, workshops and/or courses

1. Blázquez, O., “Fabrication and characterization of optoelectronics materials”, **Seminar**. *IN<sup>2</sup>UB Internal seminar*, Barcelona (Spain), 2017.

## B.5. Participation in Research Projects

1. **Title of the project:** Silicon Nanodots for Solar Cell Tandem (NASCEnT)  
**Main researcher:** Prof. Blas Garrido Fernández  
**Financing Administration:** European Union  
**Code:** NMP4-SL-2010-245977  
**Amount:** 275364 €  
**Duration:** 2010 – 2013

2. **Title of the project:** Iluminación de estado sólido innovadora e inteligente e interconexiones ópticas a 1.5 micras con fotónica de silicio basada en tecnología CMOS (LEOMIS)  
**Main researcher:** Prof. Blas Garrido Fernández  
**Financing Administration:** Spanish Ministry of Economy and Competitiveness  
**Code:** TEC2012-38540-C02-01  
**Amount:** 200800 €  
**Duration:** 2013 – 2015
  
3. **Title of the project:** Desarrollo de óxidos de metales de transición con tecnología de silicio para conmutadores electrónicos (memristores) y células solares (METALONIC)  
**Main researcher:** Prof. Blas Garrido Fernández and Dr. Sergi Hernández Márquez  
**Financing Administration:** Spanish Ministry of Economy and Competitiveness  
**Code:** TEC2016-76849-C2-1-R  
**Amount:** 139755 €  
**Duration:** 2016 – 2018

## **B.6. Experience supervising thesis and/or degree projects**

1. Vales, P., “Fabrication and characterization of ZnO thin films by electron beam evaporation”, **Master’s thesis**. *Master in Nanoscience and Nanotechnology (University of Barcelona)*, Barcelona (Spain), 2016.
  
2. Mariño, E., “Characterization of SiAlON thin films and study of its memristive behavior”, **Master’s thesis**. *Master in Nanoscience and Nanotechnology (University of Barcelona)*, Barcelona (Spain), 2016.
  
3. Doblas, A., “Resistive switching in Al/Tb/SiO<sub>2</sub> nanomultilayers”, **Master’s thesis**. *Master in Nanoscience and Nanotechnology (University of Barcelona)*, Barcelona (Spain), 2017.

## B. Curriculum Vitae

4. Frieiro, J.L., “Optoelectronic device based on Rare Earth electroluminescence”, **Master’s thesis**. *Master in Nanoscience and Nanotechnology (University of Barcelona)*, Barcelona (Spain), 2017.
5. Cerda, G., “Characterization of the ZnO-based Memristor”, **Master’s thesis**. *Master in Nanoscience and Nanotechnology (University of Barcelona)*, Barcelona (Spain), 2018.
6. Bonet, F., “Effect of rare earth on ZnO-based memristors”, **Master’s thesis**. *Master in Nanoscience and Nanotechnology (University of Barcelona)*, Barcelona (Spain), 2018.

## B.7. Teaching experience

Course 2015 – 2016 (H.GR@D: **98.0**, H.PDA: **311.7**)

1. 363752 – Enginyeria de Materials i Biomaterials, *TG1074 - Enginyeria Biomèdica*. (Pràctiques de laboratori).  
H.GR@D: 12.0, H.PDA: 39.6
2. 360572 – Informàtica, *TG1035 - Física*, (Pràctiques d’ordinador).  
H.GR@D: 52.0, H.PDA: 197.6
3. 571424 – Nanoenergia, *M0802 - Nanociència i Nanotecnologia*. (Teoricopràctica).  
H.GR@D: 2.0, H.PDA: 10.5
4. 571432 – Tesi de Master, *M0802 - Nanociència i Nanotecnologia*. (Teoricopràctica).  
H.GR@D: 32.0, H.PDA: 64.0

Course 2016 – 2017 (H.GR@D: **103.0**, H.PDA: **332.1**)

1. 364289 – Desseny Digital Bàsic, *TG1077 - Enginyeria Informàtica*. (Pràctiques de laboratori).  
H.GR@D: 15.0, H.PDA: 49.5

2. 360572 – Informàtica, *TG1035* – Física, (Pràctiques d'ordinador).  
H.GR@D: 52.0, H.PDA: 197.6
3. 571426 – Nanoelectrònica, *M0802* – Nanociència i Nanotecnologia. (Teoricopràctica).  
H.GR@D: 2.0, H.PDA: 10.5
4. 571424 – Nanoenergia, *M0802* – Nanociència i Nanotecnologia. (Teoricopràctica).  
H.GR@D: 2.0, H.PDA: 10.5
5. 571432 – Tesi de Master, *M0802* – Nanociència i Nanotecnologia. (Teoricopràctica).  
H.GR@D: 32.0, H.PDA: 64.0

Course 2017 – 2018 (H.GR@D: **90.0**, H.PDA: **293.1**)

1. 360572 – Informàtica, *TG1035* – Física, (Pràctiques d'ordinador).  
H.GR@D: 52.0, H.PDA: 197.6
2. 571419 – Ciència i Anàlisi de Superfícies, *M0802* – Nanociència i Nanotecnologia. (Pràctiques de laboratori).  
H.GR@D: 4.0, H.PDA: 21.0
3. 571424 – Nanoenergia, *M0802* – Nanociència i Nanotecnologia. (Teoricopràctica).  
H.GR@D: 2.0, H.PDA: 10.5
4. 571432 – Tesi de Master, *M0802* – Nanociència i Nanotecnologia. (Teoricopràctica).  
H.GR@D: 32.0, H.PDA: 64.0



## Bibliography

- [1] SOREF, Richard A. a Brian R. BENNETT. Electrooptical effects in silicon. *IEEE Journal of Quantum Electronics* [online]. 1987, **23**(1), 123–129. ISSN 15581713. Dostupné z: doi:10.1109/JQE.1987.1073206
- [2] JALALI, Bahram, Mario PANICCIA a Graham REED. Silicon photonics. *IEEE Microwave Magazine* [online]. 2006, **7**(3), 58–68. ISSN 1527-3342. Dostupné z: doi:10.1109/MMW.2006.1638290
- [3] RYCKEBOER, Eva, Xiaomin NIE, Ashim DHAKAL, Daan MARTENS, Peter BIENSTMAN, Gunther ROELKENS a Roel BAETS. Spectroscopic sensing and applications in Silicon Photonics. In: *2017 IEEE 14th International Conference on Group IV Photonics (GFP)* [online]. B.m.: IEEE, 2017, s. 81–82. ISBN 978-1-5090-6568-4. Dostupné z: doi:10.1109/GROUP4.2017.8082206
- [4] CROWE, Iain F., Matthew P. HALSALL, Oksana HULKO, Andrew P. KNIGHTS, Russell M. GWILLIAM, Maciej WOJDAK a Anthony J. KENYON. Probing the phonon confinement in ultrasmall silicon nanocrystals reveals a size-dependent surface energy. *Journal of Applied Physics* [online]. 2011, **109**(8). ISSN 00218979. Dostupné z: doi:10.1063/1.3575181
- [5] JUAN-COLÁS, José, Alison PARKIN, Katherine E. DUNN, Mark G. SCULLION, Thomas F. KRAUSS a Steven D. JOHNSON. The electrophotonic silicon biosensor. *Nature Communications* [online]. 2016, **7**, 1–7. ISSN 20411723. Dostupné z: doi:10.1038/ncomms12769
- [6] XU, D.-X., A. DENSMORE, P. CHEBEN, M. VACHON, R. MA, S. JANZ, A. DELAGE, J.H. SCHMID, J. LAPOINTE, Y. LI, G LOPINSKI, R. HALIR a I. MOLINA-FERNANDEZ. Silicon photonic wire devices for biosensing and communications. In: *Asia Communications and Photonics Conference and Exhibition* [online]. B.m.: IEEE, 2010, s. 52–53. ISBN 978-1-4244-7111-9. Dostupné z: doi:10.1109/ACP.2010.5682839
- [7] KEISER, Gerd. Optical Fiber Communications. In: *Wiley Encyclopedia of Telecommunications* [online]. Hoboken, NJ, USA: John Wiley & Sons, Inc., 2003. Dostupné z: doi:10.1002/0471219282.eot158
- [8] LIN, Keng-Te, Hsuen-Li CHEN, Yu-Sheng LAI a Chen-Chieh YU. Silicon-based broadband antenna for high responsivity and polarization-insensitive photodetection at telecommunication wavelengths. *Nature Communications* [online]. 2014, **5**, 1–10. ISSN 2041-1723. Dostupné z: doi:10.1038/ncomms4288
- [9] PAVESI, Lorenzo a Gérard GUILLOT, ed. *Optical Interconnects* [online]. Berlin, Heidelberg: Springer Berlin Heidelberg, 2006. Springer Series in Optical Sciences. ISBN 978-3-540-28910-4. Dostupné z: doi:10.1007/978-3-540-28912-8
- [10] NANISHI, Yasushi. The birth of the blue LED. *Nature Photonics* [online]. 2014, **8**(12), 884–886. ISSN 1749-4885. Dostupné z: doi:10.1038/nphoton.2014.291



## Bibliography

- [11] YOU, Han, Yanfeng DAI, Zhiqiang ZHANG a Dongge MA. Improved performances of organic light-emitting diodes with metal oxide as anode buffer. *Journal of Applied Physics* [online]. 2007, **101**(2), 026105. ISSN 0021-8979. Dostupné z: doi:10.1063/1.2430511
- [12] GERSHON, T. Metal oxide applications in organic-based photovoltaics. *Materials Science and Technology* [online]. 2011, **27**(9), 1357–1371 [vid. 2018-04-30]. ISSN 0267-0836. Dostupné z: doi:10.1179/026708311X13081465539809
- [13] BAYAT, Khadijeh, Sujeet K CHAUDHURI a Saffiedin SAFAVI-NAEINI. Low Temperature Silicon Oxinitride Technology for Compact CMOS Compatible Planar Optical Devices. *IEEE, 345 E 47TH ST, NEW YORK, NY 10017 USA*. 2007, **4**(June), 3–5.
- [14] YOSHIHARA, M, A SEKIYA, T MORITA, K ISHII, S SHIMOTO, S SAKAI a Y OHKI. Rare-earth-doped films prepared by plasma-enhanced chemical vapour deposition. *Journal of Physics D: Applied Physics* [online]. 1997, **30**(13), 1908–1912. ISSN 0022-3727. Dostupné z: doi:10.1088/0022-3727/30/13/012
- [15] WEN, Yuehong, Tianlu SHENG, Xiaoquan ZHU, Chao ZHUO, Shaodong SU, Haoran LI, Shengmin HU, Qi Long ZHU a Xintao WU. Introduction of Red-Green-Blue Fluorescent Dyes into a Metal–Organic Framework for Tunable White Light Emission. *Advanced Materials* [online]. 2017, **29**(37), 1–8. ISSN 15214095. Dostupné z: doi:10.1002/adma.201700778
- [16] HEITMANN, J, R SCHOLZ, M SCHMIDT a M ZACHARIAS. Size controlled nc-Si synthesis by SiO/SiO<sub>2</sub> superlattices. *Journal of Non-Crystalline Solids* [online]. 2002, **299–302**, 1075–1078. ISSN 00223093. Dostupné z: doi:10.1016/S0022-3093(01)01074-2
- [17] HILLER, Daniel, Silvana GOETZE, Frans MUNNIK, Mihaela JIVANESCU, Jürgen W. GERLACH, Jürgen VOGT, Eckhard PIPPEL, Nikolai ZAKHAROV, Andre STESMANS a Margit ZACHARIAS. Nitrogen at the Si-nanocrystal/SiO<sub>2</sub> interface and its influence on luminescence and interface defects. *Physical Review B - Condensed Matter and Materials Physics* [online]. 2010, **82**(19), 1–9. ISSN 10980121. Dostupné z: doi:10.1103/PhysRevB.82.195401
- [18] PICKETT, Matthew D., Gilberto MEDEIROS-RIBEIRO a R. Stanley WILLIAMS. A scalable neuristor built with Mott memristors. *Nature Materials* [online]. 2012, **12**(2), 114–117. ISSN 1476-1122. Dostupné z: doi:10.1038/nmat3510
- [19] JO, Sung Hyun, Ting CHANG, Idongesit EBONG, Bhavitavya B. BHADVIYA, Pinaki MAZUMDER a Wei LU. Nanoscale memristor device as synapse in neuromorphic systems. *Nano Letters* [online]. 2010, **10**(4), 1297–1301. ISSN 15306984. Dostupné z: doi:10.1021/nl904092h
- [20] OHNO, Takeo, Tsuyoshi HASEGAWA, Tohru TSURUOKA, Kazuya TERABE, James K. GIMZEWSKI a Masakazu AONO. Short-term plasticity and long-term potentiation mimicked in single inorganic synapses. *Nature Materials* [online]. 2011, **10**(8), 591–595. ISSN 1476-1122. Dostupné z: doi:10.1038/nmat3054
- [21] TORREZAN, Antonio C, John Paul STRACHAN, Gilberto MEDEIROS-RIBEIRO

- a R Stanley WILLIAMS. Sub-nanosecond switching of a tantalum oxide memristor. *Nanotechnology* [online]. 2011, **22**(48), 485203. ISSN 0957-4484. Dostupné z: doi:10.1088/0957-4484/22/48/485203
- [22] HASEGAWA, Tsuyoshi, Kazuya TERABE, Tohru TSURUOKA a Masakazu AONO. Atomic switch: Atom/ion movement controlled devices for beyond von-Neumann computers. *Advanced Materials* [online]. 2012, **24**(2), 252–267. ISSN 09359648. Dostupné z: doi:10.1002/adma.201102597
- [23] VALOV, Ilija, Rainer WASER, John R JAMESON a Michael N KOZICKI. Electrochemical metallization memories—fundamentals, applications, prospects. *Nanotechnology* [online]. 2011, **22**(28), 289502. ISSN 0957-4484. Dostupné z: doi:10.1088/0957-4484/22/28/289502
- [24] VALOV, Ilija. Redox-Based Resistive Switching Memories (ReRAMs): Electrochemical Systems at the Atomic Scale. *ChemElectroChem* [online]. 2014, **1**(1), 26–36. ISSN 21960216. Dostupné z: doi:10.1002/celec.201300165
- [25] VESCIO, Giovanni, A. CRESPO-YEPES, D. ALONSO, Sergi CLARAMUNT, Marc PORTI, Rosana RODRIGUEZ, A. CORNET, A. CIRERA, Montserrat NAFRIA a Xavier AYMERICH. Inkjet Printed HfO<sub>2</sub>-Based ReRAMs: First Demonstration and Performance Characterization. *IEEE Electron Device Letters* [online]. 2017, **38**(4), 457–460. ISSN 0741-3106. Dostupné z: doi:10.1109/LED.2017.2668599
- [26] MARTÍN, Gemma, Mireia B GONZÁLEZ, Francesca CAMPABADAL, Francesca PEIRÓ, Albert CORNET a Sònia ESTRADÉ. Transmission electron microscopy assessment of conductive-filament formation in Ni–HfO<sub>2</sub>–Si resistive-switching operational devices. *Applied Physics Express* [online]. 2018, **11**, 014101. Dostupné z: doi:https://doi.org/10.7567/APEX.11.014101
- [27] KLASSENS, H.A. a H. KOELMANS. A tin oxide field-effect transistor. *Solid-State Electronics* [online]. 1964, **7**(9), 701–702 [vid. 2018-04-27]. ISSN 00381101. Dostupné z: doi:10.1016/0038-1101(64)90057-7
- [28] NOMURA, K. Thin-Film Transistor Fabricated in Single-Crystalline Transparent Oxide Semiconductor. *Science* [online]. 2003, **300**(5623), 1269–1272 [vid. 2018-04-27]. ISSN 00368075. Dostupné z: doi:10.1126/science.1083212
- [29] WANG, Lian, Myung-Han YOON, Gang LU, Yu YANG, Antonio FACCHETTI a Tobin J. MARKS. Erratum: High-performance transparent inorganic–organic hybrid thin-film n-type transistors. *Nature Materials* [online]. 2007, **6**(4), 317–317 [vid. 2018-04-27]. ISSN 1476-1122. Dostupné z: doi:10.1038/nmat1878
- [30] HOFFMAN, R. L., B. J. NORRIS a J. F. WAGER. ZnO-based transparent thin-film transistors. *Applied Physics Letters* [online]. 2003, **82**(5), 733–735. ISSN 0003-6951. Dostupné z: doi:10.1063/1.1542677
- [31] NOMURA, Kenji, Hiromichi; OHTA, Akihiro TAKAGI a Toshio KAMIYA. Room-temperature fabrication of transparent flexible thin-film. *Nature*. 2004, **432**(7016).

## Bibliography

- [32] LEE, Eungkyu, Jieun KO, Keon Hee LIM, Kyongjun KIM, Si Yun PARK, Jae M. MYOUNG a Youn Sang KIM. Gate capacitance-dependent field-effect mobility in solution-processed oxide semiconductor thin-film transistors. *Advanced Functional Materials* [online]. 2014, **24**(29), 4689–4697. ISSN 16163028. Dostupné z: doi:10.1002/adfm.201400588
- [33] BROX-NILSEN, Christian, Jidong JIN, Yi LUO, Peng BAO a Aimin M. SONG. Sputtered ZnO Thin-Film Transistors With Carrier Mobility Over 50  $\text{cm}^2/\text{Vs}$ . *IEEE Transactions on Electron Devices* [online]. 2013, **60**(10), 3424–3429. ISSN 0018-9383. Dostupné z: doi:10.1109/TED.2013.2279401
- [34] ZHANG, Lei, Yuanjun ZHOU, Lu GUO, Weiwei ZHAO, Anna BARNES, Hai-Tian ZHANG, Craig EATON, Yuanxia ZHENG, Matthew BRAHLEK, Hamna F. HANEEF, Nikolas J. PODRAZA, Moses H. W. CHAN, Venkatraman GOPALAN, Karin M. RABE a Roman ENGEL-HERBERT. Correlated metals as transparent conductors. *Nature Materials* [online]. 2016, **15**(2), 204–210. ISSN 1476-1122. Dostupné z: doi:10.1038/nmat4493
- [35] PENILLA, Elias H., Yasuhiro KODERA a Javier E. GARAY. Blue-green emission in terbium-doped alumina (Tb:Al<sub>2</sub>O<sub>3</sub>) transparent ceramics. *Advanced Functional Materials* [online]. 2013, **23**(48), 6036–6043. ISSN 1616301X. Dostupné z: doi:10.1002/adfm.201300906
- [36] PATEL, Ketan, Victoria BLAIR, Justin DOUGLAS, Qilin DAI, Yaohua LIU, Shenqiang REN a Raymond BRENNAN. Structural Effects of Lanthanide Dopants on Alumina. *Scientific Reports* [online]. 2017, **7**, 39946. ISSN 2045-2322. Dostupné z: doi:10.1038/srep39946
- [37] DAVESNNE, C., A. ZIANI, C. LABBÉ, P. MARIE, C. FRILAY a X. PORTIER. Energy transfer mechanism between terbium and europium ions in zinc oxide and zinc silicates thin films. *Thin Solid Films* [online]. 2014, **553**, 33–37. ISSN 00406090. Dostupné z: doi:10.1016/j.tsf.2013.11.122
- [38] LIMA, S A M, M R DAVOLOS, C LEGNANI, W G QUIRINO a M CREMONA. Low voltage electroluminescence of terbium- and thulium-doped zinc oxide films [online]. 2006, **418**, 35–38. Dostupné z: doi:10.1016/j.jallcom.2005.10.066
- [39] SPIE, Proceedings O F, T H E INTERNATIONAL, Society FOR, Optical ENGINEERING a St ANDREWS. Transition metal- And rare earth-doped ZnO : A comparison of optical , magnetic , and structural behavior of bulk and thin films [online]. 2007, (February 2016). Dostupné z: doi:10.1117/12.717788
- [40] FUKUSHIMA, Masanori, Nobuto MANAGAKI, Minoru FUJII, Hisao YANAGI a Shinji HAYASHI. Enhancement of 1.54- $\mu\text{m}$  emission from Er-doped sol-gel SiO<sub>2</sub> films by Au nanoparticles doping. *Journal of Applied Physics* [online]. 2005, **98**(2), 024316. ISSN 0021-8979. Dostupné z: doi:10.1063/1.1990257
- [41] RAMÍREZ, J. M., J. WOJCIK, Y. BERENCÉN, P. MASCHER a B. GARRIDO. On the photoluminescence of as-deposited Tb-doped silicon oxides and oxynitrides fabricated by ECR-PECVD [online]. 2014, **9133**, 913309. Dostupné z: doi:10.1117/12.2052571

- [42] BERENCEN, Y., J. M. RAMIREZ a B. GARRIDO. Er-doped Si-based electroluminescent capacitors: Role of different host matrices on the electrical and luminescence properties. In: *2013 Spanish Conference on Electron Devices* [online]. B.m.: IEEE, 2013, s. 245–248. ISBN 978-1-4673-4668-9. Dostupné z: doi:10.1109/CDE.2013.6481388
- [43] DORENBOS, P. The transitions of the trivalent lanthanides in halogenides and chalcogenides. *Journal of Luminescence* [online]. 2000, **91**(1–2), 91–106. ISSN 00222313. Dostupné z: doi:10.1016/S0022-2313(00)00197-6
- [44] ISHII, Masashi, Shuji KOMURO, Takitaro MORIKAWA a Yoshinobu AOYAGI. Local structure analysis of an optically active center in Er-doped ZnO thin film. *Journal of Applied Physics* [online]. 2001, **89**(7), 3679–3684. ISSN 00218979. Dostupné z: doi:10.1063/1.1355284
- [45] JUDD, B.R. R. Optical Absorption Intensities of Rare-Earth Ions. *Physical Review* [online]. 1962, **127**(3), 750–761. ISSN 0031-899X. Dostupné z: doi:10.1103/PhysRev.127.750
- [46] MECH, Agnieszka, Angelo MONGUZZI, Francesco MEINARDI, Jakub MEZYK, Giorgio MACCHI a Riccardo TUBINO. Sensitized NIR Erbium(III) Emission in Confined Geometries: A New Strategy for Light Emitters in Telecom Applications. *Journal of the American Chemical Society* [online]. 2010, **132**(13), 4574–4576. ISSN 0002-7863. Dostupné z: doi:10.1021/ja907927s
- [47] EHRÉ, F., C. LABBÉ, Christian DUFOUR, W. M. JADWISIENCZAK, Jennifer WEIMMERSKIRCH-AUBATIN, Xavier PORTIER, J.-L. DOUALAN, Julien CARDIN, A. L. RICHARD, D. C. INGRAM, C. LABRUGÈRE a Fabrice GOURBILLEAU. The nitrogen concentration effect on Ce doped SiO<sub>x</sub>N<sub>y</sub> emission: towards optimized Ce<sup>3+</sup> for LED applications. *Nanoscale* [online]. 2018, **10**(8), 3823–3837. ISSN 2040-3364. Dostupné z: doi:10.1039/C7NR06139K
- [48] RAMÍREZ, J. M., A. RUIZ-CARIDAD, J. WOJCIK, A. M. GUTIERREZ, S. ESTRADÉ, F. PEIRÓ, P. SANCHÍS, P. MASCHER a B. GARRIDO. Luminescence properties of Ce<sup>3+</sup> and Tb<sup>3+</sup> co-doped SiO<sub>x</sub>N<sub>y</sub> thin films: Prospects for color tunability in silicon-based hosts. *Journal of Applied Physics* [online]. 2016, **119**(11), 113108. ISSN 0021-8979. Dostupné z: doi:10.1063/1.4944433
- [49] LOZYKOWSKI, H. J., W. M. JADWISIENCZAK a I. BROWN. Visible cathodoluminescence of GaN doped with Dy, Er, and Tm. *Applied Physics Letters* [online]. 1999, **74**(8), 1129–1131. ISSN 00036951. Dostupné z: doi:10.1063/1.123465
- [50] BLÁZQUEZ, O., J. LÓPEZ-VIDRIER, S. HERNÁNDEZ, J. MONTSERRAT a B. GARRIDO. Electro-optical Properties of Non-stoichiometric Silicon Nitride Films for Photovoltaic Applications. *Energy Procedia* [online]. 2014, **44**, 145–150. ISSN 18766102. Dostupné z: doi:10.1016/j.egypro.2013.12.021
- [51] LLUSCÀ, M, J. LÓPEZ-VIDRIER, S LAUZURICA, M.I. SÁNCHEZ-ANIORTE, A ANTONY, C. MOLPECERES, S. HERNÁNDEZ, B. GARRIDO a J. BERTOMEU. Activation of visible up-conversion luminescence in transparent and conducting ZnO:Er:Yb films by laser annealing. *Journal of Luminescence* [online].

## Bibliography

- 2015, **167**, 101–105. ISSN 00222313. Dostupné z: doi:10.1016/j.jlumin.2015.06.017
- [52] CAMPS, I., J.M. RAMÍREZ, A. MARISCAL, R. SERNA, B. GARRIDO, M. PERÁLVAREZ, J. CARRERAS, N.P. BARRADAS, L.C. ALVES a E. ALVES. Optical performance of thin films produced by the pulsed laser deposition of SiAlON and Er targets. *Applied Surface Science* [online]. 2015, **336**, 274–277. ISSN 01694332. Dostupné z: doi:10.1016/j.apsusc.2014.12.013
- [53] GU, Feng, Shu Fen WANG, Meng Kai LÜ, Guang Jun ZHOU, Dong XU a Duo Rong YUAN. Structure Evaluation and Highly Enhanced Luminescence of Dy<sup>3+</sup>-Doped ZnO Nanocrystals by Li<sup>+</sup> Doping via Combustion Method. *Langmuir* [online]. 2004, **20**(9), 3528–3531. ISSN 0743-7463. Dostupné z: doi:10.1021/la049874f
- [54] LI, Yu Chun, Yen Hwei CHANG, Yu Feng LIN, Yee Shin CHANG a Yi Jing LIN. Synthesis and luminescent properties of Ln<sup>3+</sup>(Eu<sup>3+</sup>, Sm<sup>3+</sup>, Dy<sup>3+</sup>)-doped lanthanum aluminum germanate LaAlGe<sub>2</sub>O<sub>7</sub> phosphors. *Journal of Alloys and Compounds* [online]. 2007, **439**(1–2), 367–375. ISSN 09258388. Dostupné z: doi:10.1016/j.jallcom.2006.08.269
- [55] BALLATO, John, John S. LEWIS a Paul HOLLOWAY. Display Applications of Rare-Earth-Doped Materials. *MRS Bulletin* [online]. 1999, **24**(09), 51–56. ISSN 0883-7694. Dostupné z: doi:10.1557/S0883769400053070
- [56] STEVELER, E., H. RINNERT a M. VERGNAT. Photoluminescence properties of Nd-doped silicon oxide thin films containing silicon nanoparticles. *Journal of Luminescence* [online]. 2014, **150**, 35–39. ISSN 00222313. Dostupné z: doi:10.1016/j.jlumin.2014.01.061
- [57] HENG, C. L., J. T. LI, Z. HAN a P. G. YIN. An Abnormal Photoluminescence Enhancement in (Eu, Yb) Co-doped SiO<sub>2</sub> Thin Film. *Integrated Ferroelectrics* [online]. 2014, **151**(1), 179–186. ISSN 1058-4587. Dostupné z: doi:10.1080/10584587.2014.901125
- [58] SILVERSMITH, a. J., N. T T NGUYEN, B. W. SULLIVAN, D. M. BOYE, C. ORTIZ a K. R. HOFFMAN. Rare-earth ion distribution in sol-gel glasses co-doped with Al<sup>3+</sup>. *Journal of Luminescence* [online]. 2008, **128**(5–6), 931–933. ISSN 00222313. Dostupné z: doi:10.1016/j.jlumin.2007.11.049
- [59] BOYE, D.M., A.J. SILVERSMITH, Thao Nguyen NGUYEN a K.R. HOFFMAN. Effects of rehydration on Tb<sup>3+</sup> spectroscopy in sol-gel glasses. *Journal of Non-Crystalline Solids* [online]. 2007, **353**(24–25), 2350–2354. ISSN 00223093. Dostupné z: doi:10.1016/j.jnoncrysol.2007.03.021
- [60] VILA, M., C. DÍAZ-GUERRA, K. LORENZ, J. PIQUERAS, I. PÍŠ, E. MAGNANO, C. MUNUERA, E. ALVES a M. GARCÍA-HERNÁNDEZ. Effects of thermal annealing on the structural and electronic properties of rare earth-implanted MoO<sub>3</sub> nanoplates. *CrystEngComm* [online]. 2017, **19**(17), 2339–2348. ISSN 1466-8033. Dostupné z: doi:10.1039/C7CE00242D
- [61] MINISCALCO, W.J. Erbium-doped glasses for fiber amplifiers at 1500 nm. *Journal*

- of Lightwave Technology* [online]. 1991, **9**(2), 234–250. ISSN 07338724. Dostupné z: doi:10.1109/50.65882
- [62] AUZEL, F. a P. GOLDNER. Towards rare-earth clustering control in doped glasses. *Optical Materials* [online]. 2001, **16**(1–2), 93–103. ISSN 09253467. Dostupné z: doi:10.1016/S0925-3467(00)00064-1
- [63] MIGDISOV, Art A., A. E. WILLIAMS-JONES a T. WAGNER. An experimental study of the solubility and speciation of the Rare Earth Elements (III) in fluoride- and chloride-bearing aqueous solutions at temperatures up to 300 °C. *Geochimica et Cosmochimica Acta* [online]. 2009, **73**(23), 7087–7109. ISSN 00167037. Dostupné z: doi:10.1016/j.gca.2009.08.023
- [64] FIRSCHING, F. Henry. Solubility products of the trivalent rare-earth arsenates. *Journal of Chemical & Engineering Data* [online]. 1992, **37**(4), 497–499. ISSN 0021-9568. Dostupné z: doi:10.1021/je00008a028
- [65] MONTEIL, A., S. CHAUSSEMENT, G. ALOMBERT-GOGET, N. GAUMER, J. OBRIOT, S.J.L. RIBEIRO, Y. MESSADDEQ, A. CHIASERA a M. FERRARI. Clustering of rare earth in glasses, aluminum effect: experiments and modeling. *Journal of Non-Crystalline Solids* [online]. 2004, **348**, 44–50. ISSN 00223093. Dostupné z: doi:10.1016/j.jnoncrysol.2004.08.124
- [66] LÆGSGAARD, J. Dissolution of rare-earth clusters in SiO<sub>2</sub> by Al codoping: A microscopic model. *Physical Review B* [online]. 2002, **65**(17), 174114. ISSN 0163-1829. Dostupné z: doi:10.1103/PhysRevB.65.174114
- [67] KULAKCI, Mustafa a Rasit TURAN. Improvement of light emission from Tb-doped Si-based MOS-LED using excess Si in the oxide layer. *Journal of Luminescence* [online]. 2013, **137**, 37–42. ISSN 0022-2313. Dostupné z: doi:10.1016/j.jlumin.2012.11.005
- [68] LI, Dongsheng, Xuwu ZHANG, Lu JIN a Deren YANG. Structure and luminescence evolution of annealed Europium-doped silicon oxides films. *Optics express* [online]. 2010, **18**(26), 27191–6. ISSN 1094-4087. Dostupné z: doi:10.1364/OE.18.027191
- [69] MINISCALCO, W.J. Erbium-doped glasses for fiber amplifiers at 1500 nm. *Journal of Lightwave Technology* [online]. 1991, **9**(2), 234–250. ISSN 07338724. Dostupné z: doi:10.1109/50.65882
- [70] KIK, P. G. a A. POLMAN. Cooperative upconversion as the gain-limiting factor in Er doped miniature Al<sub>2</sub>O<sub>3</sub> optical waveguide amplifiers. *Journal of Applied Physics* [online]. 2003, **93**(9), 5008–5012. ISSN 0021-8979. Dostupné z: doi:10.1063/1.1565697
- [71] JIMÉNEZ DE CASTRO, M., R. SERNA, J.A. CHAOS, C.N. AFONSO a E.R. HODGSON. Influence of defects on the photoluminescence of pulsed-laser deposited Er-doped amorphous Al<sub>2</sub>O<sub>3</sub> films. *Nuclear Instruments and Methods in Physics Research Section B: Beam Interactions with Materials and Atoms* [online]. 2000, **166–167**, 793–797. ISSN 0168583X. Dostupné z: doi:10.1016/S0168-583X(99)01178-7

## Bibliography

- [72] XU, An-Wu, Yuan GAO a Han-Qin LIU. The Preparation, Characterization, and their Photocatalytic Activities of Rare-Earth-Doped TiO<sub>2</sub> Nanoparticles. *Journal of Catalysis* [online]. 2002, **207**(2), 151–157. ISSN 00219517. Dostupné z: doi:10.1006/jcat.2002.3539
- [73] ŠTENGL, Václav, Snejana BAKARDJIEVA a Nataliya MURAFÁ. Preparation and photocatalytic activity of rare earth doped TiO<sub>2</sub> nanoparticles. *Materials Chemistry and Physics* [online]. 2009, **114**(1), 217–226. ISSN 02540584. Dostupné z: doi:10.1016/j.matchemphys.2008.09.025
- [74] SLOOFF, L. H., A. VAN BLAADEREN, A. POLMAN, G. A. HEBBINK, S. I. KLINK, F. C. J. M. VAN VEGGEL, D. N. REINHOUDT a J. W. HOFSTRAAT. Rare-earth doped polymers for planar optical amplifiers. *Journal of Applied Physics* [online]. 2002, **91**(7), 3955–3980. ISSN 0021-8979. Dostupné z: doi:10.1063/1.1454190
- [75] ROBINSON, M.R., J.C. OSTROWSKI, G.C. BAZAN a M.D. MCGEHEE. Reduced Operating Voltages in Polymer Light-Emitting Diodes Doped with Rare-Earth Complexes. *Advanced Materials* [online]. 2003, **15**(18), 1547–1551. ISSN 0935-9648. Dostupné z: doi:10.1002/adma.200304651
- [76] LI, J, O H Y ZALLOUM, T ROSCHUK, C L HENG, J WOJCIK a P MASCHER. Light Emission from Rare-Earth Doped Silicon Nanostructures. *Advances in Optical Technologies* [online]. 2008, **2008**, 1–10. ISSN 1687-6393. Dostupné z: doi:10.1155/2008/295601
- [77] LEDOUX, G., J. GONG, F. HUISKEN, O. GUILLOIS a C. REYNAUD. Photoluminescence of size-separated silicon nanocrystals: Confirmation of quantum confinement. *Applied Physics Letters* [online]. 2002, **80**(25), 4834–4836. ISSN 00036951. Dostupné z: doi:10.1063/1.1485302
- [78] SUMMONTE, C., M. ALLEGREZZA, M. BELLETTATO, F. LISCIO, M. CANINO, A. DESALVO, J. LÓPEZ-VIDRIER, S. HERNÁNDEZ, L. LÓPEZ-CONESA, S. ESTRADÉ, F. PEIRÓ, B. GARRIDO, P. LÖPER, M. SCHNABEL, S. JANZ, R. GUERRA a S. OSSICINI. Silicon nanocrystals in carbide matrix. *Solar Energy Materials and Solar Cells* [online]. 2014, **128**, 138–149. ISSN 09270248. Dostupné z: doi:10.1016/j.solmat.2014.05.003
- [79] GARRIDO, B., M. LÓPEZ, O. GONZÁLEZ, A. PÉREZ-RODRÍGUEZ, J. R. MORANTE a C. BONAFOS. Correlation between structural and optical properties of Si nanocrystals embedded in SiO<sub>2</sub>: The mechanism of visible light emission. *Applied Physics Letters* [online]. 2000, **77**(20), 3143–3145. ISSN 0003-6951. Dostupné z: doi:10.1063/1.1325392
- [80] DELERUE, C., G. ALLAN a M. LANNOO. Theoretical aspects of the luminescence of porous silicon. *Physical Review B* [online]. 1993, **48**(15), 11024–11036. ISSN 0163-1829. Dostupné z: doi:10.1103/PhysRevB.48.11024
- [81] LUPPI, Marcello a Stefano OSSICINI. Ab initio study on oxidized silicon clusters and silicon nanocrystals embedded in Si O<sub>2</sub>: Beyond the quantum confinement effect. *Physical Review B* [online]. 2005, **71**(3), 035340. ISSN 1098-0121. Dostupné z: doi:10.1103/PhysRevB.71.035340

- [82] PALUMMO, M., M. BRUNO, O. PULCI, E. LUPPI, E. DEGOLI, S. OSSICINI a R. DEL SOLE. Ab-initio electronic and optical properties of low dimensional systems: From single particle to many-body approaches. *Surface Science* [online]. 2007, **601**(13), 2696–2701. ISSN 00396028. Dostupné z: doi:10.1016/j.susc.2006.12.019
- [83] GUERRA, Roberto, Elena DEGOLI a Stefano OSSICINI. Size, oxidation, and strain in small  $\langle \text{Si} \rangle_{\text{SiO}_2}$  nanocrystals. *Physical Review B* [online]. 2009, **80**(15), 155332. ISSN 1098-0121. Dostupné z: doi:10.1103/PhysRevB.80.155332
- [84] FURUKAWA, Shoji a Tatsuro MIYASATO. Quantum size effects on the optical band gap of microcrystalline Si:H. *Physical Review B* [online]. 1988, **38**(8), 5726–5729. ISSN 0163-1829. Dostupné z: doi:10.1103/PhysRevB.38.5726
- [85] CANHAM, L. T. Silicon quantum wire array fabrication by electrochemical and chemical dissolution of wafers. *Applied Physics Letters* [online]. 1990, **57**(10), 1046–1048. ISSN 0003-6951. Dostupné z: doi:10.1063/1.103561
- [86] PERÁLVAREZ, M., C. GARCÍA, M. LÓPEZ, B. GARRIDO, J. BARRETO, C. DOMÍNGUEZ a J. A. RODRÍGUEZ. Field effect luminescence from Si nanocrystals obtained by plasma-enhanced chemical vapor deposition. *Applied Physics Letters* [online]. 2006, **89**(5), 051112. ISSN 0003-6951. Dostupné z: doi:10.1063/1.2268706
- [87] HILLER, D., A. ZELENINA, S. GUTSCH, S. A. DYAKOV, L. LÓPEZ-CONESA, J. LÓPEZ-VIDRIER, S. ESTRADÉ, F. PEIRÓ, B. GARRIDO, J. VALENTA, M. KOŘÍNEK, F. TROJÁNEK, P. MALÝ, M. SCHNABEL, C. WEISS, S. JANZ a M. ZACHARIAS. Absence of quantum confinement effects in the photoluminescence of Si<sub>3</sub>N<sub>4</sub>-embedded Si nanocrystals. *Journal of Applied Physics* [online]. 2014, **115**(20), 204301. ISSN 0021-8979. Dostupné z: doi:10.1063/1.4878699
- [88] BERENCÉN, Y., J. M. RAMÍREZ, O. JAMBOIS, C. DOMÍNGUEZ, J. A. RODRÍGUEZ a B. GARRIDO. Correlation between charge transport and electroluminescence properties of Si-rich oxide/nitride/oxide-based light emitting capacitors. *Journal of Applied Physics* [online]. 2012, **112**(3). ISSN 00218979. Dostupné z: doi:10.1063/1.4742054
- [89] VALENTA, J, N LALIC a J LINNROS. Electroluminescence microscopy and spectroscopy of silicon nanocrystals in thin SiO<sub>2</sub> layers. 2001, **17**, 45–50.
- [90] HERNÁNDEZ, S., A. MARTÍNEZ, P. PELLEGRINO, Y. LEBOUR, B. GARRIDO, E. JORDANA a J. M. FEDELI. Silicon nanocluster crystallization in SiO<sub>x</sub> films studied by Raman scattering. *Journal of Applied Physics* [online]. 2008, **104**(4), 044304. ISSN 0021-8979. Dostupné z: doi:10.1063/1.2968244
- [91] HILLER, D., A. ZELENINA, S. GUTSCH, S. A. DYAKOV, L. LÓPEZ-CONESA, J. LÓPEZ-VIDRIER, S. ESTRADÉ, F. PEIRÓ, B. GARRIDO, J. VALENTA, M. KOŘÍNEK, F. TROJÁNEK, P. MALÝ, M. SCHNABEL, C. WEISS, S. JANZ a M. ZACHARIAS. Absence of quantum confinement effects in the photoluminescence of Si<sub>3</sub>N<sub>4</sub>-embedded Si nanocrystals. *Journal of Applied Physics* [online]. 2014, **115**(20), 204301. ISSN 0021-8979. Dostupné z: doi:10.1063/1.4878699



## Bibliography

- [92] ZELENINA, A., S. A. DYAKOV, D. HILLER, S. GUTSCH, V. TROUILLET, M. BRUNS, S. MIRABELLA, P. LÖPER, L. LÓPEZ-CONESA, J. LÓPEZ-VIDRIER, S. ESTRADÉ, F. PEIRÓ, B. GARRIDO, J. BLÁSING, A. KROST, D. M. ZHIGUNOV a M. ZACHARIAS. Structural and optical properties of size controlled Si nanocrystals in Si<sub>3</sub>N<sub>4</sub> matrix: The nature of photoluminescence peak shift. *Journal of Applied Physics* [online]. 2013, **114**(18), 184311. ISSN 0021-8979. Dostupné z: doi:10.1063/1.4830026
- [93] SONG, Dengyuan, Eun-Chel CHO, Gavin CONIBEER, Yidan HUANG, Chris FLYNN a Martin A. GREEN. Structural characterization of annealed Si<sub>1-x</sub>C<sub>x</sub>/SiC multilayers targeting formation of Si nanocrystals in a SiC matrix. *Journal of Applied Physics* [online]. 2008, **103**(8), 083544. ISSN 0021-8979. Dostupné z: doi:10.1063/1.2909913
- [94] HICKMOTT, T. W. Low-Frequency Negative Resistance in Thin Anodic Oxide Films. *Journal of Applied Physics* [online]. 1962, **33**(9), 2669–2682. ISSN 0021-8979. Dostupné z: doi:10.1063/1.1702530
- [95] GIBBONS, J.F. a W.E. BEADLE. Switching properties of thin Nio films. *Solid-State Electronics* [online]. 1964, **7**(11), 785–790. ISSN 00381101. Dostupné z: doi:10.1016/0038-1101(64)90131-5
- [96] SIMMONS, J. G. a R. R. VERDERBER. New Conduction and Reversible Memory Phenomena in Thin Insulating Films. *Proceedings of the Royal Society A: Mathematical, Physical and Engineering Sciences* [online]. 1967, **301**(1464), 77–102. ISSN 1364-5021. Dostupné z: doi:10.1098/rspa.1967.0191
- [97] CHUA, Leon. Memristor-The missing circuit element. *IEEE Transactions on Circuit Theory* [online]. 1971, **18**(5), 507–519. ISSN 0018-9324. Dostupné z: doi:10.1109/TCT.1971.1083337
- [98] ZHUANG, W.W., W. PAN, B.D. ULRICH, J.J. LEE, L. STECKER, a. BURMASTER, D.R. EVANS, S.T. HSU, M. TAJIRI, a. SHIMAOKA, K. INOUE, T. NAKA, N. AWAYA, a. SAKIYAMA, Y. WANG, S.Q. LIU, N.J. WU a a. IGNATIEV. Novel colossal magnetoresistive thin film nonvolatile resistance random access memory (RRAM). *Digest. International Electron Devices Meeting*, [online]. 2002, 193–196. ISSN 01631918. Dostupné z: doi:10.1109/IEDM.2002.1175811
- [99] BAEK, I.G., M.S. LEE, S. SCO, M.J. LEE, D.H. SEO, D.-S. SUH, J.C. PARK, S.O. PARK, H.S. KIM, I.K. YOO, U.-I. CHUNG a J.T. MOON. Highly scalable non-volatile resistive memory using simple binary oxide driven by asymmetric unipolar voltage pulses. *IEDM Technical Digest. IEEE International Electron Devices Meeting, 2004.* [online]. nedatováno, 587–590. ISSN 01631918. Dostupné z: doi:10.1109/IEDM.2004.1419228
- [100] SZOT, Krzysztof, Wolfgang SPEIER, Gustav BIHLMAYER a Rainer WASER. Switching the electrical resistance of individual dislocations in single-crystalline SrTiO<sub>3</sub>. *Nature Materials* [online]. 2006, **5**(4), 312–320. ISSN 1476-1122. Dostupné z: doi:10.1038/nmat1614
- [101] INOUE, I. H., S. YASUDA, H. AKINAGA a H. TAKAGI. Nonpolar resistance switching of metal/binary-transition-metal oxides/metal sandwiches:

- Homogeneous/inhomogeneous transition of current distribution. *Physical Review B* [online]. 2008, **77**(3), 035105. ISSN 1098-0121. Dostupné z: doi:10.1103/PhysRevB.77.035105
- [102] JEON, Sang Ho, Bae Ho PARK, Jaichan LEE, Bora LEE a Seungwu HAN. First-principles modeling of resistance switching in perovskite oxide material. *Applied Physics Letters* [online]. 2006, **89**(4), 1–4. ISSN 00036951. Dostupné z: doi:10.1063/1.2234840
- [103] ROZENBERG, M. J., I. H. INOUE a M. J. SÁNCHEZ. Strong electron correlation effects in nonvolatile electronic memory devices. *Applied Physics Letters* [online]. 2006, **88**(3), 1–3. ISSN 00036951. Dostupné z: doi:10.1063/1.2164917
- [104] HIROSE, Yooichi a Haruo HIROSE. Polarity-dependent memory switching and behavior of Ag dendrite in Ag-photodoped amorphous As<sub>2</sub>S<sub>3</sub> films. *Journal of Applied Physics* [online]. 1976, **47**(6), 2767–2772. ISSN 0021-8979. Dostupné z: doi:10.1063/1.322942
- [105] PICKUP, David M, Gavin MOUNTJOY, Mark a HOLLAND, Graham W WALLIDGE, J NEWPORT a Mark E SMITH. Structure of (Ta<sub>2</sub>O<sub>5</sub>) [online]. 2000, **7**(October), 1887–1894. Dostupné z: doi:10.1039/b000947o
- [106] WANG, Zheng, Peter B. GRIFFIN, Jim MCVITTIE, Simon WONG, Paul C. MCINTYRE a Yoshio NISHI. Resistive Switching Mechanism in ZnxCd1-xS Nonvolatile Memory Devices. *IEEE Electron Device Letters* [online]. 2007, **28**(1), 14–16. ISSN 0741-3106. Dostupné z: doi:10.1109/LED.2006.887640
- [107] SCHINDLER, C., S.C.P. THERMADAM, R. WASER a M.N. KOZICKI. Bipolar and Unipolar Resistive Switching in Cu-Doped SiO<sub>2</sub>. *IEEE Transactions on Electron Devices* [online]. 2007, **54**(10), 2762–2768. ISSN 0018-9383. Dostupné z: doi:10.1109/TED.2007.904402
- [108] OGIMOTO, Yasushi, Yukio TAMAI, Masashi KAWASAKI a Yoshinori TOKURA. Resistance switching memory device with a nanoscale confined current path. *Applied Physics Letters* [online]. 2007, **90**(14), 1–4. ISSN 00036951. Dostupné z: doi:10.1063/1.2720747
- [109] CHOI, B. J., D. S. JEONG, S. K. KIM, C. ROHDE, S. CHOI, J. H. OH, H. J. KIM, C. S. HWANG, K. SZOT, R. WASER, B. REICHENBERG a S. TIEDKE. Resistive switching mechanism of TiO<sub>2</sub> thin films grown by atomic-layer deposition. *Journal of Applied Physics* [online]. 2005, **98**(3), 033715. ISSN 0021-8979. Dostupné z: doi:10.1063/1.2001146
- [110] PINTO, R. Filamentary switching and memory action in thin anodic oxides. *Physics Letters A* [online]. 1971, **35**(3), 155–156. ISSN 03759601. Dostupné z: doi:10.1016/0375-9601(71)90122-8
- [111] MEHONIC, Adnan, Sébastien CUEFF, Maciej WOJDAK, Stephen HUDZIAK, Christophe LABBÉ, Richard RIZK a Anthony J KENYON. Electrically tailored resistance switching in silicon oxide. *Nanotechnology* [online]. 2012, **23**(45), 455201. ISSN 0957-4484. Dostupné z: doi:10.1088/0957-4484/23/45/455201

## Bibliography

- [112] HARTEL, A.M., D HILLER, S GUTSCH, P LÖPER, S ESTRADÉ, F PEIRÓ, B GARRIDO a M ZACHARIAS. Formation of size-controlled silicon nanocrystals in plasma enhanced chemical vapor deposition grown SiO<sub>x</sub>N<sub>y</sub>/SiO<sub>2</sub> superlattices. *Thin Solid Films* [online]. 2011, **520**(1), 121–125. ISSN 00406090. Dostupné z: doi:10.1016/j.tsf.2011.06.084
- [113] SELVAKUMAR, N. a Harish C. BARSHILIA. Review of physical vapor deposited (PVD) spectrally selective coatings for mid- and high-temperature solar thermal applications. *Solar Energy Materials and Solar Cells* [online]. 2012, **98**, 1–23. ISSN 09270248. Dostupné z: doi:10.1016/j.solmat.2011.10.028
- [114] WEIMMERSKIRCH-AUBATIN, J., M. STOFFEL, X. DEVAUX, A. BOUCHÉ, G. BEAINY, E. TALBOT, P. PAREIGE, Y. FAGOT-RÉVURAT, M. VERGNAT a H. RINNERT. Observation of a nanoscale phase separation in blue-emitting Ce-doped SiO<sub>2</sub> thin films. *Journal of Materials Chemistry C* [online]. 2015, **3**(48), 12499–12506. ISSN 2050-7526. Dostupné z: doi:10.1039/C5TC02722E
- [115] DUMONT, Lucile, Julien CARDIN, Patrizio BENZO, Marzia CARRADA, Christophe LABBÉ, Andrea L. RICHARD, David C. INGRAM, Wojciech M. JADWISIENCZAK a Fabrice GOURBILLEAU. SiN<sub>x</sub>:Tb<sup>3+</sup>–Yb<sup>3+</sup>, an efficient down-conversion layer compatible with a silicon solar cell process. *Solar Energy Materials and Solar Cells* [online]. 2016, **145**, 84–92. ISSN 09270248. Dostupné z: doi:10.1016/j.solmat.2015.09.031
- [116] MEHONIC, Adnan, Sébastien CUEFF, Maciej WOJDAK, Stephen HUDZIAK, Olivier JAMBOIS, Maciej WOJDAK, Stephen HUDZIAK, Olivier JAMBOIS, Blas GARRIDO, Richard RIZK a Anthony J KENYON. Resistive switching in silicon suboxide films Resistive switching in silicon suboxide films [online]. 2012, **074507**. Dostupné z: doi:10.1063/1.3701581
- [117] SILES, Pablo F, Muriel De PAULI, Carlos CESAR, Bof BUFON, Vittorio FOGLIETTI, Nan YANG, Carmela ARUTA, Doo Seok JEONG, Reji THOMAS, R S KATIYAR, Al O TIO a Tio Al O. Resistive switching characteristics in memristors with Al<sub>2</sub>O<sub>3</sub> / TiO<sub>2</sub> and TiO<sub>2</sub> / Al<sub>2</sub>O<sub>3</sub> bilayers Electrically tailored resistance switching in silicon oxide outlook structures Resistive switching characteristics in memristors. nedatováno.
- [118] CHOI, Byung Joon, Antonio C. TORREZAN, John Paul STRACHAN, P. G. KOTULA, A. J. LOHN, Matthew J. MARINELLA, Zhiyong LI, R. Stanley WILLIAMS a J. Joshua YANG. High-Speed and Low-Energy Nitride Memristors. *Advanced Functional Materials* [online]. 2016, **26**(29), 5290–5296. ISSN 1616301X. Dostupné z: doi:10.1002/adfm.201600680
- [119] CAMPS, I., A. MARISCAL a R. SERNA. Preparation and broadband white emission of Eu-doped thin films based on SiAlON. *Journal of Luminescence* [online]. 2017, **191**, 97–101. ISSN 00222313. Dostupné z: doi:10.1016/j.jlumin.2016.10.040
- [120] MEHONIC, Adnan, Mark BUCKWELL, Luca MONTESI, Leon GARNETT, Stephen HUDZIAK, Sarah FEARN, Richard CHATER, David MCPHAIL a Anthony J. KENYON. Structural changes and conductance thresholds in metal-free intrinsic SiO<sub>x</sub> resistive random access memory. *Journal of Applied Physics* [online]. 2015, **117**(12), 124505. ISSN 0021-8979. Dostupné z: doi:10.1063/1.4916259

- [121] PARK, Jin Young, Hong Chae JUNG, G. SEETA RAMA RAJU, Byung Kee MOON, Jung Hyun JEONG a Jung Hwan KIM. Tunable luminescence and energy transfer process between Tb<sup>3+</sup> and Eu<sup>3+</sup> in GYAG:Bi<sup>3+</sup>, Tb<sup>3+</sup>, Eu<sup>3+</sup> phosphors. *Solid State Sciences* [online]. 2010, **12**(5), 719–724. ISSN 12932558. Dostupné z: doi:10.1016/j.solidstatesciences.2010.02.032
- [122] DEJNEKA, M. J., A. STRELTSOV, S. PAL, A. G. FRUTOS, C. L. POWELL, K. YOST, P. K. YUEN, U. MULLER a J. LAHIRI. Rare earth-doped glass microbarcodes. *Proceedings of the National Academy of Sciences* [online]. 2003, **100**(2), 389–393. ISSN 0027-8424. Dostupné z: doi:10.1073/pnas.0236044100
- [123] DJURIŠIĆ, A.B., A.M.C. NG a X.Y. CHEN. ZnO nanostructures for optoelectronics: Material properties and device applications. *Progress in Quantum Electronics* [online]. 2010, **34**(4), 191–259. ISSN 00796727. Dostupné z: doi:10.1016/j.pquantelec.2010.04.001